Diagnostics et cinétiques des espèces réactives oxygénées et azotées dans des décharges hors-équilibre à pression atmosphérique pour la bio-décontamination

Arthur Salmon

Diagnostics and kinetics of reactive oxygen and nitrogen species in atmospheric pressure non-equilibrium discharges for bio-decontamination

Thèse de doctorat de l'Université Paris-Saclay
préparée à CentraleSupélec

École doctorale n°579 : sciences mécaniques et énergétiques, matériaux et géosciences (SMEMAG)
Spécialité de doctorat: énergétique

Thèse présentée et soutenue à Gif-sur-Yvette, le 29 janvier 2018, par

M. Arthur Salmon

Composition du Jury :

Brigitte Attal-Trétout	
Directrice de recherche, ONERA	Présidente
Zdenko Machala	
Associate professor, Comenius University	Rapporteur
Thierry Belmonte	
Directeur de recherche CNRS, Université de Lorraine	Rapporteur
Svetlana Starikovskaya	
Directrice de recherche CNRS, Ecole Polytechnique (-LPP)	Examinatrice
Deborah O'Connell	
Assistant professor, University of York	Examinatrice
Jean-Michel Pouvesle	
Directeur de recherche CNRS, Université d'Orléans (-GREMI)	Examinateur
Katharina Stapelmann	
Assistant professor, North Carolina State University	Invitée
Christophe Laux	
Professeur, CentraleSupélec	Directeur de thèse
Gabi Stancu	
Professeur, CentraleSupélec	Co-Directeur de thèse

Thèse de doctorat

Résumé

Les méthodes de stérilisation à basse température prennent une importance croissante pour la décontamination de matériaux thermosensibles utilisés dans les appareils exposés aux risques microbiologiques tels que les endoscopes dans les hôpitaux, les emballages dans l'industrie agroalimentaire, ou les équipements soumis aux agents microbiologiques de guerre dans les zones de conflits. Les méthodes de stérilisation standards non-thermiques souffrent de limitations liées à leur toxicité, leurs coûts élevés, leurs faibles compatibilités avec les matériaux, et/ou leurs longs cycles de stérilisation (quelques heures). Une approche alternative consiste à utiliser des plasmas hors équilibre à pression atmosphérique produits par décharges électriques. Les plasmas permettent des cycles de stérilisation plus courts car les surfaces traitées sont exposées à de nombreux agents biocides, notamment à du rayonnement, à des espèces réactives oxygénées et azotées (RONS), et à des espèces chargées. Cependant, à pression atmosphérique, le volume du plasma est généralement faible. Les traitements en post-décharge permettent d'augmenter la surface de traitement, tout en réduisant la dégradation du matériau par les espèces chargées. Dans la post-décharge, les principaux agents biocides sont les RONS. L'objectif de cette thèse est d'étudier la production et le transport des RONS générés par des décharges pulsées non-thermiques dans l'air et l'azote à pression atmosphérique.

D'abord, le transport de l'azote atomique dans l'état fondamental $N(^4S)$ à l'intérieur de longs tubes de polyuréthane est examinée. Le coefficient de recombinaison à trois corps de $N(^4S)$ est mal connu bien que déterminant dans la modélisation de la recombinaison de $N(^4S)$ à pression atmosphérique. Ce coefficient est réévalué à partir d'une nouvelle approche basée sur de la spectroscopie d'émission absolue et une inversion d'Abel. La probabilité de recombinaison de $N(^4S)$ à la surface du polyuréthane est également déterminée (chapitre II).

Ensuite, la production de RONS par des décharges nanosecondes répétitives pulsées (NRP) dans l'air est étudiée par des techniques d'absorption, notamment spectroscopie d'absorption par laser à cascade quantique (QCLAS) et spectroscopie d'absorption UV large bande Une étude paramétrique montre que des concentrations significatives d'ozone (O_3) et d'oxydes d'azote (NO_X) sont produites à faible coût énergétique. Des tests microbiologiques révèlent que faire varier la production de RONS d'un régime riche en NO_X à un régime riche en O_3 augmente l'efficacité sporicide des NRP (chapitre III).

Enfin, la recirculation du gaz entre les électrodes suite à une décharge nanoseconde 'spark' est étudiée par fluorescence induite par laser (LIF). Les effets de recirculation du gaz sur la température et la production de NO sont examinés par QCLAS temporellement résolue. Il est montré que la recirculation cause un refroidissement rapide du gaz mais n'entraîne aucun effet sur la production de NO (chapitre IV). La recirculation du gaz pourrait donc être bénéfique pour le traitement plasma de matériaux thermosensibles dans la mesure où elle assure une basse température des espèces réactives sans réduire leur efficacité de production dans la décharge.

Abstract

Low-temperature sterilization methods are of increasing importance for the decontamination of heat-sensitive materials in devices exposed to biohazards, such as endoscopes in hospitals, containers in the food industry, or contaminated equipment in areas exposed to war acts. Standard non-thermal sterilization methods suffer from limitations related to their toxicity, high cost, low material compatibility, and/or long sterilization cycles (several hours). An alternative approach consists in using atmospheric pressure nonequilibrium plasmas produced by electric discharges. Plasmas provide shorter sterilization cycles because they combine various biocidal agents including radiation, reactive oxygen and nitrogen species (RONS), and charged species. However, at atmospheric pressure the plasma volume is usually small. Post-discharge treatment allows to increase the treated surface area, and in addition to reduce surface degradation by charged species. In post-discharge treatment, the main biocidal agents are the RONS. The objective of this thesis is to study the production and transport of RONS generated by non-thermal pulsed discharges in nitrogen and air at atmospheric pressure.

First, the transport of ground state atomic nitrogen $N(^4S)$ inside long polyurethane tubes is investigated. The poorly known $N(^4S)$ three-body recombination rate coefficient is re-evaluated using a new approach based on absolute emission spectroscopy and an Abel inversion. The probability of $N(^4S)$ surface recombination on the polyurethane surface is also determined (chapter II).

Second, the production of RONS by nanosecond repetitively pulsed (NRP) discharges in air is studied by absorption techniques, namely by Mid-IR Quantum Cascade Laser Absorption Spectroscopy (QCLAS) and by broad-band UV absorption spectroscopy. A parametric study shows that significant concentrations of ozone (O_3) and nitrogen oxides (NO_X) are produced at low energy cost. Microbiological tests reveal that tuning the RONS production from NO_X-rich to O_3-rich regimes increases the sporicidal efficacy of NRP discharges (chapter III).

Third, the gas recirculation between the electrodes following a nanosecond spark discharge in air is studied by laser induced fluorescence (LIF). The effects of gas motion on the gas temperature and NO production are investigated by time-resoled quantum cascade laser absorption spectroscopy (QCLAS). It is shown that gas recirculation causes faster gas cooling without reducing the NO production efficiency (chapter IV). Therefore gas recirculation may be beneficial for plasma treatment of heat-sensitive

materials because it ensures a low temperature of the reactive species without influencing their production efficiency in the discharge phase.

Remerciements

Contents

Chapter I

Introduction to plasma decontamination of surfaces

This chapter presents an introduction to the topic of plasma decontamination of surfaces. Section 1 introduces the challenges related to non-thermal decontamination. Section 2 presents background on the microorganisms and on the evaluation of a decontamination method. Section 3 reviews the state-of-the art of plasma decontamination. Finally, section 4 summarizes the objectives of this thesis.

1. Context and applications

1.1. Introduction

Bio-decontamination refers to the inactivation of microorganisms from a surface or a liquid. Three levels of bio-decontamination methods are defined depending on their efficacy in killing microorganisms [1]: i/ sterilization, which corresponds to the complete removal or destruction of microorganisms, ii/ disinfection, which kills most pathogenic microorganisms, except bacterial spores, iii/ cleaning, which removes soil and organic matter from the object and usually preceeds a disinfection or a sterilization process.

Standard heat sterilization methods, e.g. dry heat, autoclave, are widely used because of their short sterilization cycle, high efficiency and low cost. However the sterilization of complex and heat-sensitive materials, e.g. polymers, is not possible using these technologies. This kind of materials is increasingly used in devices exposed to biohazards in various fields introduced in the next section.

1.2. Applications

Non-thermal decontamination is required in a wide range of applications. Here, we briefly introduce the challenges associated to the non-thermal decontamination of surfaces in healthcare facilities, food industry and space exploration.

- **Medical safety**

In Europe and the USA, healthcare-related infections affect 4.5 million and 1.7 million patients per year, respectively, accounting for 100,000 and 37,000 deaths, respectively [2]. These numbers remain high because of the increasing resistance of microorganisms against chemical sterilization methods used to process heat-sensitive devices, e.g. endoscopes, catheters [3]. In addition, it is necessary to re-use medical devices because of their increasing complexity and cost. This increases the risk of patient-to-patient outbreaks [4] because the devices encounter pathogens during their use that may contaminate subsequent patients. Moreover, the bioburden on the device is higher after use, thus making the decontamination process more difficult.

Endoscopes, which are widely used for therapy and diagnostics of medical disorders [5], are contaminated by about 10^9 colony-forming-units (cfu) per device in average after use [6]. Preliminary cleaning is critical to lower the initial load before disinfection [5]. Cleaning typically reduces the bioburden below 10^5 cfu [6], [7]. Following the cleaning, the most common way to treat an endoscope is to flow a solution of 2% glutaraldehyde through its channels. However the technique has several diasvantages. Once activated, glutaraldehyde produces toxic vapour that may cause occupational asthma and contact dermatitis to the user [3]. Daily exposure to glutaraldehyde vapour is limited to 0.02 to 0.05 ppm as defined by the World Health Organization [1]. In addition, transmissions of *Pseudomonas*, *Salmonellas*, and *Mycobacterium* species are regularly reported after the reprocessing of endoscopes by glutaraldehyde [3], [4], [8], [9]. Therefore, the demand of decontamination technologies able to treat endoscopes with minimal degradation remains high in healthcare facilites.

- **Food safety**

Decontamination is involved in food processing and packaging to prevent foodborne diseases provoked by various types of bacteria, viruses, parasites, toxins, and chemicals [10], [11]. The World Health Organization estimates that 33 million lives are affected by foodborne diseases, including 420,000 deaths in 2010 [12]. Most of them are located in low income countries, but foodborne diseases can readily cross borders because of world globalization.

Heat processing is a conventional way to eliminate pathogens but it alters the contents of nutrients, as well as the taste, color, and smell of food. For these reasons, the consumption of minimally processed food is continuously increasing. However, the consumption of fresh produce contributes to the transmission of bacteria, viral and parasitic pathogens [11], [13]. Washing and cleaning techniques are not efficient against vari-

ous microorganisms, especially when bacteria attach to the surface and form biofilms. Alternative techniques have emerged to reduce the alteration of food quality by the decontamination process. These new processing technologies include ionizing radiation, ultrasounds, high hydrostatic pressure, or pulsed electric fields [11].

- Space exploration

Decontamination of spacecraft is critical in space exploration in order to avoid interplanetary contamination. Planetary protection is divided into *forward contamination*, which refers to the contamination by Earth's species of explored bodies, and *backward contamination*, which refers to the contamination of Earth's biosphere from returned samples carried from the explored bodies. Forward contamination is especially critical for the exploration of bodies susceptible to develop extraterrestrial life –e.g. Europa. Contamination with Earth's bacteria may definitely spoil the research of life on that body. Backward contamination is important for the protection of Earth from extraterrestrial life which may interfere irreversibly with Earth's biosphere. The Panel on planetary protection of the Committee on Space Research (COSPAR) issued recommendations to avoid interplanetary contamination, and defined five categories indicating the required level of sterilization of the spacecraft [14]. Criteria depend on the type of mission (e.g. lander, flyby), the destination (e.g. planet, asteroid, moon) and on the planetary bodies that may be encountered during the mission. Various components of the spacecraft, e.g. electronics, cannot be decontaminated by classical thermal methods

1.3. Motivation

Thermal sterilization is not suitable for the processing of materials mentionned in the previous section. Table I.1 shows a non-exhaustive list of alternative non-thermal methods widely used nowadays. These methods suffer from limitations related to their dangerousity, high cost, material compatibility and long sterilization cycles (30 min to several hours). Therefore non-thermal decontamination is still an important subject of researches. In this thesis, the use of atmospheric pressure plasmas for low-temperature decontamination is studied.

The next section gives a description of the main types of microorganisms encountered in decontamination studies, and presents the method of evaluation of a decontamination process.

Table I.1 : Features of some decontamination methods, modified from [7]

Method	Sterilization cycle	Material compatibility issues [15]	Safety issues	Cost
Steam (autoclave)	120-180 min	Heat-sensitive materials	None	Low
Gamma rays	Short	PVC, PTFE, Acetal, [16]	None	High
Ethylene Oxide (EtO, 100%)	3-10h+12h aeration	Aluminium, brass, copper, epoxy, natural rubber, silicone, polyurethane	Toxic, carcinogenic, flammable	Fair
Hydrogen peroxide	30-45 min	Lead, brass, copper, zinc, cellulose	Harmful to eye, possibly toxic >1 ppm TWA	Fair
Peracetic Acid	30-45 min	Non-immersible devices	Harmful to eye and skin	Fair
Formalde-hyde	>22h	Carbon steel, nylon, Viton	Carcinogenic, irritating	Fair
Glutaralde-hyde	>10 h	None	Irritating vapors	Fair

TWA=time-weighted average for a conventional 8-hour workday; RH=relative humidity

2. Decontamination: theoretical background

The present section gives a description of the structure and resistance mechanisms of the microorganisms commonly encountered in decontamination studies. Then, the method of evaluation of a decontamination procedure is presented. Finally, we discuss the limitations of non-thermal methods to ensure sterility of surfaces.

2.1. Microorganisms: structure and resistance

2.1.1. Biofilms and planktonic state

Microorganisms present on surfaces can either form **biofilms** or stay in a **planktonic state,** i.e. isolated organisms. In nature, about 99% of microorganisms form biofilms in humid media. The formation of biofilms is initiated by a robust adhesion of microorganisms on a surface, followed by the aggregation of other microorganisms [17]**.** Several mechanisms explain the high resistance of biofilms. First the barrier properties limit the influence of UV radiation (short absorption length) and chemicals (short diffusion

length). Second, intercellular communication allows some portions of the biofilm to stay in a dormant state (i.e. non-dividing cells with reduced metabolic activity), in which the resistance of microorganisms is increased [18]. These dormant cells prevent complete biofilm removal, thus they allow biofilm to recur after germicidal treatment. A third resistance mechanism is the presence in the biofilm of a resistant sub-population referred as persisters. Details on the formation of *E. Coli* biofilms can be found in Ref. [19]. Although they are less resistant, almost all microbiological tests are routinely developed using microorganisms in planktonic states because they are more suitable to reproduce [20]. In this thesis, the focus was done on microorganisms in a planktonic state.

2.1.2. Classification of microorganisms

Figure I.1 shows a simplified classification of the microorganisms most commonly used in bio-decontamination. Microorganisms are classified into six main kingdoms: bacteria, archae, fungi, protozoa, algae and viruses. The kingdoms are subdivided into different categories which are detailed in the following paragraphs. Here, we will focus on kingdoms bacteria and fungi because of their predominant use in decontamination studies. For a description of other types of microorganisms, interested readers are referred to Ref. [21].
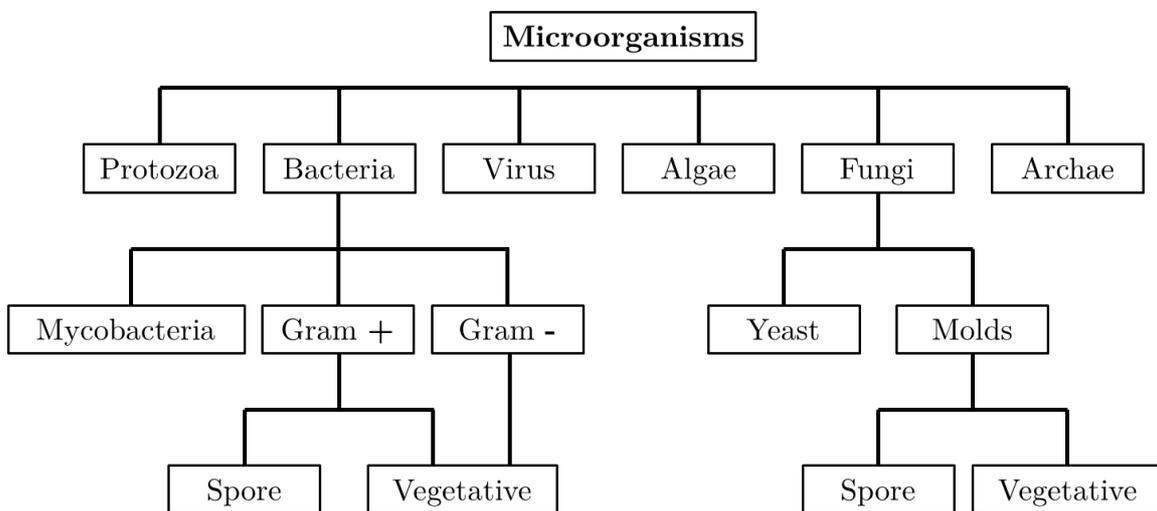
Figure I.1: Simplified arborescence of the most commonly studied microorganisms in bio-decontamination.

- Bacteria in a vegetative state

Bacteria are unicellular prokaryotic organisms. They are named according to their genus, which refers to the shape of the bacteria, e.g. rodlike for *Bacillus* genus and spheri-

cal for *Coccu*, and their species, e.g. *Atrophaeus*. As can be observed by scanning electron microscopy (Figure I.2), bacteria have the ability to form clusters, e.g. chains for *Streptococcus* or grapelike clusters for *Staphylococcus*. Bacteria have dimensions on the micrometer scales, one of the largest being *Bacillus Anthracis* (1×3-10 µm), and *Pasteurella tularensis* being among the smallest (0.2x0.2-0.7 µm) [22].

├─┤ 1 µm   ├─┤ 1 µm
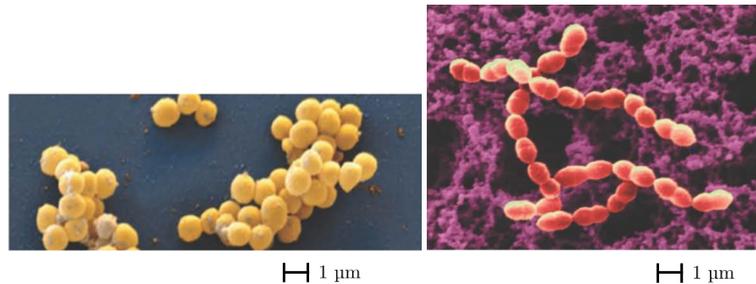
Figure I.2: Clusters of bacteria – *Staphylococcus Aureus* grapelike cluster (left) and *Streptococcus* chain (right) (taken from [21])

The cell wall of bacteria is mainly composed of carbohydrate and peptidoglycan. Depending on the structure of the cell wall, bacteria are subdivided into two groups: Gram-positive (Gram +) and Gram-negative (Gram -) bacteria. Figure I.3 gives a description of the structure of the cell wall of Gram + and Gram - bacteria. The cell wall of Gram + bacteria is composed of several layers of peptidoglycan. Gram – cell wall is composed of a few layers of peptidoglycan surrounded by a bi-lipidic membrane and lipopolysaccharides (LPS) [23].
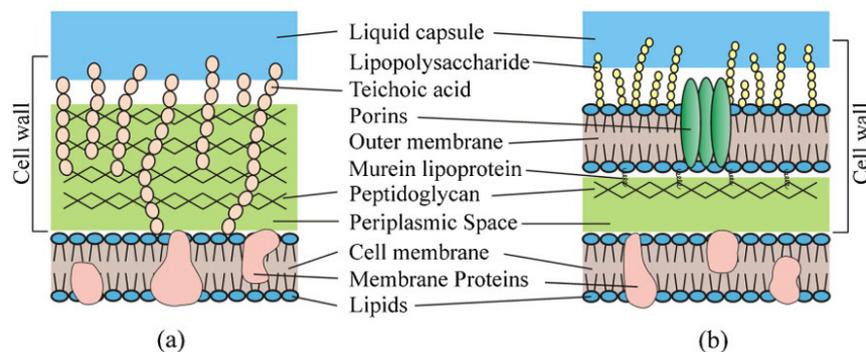
Figure I.3: Schematic diagram of the cell envelope arrangement of the Gram-positive *S. aureus* (a) and Gram-negative *P. aeruginosa* (b) bacteria (not drawn to scale). The cell envelope is defined as the cell membrane and cell wall plus an outer membrane, if one is present, taken from [24].

The wall of Gram + cells is much thicker (20-80 nm) than the wall of Gram – cells (peptidoglycan 5-10 µm thick + outer membrane 7.5-10 µm thick) [22]. This makes

Gram + bacteria less permeable to chemicals than Gram – bacteria, thus giving them a higher resistance to chemical sterilization.

- Bacteria in a sporulated state (endospores)

Bacillus and *Clostridium* Gram + bacteria can change their structure in response to environmental stress –e.g. UV radiation, high temperature, lack of nutrients – to form an endospore during a process known as sporulation. During sporulation, the DNA is replicated and encapsulated in a capsule before being expelled from the bacterial cell. A description of the mechanism of sporulation is given in Ref. [21]. Expelled endospores are in a resistant dormant state in which they can survive for thousands of years.

Because of their high level of resistance, endospores are widely used as reference microorganisms named bio-indicators to assess the efficiency of a sterilization process. Endospores are composed of a dehydrated core surrounded by several proteic layers (about 50% of their volume, [25]). The main resistance mechanisms of endospores have been identified in Refs. [26], [27]. First, the proteins of the exosporium act as a barrier against oxidizing agents such as hydrogen peroxide, ozone, peroxynitrite, chlorine dioxide and hypochlorite. Second, the inner membrane of the spore is impermeable, so that introduction of chemicals inside the spore is limited. Third, the low water content of the endospore limits the action of heat. Fourth, the DNA of endospores is saturated by proteins that protect the DNA against radiation and heat. Finally, some mechanisms can be triggered to repair DNA in case of damage.

- Mycobacteria

Mycobacteria are aerobic, non-endospore forming rods. The *myco* prefix, which means fungus-like, refers to their filamentary growth. The structure of the mycobacteria cell wall is quite similar to that of Gram – bacteria except that the lipopolysaccharides are replaced by mycolic acids that form a water-resistant layer [21], [28]. This makes mycobacteria resistant to stress such as drying. The most important pathogens of genus mycobacteria are *Mycobacterium tuberculosis* responsible of tuberculosis and *Mycobacterium leprae* which causes leprosy. The resistance of mycobacteria to chemicals comes from the slow diffusion of species through the cell wall and a reduced number of pores through which chemicals can access the cell. Additionally UV repairing has been identified but the susceptibility to UV exposure varies with the species. It is estimated that mycobacteria are two to three times more resistant to UV than other bacteria [29]. They are however less resistant to UV than bacterial spores *B. Subtilis* [30]. The two main chemicals used as anti-mycobacteria agents are isoniiazid (INH) and ethambutol.

Both chemicals have the ability to inhibit the synthesis of mycolic acid, thus inactivating mycobacteria.

- Fungi

Fungi are eukaryotic cells studied in agriculture to prevent plant infection [31], but also because the number of human infections caused by fungi is increasing [32]. Fungi are sub-divided into two categories: multicellular molds, e.g. *Aspergillus Niger*, and unicellular yeasts, e.g. *Candida Albicans* [21]. Molds are composed of long filaments of cells called *hyphae.* In most molds, cells are separated by the *septa.* Like bacteria, molds can form spores. *Hyphae* can grow from a fungal spore so that reproduction continues. The resistance of *fungi* spores to heat and dry treatment is high but not as much as endospores. Yeasts are a unicellular form of *fungi*, with oval shape. Yeasts form grapes, so they do not have the filamentary structure of multicellular molds. The cell wall of most *fungi* is composed of glucan linked to chitin, which are polysaccharides [33]. Both species have a bi-lipidic cell membrane, commonly present in cells.

The most important antifungal chemicals are azole compounds and polyenes (amphotericin B) [34], [35]. Azole compounds prevent the synthesis of ergosterol and thus destabilize the cell membrane, while polyenes induce the formation of pores in the cell membrane leading to impaired cell function. *Aspergillus Brasiliensis* moulds are bioindicators of UV sterilization.

The resistance of microorganisms is thus mainly due to their structure and cell wall composition which avoid the penetration of chemicals, heat or radiation. Figure I.4 summarizes the order of resistance of the microorganisms defined in this section to chemical sterilization methods [36], together with the main components of the cell wall. In the next section we present the method of evaluation of a decontamination method.
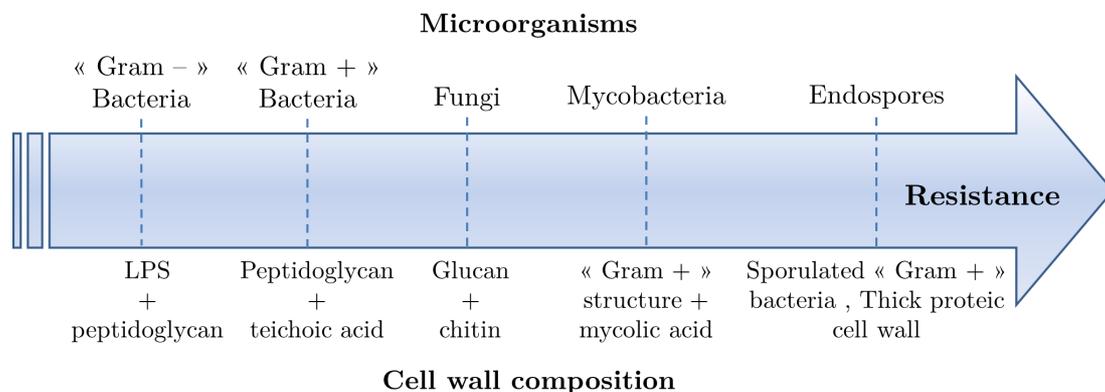
Figure I.4: Resistance of microorganisms to disinfection and sterilization together with their cell wall composition, modified from [7] – LPS: lipopolysaccharide

2.2. Evaluation of a decontamination method

The evaluation of a decontamination method is usually done by direct counting cell methods based on the following procedure. First, a suspension of microorganisms is prepared, generally in sterile water. Concentration of the suspension is adjusted by subsequent dilution. Second a fraction of the suspension is deposited on two carriers and dried. In general, $\sim 10^6$ microorganisms are deposited on the carriers so as to follow ISO 11138 series and ISO 14161 norms [37]. Third, one of the carriers is treated while the other is used as a control. Fourth, the microorganisms are extracted from the carriers and counted using a plate count method. Basically, the suspension of recovered microorganisms is diluted, spread on plates and incubated. The number of colony forming units (CFU) on the plate is finally counted. If N is the number of CFU after the decontamination treatment, and N_0 the number of CFU on the control sample, the log-reduction factor (RF) is defined as follows:

$$RF = \log\left(\frac{N_o}{N}\right) \tag{I.1}$$

For an initial load of 10^6 microorganisms onto a surface the maximum reduction factor measurable by direct cell counting is 6-log. On the basis of a statistical analysis, a reduction factor as low as 8-log can be determined by a fraction negative method [38].

2.3. Non-thermal sterilization: limitations

The ISO 11138 series and ISO 14161 norms define sterility as a sterility assurance level (SAL) of 10^{-6}, i.e. ensurance of a minimal 12-log reduction. This SAL denotes the probability that not more than one viable microorganism survived to the treatment of one million items. The sterility cannot be verified in practice but is extrapolated from the kinetic of the inactivation rate of the most resistant microorganism, i.e. bio-indicator (BI). Table I.2 lists some of the commonly used bio-indicators.

Figure I.5 **s**hows the inactivation kinetic in a semi-logarithmic scale, and the methods used to analyze it. For steam heat sterilization, the inactivation kinetic follows the ideal exponential behaviour, so the inactivation rate can be easily extrapolated to know under which conditions sterility can be warranted. The slope of the semi-logarithmic line is named the *D-value* and is widely used to evaluate the efficiency of a sterilization process.

Table I.2 : Bio-indicators used in standard sterilization methods, modified from [39]

Method	Microorganism	Form
Wet heat	G. Stearothermophilius	Spore
Dry heat	B. Atrophaeus	Spore
UV rays	B. Pumilus	Spore
	A. Brasiliensis	Fungi
γ rays	D. Radiodurans	Vegetative
	B. Pumilus	Spore
Ozone	G. Stearothermophilius	Spore
C_2H_4O	B. Atrophaeus	Spore
CH_2O	G. Stearothermophilius	Spore
H_2O_2	B. Atrophaeus	Spore

C_2H_4O: ethylene oxide; CH_2O: formaldehyde; H_2O_2: hydrogen peroxide

In the case of non-thermal decontamination, multiphasic decay of microorganisms is regularly reported, e.g. [40]–[44]. The multiphasic decay is generally attributed to the clumping of microorganisms that reduces the number of microorganisms attainable by the antimicrobial agents [40]. However such multiphasic decay is also observed when a monolayer of spores is deposed on the surface, e.g. [45], [46], thus suggesting time-variations of the mechanisms of inactivation or slower inactivation at low bioburden [38].
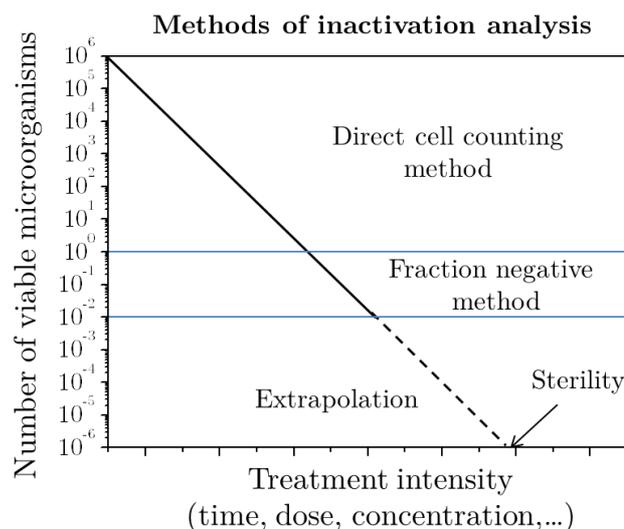
Figure I.5: Ideal inactivation kinetics of microorganisms analyzed by different methods, modified from [38].

Figure I.6 compares the inactivation kinetic of non-thermal and heat decontamination methods. The inactivation rate of heat decontamination can be extrapolated at low number of viable microorganisms while the behaviour is unpredictable for non-thermal decontamination. As a result, ensuring a SAL of 10^{-6} using non-thermal decontamination methods is nearly impossible.
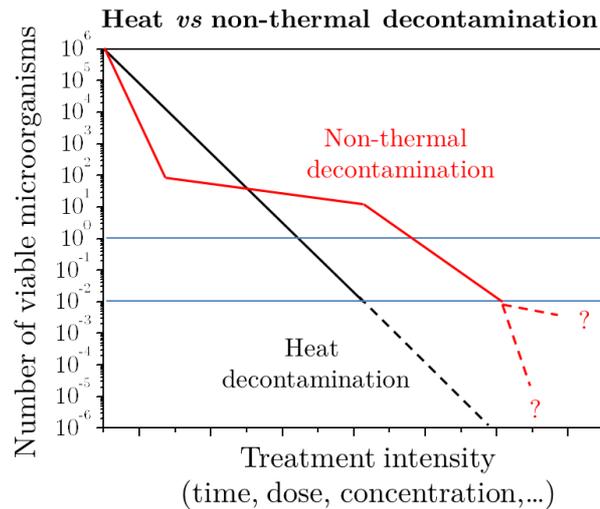
Figure I.6 : Characteristic inactivation kinetic of heat sterilization and non-thermal decontamination methods.

The complex inactivation kinetic of non-thermal methods prevents their use as a universal sterilization technique because the inactivation cannot be extrapolated and sterility warranted (SAL of 10^{-6}). Rather than sterilization, von Woedtke et al. [38] proposed the microbiological safety qualification "proof of antimicrobial efficacy on the highest experimentally accessible level" as the highest possible qualification for heat-sensitive devices. This qualification more precisely represents the level of safety atteinable with non-thermal methods, including non-equilibrium plasma introduced in the next section.

3. Low-temperature plasmas for decontamination

A plasma is a neutral gas in which a significant fraction of the molecules and atoms are ionized. Non-equilibrium low-temperature plasmas can be produced at atmospheric pressure by electrical discharges (section 3.1). They are promising for low-temperature decontamination since they provide numerous biologically active agents (section 3.2). Combining antimicrobial agents may increase the rate of inactivation of microbes, and thus reduce treatment time and minimize the degradation of materials. However, the

efficiency of plasma decontamination process depends on various environmental factors that are necessary to identify in order to define standards for microbiological test procedures (section 3.3). An overview of inactivation results of spores by non-equilibrium plasma and standard sterilization techniques (section 3.4) is discussed on that basis. The conclusions of this review will help to define the decontamination strategy chosen in this thesis (section 4).

3.1. Non-equilibrium plasma generation

A plasma is produced by providing energy to the gas, either by heating –e.g. solar plasma, fusion plasma – or by applying an electric field to induce electrical breakdown of the gas –e.g. electric discharge, lightning.

- Plasma initiation: breakdown

In ambient air, free electrons are naturally present at a concentration of about 1000 per cubic centimeter because of natural radioactivity or cosmic rays bombardment of the Earth. Applying an electric field between electrodes in air accelerates the free electrons, which are much more mobile than ions. Electrons transfer part of their kinetic energy to the surrounding gas molecules and atoms through collisions. If the electric field is high enough, electrons gain sufficient energy to ionize the surrounding species, thus allowing the propagation of an electric current through the gas. This process is called gas breakdown. The breakdown voltage is predicted by the Paschen law and depends on the product of the gas pressure, p, and inter-electrode gap distance, d. This law is valid for typical values pd < 4000 torr.cm. Above these values, breakdown occurs through a different mechanism called streamer breakdown [47].

- Temperature stabilization

After breakdown, a conductive channel is established between the electrodes. The electric current grows because of successive ionization. Under continuous DC excitation at atmospheric pressure, the gas temperature T_g tends to equilibrate with the electron temperature T_e (typically at several 1000 K) on millisecond timescales (see Figure I.7) because of Ohmic heating, and the plasma is said thermal –e.g. arc discharge [48].

In low-temperature plasmas the average electric current is maintained low by various means –e.g. introduction of a dielectric barrier, pulsing the plasma, etc. Ohmic heating is thus limited and the gas temperature remains low [49].
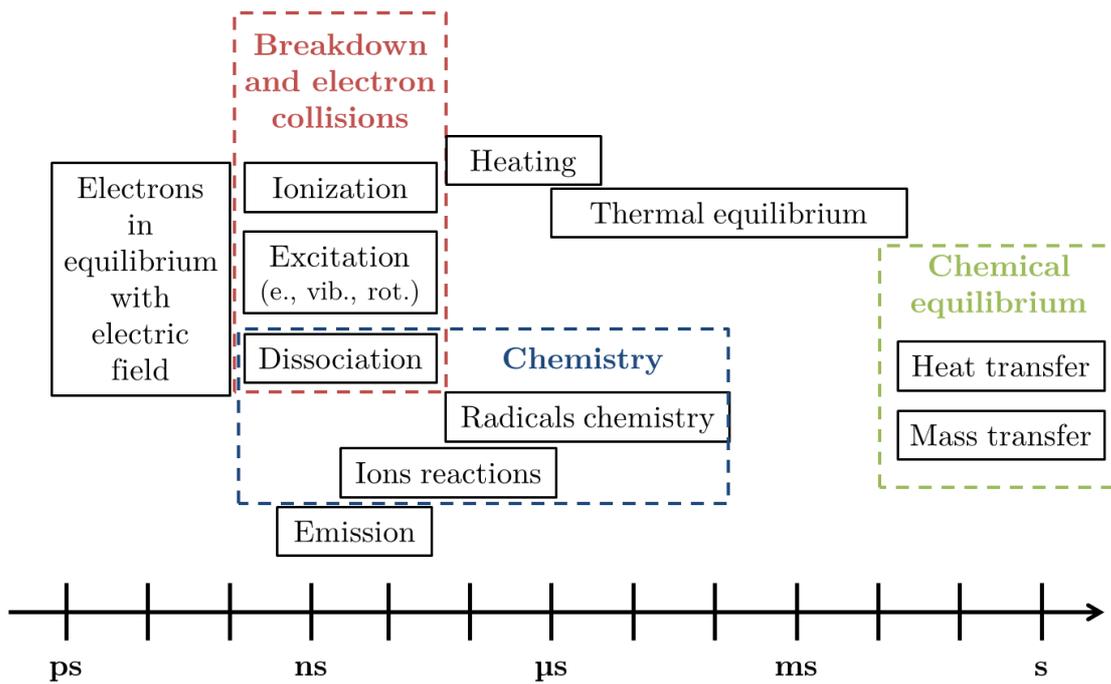
Figure I.7: Atmospheric pressure timescales of relevant chemical and physical processes, modified from [49]

- Source of radicals and radiation

In air or nitrogen plasmas, electrons transfer their energy to surrounding neutrals mostly through inelastic collisions that produce rotational, vibrational, and electronic excitation as well as ionization and molecular dissociation. Reaction rates are determined by the cross-section associated to each chemical reaction and by the energy distribution of the electrons determined from the Boltzmann equation. Figure I.8 shows calculated rate coefficients of elastic and inelastic collisions in synthetic air at different values of the reduced electric field E/N (ratio of electric field strength to the gas particle number density). The calculations were perfomed solving the Boltzmann equation using the Bolsig + solver [50] and using the cross sections given in the databases of Phelps and Morgan for N_2 and O_2, respectively [51], [52]. Figure I.8 shows that the energy deposited into vibrational/electronic excitation, molecular dissociation, and ionization can be controlled to some extent by adjusting the reduced electric field. At low reduced electric fields (say below 100 Td), most of the energy introduced into the plasma is converted into vibrational excitation of nitrogen. At higher reduced electric fields, a larger fraction of the energy is spent into ionization and dissociation, thus increasing the efficiency of production of radicals. These radicals are useful for a wide range of applications [53] -e.g. surface modification, etching, pollutant abatement, and biolomedical applications. The low temperature of non-equilibrium plasmas allows

the development of biological applications ranging from decontamination [39], food and plant treatment [54], wound healing [55], to anti-cancer therapy [56]. An introductory review can be found in Ref. [57].
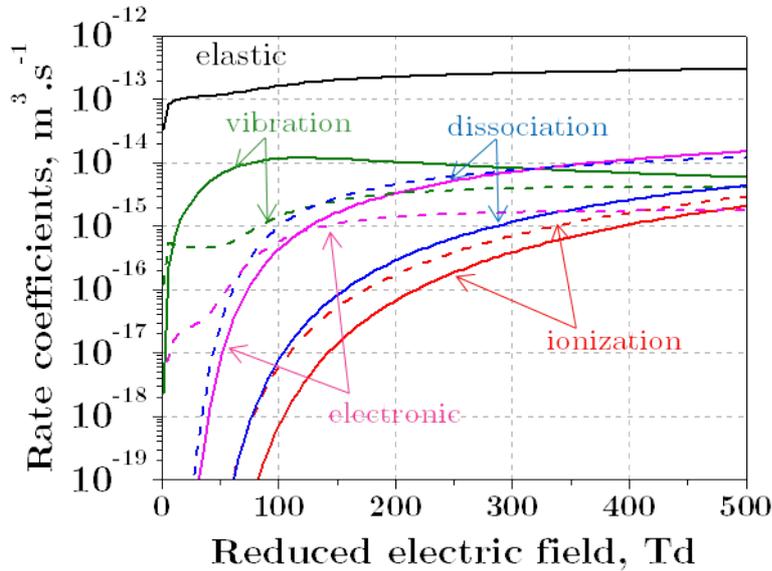
Figure I.8 : Rate coefficients of elastic collisions, vibrational and electronic excitation, dissociation and ionization of oxygen (dash) and nitrogen (line) molecules in synthetic air plasma – cross sections are from the Phelps database [51] for N_2 and the Morgan database [52] for O_2, calculations are performed using the Bolsig + solver [50].

3.2. Decontamination agents of plasma

In the field of decontamination, cold plasma sources at reduced pressure have already proved their efficiency to treat large areas, e.g. [58]–[61]. However atmospheric pressure plasmas are increasingly studied because they are more practical to implement. Three main agents have been identified to cause germicidal effects: radiation, chemical species, and charged species (and associated electric field).

3.2.1. Radiation

Exposure to UV-c (200-290 nm) radiation is among the well-known decontamination techniques routinely used in laboratories [62]. With UV doses in the range ~1-10 mJ/cm² [63], absorption of the radiation by DNA induces damages causing interruption of transcription and replication, and finally cell death [64]. Slightly lower sporicidal effect of VUV radiation has also been demonstrated in Ref. [65]. In most reduced pressure discharges, the contribution of radiation to the inactivation of microorganisms is particularly important [58]. Radiation is particularly efficient against bacterial spores,

in combination with etching of the spore's coat by plasma species [40], [65]. UV radiation can also be generated in atmospheric pressure plasmas, but it is rarely the dominant decontamination means [66] –e.g. in air [67] and pure nitrogen [68], [69]- except in argon discharges [39] and N_2-N_2O plasma [41].

3.2.2. Reactive oxygen and nitrogen species

Plasma discharges produce atomic species, atoms and molecules in excited states, and radicals. Among them, reactive oxygen and nitrogen species (RONS) –e.g. O, OH, O_2^-, $O_2(a^1\Delta_g)$, H_2O_2, NO, NO_2, O_3 - are known to cause oxidative stress under high concentration [68], [70]–[72]. An oxidant-antioxidant unbalance in cells is known to play a role in the development of diseases, and thus maintaining the proper balance with administration of RONS at therapeutic concentration is a novel strategy for therapy [72],[73]. Because of their small size, a significant fraction of the species can pass through the membrane or through pores [74]–[76]. Inside the cells, several action mechanisms are possible, including protein denaturation [77], oxidation of membrane lipids [78], [79], and damage of nucleic acids of DNA [80].

3.2.3. Charged species and electric field

Microsecond pulsed electric fields allow transient formation of pores in the cell membrane, a process studied for several decades and known as electroporation [81]. The electric field induces a transmembrane potential difference (about 1 V) which can open the membrane. This effect is reversible if the diameter of the pores is not too large, and can then be used to transfer drugs to the cell without causing structural damage to the membrane. This is particularly studied in plasma medicine to facilitate drug delivery into the cells. If the applied electric field is high enough, the diameter of the pores increases and can cause irreversible damage to the cell membrane, leading to cell death.

Pulsed electric fields (PEF) can eliminate yeasts and bacteria. Elimination of endospores is still not feasible according to Refs [82], [83] with electric field strengths of about 7.5 kV/cm. However, a cumulative effect of pulses on inactivation of endospores and a linear dependence on the electric field have been reported in [84], where a 3 log-reduction of *B. Subtilis* was observed after 300 pulses of 23.3 kV/cm. In Ref. [85], a pulsed electric field of 22.4 kV/cm was sufficient to observe a slight effect on *C. tyrobutyricum*, but a possible cumulative effect was not investigated. A recent study [86] showed a sporicidal effect of PEF in combination with a heat source (70-90°C). PEF is particularly used for microbial food inactivation [87]. For this application, the use of short pulses allows to limit heating of food, and to use lower energy input [88]. Because electric fields induce cell lysis, a release of endotoxins –e.g. lipopolysaccharides in

Gram-negative bacteria – is expected [89]. These endotoxins can induce pathological effects such as fever and septic shock.

PEF is thus a promising technique but a complete inactivation of bacterial spores has not been demonstrated yet, and the technique is limited to the treatment of liquids [11].

Charged species produced in a plasma discharge can induce similar effects, since they can charge the outer membrane, thus increasing the transmembrane potential difference until cell disruption [73], [90], [91]. An alternative theory proposes that cell disruption is caused by the alteration of cell membrane components by oxidation decreasing the tensile strength [92]. This theory was supported in Ref. [31] by the observed disruption of fungal hyphae. In Ref. [93], the effects of UV radiation, ozone, and hydrogen peroxide produced by a Floating Electrode Dielectric Barrier Discharge (FE-DBD) discharge were shown to be secondary in comparison to the effect of charged species. It was proposed that ions catalyze oxidation and peroxidation chain reactions leading to the damage of the cell membrane of bacteria. Hence, charged species may act on the cell membrane either by catalyzing degradation reactions, or by increasing the transmembrane potential leading to cell lysis.

3.3. Environmental factors influencing plasma decontamination of surfaces

Microbes inactivation rate does not only depends on the efficiency of the tested decontamination method, but is also influenced by the environment of the microbes. Therefore, comparison between inactivation results of microbes treated, prepared in different environmental conditions is nearly impossible. To facilitate the comparison standardized microbiological test procedures are defined and a bio-indicator (BI) is identified.

It is regularly mentioned that defining decontamination standards is a necessary step to adress future validation of the plasma decontamination method [39], [46]. The present section aims to identify key environmental factors influencing the inactivation results of microbes treated by plasma.

3.3.1. Effect of microbes manufacture method

The initial suspension of microorganisms is generally prepared in sterile water. However, in realistic conditions, the bioburden is surrounded by organic and inorganic matter (soil). The soil can be well-removed by a preliminary cleaning using water

(lowest bio-decontamination level) according to the guidelines of Rutala et al. [7]. However inorganic residues may still persist after cleaning. This can be simulated in the microbiological treatments by adding salt or serum to the initial suspension of microorganisms. Such additives are known to strongly reduce the efficiency of most decontamination methods [94]. In particular, it has been shown that a high concentration of crystalline-type materials provide a greater protection to spores than serum wih high protein content [7].

In plasma decontamination, Klämpfl et al. [95] observed by scanning electron microscopy (SEM) that *Clostridium Difficile* (NCTC 13366) endospores prepared with 0.03 % BSA, deposited and dried on stainless steel carriers form clusters with surrounding saline structures, thus decreasing the number of spores attainable by plasma species produced by the SMD plasma source. As a result, the inactivation rate was lowered by 3-log when BSA was added to the suspension.

3.3.2. Effect of microbes deposition method

Two main techniques of deposition of the microorganisms on the carriers are commonly used: the spot and spray deposition methods. The spot method is more commonly used and consists in placing a droplet of the prepared suspension of microbes on the inoculation surface. This method does not allow an accurate control of the local concentration of microorganisms which readily form clusters and multilayered structures. On the contrary, the spray method allows to deposit a monolayer of microorganisms onto the surface thus ensuring homogeneous and controllable surface concentration of microorganisms [45], [60], [96]. For this reason the spray deposition method is extremely interesting for standardized inoculation on carriers [46]. Raguse et al. [46] compared the reduction factor of 5×10^7 *B. Subtilis* spores deposited by spray and liquid spot methods on a glass carrier exposed to low-pressure argon plasma. After 90 s of exposure, 0.8 log reduction was measured on the carrier inoculated using the spot method while 4.8 log-reduction was achieved using the spray method. The slower inactivation observed using the spot method can be attributed to the slower diffusion of germicidal agents inside the multi-layered cell structures. According to Shintani et al. [37], [97], the characteristic penetration depth of plasma species is about ~10 nm, and ~1 µm for hydrogen peroxide. Since, the dimension of a microbe is typically ~1 µm, chemical sterilants are readily to diffuse deeply through multiple layers of cells while plasma species only access the first layer.

As a result, the method of microorganisms deposition strongly influence the decontamination efficiency of non-penetrating surface agents such as plasma species,

but also UV-C radiation [62]. On the contrary, Raguse et al. [46] showed that highly-penetrating agents such as X-rays were not influenced by the deposition technique.

3.3.3. Effect of microbes surface concentration

The surface concentration of microbes is defined as the ratio of the initial microorganisms load to the inoculation area. Increasing surface concentration of microbes enhances the formation of multi-layered structures avoiding diffusion of plasma species in the case of microorganisms deposition by a spot method [98]. Thus, decreasing the initial load of microorganisms or increasing the inoculation area may lead to higher inactivation rates. In Ref. [99], different dilutions of *E. Coli* on Agar were treated by SMD (Figure I.9). An intial difference of 4 log in the initial load caused a difference of about 1 log in the inactivation rate after 10 s of treatment. A similar behaviour was observed in Ref. [93] with a corona discharge.
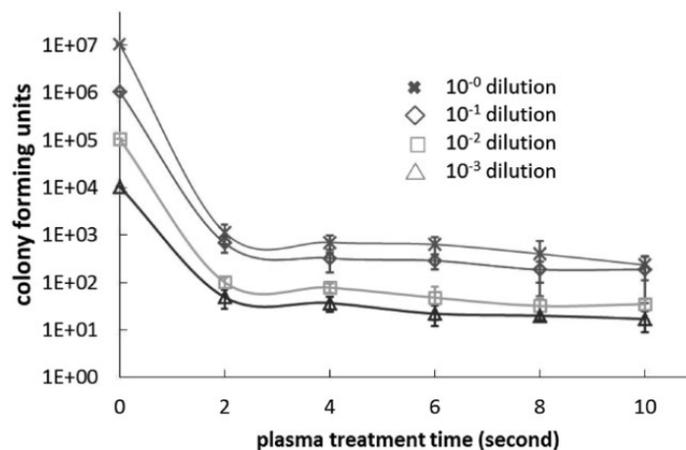
Figure I.9 : Treatment of different dilutions of *E. Coli* on Agar plate by SMD, taken from [99].

3.3.4. Effect of microbes strain

Variations in the strains of a single microorganism species are referenced in collections –e.g. American Type Culture Collection (ATCC), National Collection of Type Culture (NCTC). The susceptibility of different strains of E. Coli (ATCC 25922 and NCTC12900) to air DBD exposure was studied in Ref. [100]. After 30 sec of air plasma treatment, it was shown that strain ATCC 25922 was reduced by 3.4 log while strain NCTC 12900 was only reduced by 1.8 log. The different efficiencies are due to intrinsinc DNA variations within the same type of microorganism. It is the occasion to note that the name of microorganisms is subject to adjustments. Table I.3 gives the correspondance of DSM collection numbers with other collection numbers of some bacillus strains of bacteria, and their previous designations that may be encountered.

Table I.3 : Different names of some bacillus strains of bacteria (modified from [101])

Microorganism	DSM collection n°	Previous names	Other collection n°
B. Atrophaeus	DSM675	*Bacillus Globigii* 'red strain' → *Bacillus Subtilis var. Niger* → *Bacillus Subtilis*	ATCC9372 NCIB8058, CIP77.17, NRS121A IFO13721, NCDO738
B. Atrophaeus	DSM2277	*Bacillus Globigii* → *Bacillus Subtilis*	NCTC10073, NCIB8649, CIP103406
B. Atrophaeus	DSM7264[T]	*Bacillus Subtilis var. Niger*	NRRL-NRS213[T], ATCC49337 [T]
B. Subtilis	DSM10[T]		NS744[T], ATCC6051[T], CCM2216[T], NCIB3610[T], NCTC3610[T], IFO12210[T]

CCM: Czech Collection of Microorganisms; CIP: Collection de l'Institut Pasteur; DSM, DSMZ: Deutsche Sammlung von Mikroorganismen und Zellkulturen; IFO: Institute for Fermentation, Osaka; NCDO: National Collection of Dairy Organisms; NCIB: National Collection of Industrial Bacteria; NCTC: National Collection of Type Cultures; NRRL: Northern Regional Research Laboratory; NRS: Nathan R. Smith

3.3.5. Effect of relative humidity

The relative humidity (RH) induces important changes in the gas-phase plasma chemistry, e.g. [102]. High relative humidity (RH) is known to cause the swelling of endospores [102], which enhances the efficiency of many decontamination methods –e.g. EtO and formaldehyde [103] – because of the higher water content in the spore core allowing the formation of aggressive chemicals, e.g. OH, inside the spore. In Ref. [103], the moisture content (hydration) of *B. Subtilis* was measured for different RH. It was shown that the moisture content slightly increases from 0 to 20% between 0% and 75% RH, and strongly increases at RH higher from 20 to between 75% and 95% RH. At RH>75 %, the strong increase of the water content causes the swelling of spores.
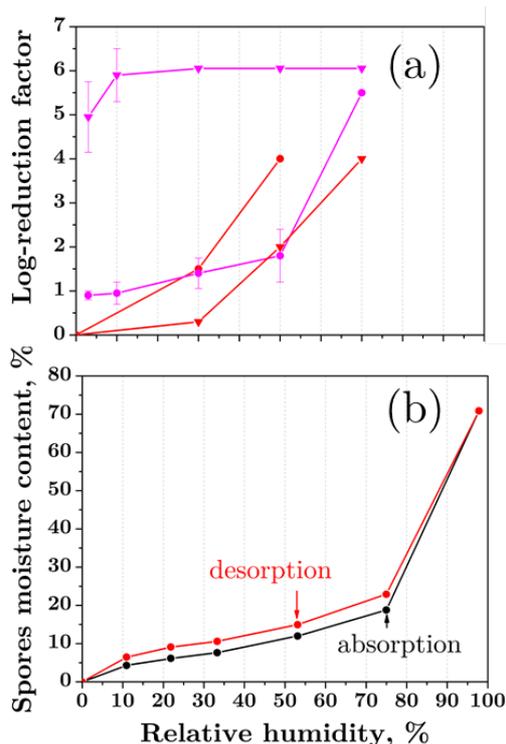
Figure I.10 : Effect of air relative humidity on endospores – (a): Inactivation of *Bacillus Atrophaeus* endospore by direct (▼) and indirect (●) ACP [104], by surface DBD after 150 s (▼) and 450 s (●), [105] – (b): Moisture content of *B. Subtilis* in contact with air at 25°C estimated from desorption and adsorption [103].

Figure I.10 shows this dependence together with log-reduction of spores treated by various plasmas. Higher relative humidity is always correlated with higher sporicidal activity. Similar conclusions were obtained in Ref. [106]. However, the moisture content inside the spores is not known in these studies. Therefore, it can not be concluded if the increased efficiency is only due to the gas phase chemistry, or if the moisture content significantly helped the decontamination process.

3.3.6. Effect of surface material

The effect of the material and the structure of the treated surface on the antimicrobial agent efficacy is complex. Sigwarth et al. [107] studied the reduction of *G. Stearothermophilius* (ATCC 7953) endospores deposited on various surface materials after exposure to hydrogen peroxide. Up to 3-log difference in the inactivation rate was measured depending on the material, but the author saw no clear correlation between material properties and the shift in resistance of endospores.
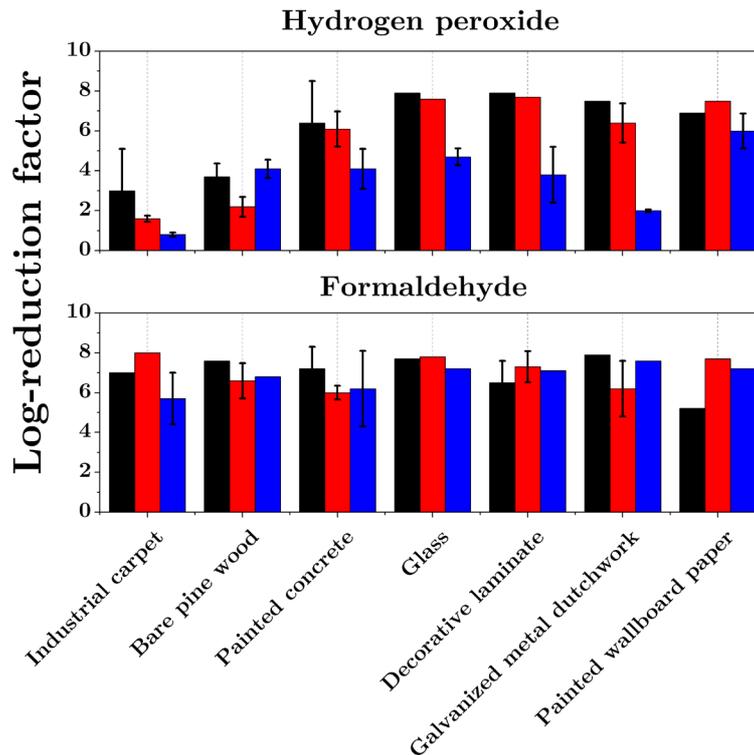
Figure I.11 : Inactivation of *B. Anthracis* (■), *B. Subtilis* (■) and *G. Stearothermo-philius* (■) endospores dried on various surface materials and exposed to hydrogen peroxide H_2O_2 (top graph) and gaseous formaldehyde CH_2O (bottom), modified from [108] and [109]. Experimental conditions are given in Appendix D.

Figure I.11 shows the inactivation of endospores *B. Anthracis*, *B. Subtilis* and *G. Stearothermophilius* on different substrates exposed to formaldehyde and hydrogen peroxide [108], [109]. Using formaldehyde, there is no great variation of the inactivation rate among the materials. On the contrary, for hydrogen peroxide exposure, the inactivation rate strongly depends on the material of the substrate as seen in Ref. [107]. Their results suggest that endospores are less likely inactivated by H_2O_2 when they are deposed on porous materials. According to the authors, possible penetration of spores inside porous substrates precludes interaction of H_2O_2 with a significant fraction of spores because of the rather small penetration depth of H_2O_2 [7].

The effect of material permeability can be further investigated from the work of Mahfoudh et al. [102] who studied the effect of dry gaseous ozone on the inactivation of endospores deposited on different polymeric surfaces. Figure I.12 shows the results they obtained by exposing the samples contaminated by *B. Atrophaeus* to 4000 ppm of dry ozone for 1 hour. The log-reductions are shown together with the permeability coefficients of the materials studied (values taken from GoodFellow [110]). The results show a correlation between the permeability of the surface material and the achieved

inactivation rate with a maximum 4.6-log reduction obtained on highly permeable silicone surface. Similar results were obtained in decontamination using EtO in Ref. [103].
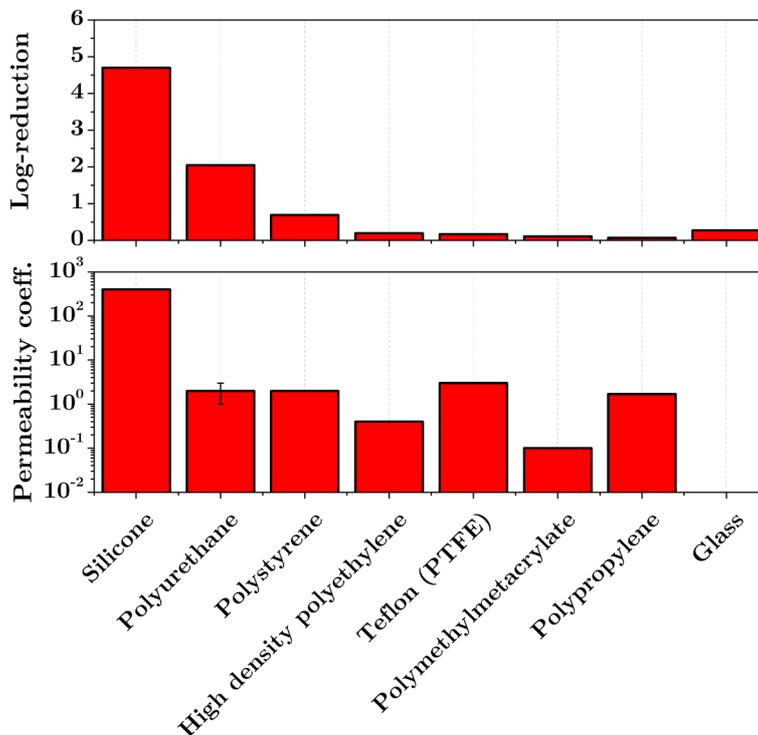
Figure I.12 : Effect of the exposure of dry gaseous ozone (4000 ppm, 60 min, RH<2 %) on the inactivation of *B. Atrophaeus* endospores dried on pyrex glass and polymeric surfaces (top, modified from [102]), and permeability coefficients (units: 10^{-13} $cm^3.cm.cm^{-2}.s^{-1}.Pa^{-1}$) of treated materials (bottom, data taken from GoodFellow [110]).

In direct plasma decontamination, additional interactions between the plasma and the surfaces increase the influence of the surface material. Interferences between the surface material and the species in the gas phase were observed by Levif et al. [111]. Using a reduced pressure the authors demonstrated that *B. Atrophaeus* spores deposited on polystyrene petri dishes were more resistant than on a glass surface as a result of the interaction between the plasma and the surface material. As a result, treating microorganisms on porous surfaces significantly increase the inactivation rate. A possible reason for this is the penetration of spores inside the material, thus avoiding clumpings and shieldings of microorganisms at the surface. In the case of direct plasma treatment, interaction of the plasma with the surface material influences the gas phase chemistry and thus the inactivation mechanisms.

In this section, we identified factors influencing the inactivation rate of microorganisms. Briefly the presence of salt or serum in the initial suspension of microorganisms induces

formation of aggregates precluding contact of the antimicrobial agent with deeper cell layers. Second, the relative humidity increases the moisture content of the microorganism and possibly increases the penetration depth of the chemical agents. Third, the porosity of the material may reduce resistance of the treated microorganisms. In direct plasma treatment however this may not be verified because of significant influence of the surface on the gas phase chemistry. Fourth, the spot deposition technique increases the resistance of microorganisms because of local concentration gradients of microorganisms. The spray method allows deposition of a monolayer of microorganisms eliminating the effect of microorganisms clumping in the analysis of the results. Finally, the strain of microorganism can slightly affect the inactivation.

3.4. Survey of elimination of bio-indicators by low-temperature plasma

In this section we review the results of bio-indicators inactivation by low-temperature plasmas and we provide a comparison with other non-thermal decontamination methods.

The multiphasic decay of BIs prevents the use of D-values to compare experimental inactivation data, as discussed in section 2.3. A more appropriate data is the time required to ensure a 6-log reduction of BIs, referred as T_{6log} here. When reviewing experimental data, if a 6-log reduction was not reached, data was rejected, except if a monophasic decay of BIs is observed. In the latter case, T_{6log} was determined from the D-value. Figure I.13 shows an overview of spore inactivation by atmospheric and reduced pressure plasmas in various operating conditions as a function of the distance between the plasma source and the sample. The graph also shows typical T_{6log} values for standard low-temperature decontamination for comparison. Experimental conditions of reported data are given in Appendix D.

From the data reported in Figure I.13, it can be confirmed that plasma decontamination methods are at least as efficient as the standard methods based on chemicals in a wide range of surface materials. It should be noted that the spores concentration were comparable in standard and plasma decontamination methods, i.e. 10^5-10^7 spores/cm^2.
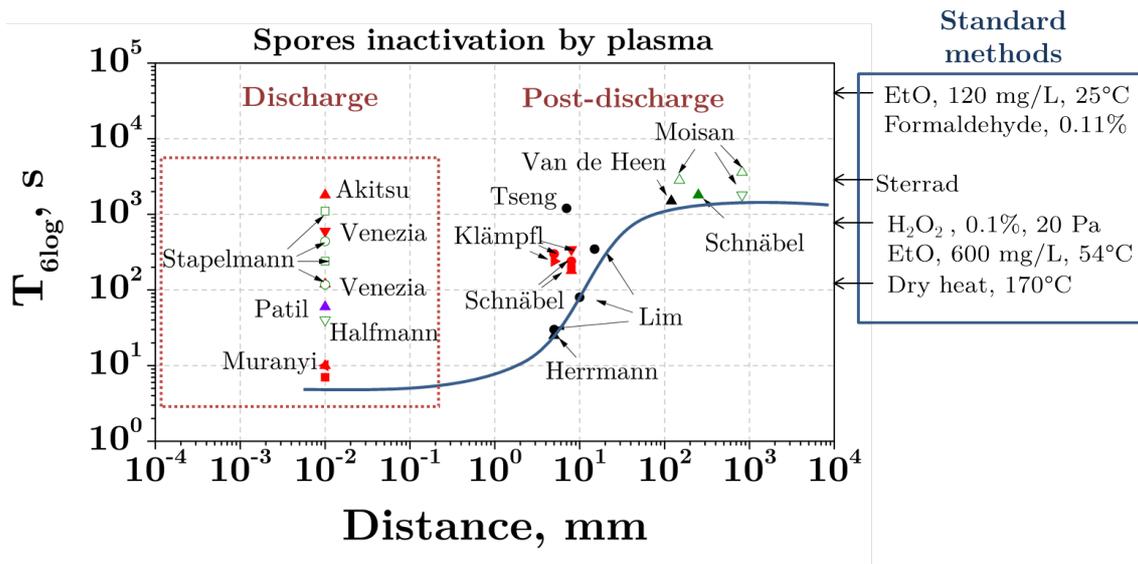
Figure I.13 : Exposure time T_{6log} required to achieve 6 log reduction of endospores *B. Atrophaeus* (▲), *B. Subtilis* (●), *C. Difficile*(►), *B. Pumilus* (■), *G. Stearothermophilius* (▼), and fungal spore *A. Niger* (◄) dried on surfaces by RF-APPJ (black symbols), DBD (red symbol), microwave discharge (green symbols), and pulsed DC discharge (purple symbols) exposures in various gases. The empty symbols refer to reduced pressure treatment. Position 10^{-2} mm refers to the plasma phase. The blue line gives a trend of the maximal inactivation rate achievable today by low-temperature plasma. Comparison is done with standard decontamination methods. Experimental conditions and references are detailed in Appendix D.

The smallest T_{6log} values equal about ~10 s and are obtained in a cascaded-DBD (CDBD) in atmospheric pressure air by Muranyi et al. [45]. The CDBD setup is similar to planar DBD where a dielectric layer was replaced by an excimer lamp radiating in the UV-c range. About 10^6 spores *B. Pumilis*, *B. Atrophaeus* and *A. Niger* were sprayed on a dried PET sample of 16 cm², thus ensuring a homogenous concentration of spores of about 6×10^4 spores/cm². This concentration is quite small in comparison with typical values in the range 10^5-10^7 spores/cm². Therefore, this probably reduced the resistance of spores in this case. However comparison can still be made with the experiment of Halfmann et al. [60] (T_{6log}=40s) where a spray deposition technique was also used to treat 10^6 B. Subtilis spores (same strain) on a glass surface. In air CDBD it has been shown by Heise et al. [96] that the strongest inactivation agent is the UV-c radiation. Since the UV-c penetration depth is quite low [46], faster inactivation is expected on non-porous surfaces such as glass. Therefore, it can be inferred that the CDBD setup at atmospheric pressure shows higher inactivation rate on *B. Subtilis* (DSM2277) than the reduced pressure Ar-H₂ ICP source (P=1 kW). The CDBD is

however limited to the treatment of objects of dimensions smaller than the inter-electrode gap while the ICP operates in large decontamination chambers. Making such qualitative comparison is not always possible, because the minimum set of information required for this (e.g., technique of spores deposition, surface area, etc) is rarely completely available in the description of experimental data.

Increasing the distance between the sample and the plasma reduces the intensity of the antimicrobial agents. At about 1 cm, atmospheric pressure plasma jets (APPJ) in Ar-O_2 and He-O_2 exhibit the higher inactivation rate against *B. Subtilis* (DSM2277) and have comparable T_{6log} values as what is obtained in ICP discharges at reduced pressure. Surface micro-discharges (SMD) exhibit lower inactivation rates, with T_{6log} values ~100 s at a distance of about 1 cm. The difference is probably due to the presence of electrons and electric field in the front of the plasma jet enhancing the antimicrobial activity in comparison with the SMD, where only RONS contribute [112], [113].

At ~10-100 cm from the discharge, only two microwave plasma sources were able to reach 6-log reduction of spores, with T_{6log} ~2000-3000 s. The antimicrobial activity of the reduced pressure N_2-xO_2 surfatron afterglow used by Moisan et al. [114] combines RONS production and UV-c radiation generated in the afterglow by the NO_γ emission [115]. The other source [116] operates in atmospheric pressure air. The authors attributed the BIs inactivation to the lethal concentrations of reactive nitrogen species produced by their system (NO: 0.6%, NO_2: 1.8%).

In summary, the comparison of inactivation results indicates that the plasma sources are as efficient as standard non-thermal decontamination methods. In the plasma phase, 6-log reduction of endospores can be achieved within tens of seconds at atmospheric pressure with air CDBD. However, only small volumes can be treated by atmospheric pressure discharges in the plasma phase. In the post discharges, plasma jet exhibit fast inactivation but the treated area is small. SMD and microwave plasma sources provides lethal concentrations of RONS which can be transported away from the discharge, thus increasing the treated area.

4. Scope of the thesis

In recent years, significant progress has been made in the treatment of microorganisms in the-post discharge using atmospheric pressure plasmas as seen in the previous section. This approach allows minimal degradation of the surface from the plasma and possibly homogenous treatment of volumetric objects. For instance, Shimizu et al. [117] reduced *B. Atrophaeus* (DSM675) endospores (10^7 spores/cm^2 on aluminum) by

3-4-log in a 2.2 L chamber placed at 27 cm from the SMD device used for the treatment. The homogeneity of the treatment was ensured by placing samples at different locations inside the chamber. The inactivation was attributed to lethal concentration of RONS produced by the discharge. In this thesis, the production and transport of RONS in atmospheric pressure pulsed DC discharges are studied.

- Thesis outline

The work presented in this thesis was performed as part of a collaborative Rapid DGA project (DESDEMONA, contract EJ nr. 2101 241 872) involving two companies (Plasmabiotics and RLC Consulting) and the EM2C laboratory of CNRS and CentraleSupélec. The objective was to develop new decontamination strategies based on nanosecond pulsing systems. The role of the EM2C laboratory was to characterize the production of reactive oxygen and nitrogen species in the systems developed by the two companies in order to optimize their efficacy. To this end, several advanced diagnostic techniques were developed. The thesis is divided as follows:

In Chapter II, we study the transport of ground state atomic nitrogen $N(^4S)$ in atmospheric pressure nitrogen afterglow using a technique based on absolute optical emission spectroscopy. We use a new approach to re-evaluate the rate coefficient of three-body recombination of $N(^4S)$. On that basis, a model of $N(^4S)$ recombination is used to study the surface recombination. The model is also applied to the decontamination of endoscopes by N_2 afterglow.

In Chapter III, production of RONS by a nanosecond repetitively pulsed (NRP) discharge in atmospheric pressure air is measured by absorption techniques. The efficiency of production of RONS is compared with other plasma sources, and the effect of RONS tuning by the NRP on microorganisms inactivation is studied.

In Chapter IV, we investigate the hydrodynamic expansion of the reactive products in the NRP discharge. This effect may be interesting for bio-medical applications because of the subsequent gas cooling that ensures the low temperature of RONS. The gas temperature is measured by combining time-resolved quantum cascade laser absorption spectroscopy (QCLAS) and planar laser induced fluorescence (PLIF). In addition, the effect of the hydrodynamic motion on the nitric oxide (NO) production is studied.

Chapter II

N(^{4}S) recombination in N$_2$ afterglow at atmospheric pressure

Nitrogen plasmas are promising solution for the treatment of surfaces because of the low degradation and modification of the treated surface, especially in the post discharge [97], [118]. In addition antimicrobial atomic nitrogen ground state N(^{4}S) produced by the plasma can propagate over long distances in tubes. It is thus a promising approach to treat the inner space of small tubes such as endoscopes. However, the mechanisms of recombination of N(^{4}S) are complex and still not completely known [119]–[121]. In this chapter, the recombination of atomic nitrogen inside polyurethane tubes commonly used in catheters is studied.

Section 1 presents the biocidal mechanisms of N$_2$ plasmas and afterglows. Section 2 defines the problem studied in this chapter. A critical review of N(^{4}S) measurement techniques is then presented (section 3). In section 4, 3D N(^{4}S) density measurements by a technique based on absolute emission spectroscopy are presented. We infer the 3-body recombination coefficient from the volumetric decay of N(^{4}S) and we validate the measured reaction coefficient by comparing our predictions with the N(^{4}S) experimental data of Es-Sebbar et al. [119] (section 5). The probability of losses of N(^{4}S) atoms at the surface of the polyurethane tube is determined from a zero-dimensional kinetic model (section 6). Then, we present a simple method of determination of N(^{4}S) based on relative OES measurements, and we compare it with the absolute OES technique (section 7). Finally, an application of our results to model the decontamination of the inner of long tubes, e.g. endoscopes and catheters, is presented in section 8.

1. Introduction: nitrogen plasma biocidal efficiency

Sporicidal and bactericidal activities of nitrogen discharges and afterglows have been reported in Refs. [41], [42], [69], [96], [122]. The mechanisms of microorganisms inactivation by the nitrogen discharge are membrane cell disruption under the effect of

charged species, UV radiation, and free radicals [97]. In the afterglow, the charged species concentration is too low to induce significant damage, and UV radiation from the N$_2$ second-positive system does not contribute significantly [68], [69]. This was shown by Mols et al. [68], who analyzed DNA response following exposure to a nitrogen plasma jet, and by Van Bokhorst-van de Veen et al. [69]. This is probably because the N$_2$ second-positive system radiates in the UV-b spectral range which is less likely absorbed by DNA, thus reducing the contribution of UV radiation to the inactivation.

In the nitrogen afterglow, the biocidal action thus comes from radicals produced in the discharge such as N(^{4}S) ground state atoms, N(^{2}P,^{2}D) and N$_2$(A$^3\Sigma_u^+$) metastable states. The atomic nitrogen ground state is the most populated species and is thought to be involved either directly or indirectly in the inactivation of the treated microorganisms [42], [69]. The radical transport far from the discharge region is essential for large surface treatment and for the inactivation rate. The recombination of the ground state atomic nitrogen N(^{4}S) in the afterglow is studied in the present chapter.

2. Position of the problem

In the nitrogen discharge, various electronic states of N$_2$ are excited by electron impact. At high E/N (>100 Td), dissociation of N$_2$ occurs via the formation of the predissociative states N$_2$(b$^1\Pi_u$, c$^1\Pi_u$, o$^1\Pi_u$, e$^1\Pi_u$, b$^1\Pi_u$, b'$^1\Sigma_u^+$, c$^1\Pi_u$ c'$^1\Sigma_u^+$, e$^1\Sigma_u^+$,…), which have a high predissociation rate of about 10^{10} s^{-1} [120].

In the nitrogen afterglow, three regions are typically considered, namely the early, the pink, and the late afterglow. The early afterglow corresponds to the decay of nitrogen excited states immediately following their excitation by electron impact in the discharge region. The pink afterglow begins when nitrogen molecules are no longer excited by electron impact, but by v-v pumping of N$_2$(X$^1\Sigma_g^+$,v) molecules. In the late afterglow, N(^{4}S) ground state atoms recombine in the volume and at the surface, via the following mechanisms:

$$N(^4S) + N(^4S) + N_2 \rightarrow N_2(X,A,B) + N_2$$
$$N(^4S) + wall \rightarrow 1/2\,N_2(X,A,B) + wall$$
$$N(^4S) + N(^4S) + wall \rightarrow N_2(X,A,B) + wall$$
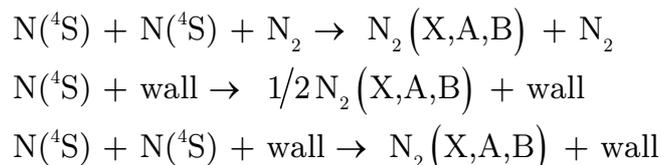
In volume, the main loss mechanism is three-body recombination with N$_2$ as the third body, and to some extent recombination with potential impurities. The rate coefficient of three-body recombination with N$_2$ is a key rate for N$_2$ afterglow modeling [120],

[121], for emission-based methods of N(^{4}S) density measurement [42], [123], [124], and for the determination of the surface recombination probability of N(^{4}S) from its gas phase decay [125]–[127]. The rate coefficient of this process has been extensively studied for several decades in static [128], [129] and flowing [129]–[132] systems using various N(^{4}S) measurement techniques such as electron spin resonance [129], NO titration [130], [132], and mass spectrometry [128]. However, discrepancies of about an order of magnitude have been reported in Ref. [128] for the value of this coefficient. A review of the most significant values reported in the literature for this rate is given in Table II.1. Here, we provide an improved method to determine the value of this coefficient.

The common approach consists in measuring the decay of N(^{4}S) density at different N$_2$ gas pressures and fitting the observed decays by adjusting the coefficients of the N(^{4}S) loss mechanisms listed above [128]. The linear increase of the decay rate with gas pressure is then attributed to three-body recombination with N$_2$ as third body, and the slope gives the value of the rate coefficient [132]. However, the method may fail for two reasons. First, this approach does not take into account the pressure dependence of the surface recombination probability of N(^{4}S) [133]. Between 2 and 5 torr, this probability can vary by a factor 2 to 5 depending on the surface material, thus considerably affecting the observed decay. Second, oxygen impurities, and in particular O and NO byproducts, are known to strongly influence the N(^{4}S) recombination in volume and at the surface [134].

In the present chapter, we measured the 3D distribution of N(^{4}S) density inside the tube of a flowing nitrogen afterglow at atmospheric pressure, by combining absolute emission spectroscopy and an Abel inversion of the measured emission spectra. This enabled us to separate the decay rate in volume and near the surface. A simple kinetic model was employed to model the observed decay of N(^{4}S) in the volume. The losses due to recombination with O and NO impurities were taken into account by monitoring the [O]/[N] ratio from the NO(B,v'=0→X,v''=8) emission at 320 nm [135].

Table II.1: Literature review of the rate coefficient of

N(^{4}S) + N(^{4}S) + N$_2$ → N$_2$(X$^1\Sigma_g^+$,A$^3\Sigma_u^+$,B$^3\Pi_g$) + N$_2$ at T=300 K

Author	Method	Conditions	$k_3 \times 10^{-33} \text{cm}^6.\text{s}^{-1}$	Ref.
Clyne et al., 1967	NO titration (4 points)	T=90-6400 K P=1-13 torr	7.45±0.55	[132]
Thrush et al., 1967	NO titration (5 points)– photometry	T=298 K P=2-10 torr	3.8± 0.3	[136]
Yamashita et al., 1979	Mass spectrometry calibrated by NO titration	Static	3.6 ± 0.1	[128]
Herron et al., 1959	NO titration (4 points) – mass spectrometry	T=195-450 K P=1-10 torr	7.85 ± 1.1	[130]
Harteck et al., 1958	NO titration (1 point) – photometry	P=0.5-1.3 torr	17.2 ± 1.7	[131]
Evenson et al., 1966	ESR	P=0.3-5 torr	11.25±1	[129]
		P=9-35 torr	3±1.5	
Marshall et al., 1962	EPR	P=1-10 torr	7.75±1.55	[137]
Brennen et al., 1970	Photometry + NO titration	P=0.047 torr T=294±1.5 K	7.9±1	[138]
Miyazaki et al., 1967	Photometry + NO titration	T=300 K	7.25±0.25	[139]
Kretschmer et al., 1963	NO titration	P=2-8.5 torr T=300 K	2.12	[140]
Kossyi et al., 1992	Literature		4.4	[141]
Partridge et al., 1988	Calculation		8.7	[142]
This work	Calibrated emission	P=1 bar	7.77±1.04	

3. Review of measurement techniques of N(^{4}S)

This section reviews the various diagnostics that have been developed for nitrogen ground state density measurements. For the sake of brevity, we only emphasize here the main advantages and drawbacks of these techniques.

Direct absorption of N(^{4}S) is relatively difficult to perform, because the visible and UV transitions, corresponding to absorption from the ground state to metastable states, N(^{2}D) and N(^{2}P), are forbidden. The first allowed transtion from N(^{4}S) requires vacuum UV radiation to perform the absorption measurement. This approach was employed in Ref. [143] to measure O and N densities in an RF-APPJ, using the Soleil synchrotron facility. However, the technique is experimentally difficult to implement and is not available in most laboratories.

Molecular Beam Mass Spectrometry (MBMS) was used in Ref. [144]. We should note that the calibration of MBMS requires a known source of atomic nitrogen or another technique of measurement of N(^{4}S) [128]. Moreover, it does not allow *in situ* measurements.

Electron Paramagnetic Resonance (EPR) is a diagnostic based on the absorption of microwave photons between energy levels with Zeeman splitting. Thus, a necessary condition for EPR is the existence of a non-zero magnetic moment and the application of an external magnetic field. The technique has been used for N(^{4}S) [145], [146], O(^{3}P) [146] and electron density measurements. Calibration can be easily performed using molecular oxygen since it is paramagnetic, but the detection limit is slightly lower than that of laser-based techniques [147]. However, the method requires an external magnetic field and therefore suitable only for the afterglow.

Actinometry is a line-ratio technique based on the addition of a rare gas, usualy argon, to the plasma discharge followed by the observation of the ratio of two argon and nitrogen atomic lines [148], [149]. This technique assumes that (i) the excited nitrogen and argon atoms are produced directly by electron impact from the ground state, (ii) with the rate ratio constant for plasma changes under study and (iii) the main loss channel being the sponaneous emission. These assumptions can be confirmed using a kinetic model [150]. The advantage of the technique is that it only requires a relative calibration of the optical device. It provides N(^{4}S) density measurements with a time resolution determined by the detection system. However, the accuracy of the measurement depends on the validity of the assumptions and on the precision of the

reaction rate coefficients involved. The technique only works in the discharge region, it can be used in the afterglow if combined with the double-pulse technique.

Two-photon Absorption Laser Induced Fluorescence (TALIF) is a well-known technique for the measurement of nitrogen atoms. The main advantage of TALIF is that it does not require any assumptions about the kinetics, thus, providing a direct measurement of N(^{4}S). Time- and space-resolved measurements can be performed with resolution determined by the laser pulse duration (e.g. 10 ns for ns-TALIF) and by the intersection of the laser beam and the fluorescence collection volume (e.g. 1 mm or even below). For N(^{4}S) density measurements, the calibration can be performed with krypton as suggested in [151]. The N(^{4}S) density is then given by:

$$[N(^4S)] = \frac{S_N \sigma_{Kr}^{(2)}}{S_{Kr} \sigma_N^{(2)}} \left(\frac{E_{Kr} \nu_N}{E_N \nu_{Kr}} \right)^2 \frac{a_{Kr}}{a_N} \frac{\eta_{Kr} T_{Kr}}{\eta_N T_N} [Kr] \qquad \text{(II.1)}$$

where $\sigma_i^{(2)}$ is the two-photon absorption cross-section, S_i the fluorescence signal, a_i the branching ratio, η_i the detector quantum efficiency, T_i the transmissivity of the optics (both η_i and T_i are determined by relative calibration), and the rest of the expression is a factor composed of known constants. The branching ratio depends on the quenching rate, which is either estimated on the basis of the gas composition or measured from the fluorescence decay. At atmospheric pressure, the latter option requires a picosecond laser for excitation and fast detectors for the measurements of the fluorescence decay which is on the picosecond timescale [152], [153]. The ratio of cross-sections has been measured by Niemi et al. [151] combining NO titration and TALIF: $\sigma_{Kr}^{(2)} / \sigma_N^{(2)} = 0.67 \pm 50\%$.

NO titration has been widely used for N(^{4}S) measurements in low pressure afterglows for several decades [128], [130]–[132]. Basically it consists in introducing a known flow rate of NO (initially mixed with Ar) in the post-discharge and observing the chemiluminescence following the very fast reaction between N(^{4}S) and NO. At atmospheric pressure, the uncertainties increase because the titration reaction is not the only loss mechanism of the NO titrating gas, and chemiluminescence competes with quenching [146].

Optical emission spectroscopy (OES) has been used for decades for relative density measurements of N(^{4}S) in the nitrogen late afterglow. The technique is based on the measurement of N$_2$(B$^3\Pi_g$,v=11) emission following three-body recombination of N(^{4}S). The emission intensity is thus proportional to [N(^{4}S)]^2. Measurements of N(^{4}S) density are possible either by measuring directly the density of N$_2$(B$^3\Pi_g$,v=11) by

absolute emission spectroscopy using an intensity calibration procedure [154], or by simply measuring the decay of $N_2(B^3\Pi_g,v=11)$ relative emission and interpreting the results with a simplified kinetic model [42], [123], [154]. The advantage of the relative method is its ease of implementation. However, the method is only valid in the nitrogen afterglow with negligible content of impurities such as atomic oxygen. Still, this method was recently used to measure the density of N(^{4}S) at the exit of a nitrogen plasma jet in open air [123].

In summary, several techniques can be used to measure nitrogen atom densities. Note that except the TALIF method, none of them allow spatially resolved measurements (unless the plasma is axisymmetric, in which case an Abel-inversion can be applied). In this thesis we employed absolute and relative OES for N(^{4}S) mesurements to study the afterglow of a pulsed discharge in pure N_2 flowing inside a tube.

4. N(^{4}S) density by absolute optical emission spectroscopy (OES)

4.1. Principle

In the nitrogen late afterglow at low pressure, it is well known that the $N_2(B^3\Pi_g,v)$ vibrational population distribution is out of equilibrium and peaks at around v = 11. A slight nonequilibrium was also observed for v = 6. The mechanisms responsible for these departures from equilibrium were debated for several decades. Berkowitz et al. [155] first showed that the emission of the late afterglow was proportional to the squared density of atomic nitrogen, which they measured by NO titration. The authors proposed that the observed peak at v = 11 was due to N(^{4}S) recombination into the predissociative state $N_2(^5\Sigma_g^+)$. $N_2(B^3\Pi_g,v = 11)$ is then produced by intersystem collision excitation (ICT) transfer because the potential curve of $N_2(^5\Sigma_g^+)$ crosses $N_2(B^3\Pi_g)$ at v = 11. This theory was contested by Trush et al. [136] who argued that the $N_2(^5\Sigma_g^+)$ potential well was too shallow to significantly influence the $N_2(B^3\Pi_g,v = 11)$ density. However, Partridge et al. [142] computed the parameters of the $N_2(^5\Sigma_g^+)$ state and found that the potential well was deeper than expected, thus giving strong support to the theory of Berkowitz et al.

Trush et al. [136] proposed an alternative mechanism: the pooling reaction of $N_2(A^3\Sigma_u^+)$ gives rise to $N_2(C''^5\Pi_u,v=3)$, which deexcites radiatively to $N_2(^5\Sigma_g^+)$ (Herman Infrared System, HIR), and then produces $N_2(B^3\Pi_g,v=11)$ by ICT transfer. This theory is likely because it also permits to explain the nonequilibrium at $N_2(B^3\Pi_g, v = 6)$ because the

N$_2$(A$^3\Sigma_u^+$) potential curve crosses N$_2$(B$^3\Pi_g$) at v = 6, thus allowing possible excitation transfer. However, in our case N$_2$(B$^3\Pi_g$, v = 6) was not out of equilibrium (see Figure II.7) and the HIR system could not be observed, thus indicating that the contribution of N$_2$(A$^3\Sigma_u^+$) pooling to the first positive system emission is not important in our conditions.

At atmospheric pressure, because of the short time scales of vibrational relaxation, the early and pink afterglows are located in a region close to the discharge and therefore only the late afterglow is expected to be observed in the post-discharge tube. This can be confirmed a posteriori by measurements of the vibrational density distribution N$_2$(B$^3\Pi_g$,v). Thus, at atmospheric pressure, the N$_2$(B$^3\Pi_g$,v = 11) state is mainly produced by reaction R1 given in Table II.2. The main loss process of N$_2$(B$^3\Pi_g$,v = 11) is by quenching with N$_2$ molecules (reaction R2) [156]. The rate of spontaneous emission of N$_2$(B$^3\Pi_g$,v = 11), equal to 1.9 x 10^5 s^{-1} [157], is negligible compared to the quenching rate in nitrogen at 300 K and atmospheric pressure, equal to 6.9x10^8 s^{-1}. At steady-state, reactions R1 and R2 are equilibrated and therefore the density of the N$_2$(B$^3\Pi_g$,v = 11) state is proportional to the square of the density of nitrogen atoms :

$$[N_2(B^3\Pi_g,v{=}11)]=\frac{k_1}{k_2}[N(^4S)]^2 \tag{II.2}$$

The N$_2$(B$^3\Pi_g$,v = 11 $\rightarrow$ A$^3\Sigma_u^+$,v = 7) emission observed around 580 nm can thus be used to monitor the density of N(^{4}S).

Table II.2 : Reactions governing the density of the N$_2$(B$^3\Pi_g$, v=11) vibronic level, and associated rate coefficients at T=300K. In the text, k$_J$ refers to the reaction rate coefficient of reaction RJ

N°	Reaction	Rate coefficient at 300 K	Ref.
R1	N(^{4}S) + N(^{4}S) +N$_2$ $\rightarrow$ N$_2$ (B$^3\Pi_g$, v=11) + N$_2$	$(1\pm0.3)\times10^{-33}$ cm^6.s^{-1}	[158]
R2	N$_2$ (B$^3\Pi_g$, v=11) + N$_2$ $\rightarrow$ *products*	$(2.9\pm0.23)\times10^{-11}$ cm^3.s^{-1} 2.7×10^{-11} cm^3.s^{-1}	[159] [160]

The data acquisition was performed as follows. First, spectral images were calibrated in absolute intensity using a reference source (tungsten lamp) of known radiance. Second, an Abel inversion of the data was performed in order to determine the radial profile of the emissivity of the afterglow. Finally the spectra were fitted using the Specair nonequilibrium spectroscopic model [161] and the absolute density of N$_2$(B$^3\Pi_g$,v=11) was determined.

4.2. Experimental setup

4.2.1. Plasma reactor and afterglow

Figure II.1 shows our experimental setup. The plasma is generated by an industrial reactor producing a discharge between two pin electrodes (Plasmabiotics, Inpulse One, [162]). Both electrodes are encapsulated in a ceramic box and sealed with epoxy glue. A flow of pure nitrogen (Air Liquide, U grade) passes through the interelectrode gap (typically a few mm wide). The flow rate is fixed at 30 standard liters per minute (slpm) using a Bronkhorst mass flow controller. The exit of the ceramic box is connected to a polyurethane tube with an inner diameter of 4 mm, and this tube is connected to an 8-cm long quartz tube with the same inner diameter. Polyurethane tubes of different lengths were used in order to study the axial and longitudinal distribution of the emission, which was recorded across the quartz tube. The flow velocity in the post-discharge tube is about 40 m.s^{-1}.
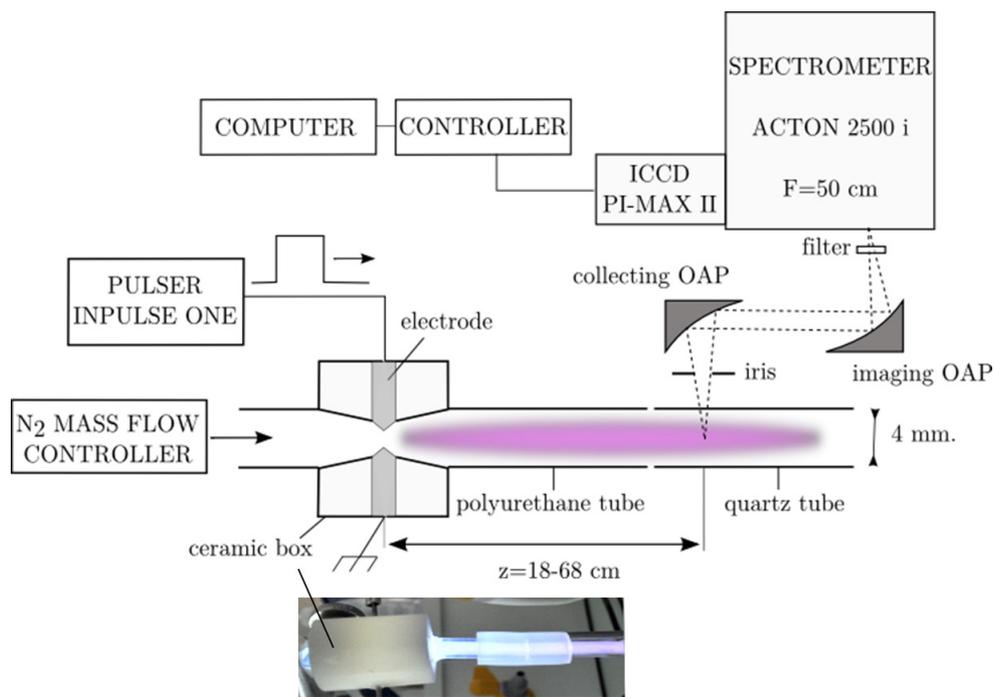
Figure II.1: Experimental setup : the distance z between the discharge and the measurement point was adjusted by inserting differents lengths of polyurethane tubes between the plasma reactor and the quartz tube. OAP: off-axis parabolic mirror.

4.2.2. Optical setup

The afterglow emission is collected through the quartz tube using a first off-axis parabolic mirror (OAP, Janos Technologies, Al-coated, UV-grade, Ø5 cm, f=10 cm) and focused on the entrance slit of the spectrometer (Acton 2500i) using a second OAP mirror (Janos Technologies, Al-coated, UV-grade, Ø5 cm , f=20 cm). The solid angle of light collection is controlled by an iris placed between the tube and the first OAP mirror. A highpass filter with cutoff at 400 nm is inserted at the entrance of the spectrometer to eliminate second order emission. For the measurements of N$_2$ first positive system, the ACTON spectrometer was equiped with a 600-groove/mm grating blazed at 400 nm and with an intensified iCCD camera (Roper Scientific PI-MAX) comprising 1024×1024 pixels of square dimension 12.8 µm×12.8 µm. The width of the entrance slit of the spectrometer was set to 50 µm. With this setup, the spectral resolution is about 0.4 nm, as determined from the FWHM of the measured instrumental function. This was obtained by recording the profile of a monochromatic and isotropic light source placed at the location of the plasma source. In practice, a He-Ne laser was directed to a diffusive paper sheet placed at the focus of the collecting OAP.

The optical system magnifies the image of the plasma by a factor of 2. Given that the entrance slit was set to 50 µm, the spatial resolution is about 25 µm (much less than the inner tube diameter, equal to 4 mm). With this magnification factor, and given that the total CCD array size is 13.1 mm, the entire cross-section of the 4-mm diameter tube can be captured. A lateral emission profile with 30 points across the diameter of the tube was measured by binning 10 pixels (128 µm) . The ICCD exposure time was set to 1 second, and each image was averaged over 100 shots.

4.2.3. Survey emission spectrum

A survey spectrum was measured using an Ocean Optics spectrometer (Maya 2000 Pro) in order to identify the main emitting systems. The spectrum measured 10 cm downstream of the discharge is shown in Figure II.2. This is shown to be dominated by the B$^3\Pi_g$→A$^3\Sigma_u^+$ first positive system of N$_2$. The red box indicates the spectral region of interest for N(^{4}S) density measurements.

The spectrum also features NO bands that reveal the presence of oxygen impurities in the feed gas (N$_2$ with <5 ppm total impurities according to manufacturer specifications). NH and CN emission bands were also identified. Hydrogen and carbon are likely to be produced by sputtering of charged species from the ceramic material surrounding the electrodes.
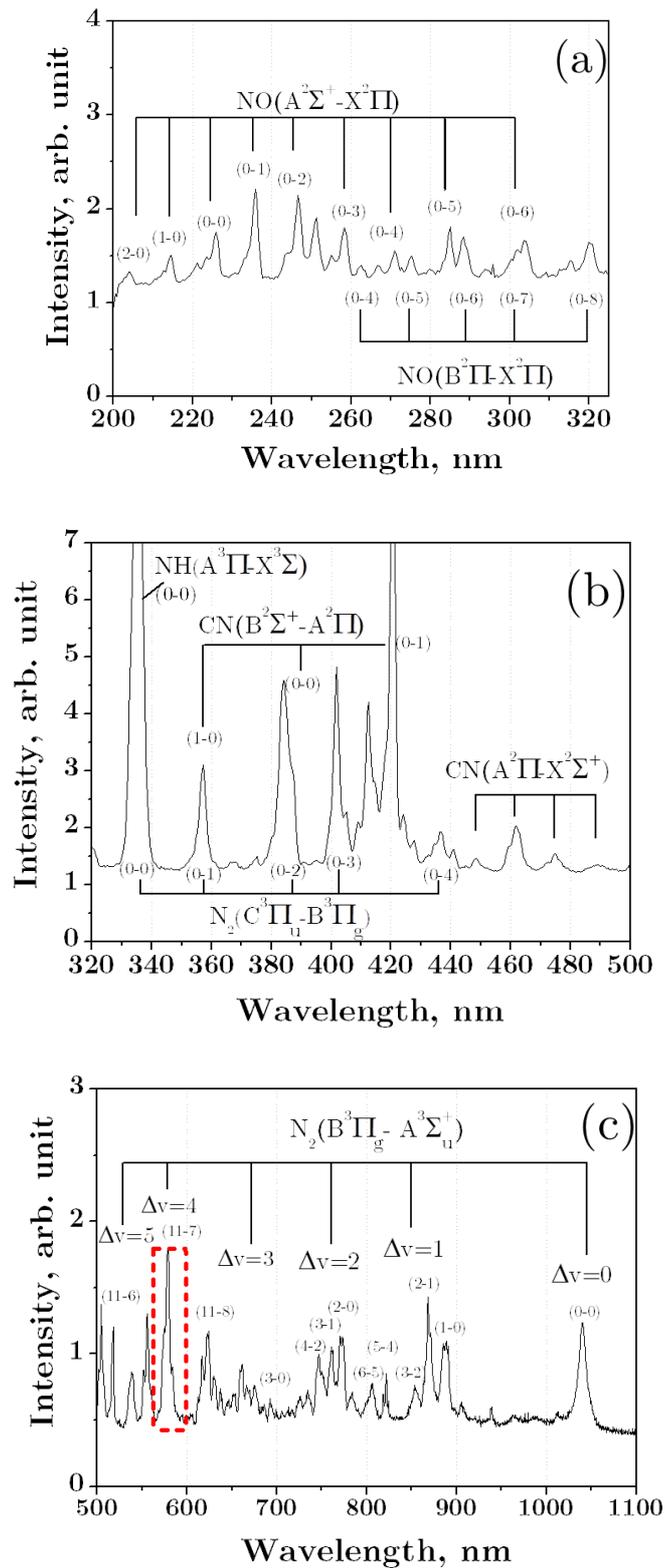
Figure II.2: Survey spectrum measured in nitrogen afterglow at 10 cm from the discharge - red dash box: $N_2(B^3\Pi_g \rightarrow A^3\Sigma_u^+, \Delta v=4)$

4.2.4. Absolute calibration of the detection system

The spectral emissivity of the afterglow can be expressed as follows:

$$\varepsilon_\lambda = \frac{1}{4\pi}\frac{hc}{\lambda}A_{e'v'J'-e''v''J''}n_{e'v'J'}\phi(\lambda)$$

(II.3)

where $A_{e'v'J'-e''v''J''}$ is the Einstein coefficient of spontaneous emission corresponding to the transition from state (e',v', J') to (e'',v'',J''), $\phi(\lambda)$ the normalized line profile, $n_{e'v'J'}$ the density of the upper state of the emitting transition, h the Planck constant, c the speed of light, and λ the photon wavelength. In practice, the intensity collected is the line-of-sight integration of the emissivity:

$$I_{abs}(\lambda) = \int_0^L \varepsilon_\lambda(r)dx$$

(II.4)

where L is the emission column length, I_{abs} the emission intensity in absolute units (i.e. mW.cm^{-2}.sr^{-1}.nm^{-1} in Specair). If the emissivity is not uniform, an Abel inversion can be performed to determine the local emissivity in an axi-symmetric system. This procedure is described in the next section.

The signal recorded by the ICCD camera also depends on the solid angle of light collection (determined here by the aperture of the diaphragm), the transmission of the optical system (e.g. grating efficiency, mirrors reflectivity), and the quantum efficiency of the ICCD. The determination of each contribution is complex and in practice a calibration is performed using a reference source.
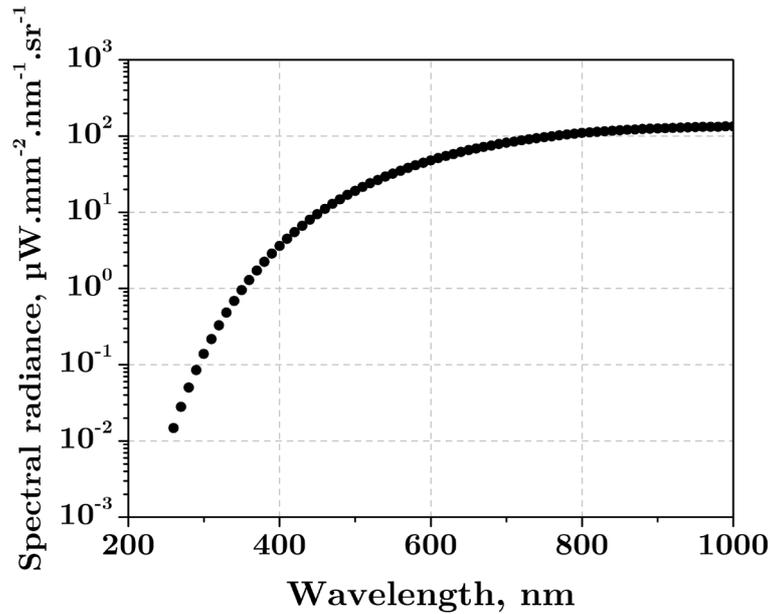
Figure II.3 : Spectral radiance of the tungsten lamp (OL550) supplied with 15 A at 5 V
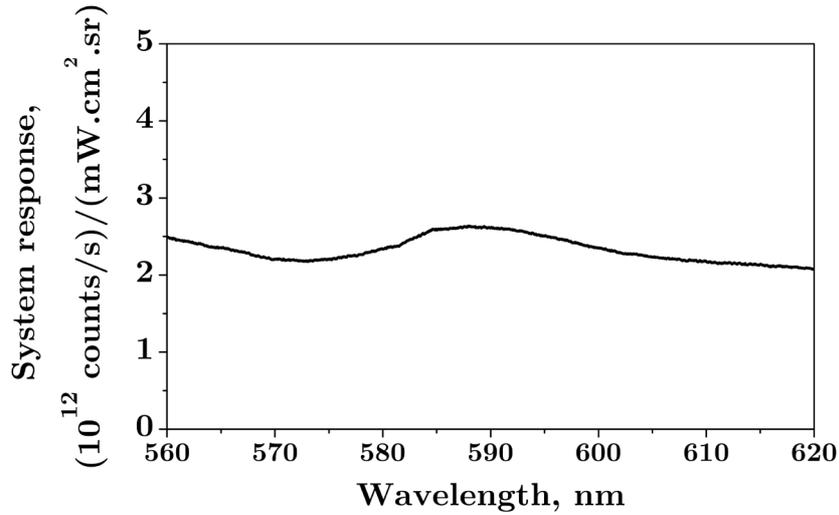
Figure II.4 : Response of the optical system determined using the OL550 tungsten ribbon lamp at 15 Amp. Conditions: 1s exposure, 100 numerical accumulations, ROI thickness of 20 pixels (software binning), 600 l/mm grating, 50 µm slit.

Here, the absolute calibration is performed with a tungsten ribbon lamp (Optronic Labs OL550) of known radiance traceable to NIST standards placed at the location of the plasma source. The lamp was supplied with 15 A at about 5 V. Under these conditions, the spectral radiance is shown in Figure II.3. The spectral response of the detection system is shown in Figure II.4.

4.2.5. Abel inversion

The Abel inversion is a mathematical technique often used in spectroscopy to extract radial profiles from measured lateral profiles in axi-symmetric environments (Figure II.5). Here, the emission was collected inside a cylindrical tube so that the lateral emission profile measured with the camera could be Abel-inverted to yield the local emissivity at radial position r:

$$\varepsilon(r) = -\frac{1}{\pi} \int_r^R \frac{dI/dy}{\sqrt{y^2 - r^2}} dy \tag{II.5}$$

It should be noted that the Abel inversion is highly sensitive to the first derivative of the lateral emission profile as seen in equation (II.5). The uncertainty propagation through the Abel-inversion procedure was calculated using a Fortran code described in [163] and named POLAB.FOR. Basically, semi-lateral intensity profiles were first fitted using a 3rd order polynomial, imposing a zero slope at the center, and the Abel-inversion of the polynomial was calculated according to equation (II.5). An interesting

feature of the POLAB code is that it also calculates the uncertainties propagated through the fitting and Abel-inversion procedures.
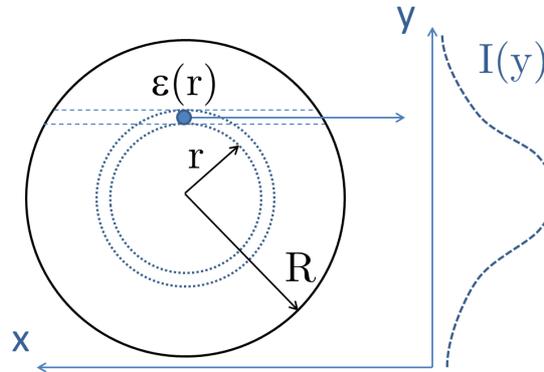
Figure II.5 : Cross-section of the tube of radius R. ε(r) is the local emissivity at radial position r, I(y) the emissivity integrated over the line-of-sight at lateral position y. ε(r) is determined from the lateral emission profile I(y) by Abel inversion.

4.3. Determination of the N(^{4}S) density profiles by absolute OES

4.3.1. N(^{4}S) densities from absolute emission spectra

Figure II.6.a) shows a typical measured absolute emission spectrum, integrated along the line-of-sight. The length of the line-of-sight is the inner diameter of the polyurethane tube, i.e. equals 4 mm.
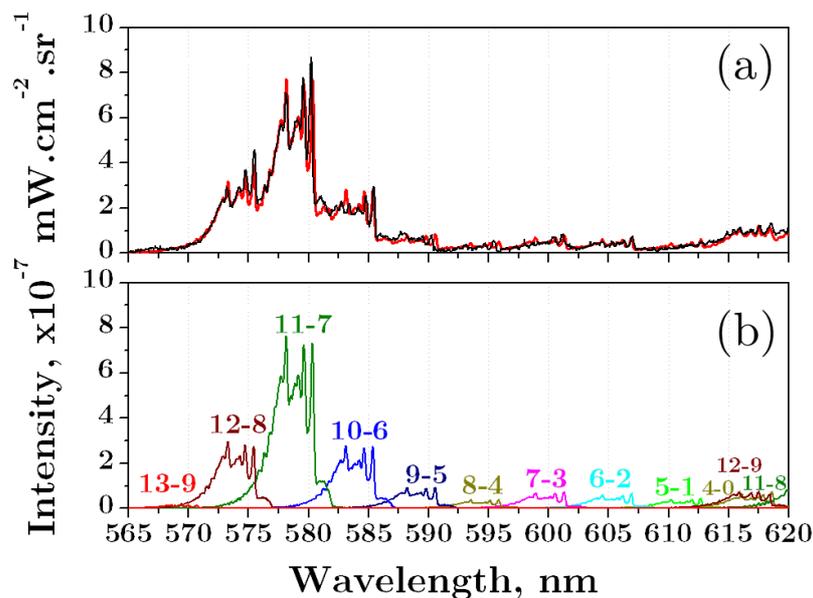
Figure II.6 : (a) - Absolute emission spectrum of $N_2(B^3\Pi_g,v' \rightarrow A^3\Sigma_u^+,v'')$ first positive system (black line) and Specair fit (red line). (b) - Contribution of each vibrational band (v'-v'') to the calculated spectrum.

Individual vibrational bands were computed with the line-by-line radiation code Specair [161] as shown in Figure II.6.b). In this work, we made use of a special feature of the Specair code that allows computing the emission of specific levels of the $N_2(B)$ state by applying vibrationally specific nonequilibrium population factors ρ_v. This procedure is documented in the user manual of Specair, available from Ref. [164]. The nonequilibrium population factors ρ_v were adjusted until agreement was obtained between the calculated and measured spectra.
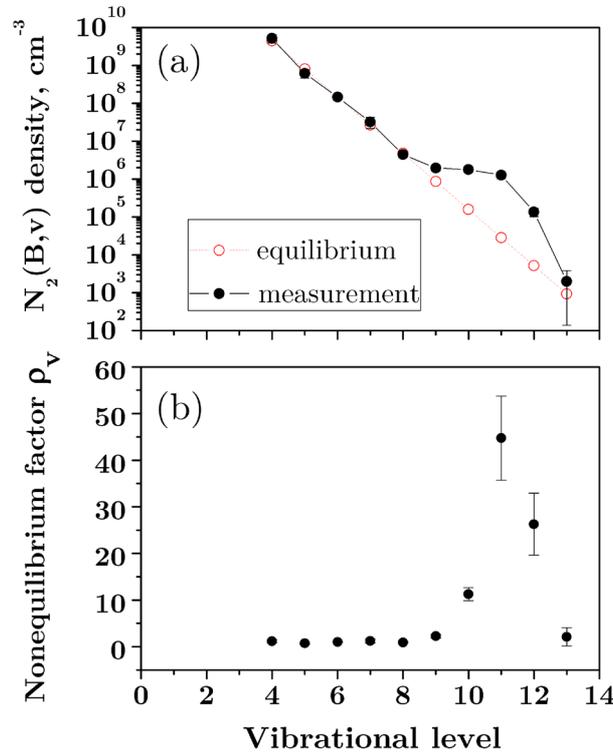
Figure II.7 : (a) - $N_2(B^3\Pi_g,v')$ vibrational density distribution: measured distribution (black symbols) and distribution at equilibrium (red symbols). (b) - Nonequilibrium factors relative to the equilibrium Boltzmann distribution at 300 K, 1 atm.

The resulting nonequilibrium $N_2(B^3\Pi_g,v)$ density distribution is shown in Figure II.7.a), and is compared with the equilibrium Boltzmann distribution at T=300 K. The applied overpopulation factors ρ_v are shown in Figure II.7.b). The $N_2(B^3\Pi_g,v=11)$ level is overpopulated relative to the equilibrium Boltzmann distribution by a factor of about 45. Its neighboring vibrational levels (v'=10, 12, 13) are also overpopulated, albeit to a lesser extent, as the result of vibrational-vibrational energy transfer.

To obtain radial N(^{4}S) density profiles, the following procedure was applied. First, we recorded the lateral profile of peak intensity of the (11-7) band (Figure II.8.a). This

profile was Abel-inverted to determine the local emissivity ε(r). The emissivity was then related to the density of N$_2$(B,11) using the Specair code, taking into account the instrumental broadening, the pressure and temperature conditions (P = 1 atm, T = 300 K). The N(^{4}S) density was finally obtained using equation (II.2). Typical N(^{4}S) density profiles obtained by this approach are shown in Figure II.8.b).
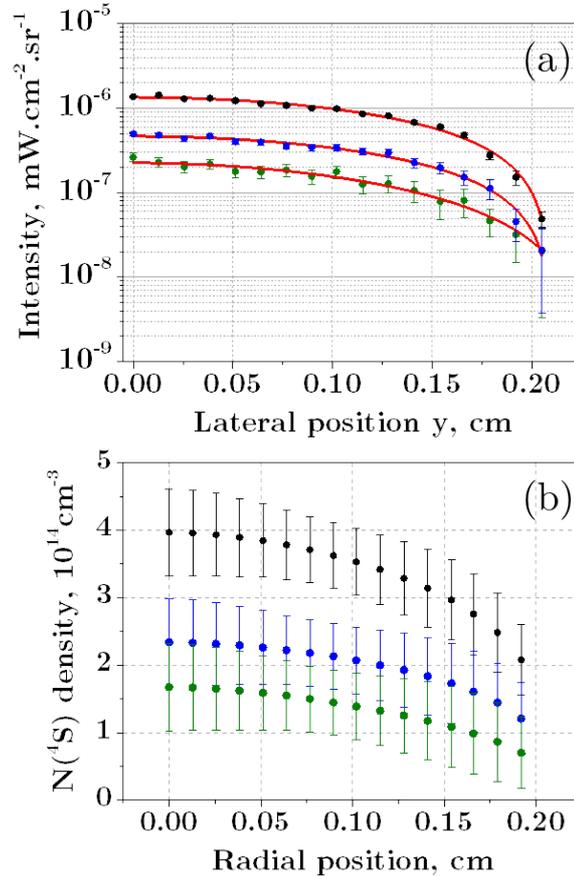
Figure II.8: (a) Lateral emission intensity profiles at the peak of the N$_2$(B$^3\Pi_g$,v=11 →A$^3\Sigma_u^+$,v=7) emission band (λ=580 nm) measured at 18 cm (black), 38 cm (blue), and 58 cm (green) from the discharge position. The lateral profiles are fitted using 3rd order polynomials (red curves) – (b) N(^{4}S) density profiles obtained from the absolute emission at the same positions as in (a).

4.3.2. Measured 3D profiles of N(^{4}S) density in the tube

Figure II.9 shows the density distribution of N(^{4}S) along the axis of the tube, from 18 to 68 cm after the discharge, obtained with the method presented in the previous section. The peak N(^{4}S) density is observed on the axis of the tube and is 3.9(0.6)×10^{14} cm^{-3} at 18 cm. It decreases to 2.1(0.5)×10^{14} cm^{-3} at the edge of the tube. The peak N(^{4}S) density decreases by less than a factor three within 50 cm (time of flight of 12.5 ms). However the decay near the surface of the tube is more pronounced, indicating the

contribution of surface recombination. At the center of the tube, the N(^{4}S) density decays inversely with distance as shown in Figure II.10. This behavior can be predicted by a simple kinetic model presented in the next section.
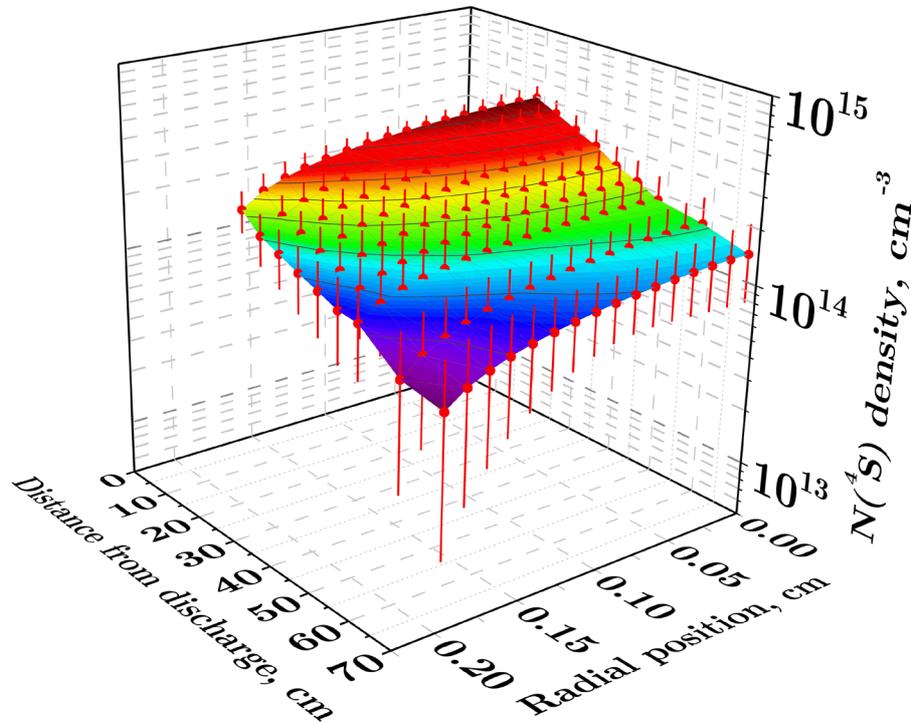
Figure II.9 : Spatial distribution of N(^{4}S) measured by the absolute emission method. Conditions: U=3 kV, F=70 kHz, flow velocity v=40 m.s^{-1}, inner diameter of the polyurethane tube: 4 mm.
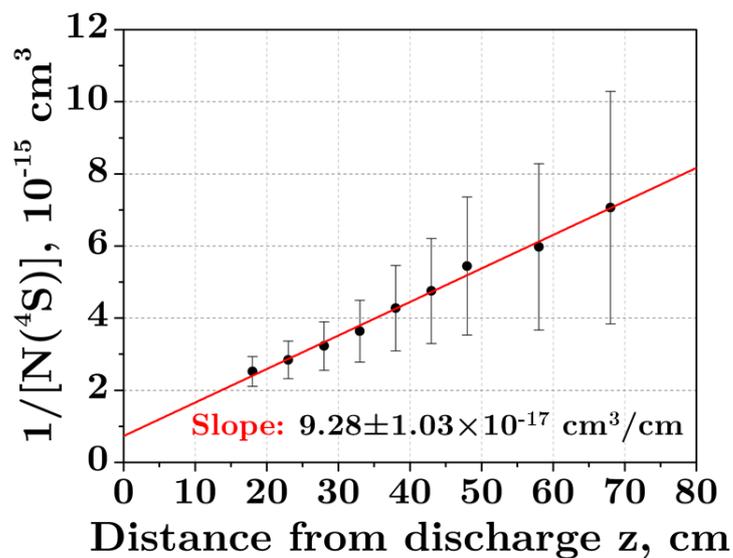
Figure II.10 : Profile of 1/[N(^{4}S)] along the tube centerline, measured by the absolute emission method. The red curve is a least-square linear fit of the experimental data.

5. Determination of the 3-body recombination coefficient

The values reported in the literature for the recombination rate coefficient of N(^{4}S) atoms with N$_2$ as the third body suffer from a large dispersion, as was shown in Table II.1. In this section, we use the measured profiles of N(^{4}S) determined by absolute emission spectroscopy along the axis of the tube to infer this recombination rate coefficient. To this end, we consider the volumetric balance equation of N(^{4}S) in cylindrical coordinates:

$$\frac{\partial[\text{N}]}{\partial t} = \left(\frac{\text{D}}{r} \frac{\partial}{\partial r} \left(r \frac{\partial}{\partial r} \right) + \text{D} \frac{\partial^2}{\partial z^2} - v \frac{\partial}{\partial z} \right)[\text{N}] - 2k_3[\text{N}_2][\text{N}]^2$$

$$- k_4[\text{N}][\text{O}][\text{N}_2] - k_5[\text{N}][\text{NO}]$$

(II.6)

On the right-hand side, the first term corresponds to the rate of species transport, the second to the three-body recombination rate, and the third and fourth terms to recombination with O and NO impurities, respectively. The rate coefficients of the various reactions are given in Table II.3. The quantity D is the diffusion coefficient of N atoms in N$_2$. To extract the rate of the three-body recombination reaction, k_3, it is first necessary to estimate the importance of the quantities related to transport and impurities. This analysis is presented in the following sections.

Table II.3 : Reactions governing the density of N(^{4}S) in the gas phase, and associated rate coefficients at T=300K. In the text, k_J refers to the reaction rate coefficient of reaction RJ

N°	Reaction	Rate coefficient at 300 K	Ref.
R3	N(^{4}S) + N(^{4}S) + N$_2$ $\rightarrow$ N$_2$ (X$^1\Sigma_g^+$,A$^3\Sigma_u^+$,B$^3\Pi_g$) + N$_2$	See review in Table II.1	-
R4	N(^{4}S) + O + N$_2$ $\rightarrow$ NO + N$_2$	1.01×10^{-32} cm^6.s^{-1}	[141]
R5	N(^{4}S) + NO $\rightarrow$ N$_2$ + O	1.81×10^{-11} cm^3.s^{-1}	[141]

5.1. Loss terms due to transport

In our flow conditions, the Reynolds number Re equals about 10^4. So, the flow regime is turbulent (Re>2300 in a pipe), and turbulent diffusion needs to be considered. In order to estimate the diffusion coefficient, we used the CFD code Fluent (Ansys 18.1) to model the flow conditions. Calculations were performed using a k-ε model of turbu-

lence. An inflation mesh was used in order to refine the mesh near the boundaries. An average velocity of 40 m/s determined from the mass flow rate and tube diameter was set at the inlet of the tube (4 mm diameter, 60 cm long). In the model, turbulent diffusion is introduced as an additional term in the diffusion coefficient, usually much higher than the laminar diffusion coefficient D_L [165]:

$$D = D_L + \frac{\mu_T}{S_{CT}\rho} \tag{II.7}$$

where μ_T is the turbulent viscosity, ρ the volumetric mass density, and S_{CT} the turbulent Schmidt number which is nearly independent on the gas composition, and set by default to 0.7. Figure II.11 shows the diffusion coefficient of N as calculated by the software. The diffusion coefficient D ranges from 1 to 3.24 cm^2/s. This is 3.4 to 11 times higher than the diffusion coefficient in the laminar regime (D_L=0.289 cm^2.s^{-1}, [166]).

The dimensionless Péclet number Pe_L gives the relative contribution of convection and diffusion mass transport: $Pe_L=v\times L/D$, where v is the mean flow velocity, L the diameter of the tube and D the diffusion coefficient. Here, the minimum value of Pe_L is found to be 280 in the tube. Therefore the diffusion transport can be neglected in comparison with the convective losses.
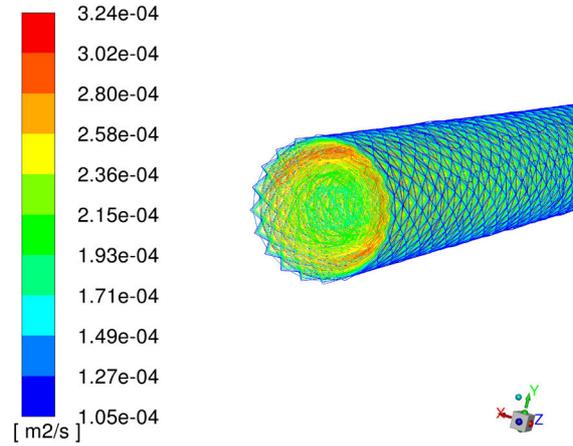
Figure II.11 : Diffusion coefficient of N(^{4}S) at the exit of the tube. Calculations are performed using the Fluent CFD k-ε model.

5.2. Loss terms due to impurities

In volume, O atoms recombine with N atoms via reaction R4 (see Table II.3). The resulting NO molecule almost instantaneously eliminates a second nitrogen atom via

reaction R5. Recombination with O and NO can be neglected if the three-body recombination rate is larger than the rates of reactions R4 and R5:

$$2k_3[N]^2[N_2] \gg \left(k_4[N_2][O] + k_5[NO]\right)[N]$$
$$\text{or } 2k_3[N]^2[N_2] \gg 2k_4[N][N_2][O] \tag{II.8}$$

The latter equation assumes that the resulting NO produced by reaction R5 recombines instantaneously with a second N atom thus explaining the factor 2 on the right-hand side of the equation Rearranging equation (II.8), it can be deduced that the O density does not significantly affect the volume decay of N(^{4}S) if:

$$\frac{[O]}{[N]} \ll \frac{k_3}{k_4} \approx 0.75 \tag{II.9}$$

To estimate the ratio [O]/[N] in our recombining tube, we resort to a technique based on the analysis of the NO$_\beta$ radiation measured in the ultraviolet. In the late afterglow the NO$_\beta$ emission comes from the recombination of atomic oxygen impurities with atomic nitrogen via reaction R6 [135] :

$$N(^4S)+O+N_2 \rightarrow NO(B^2\Pi_g, v'=0)+N_2 \tag{R6}$$
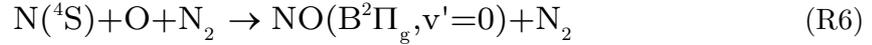
The two loss processes of NO($B^2\Pi_r$,v'=0) are spontaneous emission and collisional quenching via reaction (R7):

$$NO(B^2\Pi_g, v'=0)+N_2 \rightarrow products \tag{R7}$$
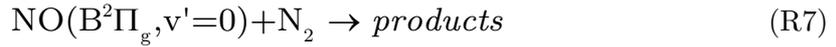
The rate coefficients of R6 and R7 are equal 3.1×10^{-34} cm^6.s^{-1} [167] and 6.1×10^{-13} cm^3.s^{-1} [168], respectively. The rate of spontaneous emission (4.7×10^5 s^{-1}) is thus much lower than the rate of collisional quenching at atmospheric pressure (1.5×10^7 s^{-1}). It can be neglected in the balance equation of the NO($B^2\Pi_r$,v'=0) state. Thus, at steady state, the rates of reactions R6 and R7 are equilibrated and the solution of the balance equation is:

$$[NO(B^2\Pi_g, v=0)]= \frac{k_6}{k_7}[N(^4S)][O] \tag{II.10}$$

The ratio [O]/[N] can thus be expressed as follows:

$$\frac{[O]}{[N(^4S)]} = \frac{k_7}{k_6} \frac{[NO(B^2\Pi_g, v=0)]}{[N(^4S)]^2} \tag{II.11}$$

The density of NO($B^2\Pi_r$,v'=0) state was determined from the absolute emission spectra of NO($B^2\Pi_r$,v'=0→$X^2\Pi_r$,v''=8) around 320 nm and Specair simulations. Figure II.12 shows the measured absolute emission spectrum, integrated along the diameter of the tube. The Specair fit shows that the spectrum comprises bands of NO beta, gamma and N_2 second positive. Based on this fit, the population of the NO($B^2\Pi_g$,v'=0) state was determined and used to estimate the [O]/[N] ratio from equation (II.11).

With this method, we estimated the [O]/[N] ratio based on the NO$_\beta$ emission at 18 cm from the discharge region. We found [O]/[N] = 0.054 at 18 cm from the discharge (thus [O] $\cong$ 6x10^{12} cm^{-3}, i.e. about 0.25 ppm). Therefore, the criterion defined in equation (II.9) is satisfied, and we conclude that O and NO impurities do not contribute to the volumetric N(^{4}S) decay in the present conditions.
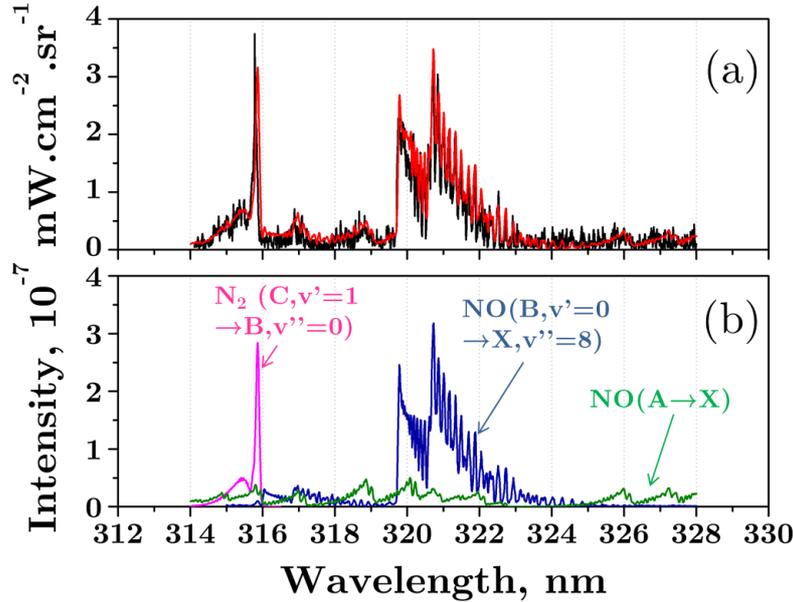
Figure II.12 : (a) - Measured absolute emission spectrum (black line) and Specair fit (red line). (b) - Contributions of NO beta ($B^2\Pi_r$→$X^2\Pi_r$), NO gamma ($A^2\Sigma^+$→$X^2\Pi_r$), and N_2 second positive ($C^3\Pi_u$→$B^3\Pi_g$) emission, all computed with Specair. Fitting parameters: Tgas =300 K Trot=300K, for all species, Te=3200 K for NO, Tv=4000K (for NO($A^2\Sigma^+$)), Tv=2000 K (for NO($B^2\Pi_r$)), Te=3400 K and Tv=2000 K for N_2($C^3\Pi_u$). [NO($B^2\Pi_r$,v'=0)]= 3.24×10^6 cm^{-3}, [NO($A^2\Sigma^+$)]=1.92×10^6 cm^{-3}, [N_2($C^3\Pi_u$)]=2.24×10^4 cm^{-3}.

5.3. Determination of the three-body recombination rate coefficient

From the analysis presented in the previous sections, only three-body recombination and convection losses need to be considered in the volumetric rate equation of N(^{4}S) for the present conditions. Therefore, the steady state solution of the balance equation is:

$$\frac{1}{[N(^4S)]} = \frac{1}{[N]_0} + \frac{2k_3[N_2]}{v}z \qquad (II.12)$$

The form of this equation predicts an inverse decay of N(⁴S) density with distance, which is consistent with the measurements shown in Figure II.10. In our conditions, the flow velocity and N₂ density are homogeneous across the section of the tube because the flow is turbulent (Reynolds number $Re_D = 10000$). The pressure drop induces a variation of less than 1 % of the N₂ density over the spatial region of the measurements. Taking $v = 40\pm1$ m.s^{-1}, $[N_2] = 2.45\times10^{19}$ cm^{-3}, and the value of the slope measured at the center of the tube $\alpha(r=0) = 9.285\pm1.03 \times10^{-17}$ cm^3 cm^{-1}, we obtain the following value of the 3-body recombination coefficient k_3:

$$k_3\left(T{=}300K\right){=}7.77\pm1.04\times10^{-33}cm^6.s^{-1}$$

This value is compared with other measurements found in the literature in Figure II.13. Experimental details of the reviewed papers can be found in Table II.1. From this table it seems that the most carefully determined experimental value is the one of Clyne et al. [132]. The authors used four NO-titration points in a flowing system to measure N(⁴S) decay. They measured the [O]/[N] ratio using a similar emission-based technique and found [O]/[N]=0.005. They poisoned the pyrex surface of the tube with metaphosphoric acid to minimize the interaction with surfaces. We note that the value determined in this thesis is about twice higher than the value proposed by Kossyi et al [141], often used in the literature. However, it is in good agreement with the average value determined from our literature review (about 8×10^{-33} cm^6.s^{-1}), and in particular with the measurements of Clyne [132], Herron [130], Brennen [138], Marshall [137], Miyazaki [139], and also with the theoretical value of Partridge et al. [142].
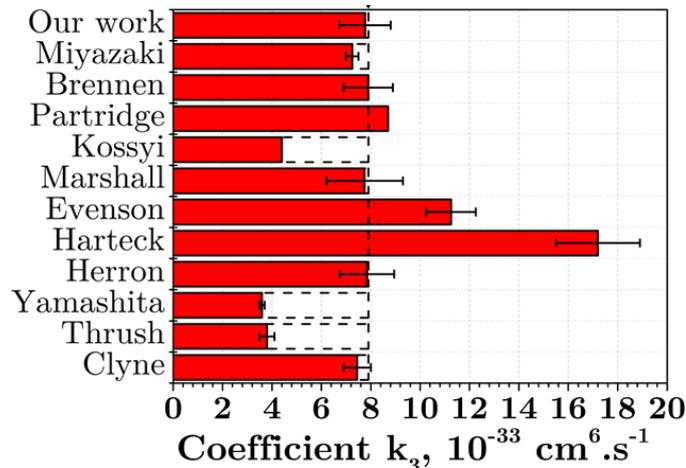
Figure II.13: Comparison of reaction rate coefficient k_3 of three-body recombination of N(⁴S) with N₂. The vertical dash line corresponds to the average of the reported values. Details can be found in Table II.1.

o   Validation on past data from the literature

At atmospheric pressure, experiments of atomic nitrogen recombination are very sensitive to the rate coefficient of three-body recombination k_3. Es-Sebbar et al. [119] published the temporal volumetric decay of $N(^4S)$ measured by TALIF in a Townsend DBD afterglow (see Figure II.14). The authors could not model the $N(^4S)$ decay on the basis of three-body recombination (Figure II.14, blue curve), so they concluded that significant additional loss processes were not included in their model. Later, Popov [120] and Tsyganov et al. [121] introduced surface recombination to improve the fit of the experimental data. However, the data of Es-Sebbar et al. are local volumetric measurements, so surface recombination should not affect the measured densities. It should be noted that Popov, Tsyganov and Es-Sebbar all used the rate coefficient value k_3 from Kossyi et al. [141]. Here, we reexamine the experiments of Es-Sebbar using the rate coefficient of three-body recombination determined in our work.

In the conditions of Es-Sebbar et al, diffusive transport can be neglected in the balance equation because of the high Péclet number and because the gas has a low level of impurities (<1 ppm). The time-decay of nitrogen can thus be written as follows:

$$[N(^4S)] = \frac{1}{2[N_2]k_3t + 1 / [N_0]} \tag{II.13}$$

where $[N_0]$ is the initial $N(^4S)$ density. We used the foregoing expression to model their experimental data. Figure II.14 shows the comparison with their data for $[N_0] = 3\times10^{14}$ cm^{-3} and for k_3 from our work and from Kossyi. Using the value of k_3 determined in this thesis (red curve) agreement with the experimental data of Es-Sebbar et al. [119] is excellent. This result confirms the sensitivity of the model to the rate coefficient k_3 at atmospheric pressure, and provides additional confirmation of the validity of the rate coefficient measured in this thesis.

Similar TALIF measurements were performed inside a pulsed parallel plate rf reactor cell at 5 torr by Adams and Miller [127]. The probability of surface recombination of $N(^4S)$ was estimated from the decay near the surface of the electrodes. The volume recombination loss rate in their conditions (about 0.02 s^{-1}) was much lower than the minimum measured decay rate of $N(^4S)$ (about 20 s^{-1}). So, $N(^4S)$ losses were only controlled by diffusion and surface recombination, and no information on three-body recombination could be extracted from their data.
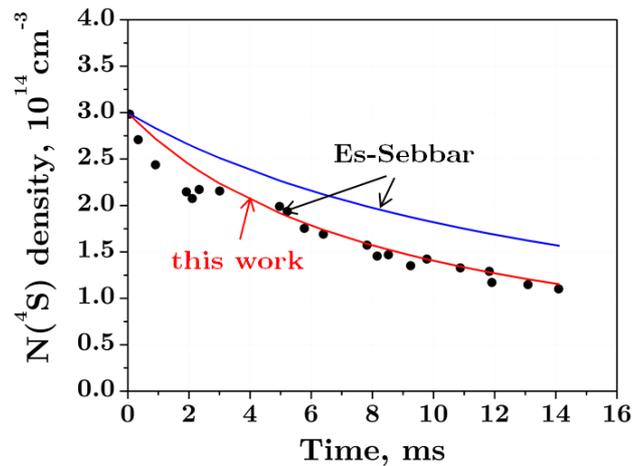
Figure II.14: Modeling of the decay of N(^{4}S) in the afterglow of a Townsend dielectric barrier discharge in N$_2$ assuming N(^{4}S) losses by three-body volume recombination only. Calculations are based on equation (II.13) with k$_3$ from our work (red line) and from Kossyi et al. [141] (blue line). Experimental data are from Es-Sebbar et al. [119].

Oinuma et al. [125] and Fromy et al. [169] also measured the N(^{4}S) density in an atmospheric pressure nitrogen afterglow with high Péclet number. However, in these references, titration-based techniques that do not allow spatially-resolved measurements were used, so the contribution of surface recombination cannot be excluded. Figure II.15 shows similar curves as in Figure II.14 using the averaged data of Fromy and Oinuma. Both sets of data are well fitted using the rate coefficient k$_3$ from our work. The slightly faster recombination in both cases can be attributed to surface recombination as discussed in the next section.
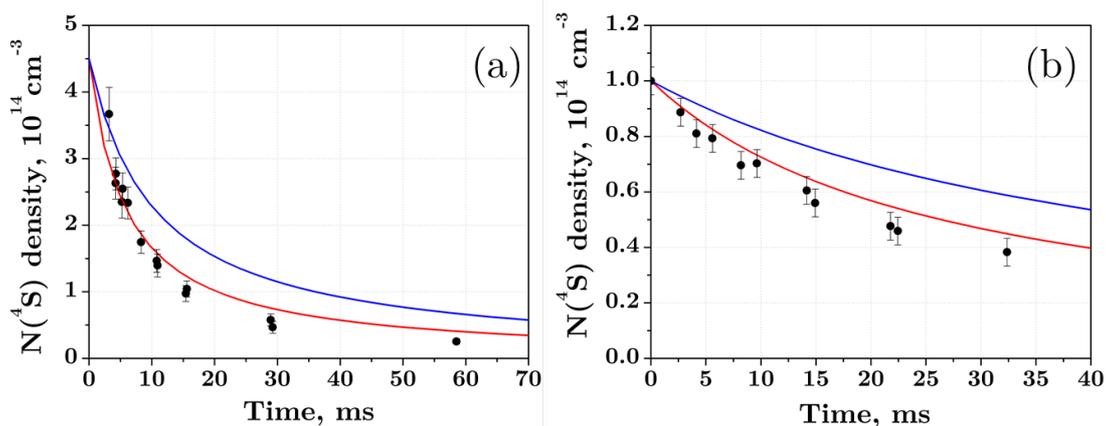
Figure II.15 : Modeling of the averaged N(^{4}S) decay in the afterglow of an atmospheric pressure pulsed corona discharge (a) and DBD (b) in N$_2$ assuming N(^{4}S) losses by three-body volume recombination only. Calculations are based on equation (II.13) with k$_3$ from our work (red line) and from Kossyi et al. [141] (blue line). Experimental

data (black dots) are titration-based measurements from Fromy et al. [119]. and Oinuma et al. [125].

In this section, we have confirmed the validity of our measured rate coefficient by the modelling of various atmospheric pressure nitrogen afterglows. The next two sections show applications of this coefficient to the determination of surface recombination of $N(^4S)$, and to $N(^4S)$ density measurements by relative OES.

6. Determination of surface recombination probability on polyurethane

The objective of this section is to determine the probability of $N(^4S)$ surface recombination on the polyurethane tube, using the $N(^4S)$ gas-phase decay measurements. The influence of the three-body recombination rate coefficient on the measured surface recombination probability is discussed.

The surface recombination of $N(^4S)$ is studied with a zero-dimensional model considering volumetric three-body recombination and an additional heterogeneous loss rate ν_{het}. The balance equation of the $N(^4S)$ density averaged over the cross-section of the tube is:

$$\frac{d\left\langle[N(^4S)]\right\rangle}{dt} = -2k_3\left\langle[N(^4S)]\right\rangle^2[N_2] - \nu_{het}\left\langle[N(^4S)]\right\rangle \tag{II.14}$$

The heterogeneous loss rate in a cylindrical tube is defined as follows [120]:

$$\nu_{het}^{-1} = \left(D_N\left(\frac{\pi}{2R}\right)^2\right)^{-1} + \left(\frac{\gamma_N\left\langle v\right\rangle}{2R}\right)^{-1} \tag{II.15}$$

where D_N is the diffusion coefficient of nitrogen atoms in N_2, γ_N is the probability of surface recombination, $<v>$ is the mean velocity of the particles near the surface, and R is the tube radius. $<v>$ is taken as the thermal velocity v_{th} of nitrogen atoms:

$$v_{th} = \left(\frac{8k_BT}{\pi m_N}\right)^{1/2} \tag{II.16}$$

where m_N is the mass of atomic nitrogen, k_B the Boltzmann constant, and T the gas temperature. The solution of equation (II.14) is [121]:

$$\left\langle [N(^4S)] \right\rangle = \frac{\nu_{het}[N]_0 \exp\left(-\nu_{het}t\right)}{\nu_{het} + 2k_3[N_2][N]_0 \left(1 - \exp\left(-\nu_{het}t\right)\right)} \tag{II.17}$$

where $[N]_0$ is the N(^{4}S) density at t=0. In Figure II.16, the averaged N(^{4}S) density measured by the absolute emission technique is plotted. The data are fitted using equation (II.17) adopting the 3-body recombination coefficient from Kossyi et al. and from the present work using the heterogeneous loss rate ν_{het} and $[N]_0$ as fitting parameters. The best fitting parameters are given in Table II.4.

Table II.4 : Fitting parameters of the N(^{4}S) recombination inside a polyurethane tube.

3-body rate coeff. k_3	Ref.	ν_{het}	$[N]_0$
4.4×10^{-33} cm^6.s^{-1}	Kossyi,[141]	46.6 ± 1.2 s^{-1}	$6.58\pm0.09 \times10^{14}$ cm^{-3}
7.77×10^{-33} cm^6.s^{-1}	Our work	11.8 ± 2.08 s^{-1}	$9.08\pm0.3 \times10^{14}$ cm^{-3}
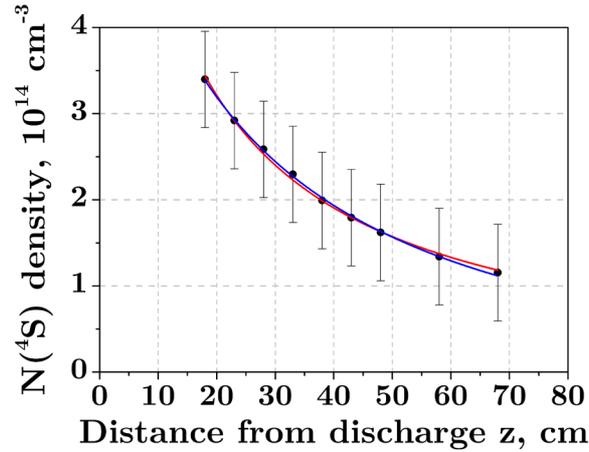
Figure II.16 : Averaged N(^{4}S) density measured by absolute emission (black dots), and fitted using equation (II.17) using k$_3$ from Kossyi et al. [141] (blue curve) or from our work (red curve).

The probability of surface recombination can then be determined from equation (II.15):

$$\gamma_N = \frac{2R}{\langle v \rangle \left(\nu_{het}^{-1} - \left(D_N \left(\frac{\pi}{2R} \right)^2 \right)^{-1} \right)} \tag{II.18}$$

The turbulent diffusion coefficient is required, but is unknown here. So, we consider two limiting flow cases. In the upper limit, the flow is laminar, and the probability is directly calculated using D$_N$ = 0.289 cm^2/s [166]. In the lower limit, the turbulent diffu-

sion is infinite, so surface recombination is the limiting process ($D_N \to \infty$). Rearranging equation (II.32), it can be obtained that the infinite turbulent diffusion case is valid if the heterogeneous losses are limited by the surface recombination, i.e.:

$$\frac{R}{D_N} \ll \frac{\pi^2}{2\gamma_N \langle v \rangle} \tag{II.19}$$

The probability of surface recombination varies from $\gamma_N = 7 \times 10^{-5}$ (laminar flow) to 8.4×10^{-5} (infinite diffusion). The average value is $\gamma_N = 7.7 \pm 2 \times 10^{-5}$.

If instead we use k_3 from Kossyi, then γ_N would range from 2.7×10^{-4} to 1 depending on the limiting flow case. Thus the determined surface recombination differs by at least a factor 3.5, whereas the rate coefficient differs by only 75 %. Therefore the measured surface recombination of N(^{4}S) is highly sensitive to the rate coefficient of three-body recombination at atmospheric pressure. This is due to an overestimation of the heterogeneous loss rate from the gas phase decay of N(^{4}S).

In this section we measured the surface recombination probability of N(^{4}S) on polyurethane in two limiting cases: laminar and infinite diffusion. We found an average value $\gamma_N = 7.7 \pm 2 \times 10^{-5}$. The use of the rate coefficient of Kossyi et al. in the modelling of recombination leads to an overestimation of the surface recombination probability of N on polyurethane by a factor 3.5 at least. In a general manner, underestimating the rate coefficient of three-body recombination induces a strong overestimation of the heterogeneous loss rate, and thus of the surface recombination probability.

7. Determination of the N(^{4}S) density profiles by relative OES

In various references, relative emission-based techniques have been used to measure N(^{4}S) absolute densities, e.g. [42], [123], [124]. In this section, we introduce the principle of the technique, and we discuss and compare it with the absolute emission technique presented in section 4.

7.1. Principle of N(^{4}S) measurement by relative OES

The relative emission technique starts with the same assumption as the absolute emission technique, namely that reactions R1 and R2 are balanced. As already stated in equation (II.2), this implies:

$$[\text{N}_2(\text{B}^3\Pi_g,\text{v}=11)]=\frac{\text{k}_1}{\text{k}_2}[\text{N}(^4\text{S})]^2 \qquad (\text{II}.20)$$

The local emissivity (in relative units) at (r,t) of the (11,7) vibrational band of the first positive system of N$_2$ is related to the density in state N$_2$(B$^3\Pi_g$,v=11) via the following expression:

$$\varepsilon_{N_2(B,v=11)}\left(r,t\right)=\text{C}(\lambda)[\text{N}_2\left(B,v=11\right)]=\text{C}(\lambda)\frac{k_1}{k_2}[\text{N}(^4\text{S})]^2(\text{r,t}) \qquad (\text{II}.21)$$

where C(λ) is a proportionality constant. In the absolute emission method, this constant is determined by calibration with a radiation standard, as described earlier. If an absolute calibration is not available, then the constant can be determined by measuring the decay of the local emissivity. This is the basis of the relative emission method. For this, we must make an additional assumption that, in the late afterglow, atomic nitrogen recombines mainly through the three-body reaction R3, so that:

$$\frac{\text{d}[\text{N}(^4\text{S})](\text{r,t})}{\text{dt}}=-2\text{k}_3[\text{N}_2][\text{N}(^4\text{S})]^2(\text{r,t}) \qquad (\text{II}.22)$$

Integrating equation (II.22), we obtain:

$$\frac{1}{[N(r,t)]}=\frac{1}{[N(r,t=0)]}+2k_3[N_2]t \qquad (\text{II}.23)$$

Then, substituting equation (II.21) into (II.23), we get:

$$\varepsilon_{N_2(B,v=11)}^{-1/2}\left(r,t\right)=\varepsilon_{N_2(B,v=11)}^{-1/2}\left(r,t=0\right)+2k_3\left(\frac{k_2}{k_1\text{C}(\lambda)}\right)^{1/2}[N_2]t \qquad (\text{II}.24)$$

The constant C(λ) can then be determined from the slope α of the inverse square root of the local emissivity vs time, with:

$$\text{C}(\lambda)=\frac{4k_3^2k_2}{\alpha^2k_1}[N_2]^2 \qquad (\text{II}.25)$$

The density N(^{4}S) is then given by:

$$[N(^4S)](r,t)=\frac{\alpha}{2k_3[N_2]}\varepsilon_{N_2(B,v=11)}^{1/2}\left(r,t\right) \qquad (\text{II}.26)$$

[N(^{4}S)] is then obtained if [N$_2$] and k$_3$ are known. In the literature this approach was used in methods based on measurement of emission decay time either directly in the

discharge, or from the time-of-flight in flowing afterglows. Note that for the flowing afterglow, the last equation becomes:

$$[N(^4S)](r,z) = \frac{\alpha v}{2k_3[N_2]}\varepsilon^{1/2}_{N_2(B,v=11)}(r,t) \tag{II.27}$$

where v is the flow velocity.

Finally, there is a simpler variant of the technique that does not require the local emissivity (thus avoiding an Abel-inversion of the spectra). In this variant, the line-of-sight intensity is measured at various times or at various positions along the afterglow tube. The line-of-sight intensity is defined as (considering that the first positive emission is optically thin):

$$I_{N_2(B,v=11)}(z) = \int_0^L \varepsilon_{N_2(B,v=11)}(r,z)dy = \frac{1}{L}C(\lambda)\frac{k_1}{k_2}\left\langle[N(^4S)]^2\right\rangle(z) \tag{II.28}$$

where L is the diameter of the afterglow (or the diameter of the tube).

We now make the following approximation, usually justified for turbulent flows in a tube (for parabolic profiles, Appendix A shows that this approximation still holds within 11%):

$$\left\langle[N(^4S)]^2\right\rangle \cong \left\langle[N(^4S)]\right\rangle^2 \tag{II.29}$$

With this approximation, equation (II.27) can be rewritten as:

$$\left\langle[N(^4S)]\right\rangle(z) = \frac{\alpha v}{2k_3[N_2]}\sqrt{I_{N_2(B,v=11)}(z)} \tag{II.30}$$

These techniques have been applied to determine the N(^{4}S) density by Babayan et al. [154] in a pulsed He-N$_2$ afterglow, by Peeters et al. [123] at the exit of a nitrogen DBD flowing in open air, and by Pointu et al. [42] inside a flowing afterglow tube. The main disadvantage of the method is the systematic error due to uncertainties on the rate coefficient k_3. For example, Pointu et al. used k_3=4.4×10^{-33} cm^6.s^{-1} from Kossyi et al [141], whereas Peeters et al. [123] used k_3=1.5×10^{-32} cm^6.s^{-1}, almost four times higher than the value chosen by Pointu et al.. Since the measured N(^{4}S) density is proportional to the rate coefficient k_3, the final results are strongly affected by the choice of k_3. Nevertheless, we believe that accurate results can be obtained using the k_3 rate coefficient deduced from the present work.

7.2. Comparison with absolute OES

Here, we present a comparison between the relative and absolute OES methods.

- Assumptions

For both methods, it is assumed that N$_2$(B$^3\Pi_g$,v=11) is mainly produced by three-body recombination (R1). This assumption can be confirmed by measuring the vibrational distribution of N$_2$(B$^3\Pi_g$,v) and verifying that it peaks at v = 11.

For absolute OES, it is additionally assumed that the quenching rate of N$_2$(B$^3\Pi_g$,v=11) and the rate coefficient of three-body recombination (R1) of N(^{4}S) are known. So the technique is limited to conditions where the quenching rate of N$_2$(B$^3\Pi_g$,v=11) is accurately known, and N$_2$ is the main third body in the three-body recombination (R1). In N$_2$-xO$_2$ gas mixture at atmospheric pressure, the quenching of N$_2$(B$^3\Pi_g$,v=11) by O$_2$ can be neglected if x<<1%.

For relative OES, it is assumed in the calibration phase (determination of coefficient α in equation (II.26)) that N(^{4}S) atoms are only lost by three-body recombination (R3) at a known rate coefficient k$_3$, i.e. recombination with O, NO impurities and surface recombination can be neglected. This can be ensured by measuring the local volumetric emissivity of N$_2$(B$^3\Pi_g$,v=11) emission in a high purity nitrogen afterglow. Measurements can then be performed in conditions where the quenching rate of N$_2$(B$^3\Pi_g$,v=11) does not significantly vary in comparison to the calibration phase, e.g. N$_2$-xO$_2$ afterglow with x<<1%, and N$_2$ is the main third body in reaction R1.

- Uncertainties

The absolute OES technique allows a direct measurement of N$_2$(B$^3\Pi_g$,v=11) absolute density from which the N(^{4}S) density can be directly inferred. The calculated N(^{4}S) density is proportional to the square root of the reactions coefficients of reaction R1 and R2 which have been measured with an uncertainty of 30 % and 8 % respectively, thus giving a systematic error of 19%. Additional errors are due to the absolute calibration procedure of the optical system. Typical calibration uncertainties in the spectral range of interest (around 580 nm) are around 3% with commercially available standards of radiance. Thus, the overall uncertainty on the N(^{4}S) density is about 22%, which is lower than the 50% uncertainty of TALIF measurements of N(^{4}S) densities with nanosecond lasers calibrated with krypton [151].

In comparison, the relative OES technique heavily relies on the validity of the assumptions used in the calibration. The only systematic error comes from the rate coefficient

of three-body recombination, determined here with an uncertainty of 15 %. Additional experimental uncertainties come from the measurement of the decay rate of the emissivity in the calibration.

The relative OES technique brings practical advantages because no calibration of the optical device is required, except to ensure that the vibrational distribution of $N_2(B^3\Pi_g,v)$ peaks at v=11 (obtained by relative calibration). The range of validity of the method is similar to the absolute OES technique and uncertainties are about the same. However, great care is required in the calibration phase to remove the contributions of impurities and surfaces on the measurement of the emission decay. On the contrary, absolute OES is more difficult to implement experimentally but allows direct measurement of $N_2(B^3\Pi_g,v=11)$ density from which $N(^4S)$ density is inferred.

8. Application to the decontamination of tubes

In this section, we combine the results of the previous sections to gain insight into the physical parameters of importance to sterilize long tubes such as endoscopes. There is a wide variety of endoscopes, with lengths from a few tens of centimeters to a few meters, inner diameters from a few millimeters to a few centimeters, and materials including glass, carbon fibers, PTFE (Teflon), polyurethane, or metal. The biocidal action of the N_2 afterglow is strongly related to the $N(^4S)$ density [42]. Therefore, the modeling of $N(^4S)$ recombination may be used to determine the $N(^4S)$ density at the exit of the tube and to infer the exposure time required to guarantee a sufficient level of treatment.

Combining microbiological studies with $N(^4S)$ absolute density measurements is required to determine the inactivation of microorganisms by the nitrogen afterglow species. Such work was performed by Limam et al. [170] for treatment of *E.Coli* (DH1:ATTC338949) in the afterglow of a nitrogen corona discharge . In this work, the authors deposed bacteria on sections of quartz tubes (2 cm length, 8 mm inner diameter) placed at 12 and 65 cm from the discharge, where the $N(^4S)$ density was estimated to be 1.7×10^{14} cm^{-3} and 5×10^{13} cm^{-3}, respectively. At 65 cm, a D-value of 11 min was determined. Sterility (12-log reduction) is thus expected for an exposure time of 132 min (12 log x 11 min/log). Thus we expect that a nitrogen afterglow can sterilize *E. Coli* bacteria inside a quartz tube of length L within 132 min provided that $[N(^4S)] > 5\times10^{13}$ cm^{-3} at the exit of the tube.

The model presented in section 6 can be used to determine the position at which $[N(^4S)] = 5\times10^{13}$ cm^{-3} , with the initial $N(^4S)$ density and surface recombination proba-

bility as input parameters. According to the model the average N(^{4}S) density is given by:

$$\left\langle [N(^4S)] \right\rangle = \frac{\nu_{het}[N]_0 \exp\left(-\nu_{het} t\right)}{\nu_{het} + 2k_3[N_2][N]_0 \left(1 - \exp\left(-\nu_{het} t\right)\right)} \tag{II.31}$$

with;

$$\nu_{het}^{-1} = \left(D_N \left(\frac{\pi}{2R}\right)^2\right)^{-1} + \left(\frac{\gamma_N \left\langle v \right\rangle}{2R}\right)^{-1} \tag{II.32}$$

In practice, we do not have values of D_N in the turbulent regime. So, we considered the two limiting cases of laminar diffusion (with D_N=0.289 cm^2/s, [166]) and infinite turbulent diffusion ($D_N \rightarrow \infty$). We will now consider the effects of the nitrogen surface recombination probability γ_N (which depends on the tube material), of the tube radius, of the initial N(^{4}S) number density, and of the flow velocity. Unless specified otherwise, the nominal parameters are those of the experimental study presented in this chapter, namely $[N]_0 = 9 \times 10^{14}$ cm^{-3}, R = 2 mm, $\gamma_N = 7.7 \times 10^{-5}$ (polyurethane), and v = 40 m.s^{-1}.
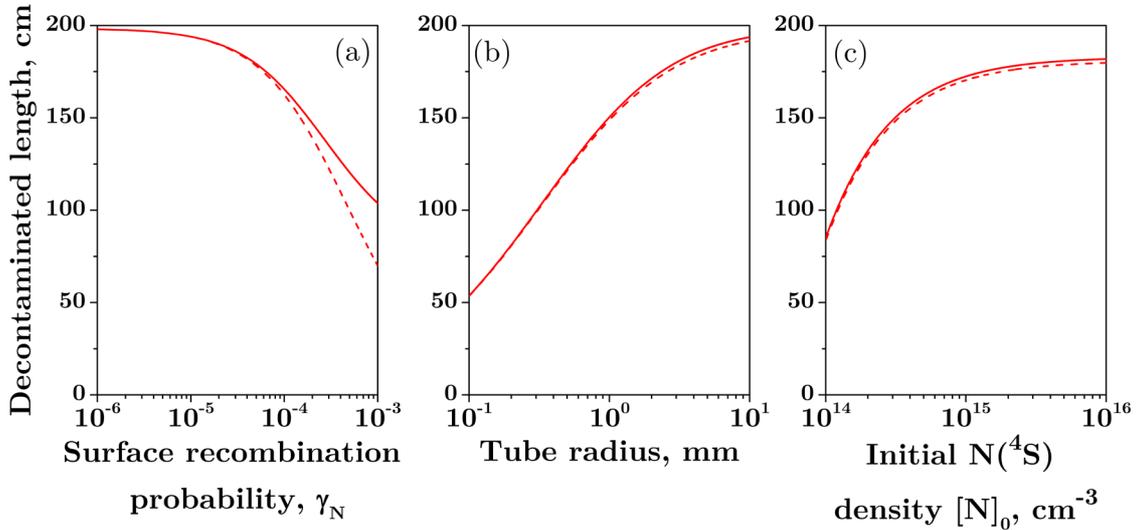
Figure II.17 : Length of tube decontaminated by the nitrogen afterglow as a function of (a) surface recombination probability of N(^{4}S), (b) tube radius, (c) initial N(^{4}S) density, and (d) flow velocity. Two limiting cases are considered: laminar flow (line) or infinite diffusion (dash). Parameters (if not specified): $[N]_0 = 9 \times 10^{14}$ cm^{-3}, R = 2 mm, $\gamma_N = 7.7 \times 10^{-5}$, v = 40 m.s^{-1}.

We define the Decontaminated Tube Length (DTL) as the tube location at which $[N(^4S)] = 5 \times 10^{13}$ cm^{-3}.

Figure II.17 (a) shows the effect of the surface recombination probability γ_N on the DTL. Up to $\gamma_N = 10^{-4}$ the DTL is not influenced by diffusion effects: the infinite turbulent diffusion and laminar flow cases give similar results because heterogeneous losses are limited by surface recombination, not diffusion. For $\gamma_N > 10^{-4}$, diffusion begins to play a role on heterogeneous losses, and therefore the DTL is different for the cases with laminar or turbulent diffusion.

For polyurethane tubes (commonly used in catheters [171]), we found $\gamma_N = 7.7 \times 10^{-5}$. Thus diffusion does not influence the N(^{4}S) decay in this case. Values of the surface recombination rate of N(^{4}S) on various materials were reviewed by Vesel [172]. Typical values of γ_N are in the range of 5×10^{-8} – 3×10^{-4} for pyrex, 7×10^{-6} – 2×10^{-3} for quartz, 2×10^{-7} – 2.5×10^{-5} for Teflon, 1.8×10^{-3} – 7×10^{-2} for stainless steel. Roughly speaking, glass and Teflon are fairly inert with respect to N(^{4}S) atom recombination, whereas metals strongly promote recombination.

Figure II.17.b shows the effect of the tube radius on the DTL. Smaller tube radii are more difficult to treat because of the increased heterogeneous loss rate. As seen in Figure II.18, the DTL decreases significantly for high values of $\gamma_N \sim 10^{-2}$, and in general when heterogeneous losses are limited by diffusion.
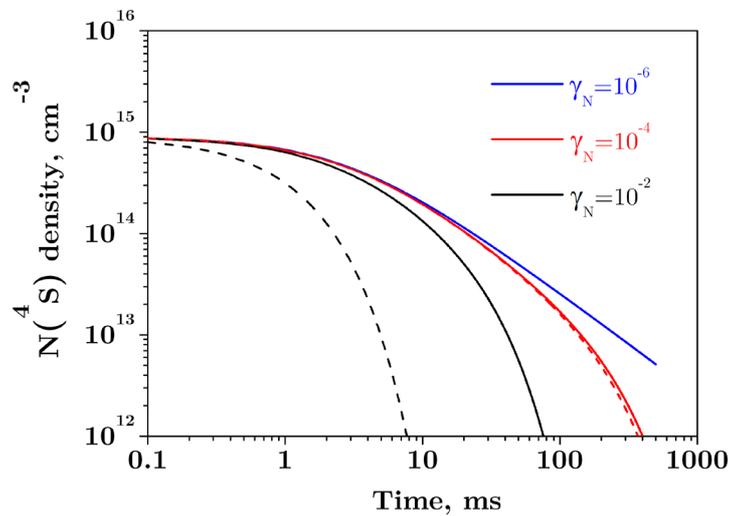
Figure II.18: Influence of the surface recombination probability γ_N on the density of N(^{4}S) in the afterglow. Calculation in the laminar (line) and infinite diffusion (dash) flow cases. Parameters: $[N]_0 = 9 \times 10^{14}$ cm^{-3}, R = 2 mm

Figure II.17.c shows the influence on the DTL of the initial N(^{4}S) density produced by the plasma. The DTL is highly sensitive to $[N]_0$ for $[N]_0 < 10^{15}$ cm^{-3}, and practically constant for $[N]_0 > 10^{15}$ cm^{-3}. Figure II.19 shows the effect of the initial N(^{4}S) density on

the profile of atomic nitrogen density along the tube. It is shown that at t~100 ms, the average N(^{4}S) density is independent on the initial N(^{4}S) density. As a result, decontamination of a quartz tube longer than 2 m contaminated by *E. Coli* is not possible using the nitrogen afterglow within 132 min at a flow velocity of 40 m/s, independently on the produced N(^{4}S) concentration.
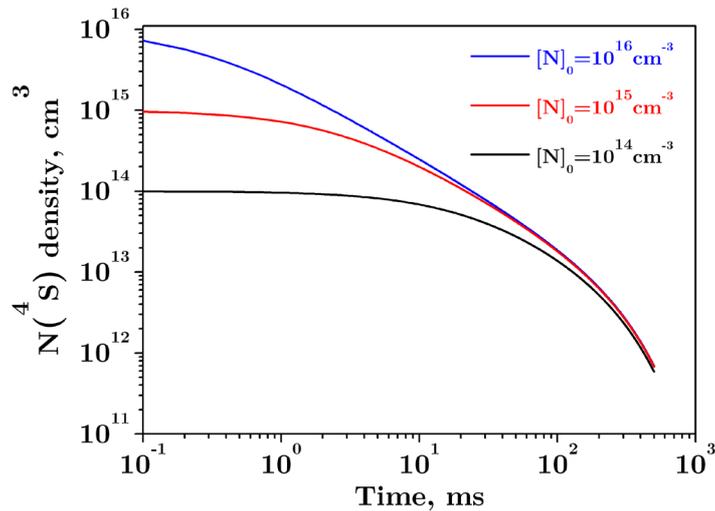
Figure II.19: Influence of the initial N(^{4}S) density [N]$_0$ on the density of N(^{4}S) in the afterglow. Parameters: γ_N=7.7$\times$10^{-6}, R=2 mm

Increasing the flow velocity is expected to increase the DTL. However, the N(^{4}S) propagation may be limited because of turbulent diffusion if surface recombination is high. In addition, increasing the velocity may cause the dislodgement of microorganisms from the tube before they are inactivated. This may increase the risk of outside contamination. So, the flow velocity has to be adjusted to limit microorganisms dislodgment and N(^{4}S) recombination at the surface.

The model of recombination of N(^{4}S) was used to predict the treatment time required to treat tubes of length L contaminated by E. *Coli* on their inner face. The model is based on the results of Limam et al. [170] who reported a D-value of 11 min for the treatment of *E. Coli* in a quartz tube by the nitrogen afterglow (with [N(^{4}S)] = 5$\times$10^{13} cm^{-3}) .

This approach can be used and tested on different surface materials and microorganisms. For this, estimates of D-values of bio-indicators on a given surface material combined with N(^{4}S) density measurements are necessary. In addition, the surface recombination probability must be determined. If literature values are not available, this recombination probability can be measured with the method presented in Section 6 of this chapter.

9. Conclusions

Modeling the density of atomic nitrogen in atmospheric pressure nitrogen afterglows strongly relies on the rate coefficient of three-body recombination of $N(^4S)$. This rate coefficient was re-evaluated in this chapter.

We performed space-resolved measurements of the $N(^4S)$ density profiles inside a cylindrical tube, based on the measurement of the $N_2(B^3\Pi_g, v=11)$ density by absolute-emission spectroscopy combined with an Abel transform. The results show that $N(^4S)$ follows an inverse decay at the center of the tube. By comparing the rates of $N(^4S)$ losses in the balance equation, we concluded that $N(^4S)$ atoms were mainly lost by three-body recombination in the volume. A fit of our experimental data gave a rate coefficient of three-body recombination $k = 7.77 \pm 1.04 \times 10^{-33}$ cm^6.s^{-1}, which is about 75 % higher than the commonly used value of Kossyi et al. [141], but in excellent agreement with several other values issued from the literature. We further confirmed the validity of the measured rate coefficient by successfully modeling two sets of $N(^4S)$ data previously obtained by TALIF and titration in atmospheric pressure nitrogen afterglows.

On the basis of this new rate coefficient, we have determined the probability of surface recombination of nitrogen atoms on polyurethane: $\gamma_N = 7.7 \pm 2 \times 10^{-5}$. We observed that a decrease of 44% of the rate coefficient of three-body recombination induced an overestimation of the surface recombination probability by at least a factor 3.5.

We compared the absolute OES technique of $N(^4S)$ measurement with the relative OES technique used in previous works [42], [123], [124]. The relative OES method is easier to implement experimentally, and the range of validity and expected uncertainties are similar to the absolute OES method. However, the relative OES method should use the correct rate coefficient of three-body recombination of $N(^4S)$. In addition, the spectra must be Abel-inverted to eliminate possible competing $N(^4S)$ losses mechanisms at the surface. Finally, the nitrogen afterglow should be sufficiently pure, i.e. with [O]/[N] $<<$ 0.75, to prevent recombination losses with impurities.

In the last section, the results of this chapter were applied to model the decontamination of small diameter tubes mimicking endoscopes and catheters used in healthcare facilities. On the basis of Limam et al. [170] work, we predicted the decontaminated length of a tube contaminated by *E. Coli*, using a recombination model of $N(^4S)$ atoms, and assuming that $N(^4S)$ is directly related to the inactivation rate. We showed that increasing the surface recombination probability of N and decreasing the tube radius

reduce the propagation length of the afterglow. It is shown that at t~100 ms after the discharge, the average N(^{4}S) density is independent of the initial N(^{4}S) density because of fast three-body recombination of N(^{4}S). Therefore increasing the initial N(^{4}S) density does not allow to increase the decontaminated tube length. For this, the flow velocity is the most significant parameter.

Chapter III

Diagnostics of RONS production and biocidal efficiency in air NRP discharges

The production of lethal concentrations of reactive oxygen and nitrogen species (RONS) is a promising approach to inactivate microorganisms in the post-discharge. Plasmas produced by air nanosecond repetitively pulsed (NRP) discharges are non-thermal and low energy-consuming (a few W/cm^3) sources of radicals [173], [174]. Therefore they are interesting candidates for the efficient decontamination of surfaces.

In this chapter, we present studies of the production of ozone (O_3) and nitrogen oxides (NO_X) RONS generated by NRP discharges in atmospheric pressure dry air. The chapter is organized as follows. First, NRP discharges and biocidal mechanisms of O_3 and NO_x are briefly introduced. Second, O_3 and NO_x produced by an NRP discharge are measured inside a decontamination chamber placed at the exit of the plasma reactor by means of mid-IR quantum cascade laser absorption spectroscopy (QCLAS) and UV broad-band absorption spectroscopy. Third, microbiological tests are performed inside the decontamination chamber. The discharge is tuned to vary the amount and nature of RONS, and the antimicrobial efficacy of this tuning is investigated.

1. Introduction

1.1. Nanosecond repetitively pulsed discharge

Nanosecond Repetitively Pulsed (NRP) discharges in atmospheric pressure air were introduced in the early 2000's [175]–[177] as a way to produce non-equilibrium plasmas with low gas heating and low input power in atmospheric pressure air. NRP discharges consist in applying short-duration (nanosecond) high voltage pulses at a high repetition rate (typically 10 to 100 kHz). The duration of the pulse is sufficiently short to avoid arc transition and to limit the gas temperature increase. Working at high repetition

rate allows to maintain a high density of active species between consecutive pulses, and to develop synergies between pulses. In the plasma, the input energy is mainly converted to electronic excitation and ionization because of the high reduced electric field (E/N=100-300 Td) as seen in Figure III.1. Therefore high concentrations of electronic states and electrons are produced during the discharge phase allowing efficient production of RONS (e.g. 50 % disssociation of O_2 [178]).

1.1.1. Corona, glow, and spark regimes

At Ecole Centrale Paris [179], three NRP regimes were observed in preheated air at 1000 K: the corona, glow and spark regimes (Figure III.2). In the corona regime, the emission of light is located in a region close to the anode where streamers are produced because of the local high electric field. The electric field is high enough to form a conductive region near (A) electrode but not high enough to cause electrical breakdown. The energy deposition of the corona is typically below 10 µJ/pulse (Table III.1).
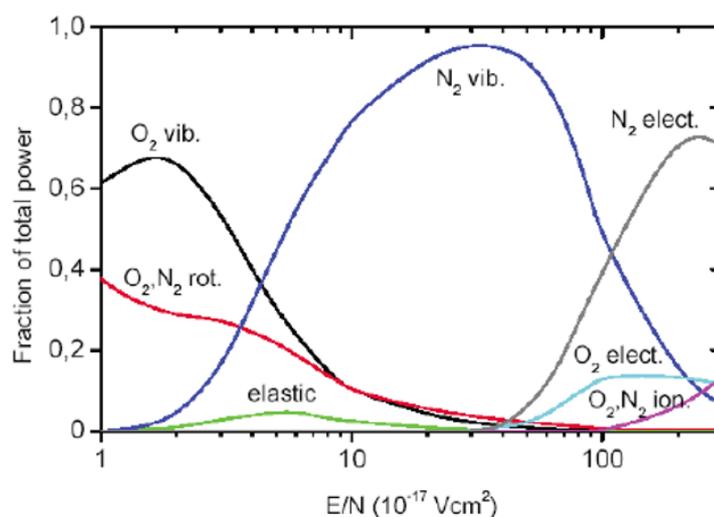
Figure III.1: Fractional power dissipated by electrons into different molecular degrees of freedom in air plasma discharges, taken from [180]

The glow regime [176], [181] appears at higher voltage in comparison to the corona regime. Electron avalanches generate a space charge field that causes the distortion of the electric field leading to the avalanche-to-streamer transition. The streamer is cathode-directed, and once it reaches the cathode, a return wave redistributes the potential. After this stage and until the end of the pulse, the discharge is similar to a DC glow discharge. The emission is diffuse and fills the whole inter-electrode gap. There is practically no elevation of the gas temperature. The existence of the glow regime at ambient temperature was predicted by the model developed in Refs. [179], [182], and first

observed by Rusterholtz [183]. Rusterholtz showed that the existence of the glow regime depends on a set of parameters: flow velocity, flow temperature and pressure, electrode radius of curvature, inter-electrode gap distance, applied voltage, pulse duration, and PRF.

Table III.1: Features of the regimes of NRP discharge in air

Regime	Energy deposited per pulse	Temperature increase
Corona	$< 10\mu J$	0
Glow	10-100 μJ	<200 K
Spark	1-100 mJ	2000-4000 K

The glow-to-spark transition occurs at higher reduced electric field (E/N) because of a significant increase of the ionization rate (see Figure III.1) and current, which cause thermal ionization instability. If this step is not aborted (e.g. by the use of a short pulse), the transition to arc is observed. Figure III.2 shows the different structures and intensities of the corona, glow and spark regimes in air at 1000 K. Table III.1 summarizes the characteristics of these three regimes.
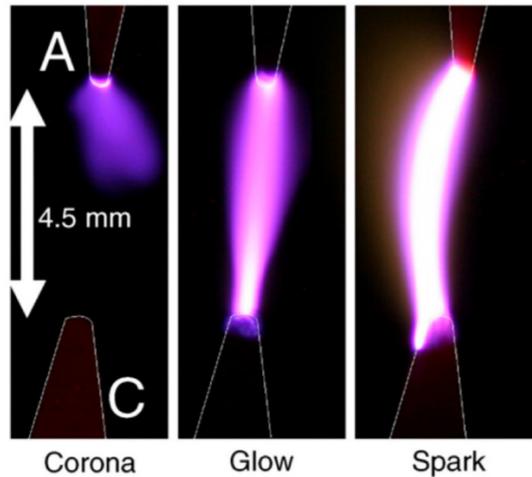
Figure III.2: The corona, glow and spark regimes in air at 1000 K and atmospheric pressure – Conditions: gap distance= 4.5 mm; PRF=10 kHz; air flow velocity=1 m.s^{-1}, images taken from [184]

1.1.2. Reactivity, fast gas heating and hydrodynamic gas expansion

Large oxygen production by dissociative quenching (i.e. ~ 50 % dissociation of O_2, [178]) with ultrafast gas heating on nanosecond timescale was observed in air, first by Pai [182], [184] and later confirmed in Refs [173], [174], [185], as seen in Figure III.3.

This ultrafast phenomenon was attributed to the two-step mechanism for E/N=100-400 Td proposed by Popov [186]. First, excited electronic states of N_2 are produced by electron impact (reaction (III.1)). Second, O_2 molecules are dissociated by the strongly exothermic dissociative quenching of N_2 electronic states (reaction (III.2)):

$$e^- + N_2(X) \rightarrow N_2(A,B,C) + e^- \tag{III.1}$$

$$N_2(A,B,C) + O_2 \rightarrow N_2(X) + 2O + \text{heat} \tag{III.2}$$
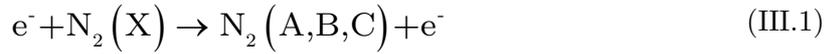
At E/N=450-900 Td, gas heating is mainly caused by ion reactions and N_2 dissociation by electron impact [187]. The intense heat release during the discharge pulse produces a shock wave that propagates outward the inter-electrodes gap within a few microseconds [188]. Subsequent hydrodynamic effects include gas expansion and recirculation which are described in greater details in Chapter IV.
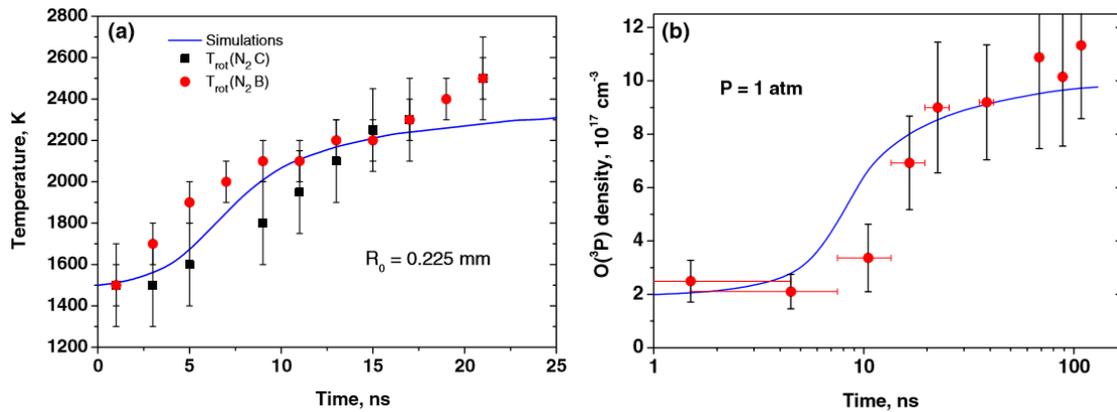
Figure III.3 : Comparison of measured (symbols) and simulated (line) temporal evolution of (a) the gas temperature (b) the ground state atomic oxygen density [173], [189]. Simulations performed in Ref. [190], graphs taken from [173].

1.2. Antimicrobial action of ozone and NO$_x$

- Ozone

Ozone is usually produced in air or oxygen by filamentary dielectric barrier discharges (DBD), by corona discharges or by photolysis using the radiation of an excimer source at 172 nm [191]–[193]. The germicidal action of ozone is mainly due to the high oxidation-reduction potential (i.e. 2.07 V, [194]) of the molecule. Oxidation by ozone can affect various components of cells such as proteins, DNA, and membranes, so that many germicidal mechanisms have been identified in the past. They are reviewed in Refs. [25], [102]. The efficiency of ozone tends to increase with the relative humidity

(RH) [102]. Combined with H_2O or UV, ozone can decompose to produce radicals such as O_2^-, HO_2, OH, H_2O_2 [194], that are more likely to induce damage. In liquids, O_3 is more efficiently decomposed into OH at high pH [194].

- Nitric oxide

Until the 1990's, NO was only considered as a pollutant produced in fossil-fuel combustion and a precursor of tropospheric ozone formation, acid rains and chemical smog [195]–[197]. In 1992, Furchgott et al. [198] determined that NO was the endothelium-derived relaxation factor –i.e. nitric oxide produced by the endothelial cells that coat blood vessels control the blood pressure by dilating the vessels. This discovery initiated therapies based on the administration of NO in order to cure cardiovascular diseases caused by blood pressure deregulation –e.g. thrombosis, restenosis [199]. NO also stimulates angiogenesis, thus accelerating wounds healing –e.g. ulcer [200]. These benefits of NO administration are observed at sufficiently low NO concentration (nM, about 5-80 ppm [201]). Therapeutical applications of nitric oxide are reviewed in Ref. [199].
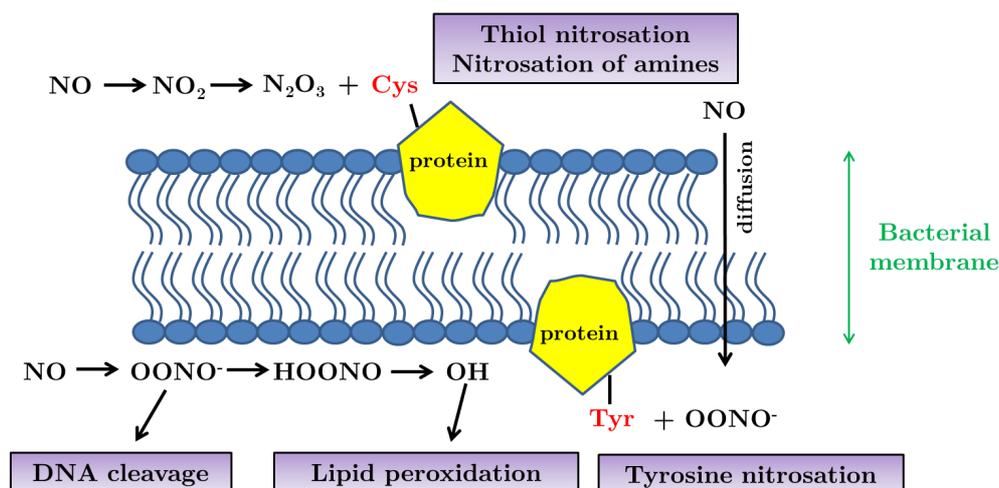
Figure III.4: Antibacterial mechanisms of nitric oxide and its byproducts, modified from [199]

At high nitric oxide concentrations (mM range), antibacterial mechanisms are dominant (see Figure III.4, and [202] for a schematic of the mechanisms). First, oxydations of NO form N_2O_3 which induces nitrosation of the thiol function (-SH) of cysteine amino acids present in several structural proteins composing the cell membrane. Second, NO can freely diffuse through the cell membrane [203] and react with the superoxide anion, O_2^-, to produce the peroxynitrite anion OONO$^-$ that can induce DNA cleavage [204] or nitration of tyrosine – an amino acid present in proteins of the cell membrane. Third, it produces peroxynitrous acid ONOOH, which can provoke peroxidation of the

lipid bilayer membrane. The diffusion length of peroxynitrite being 10^4 times longer than for OH [72], peroxynitrite can diffuse deeper into the cell to attack key components such as DNA.

- Nitrogen dioxide

Nitrogen dioxide is known as an atmospheric pollutant produced by NO oxidation. Commercial NO_2 sterilizers are available (Noxilizer, [205]) and exhibit a D-value of about 20 s on the identified bioindicator *Geaobacillus Stearothermophilius* exposed to 4000 ppm of NO_2 [206]. An advantage of NO_2 decontamination methods is the low boiling point of NO_2 (21°C at sea level), which allows to store liquid NO_2 before vaporizing it during the sterilization cycle. NO_2 decontamination is discussed from the point of view of economic cost and material compatibility in Ref. [207].

The mechanism of action of NO_2 has been identified as producing single-strand breaks in DNA [205], [208], [209]. Bermudez et al. [80] reported that no breaks of DNA could be observed after NO_2 exposure for 1.2 ppm mole fraction, thus indicating a minimum threshold concentration for biocidal effects.

Plasma sources may have a large antimicrobial spectrum because of the wide variety of inactivation mechanisms of RONS. In addition the material compatibility may be extended by tuning the relative concentrations of the various RONS. For instance, NO_2 exposure is known to be incompatible with copper and brass [210] whereas the compatibility with ozone is excellent [15]. However it has to be ensured that plasma sources readily produce lethal concentrations of RONS at a low energy cost to use this approach. Here, the efficiency of production of ozone and NO_X by air NRP discharge is studied and the effect of RONS tuning during plasma exposure on the inactivation rate is investigated.

2. Experimental setup

2.1. Discharge setup

Optical diagnostics as well as microbiological tests were all performed inside the stainless steel chamber of 15-liter volume shown in Figure III.5. The plasma reactor is the same as the one used in Chapter II. Two pin tungsten electrodes are encapsulated in a cylindrical ceramic box. The reactor is located inside the chamber and mounted on an XYZ translation stage allowing precise adjustment of the distance between the samples and the reactor for microbiological tests. Dry air is injected between the electrodes at a

flow rate adjusted by a mass flow controller (Bronkhorst model F-203AC-RA-44V). Polyamide tubes connect the gas outlet of the chamber to a fan in order to evacuate the plasma species from the chamber. The chamber is initially filled with pure air for 10 minutes before turning on the discharge. Depending on the flow rate, the residence time of the species inside the chamber is about 1 min.

The front door of the chamber allows to insert and to remove the microorganisms for microbiological tests. The production of nitric oxide, nitrogen dioxide and ozone are measured inside the chamber by high resolution mid-IR QCLAS (NO) and broad-band UV absorption spectroscopy (NO_2, O_3). Flanges at the edge of the chamber accomodate mounts and windows suitable for the mid-IR and UV spectral ranges.
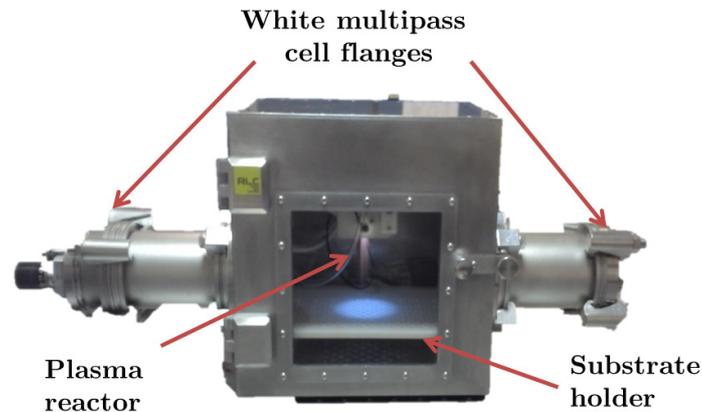
Figure III.5 : Photograph of the decontamination chamber. White multipass cell flanges on the sides of the chamber for the mid-IR experiment are replaced by mounts with windows for UV absorption measurements. Electrical power and gas are supplied from the rear face of the chamber.

The plasma is produced by a nanosecond pulser (RLC, model NANOGEN1) based on a fast high voltage transistor switch (Behlke HTS11-06-GSM). The pulser operates in two modes: normal and double pulse mode. The main features of the modes are given in Table III.2. In the normal mode, pulses of adjustable duration (>150 ns) and repetition rate are generated. In the double pulse mode, the pulser generates a sequence of two high voltage pulses of 20 ns duration each, adjustable time separation (>150 ns), and opposite polarity (Figure III.6). The repetition rate of the sequence can be adjusted in the range 0-100 kHz. Here, we only used the pulser in the double pulse mode.

Table III.2 : Characteristics of the NANOGEN1 pulser

Operating mode	Normal (not used)	Double pulse
Pulse duration	150 ns – 50 µs	20 ns
Pulse repetition frequency	1 Hz – 100 kHz	1 Hz – 100 kHz
Output voltage	0-10 kV	0-10 kV
Max. output current	50 A	50 A
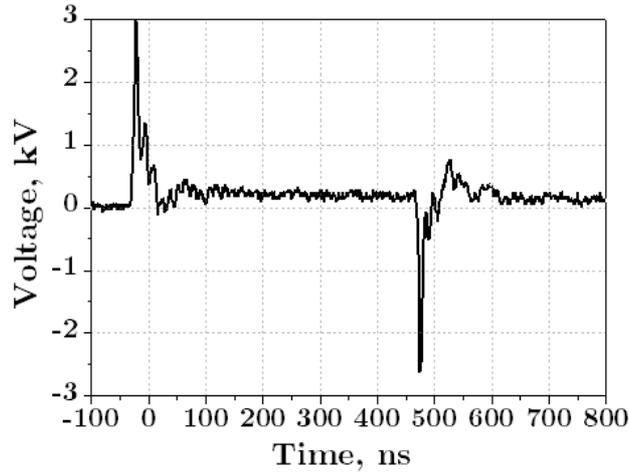
Figure III.6 : Typical voltage waveform of NANOGEN1 pulser in the double pulse mode

2.2. Electrical measurements

The energy deposited in the discharge is obtained by multiplying the voltage and conduction current waveforms, and integrating the result over time:

$$E = \int_t U I_{cond} dt \tag{III.3}$$

The measured current is the sum of conduction and displacement currents. The latter needs to be subtracted from the total current in order to correctly estimate the conduction current:

$$I_{cond} = I_{tot} - I_{disp} \tag{III.4}$$

where I_{disp} is the displacement current, determined from the reactor capacitance C and the time-derivative of the applied voltage:

$$I_{disp} = C \frac{dV}{dt} \tag{III.5}$$

The applied voltage was measured using a passive high-voltage probe (Lecroy PPE20kV, 100 MHz bandwidth) with 1000:1 attenuation factor, connected in parallel to the discharge. A current probe (Pearson coil, model 6585) was used to measure the electric current. The current-to-voltage ratio is 1 A/V. The output signals from the voltage and current probes are recorded using an oscilloscope (LeCroy Wavepro960 DSO, 2GHz, 16GS/S). Figure III.7 shows typical measured waveforms.
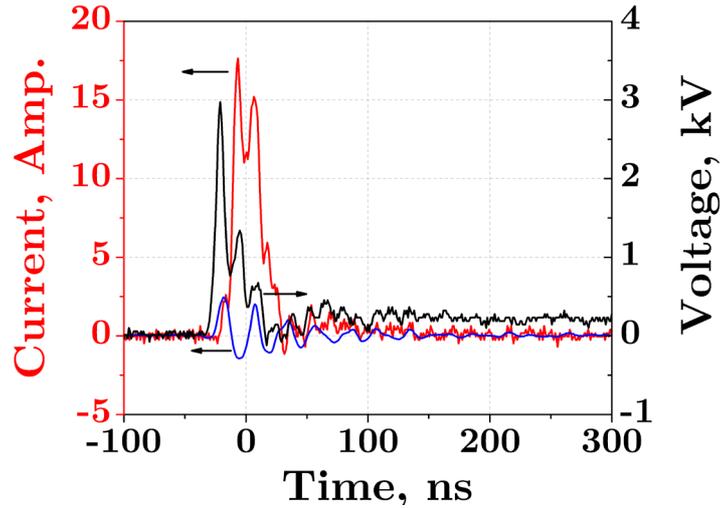
Figure III.7 : Waveforms of the total current (red), voltage (black), and displacement current (blue) of the pulse

The capacitance is obtained by applying sub-breakdown voltage pulses and measuring the displacement current, which is fitted using the voltage time-derivative with the capacitance as a fitting parameter. At sub-breakdown voltage, we inferred a capacitance of 3 pF (Figure III.8). This procedure also allows to perfectly synchronize (better than 1 ns) the current and voltage probes. The method is further detailed in Refs. [173], [182]. When the discharge was turned on, the displacement current was determined from the voltage time-derivative and the capacitance. The conduction current was obtained by subtracting the displacement current from the total current. The energy was then determined using equation (III.3) (Figure III.8).
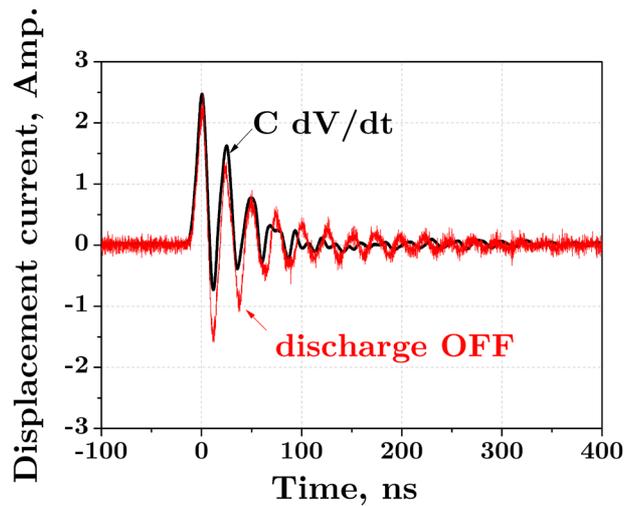
Figure III.8 : Displacement current measured without discharge (red line) and calcu-
lated from the derivative of the voltage pulse with the capacitance C as a fitting pa-
rameter (black line). Parameter: C=3 pF.
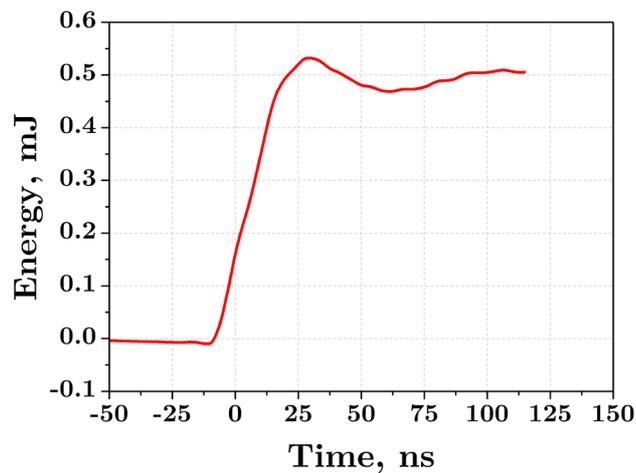
Figure III.9 : Energy deposited by a single pulse in the plasma.

3. Optical diagnostics

3.1. Mid-IR quantum cascade laser absorption spectroscopy (QCLAS)

Mid-IR quantum cascade laser absorption spectroscopy (QCLAS) is used in combina-
tion with a White multipass cell to measure the NO density inside the deco   ntami-
nation chamber. The measurement technique has been already used in our laboratory
for NO measurements and was extensively described in the thesis of Simeni Simeni
[211], [212].

The next sub-sections provide the principle of the measurement, a description of the optical setup, and the approach used for NO measurement.

3.1.1. Theory

Molecules with a permanent electric dipole moment exhibit strong absorption features in the mid-IR spectral range (2.5.-25 µm). These absorption features correspond to ro-vibrational excitations within the same electronic state. Semiconductor lasers –e.g. quantum cascade laser, diode laser– are spectrally narrow (typically 10^{-3} cm^{-1}, [213]), tunable sources that allow scanning ro-vibrational lines with high spectral resolution [213], [214]. This spectral region is thus particularly attractive for trace gas molecular spectroscopy [215] because it allows detection of species with high selectivity and sensitivity [213], [216]–[218].

- Line strength

The Beer-Lambert law predicts that if a uniform sample of length L is illuminated by an incident radiation of intensity $I_0(\nu)$ at wavenumber ν, the intensity $I(\nu)$ of the transmitted radiation is given by:

$$\ln\left(\frac{I_0(\nu)}{I(\nu)}\right) = k(\nu)L \tag{III.6}$$

where $k(\nu)$ is the absorption coefficient (in cm^{-1}), which is given by :

$$k(\nu) = \sigma(\nu)n \tag{III.7}$$

where $\sigma(\nu)$ is the absorption cross-section and n is the absolute number density of the absorbing species.

Mid-IR spectroscopic databases generally provide a list of line strengths for the ro-vibrational transitions of many molecules. The line strength S of a transition is defined as:

$$\int_{-\infty}^{+\infty} \ln\left(\frac{I_0(\nu)}{I(\nu)}\right)d\nu = S(T)\,\mathrm{Ln} \tag{III.8}$$

and for a transition (l→u), the line strength can be expressed as follows [219]:

$$S_{lu} = \frac{h\nu_{lu}}{c}\frac{n_l}{N}\left(1 - \frac{g_l n_u}{g_u n_l}\right)B_{lu} \tag{III.9}$$

where B_{lu} (in cm^3/ergs.s^2) is the Einstein coefficient of absorption, n_u and n_l refer to the number densities of the upper and lower levels, respectively, g_l and g_u refer to the statistical weights, and N is the molecular number density. If local thermodynamic equilibrium is assumed, the population of the levels is governed by the Boltzmann distribution:

$$\frac{n_u}{N} = \frac{g_u}{Q(\text{T})} \exp\left(-\frac{E_u}{k_B T} \right) \tag{III.10}$$

where $Q(\text{T})$ is the partition function at temperature T, E_u the energy of level u, and k_B the Boltzmann constant. With this expression, the line strength becomes:

$$S_{lu} = \frac{h\nu_{lu}}{c} \frac{g_l}{Q(T)} \exp\left(-\frac{hcE_l}{k_B T} \right) \left[1 - \exp\left(-\frac{hc\nu_{lu}}{k_B T} \right) \right] B_{lu} \tag{III.11}$$

Several databases such as *HITRAN* (*HI*gh resolution *TRAN*smission, [219]) and *GEISA* (Gestion et Etude des Information Spectroscopiques Atmosphérique, [220]) provide the line strengths at a reference temperature T_{ref}=296 K. The line strength at other temperatures can be determined from the line strength at the reference temperature:

$$S_{lu}\left(T\right) = S_{lu}\left(T_{ref}\right) \frac{Q(T_{ref})}{Q(T)} \frac{\exp\left(-\frac{hcE_l}{k_B T} \right) \left[1 - \exp\left(-\frac{hc\nu_{lu}}{k_B T} \right) \right]}{\exp\left(-\frac{hcE_l}{k_B T_{ref}} \right) \left[1 - \exp\left(-\frac{hc\nu_{lu}}{k_B T_{ref}} \right) \right]} \tag{III.12}$$

A method of measurement of the species density consists in integrating the absorbance spectrum over the line shape of one or more transitions using equation (III.8). However depending on the operating conditions, line broadening can become significant, and overlapping between different lines from the same species or with impurities can be a significant source of errors. An approach to circumvent this problem consists in calculating the transmittance spectrum from the line strength and the normalized line shape $f_{lu}(\nu,T,P)$ of the transition. The monochromatic absorption coefficient of transition (l→u) is given by [219]:

$$k_{lu}(\nu) = S_{lu}(T) f_{lu}(\nu, T, P) \, \text{n} \tag{III.13}$$

The next paragraph presents the broadening mechanisms of absorption and emission lines.

- Broadening mechanisms

Emission and absorption lines do not appear as monochromatic lines in a spectrum, but are broadened by various mechanisms [161]. These mechanisms depend on various environmental factors such as gas temperature, pressure, and colliding partners.

Natural broadening is a consequence of the Heisenberg uncertainty principle applied to the energies of the initial and final states of a transition. Natural broadening gives a Lorentzian profile, which is typically much narrower than other broadening mechanisms. Therefore it can generally be neglected in the calculation of the line shape.

Doppler broadening is caused by the motion of the particles, which shifts the frequency of the transition because of the Doppler effect. This broadening results in a Gaussian line shape of FWHM proportional to the square root of the gas temperature. If the distribution of the species is Maxwellian at temperature T:

$$\Delta \nu_D = 2 \sqrt{\frac{2 \ln(2) k_B T}{mc^2}} \nu_0 = 7.162 \times 10^{-7} \nu_0 \sqrt{\frac{T[K]}{M[g.mol^{-1}]}} \qquad \text{(III.14)}$$

Collisional broadening includes Van der Waals broadening and resonant broadening (also called self-broadening) [219]:

$$\Delta \nu_C = \left(\frac{T_{ref}}{T}\right)^n \left(\Delta \nu_{air}[cm^{-1}.atm^{-1}](P - P_s) + \Delta \nu_{self}[cm^{-1}.atm^{-1}]P_s\right) \qquad \text{(III.15)}$$

The first term corresponds to Van der Waals broadening –i.e. broadening caused by collisions with molecules different from the absorbing or emitting particles (partial pressure P_s), here air molecules. The second term corresponds to resonant broadening – i.e. broadening caused by collisions between 'like' particles. $\Delta \nu_{air}$ and $\Delta \nu_{self}$ correspond to the air-broadened and self-broadened half widths, respectively, at P_{ref}=1 bar and T_{ref}=296 K, and n is the temperature dependence coefficient. These parameters are given in the Hitran databases. The global broadening is Lorentzian and depends on the gas pressure, temperature, and composition.

Stark broadening is caused by the Coulomb interaction between the absorbing or emitting particle with charged species. The Coulomb interaction alters the potential energy of the molecule, thus leading to a shift of the transition frequency (Stark effect) and to a Lorentzian line shape. For post-discharge measurements, this broadening can be neglected.

Instrumental broadening is caused by the wavelength dispersion of the optics, the spectral resolution of the detector, and the laser linewidth in laser-absorption spectroscopy. For spectrometers, it can be measured by using a monochromatic source of linewidth smaller than the spectral resolution of the optical device, e.g. a laser or a low-pressure mercury lamp.

The measured line shape is the convolution of all these broadening mechanisms. At atmospheric pressure and near-ambient temperature, the line shape of absorption in the mid-IR is dominated by collisional broadening and is therefore Lorentzian.

3.1.2. Optical setup

Figure III.10 shows the experimental arrangement for the QCLAS measurement inside the decontamination chamber. The QCL beam is collimated with an off-axis parabolic (OAP) gold-coated mirror (f=1 inch) and focused with a spherical mirror (f=50 cm) at the center of a White multipass cell surrounding the decontamination chamber. After four passes inside the chamber, the QCL is collimated and leaves the multipass cell before being focused onto a HgCdTe (MCT) photoconductive detector using a third OAP (f=2 inches). The following paragraphs give further details on the QCL device, the MCT detector and the White multipass cell.
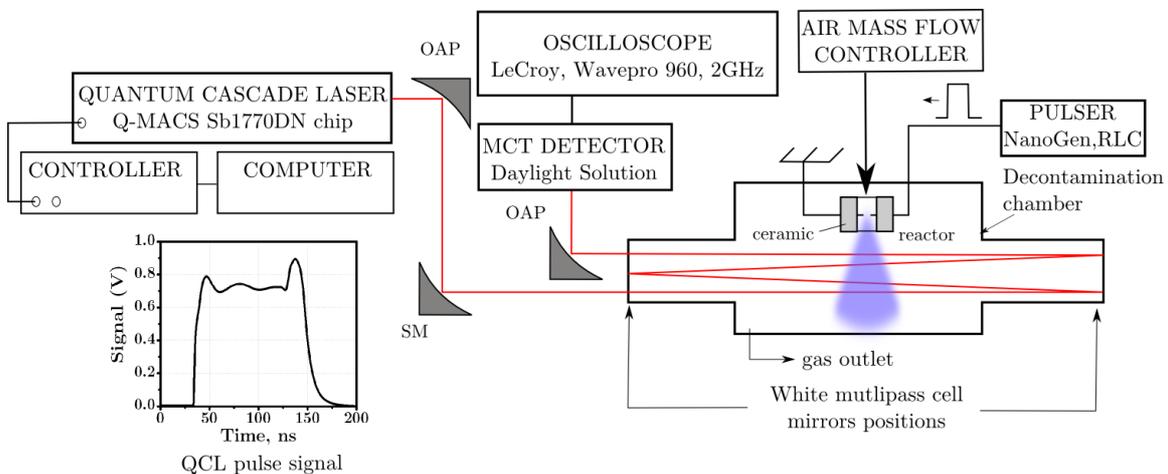
Figure III.10 : Experimental setup for NO quantum cascade laser absorption spectroscopy inside the decontamination chamber using a White multipass cell. OAP: off-axis parabolic mirror; SM: spherical mirror.

- Quantum Cascade Laser (QCL) operation modes

The quantum cascade laser (Alpes laser, Sb1770DN chip) is a pulsed distributed-feedback QCL mounted in a Q-MACS head designed by NeoplasControl GmbH (Table

III.3). The input laser current is supplied by a controller, and the pulse amplitude is controlled by adjusting a QCL voltage potentiometer. The maximum QCL voltage (without damaging the chip) is 12 V according to the datasheet. Thermal management is performed by a Peltier component driven by the controller, and by a water-cooling system (ThermoCube). The wavelength of the QCL is controlled by varying the temperature of the semiconductor through the Peltier component. The controller is connected to a computer via a data acquisition card and a RS-232 connector. The Q-MACS Configurator software allows to set the temperature, and thus the wavelength, of the QCL.

Table III.3 : Characteristics of the Q-MACS quantum cascade laser

Model	Alpes Laser
Laser chip	Sb1770DN
Laser type	Pulsed distributed-feedback
Wavenumber range	1898-1910 cm^{-1}
Spectral width	0.006 cm^{-1}
QCL voltage (from datasheet)	0 - 12 V
Peak current	0 - 0.7 A
Average output power	0 - 2.5 mW

The QCL has two operating modes: intrapulse and interpulse (see Figure III.11). In the interpulse mode, a burst of 1000 pulses of 10 ns duration at 200 kHz is produced by the QCL. The Peltier component is supplied with a ramp modulating the spectral range scanned, so that each laser pulse is produced at a different wavelength. This method allows relatively large spectral scans (typically 0.4 cm^{-1}) but the time resolution is limited to tens of milliseconds. The interpulse mode was already used in our laboratory for time-averaged measurements of NO in a nanosecond spark discharge [211], [212].

In the intrapulse mode, a single laser pulse but of longer duration (typically 10-100 ns) is used to scan the absorption profile. The wavelength of the laser changes within the pulse, because of the heat release induced by the input current, which causes a thermal expansion of the semiconductor crystal, and thus a change in the quantum well structure. The spectral range scanned by the laser pulse is determined by the chirp rate (in cm^{-1}.ns^{-1}). The repetition frequency of the pulses equals 100 kHz. The intrapulse operating mode allows time-resolved measurements with a time-resolution determined by the laser pulse duration. In this thesis, all the results were obtained using the intrapulse mode.
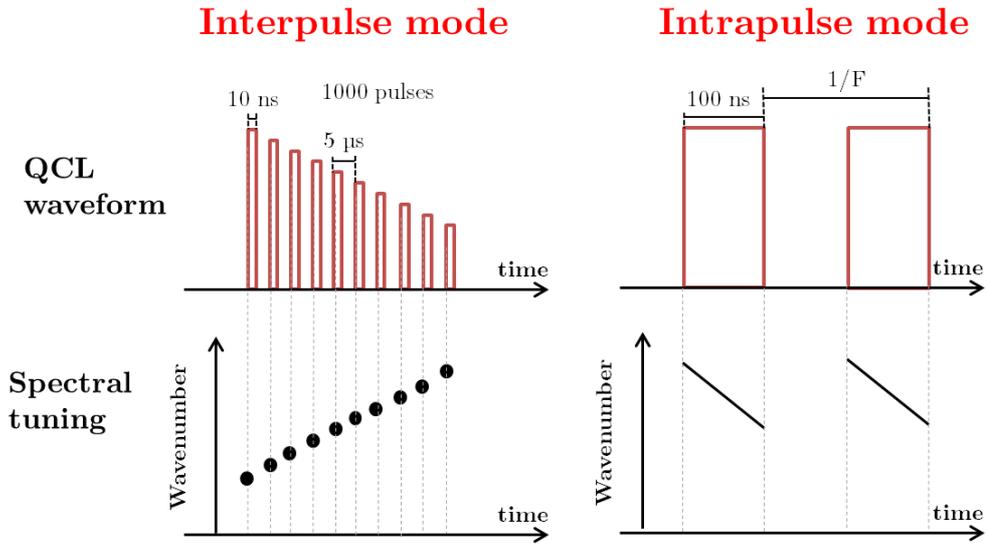
Figure III.11 : Principle of the QCL interpulse and intrapulse operating modes. F: pulses repetition rate

- White multipass cell

The White multipass cell is an arrangement composed of three concave spherical mirrors allowing the laser beam to pass multiple times across the absorption medium. Figure III.12 shows the two flanges composing the cell. The left flange is composed of two KBr windows allowing the laser beam to enter and leave the cell, and a field mirror. The right flange contains two lens mirrors. After entering the cell, the beam reflects on the objective and field mirrors. The beam can do between 4 and 28 passes inside the cell by adjusting the spindles controlling the orientation of the objective mirrors. Details on the alignment of the multipass cell can be found in Refs [211], [212]. Increasing the number of passes significantly increases the sensitivity of the measurement, and slightly decreases the signal-to-noise ratio because of reflection losses on the mirrors. Here, 4 passes were sufficient to perform the measurements so that the absorption length is 2 m.
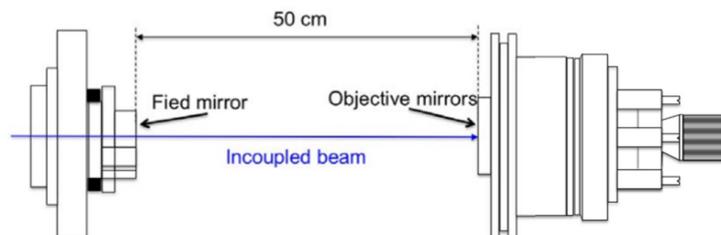
Figure III.12 : Schematic of the White multipass cell, taken from [211]

- IR-detector

IR detectors are divided into two main categories: thermal –e.g. bolometer- and semi-conductor [221]. Thermal detectors have low detection capability and slow response time, therefore semiconductor type detectors are necessary. Here we used a room-temperature amplified MCT (HgCdTe) detector (Daylight Solutions, model HPC-2TE-100) cooled by a thermoelectric current (TEC) stage down to 245 K. The detector can remove thermal background using a highpass electronic filter allowing only pulsed light detection. The main characteristics of the detector are shown in Table III.4. The MCT signal was recorded by an oscilloscope (LeCroy WavePro 960 DSO, 2 GHz, 16 GS/s) controlled by the computer using a LabVIEW (National Instruments, USA) driver and RS-232 connection. A typical QCL pulse signal is shown in Figure III.10.

The delay time of the MCT was determined by recording the emission from a discharge pulse using the MCT detector and a photomultiplier (PMT) of known delay time (300 ns). Both detectors were located at the same distance from the discharge. Output signals were sent to the oscilloscope using BNC cables of identical lengths, and the delay between the signals of both detectors was measured. The response time of the MCT was found to be 2±1 ns.

Table III.4: Characteristics of the MCT detector (Daylight Solutions)

Model	HPC-2TE-100
Detector type	Mercury Cadmium Telluride (MCT)
Spectral response	4 to 12 µm
Active area	1 x 1 mm^2
Bandwidth	300 MHz
Field of view	78°
Responsivity [V.W^{-1}]	2.5
Detectivity [cm Hz$^{1/2}$.W^{-1}]	2.5 x 10^9
Response time	3 ns

3.1.3. Wavenumber calibration

In the intrapulse mode, the laser wavenumber is tuned within the pulse at a rate defined as the chirp rate [cm^{-1}. ns^{-1}]. The chirp rate is measured by introducing a Germanium Fabry-Perot etalon on the optical path of the laser. The transmission spectrum of the Fabry-Perot etalon exhibits peaks of high transmission separated by a frequency

gap called the free spectral range (FSR, see Figure III.13). The FSR is wavelength-dependent and is determined by the following formula:

$$\Delta\lambda = \frac{\lambda_0^2}{2n(\lambda)L\cos(\alpha) + \lambda_0} \qquad \text{(III.16)}$$

where λ_0 is the central wavelength of the laser, L the length of the etalon, $n(\lambda)$ the germanium refractive index, and α the angle of incidence of the beam. With the etalon used here, the refractive index is constant on the spectral range accessible by the QCL, and the FSR equals 0.0163 cm^{-1} at 5.2 µm. A typical transmitted signal through the Ge etalon is shown in Figure III.13.a. The time position of the transmission peaks gives the wavenumber calibration curve (Figure III.13.b).
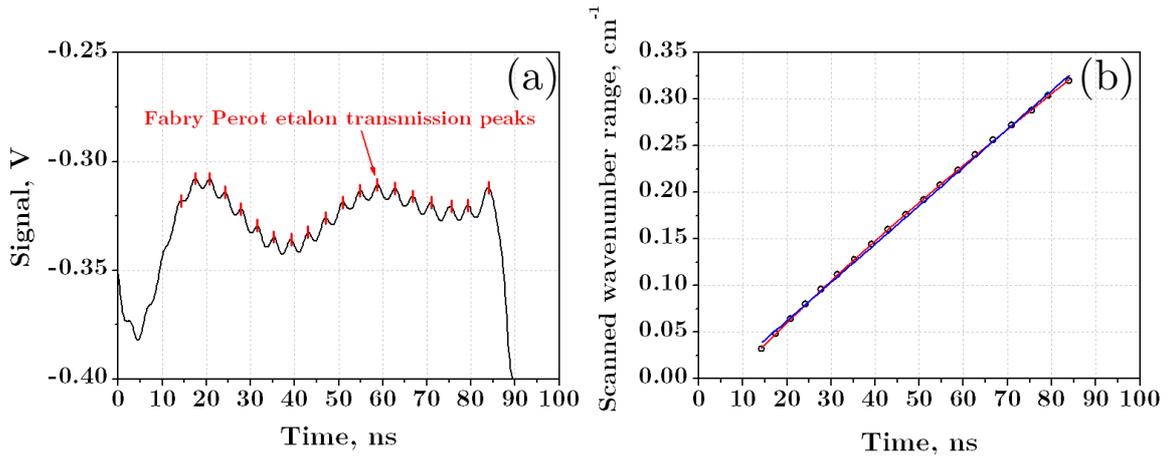
Figure III.13 : Signal transmitted by the Fabry-Perot etalon and measured by the MCT detector (a). The wavenumber calibration curve (b) is obtained by recording the transmission peaks. The spectral range between two successive peaks is determined by the free spectral range of the etalon. The calibration curve is fitted using a 3rd order polynomial (red line) and a linear fit (blue line). The slope gives the chirp rate, equal to 4×10^{-3} cm^{-1}.ns^{-1} here. Laser parameters: F=100 kHz, QCL voltage=10.2 V, T_{QCL}=17.5°C.

Figure III.14 shows the effect of QCL parameters on the chirp rate. Effect of pulse repetition rate has also been studied and no changes on the chirp rate have been observed (results not shown). QCL temperature and pulse duration do not affect the chirp rate. The chirp rate increases with the QCL voltage from 4.7 x10^{-3} to 5.7x10^{-3} cm^{-1}.ns^{-1} between 9.6 and 10.5 V. This is because a higher voltage induces a higher QCL current, and thus a larger variation of QCL temperature and wavelength.
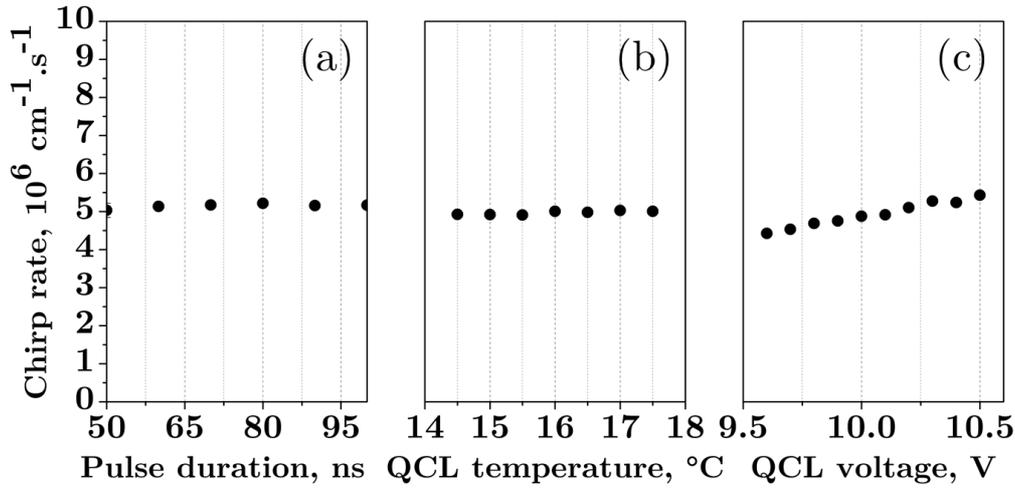
Figure III.14 : Chirp rate of the QCL – effects of laser pulse duration (a), QCL head temperature (b), and QCL voltage (c). If not specified, parameters are 100 ns, 17.5 °C and 10.2 V for pulse duration, QCL temperature and voltage respectively.

Therefore, the QCL voltage is the main parameter allowing to increase the spectral range scanned. However, possible artefacts in the absorption spectrum may be observed at high laser power [211]. This can be verified by performing a calibration of the measurement using a reference NO cell.

3.1.4. Application to NO measurement

In Simeni Simeni's thesis [211], [212], the transition $NO(X_{1/2}, v'=0 \rightarrow X_{1/2}, v''=1)R(6.5)$ at 1900.076 cm^{-1} was chosen on the basis of several criteria. First, the transition has strong line strength at room temperature. Second, simulations performed at different gas temperatures with a commercial software (Q-MACS Soft HITRAN Tool, Neoplas control) using the HITRAN and HITEMP databases showed that, in the spectral range of our QCL, this line has minimal overlap with other lines. A detailed discussion about the choice of the line can be found in Ref. [211].

- NO calibration

In theory, absorption measurements do not require calibration procedure. However, absorption artefacts can occur with QCLAS including mode overlapping or rapid passage effect which are reviewed in Ref. [211]. In addition the instrumental function is a priori not known in the intrapulse mode and needs to be determined. Since NO is a stable molecule a reference cell could be used for calibration. The calibration experimental setup is shown in Figure III.15.

In this setup the QCL beam is collimated using an off-axis parabolic mirror (f=1 inch) and sent to the reference cell. The reference cell has two CaF₂ windows. The transmitted beam is focused to the MCT detector using an off-axis parabolic mirror (f=2 inches). The NO pressure inside the reference cell is measured using a MKS Baratron pressure gauge. The line is evacuated using a Pfeiffer vacuum rotary vane pump to a pressure <0.1 mbar. Two micrometric valves permit to adjust the NO and helium pressure inside the cell. This arrangement permits to calibrate the measurement at near-atmospheric pressure. Air could not be used because of catalytic oxidation of NO by oxygen molecules in the presence of copper or inox tube. This effect rapidly removes NO molecules within a minute.
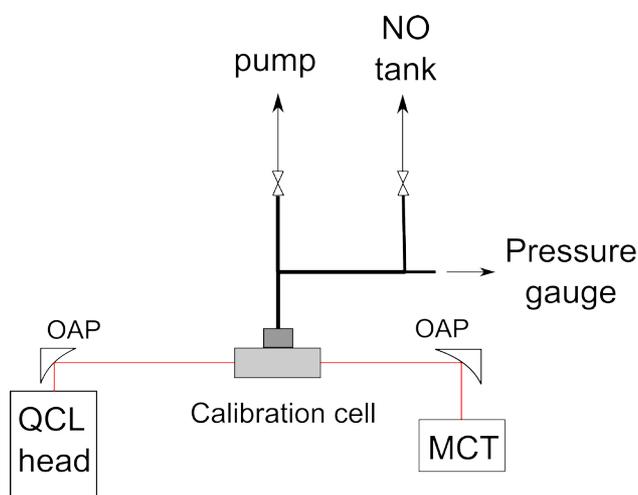
Figure III.15 : Calibration setup – OAP: off-axis parabolic mirror, MCT: HgCdTe IR detector

Figure III.16 shows the transmittance spectrum of NO cell at 40 mbar using 100 ns laser pulses at two different QCL temperatures measured by the MCT detector. Slight disagreement at the edges of the absorption lines is caused by the rapid passage effect [211]. The instrumental broadening width was set as a parameter for the Hitran calculation of the spectrum. We found a width of 0.04 cm⁻¹. Note that this instrumental broadening is lower than typical collisional broadening at atmospheric pressure (about 0.1 cm⁻¹) and will thus have minimal influence on the transmittance calculation at atmospheric pressure.
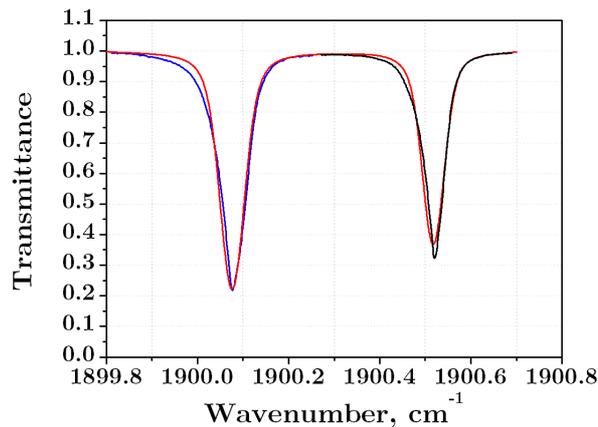
Figure III.16 : Transmittance spectrum of the reference cell filled with 40 mbar of pure NO at two QCL temperature corresponding to two spectral ranges (blue and black lines), and Q-MACS Soft calculation under these conditions (red line). The width of the gaussian apparatus function was used as a fitting parameter. Light detection is done with MCT detector.

- ## NO measurement procedure

Briefly, the measurements were carried out as follows inside the decontamination chamber. First, the chamber was filled with dry air for one minute in order to eliminate ambient air humidity. Second, a reference signal was recorded. Laser pulses were produced at 100-kHz repetition rate, for a QCL voltage of 10.2 V and a temperature of 17.5°C. The MCT signal was averaged over 2000 pulses using the oscilloscope. Third, the discharge was turned on for two minutes and a new acquisition was taken. Finally, data were exported to the computer, the timescale was converted to wavenumber using the wavenumber calibration curve (Figure III.13).
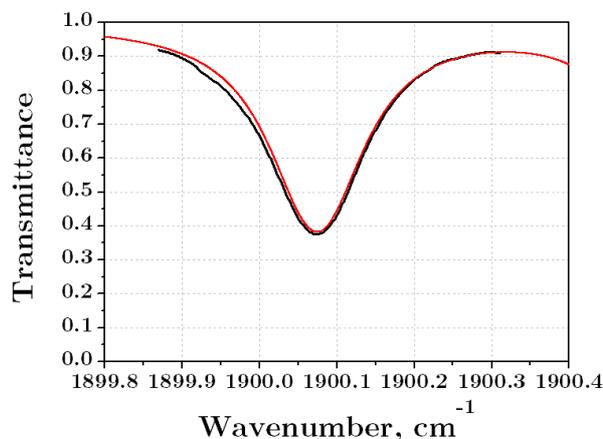
Figure III.17 : Typical NO transmittance spectrum measured in the decontamination chamber (black line) and calculated using NO mole fraction as a fitting parameter (red line). Fitting parameters: T=300 K, P=1 atm, L_{abs}=2 m, x(NO)=280 ppm.

In the results presented in the next sections, transmittance spectra were measured and fitted with NO mole fraction as a fitting parameter using the simulation software Q-MACS Soft HT. Typical measured and calculated transmittance spectra of NO inside the decontamination chamber are shown in Figure III.17.

3.2. UV broad-band absorption spectroscopy

In the UV spectral range, several species exhibit strong absorption features [222]. However, the high number of absorbing species makes spectral overlapping a possible issue. Around 250 and 400 nm, the dominant absorbers are ozone (O_3) (Hartley band) and nitrogen dioxide (NO_2), respectively. Therefore, these regions are suitable for the measurement of O_3 and NO_2.
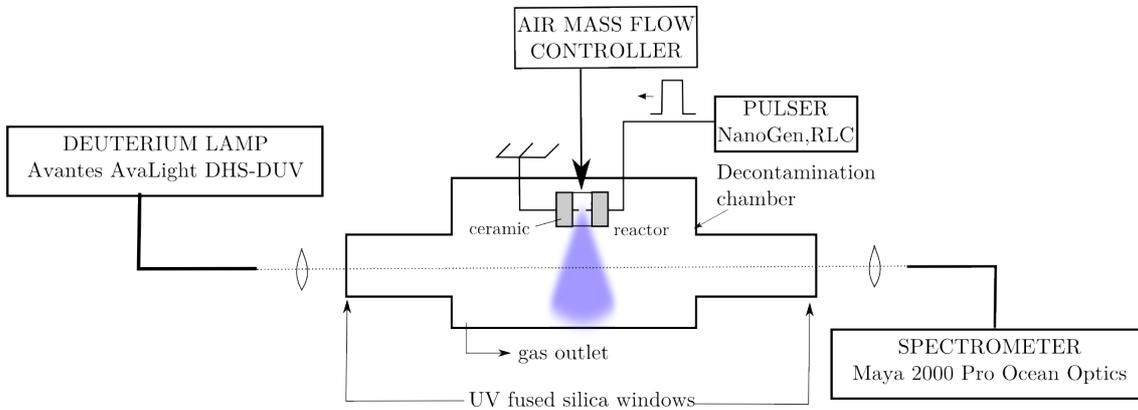
Figure III.18 : Experimental setup for broadband UV absorption spectroscopy inside the decontamination chamber. HVG: high voltage generator of nanosecond pulses

A broadband deuterium lamp (Avantes Avalight DHS-DUV) equipped with a fiber output was used as the light source. The light was collimated and directed inside the decontamination chamber by placing the output of the fiber at the focal distance of a UV plano-convex lens. The light enters and leaves the chamber by passing through UV fused-silica windows. A second lens focuses the transmitted beam onto an optical fiber attached to a low-resolution spectrometer (OceanOptics, Maya 2000Pro, 1-nm resolution). The absorbance spectra were fitted using the following relation:

$$\ln\left(\frac{I_0(\lambda)}{I(\lambda)}\right) = \sum_i \sigma_i(\lambda) n_i L \qquad \text{(III.17)}$$

where $\sigma_i(\lambda)$ is the absorption cross-section of species i, n_i the density of absorbing species i, and L the absorption length. Here, only NO_2 and O_3 absorption were considered. The absorption cross-section of the Hartley band varies by less than 2% between 200 and 295 K according to the review of Orphal et al. [223]. Kirmse et al. [224] did not

measure any variation of the NO_2 cross-section around its maximum absorption at 400 nm between 300 K and 673 K. However, between 500 and 600 nm, the cross-section increases by about 40%. The absorption cross-section of Gorshelev et al. [225] for ozone and the cross-section of Bogumil et al. [226] for NO_2 at 300 K were used in our calculations.
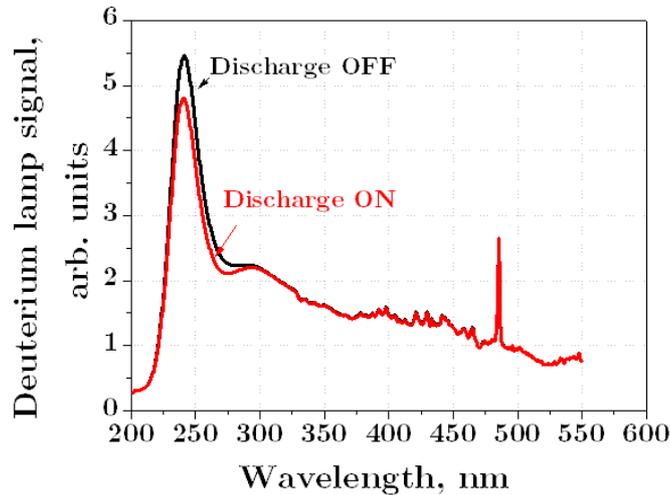
Figure III.19 : Typical signal of the deuterium lamp measured by the spectrometer. Conditions: 1-s exposure, 100 accumulations, PRF = 10 kHz, air flow rate = 30 slpm, voltage = 8 kV.
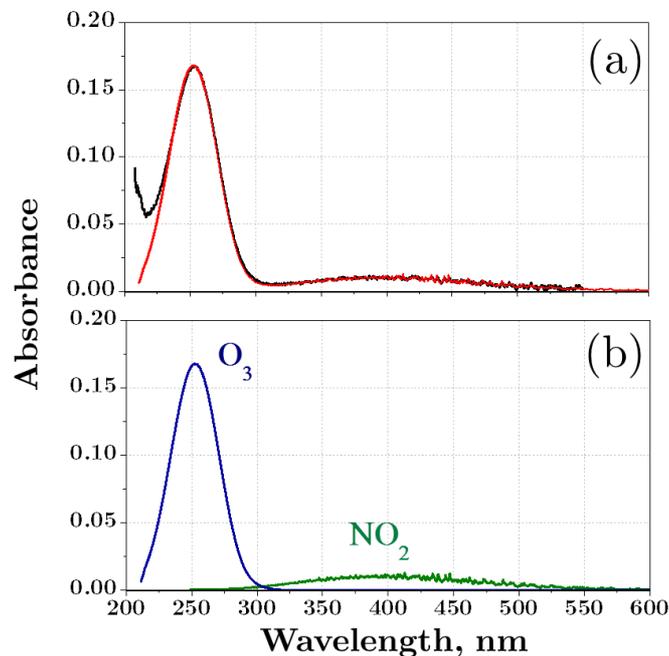
Figure III.20 : (a) Typical broadband UV absorbance spectrum measured inside the decontamination chamber (black line) and calculated spectrum (red line) using O_3 and NO_2 mole fractions as the fitting parameters, assuming a gas temperature of 300 K. (b) Contributions of O_3 and NO_2 to the calculated spectrum. Conditions: PRF = 10 kHz,

voltage = 8 kV, air flow rate = 30 slpm. Fitting parameters: $x(O_3)$ = 23 ppm, $x(NO_2)$ = 26 ppm, L_{abs} = 27 cm.

Figure III.20 shows a typical absorbance spectrum of NO_2 and O_3. The calculated spectra are in a good agreement with experimental data, indicating that overlapping with other possible absorbing species is negligible. The disagreement at wavelengths below 220 nm is due to the sharp decrease of the deuterium lamp signal as observed in Figure III.19. This is due to the decrease of lens transmission below 220 nm.

4. Experimental results

Figure III.21 shows the results of our parametric study of the various operating modes of the NRP discharge. The mole fractions of O_3, NO_2 and NO were measured inside the decontamination chamber and the influences of the pulse repetition frequency (PRF) and air flow rate were studied. At high air flow rate and low PRF, up to 65 ppm of ozone is measured. Decreasing the air flow rate and increasing the PRF, a sharp transition from an ozone-rich mode to a NO_x-rich mode is observed. Up to 190 ppm of NO_2 and 670 ppm of NO are measured in the NO_x-rich mode.

Figure III.22 shows the RONS mole fractions as a function of the energy density, which is determined using the following relation:

$$\text{energy density} = \frac{EF}{\Phi} \tag{III.18}$$

where E is the energy per pulse, F the pulse repetition rate, and Φ the air flow rate. At about 40 J/L (i.e. 0.01 eV/molec), the O_3 density decreases and the NO density rises. Therefore, adjusting the energy density allows to tune the RONS produced by the NRP discharge.

In the next sections, we first discuss the kinetic mechanisms explaining the transition from the O_3-rich to NO_X-rich regimes. Then, the energy cost of RONS is calculated and compared with reference plasma sources. Finally, the effect of RONS tuning on the inactivation rate of microorganisms is investigated.
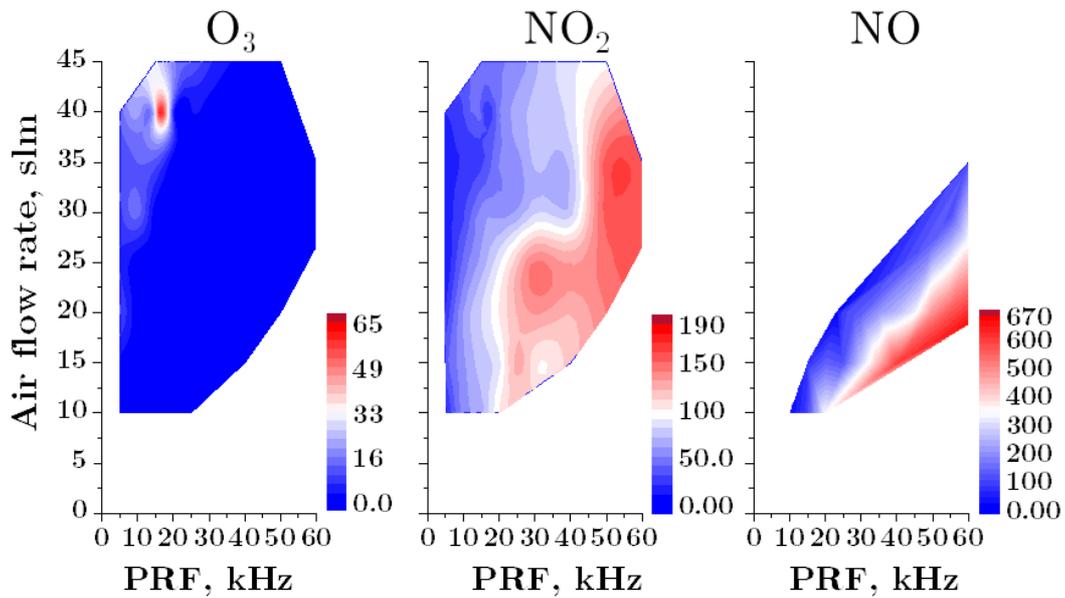
Figure III.21: O_3, NO_2 **and** NO mole fractions displayed in parts per million (ppm), averaged over the decontamination chamber volume for different conditions of flow rate and pulse repetition frequency (PRF). UV absorption spectroscopy was used for O_3 and NO_2, and QCLAS for NO. Conditions: voltage = 8 kV, inter-electrode gap = 2 mm, dry air, T = 300 K, 1 atm.
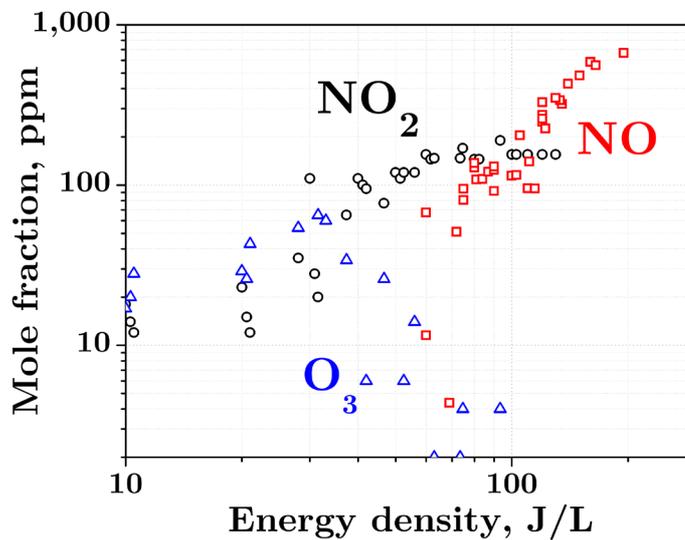
Figure III.22: O_3 and NO_x mole fractions produced by NRP discharges as a function of the deposited energy density.

5. Transition from O₃-rich to NOₓ-rich regimes

The mechanism responsible for production of O_3 is generally accepted in the literature [192], [193], [227]. In the discharge, molecular oxygen is dissociated by electron impact

and by reaction with N_2 electronic excited states. Production of ozone occurs then by the following reaction:

$$O_2 + O + M \rightarrow O_3^* + M \rightarrow O_3 + M, \quad k_1 = 3.4 \times 10^{-34} \left(\frac{300}{T_g} \right)^{1.2} \quad \text{(R1, [228])}$$
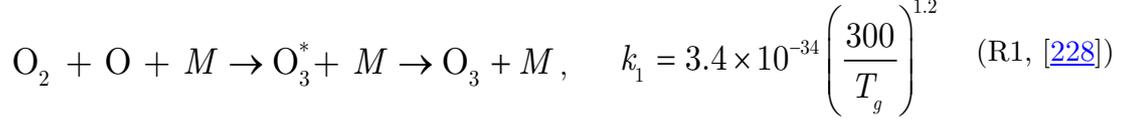
where the third body M stand for O_2 and N_2. Two mechanisms of O_3 extinction are usually considered to explain the transition from an ozone-regime to a NO_x-regime, namely the discharge poisoning and the thermal decomposition.

- Discharge poisoning effect

In air plasma, formation of nitric oxide occurs according to the following main reactions:

$$N_2 + O \rightleftarrows NO + N, \quad k_2 = 3 \times 10^{-10} \exp\left(-\frac{38300}{T_g} \right) \quad \text{(R2, [229])}$$

$$N + O_2 \rightarrow NO + O, \quad k_3 = 1.5 \times 10^{-14} \exp\left(-\frac{3270}{T_g} \right) \quad \text{(R3, [229])}$$

$$N_2^* + O \rightarrow NO + N \quad \text{(R4)}$$
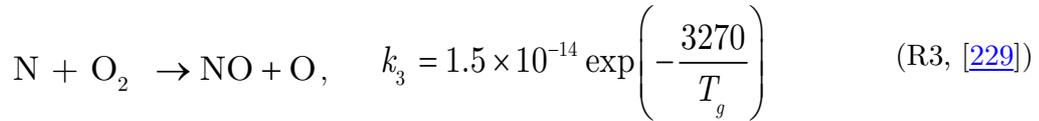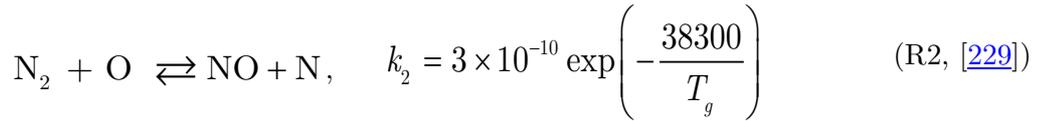
N_2* includes $N_2(X^1\Sigma_g^+, v>12)$ [95], [230], [231] and N_2 electronic states [232], [233]. Reactions R2 and R3 are the Zel'dovich mechanisms responsible for NO formation at combustion temperatures. At near ambient temperature, the reverse reaction R2 becomes important. This is known as a fast titrating reaction for N measurement in flowing afterglow experiments (Chapter II, section 3). The presence of nitric oxide in the discharge products causes the so-called poisoning effect of ozone [192], [227], [234]. If nitric oxide density is high enough, the O atoms are consumed and the main source of ozone R1 is suppressed by the following mechanisms:

$$O + NO + M \rightarrow NO_2 + M, \quad k_5 = 10^{-31} \left(\frac{300}{T_g} \right)^{1.6} \quad \text{(R5, [235])}$$

$$O + NO_2 \rightarrow NO + O_2, \quad k_6 = 5.5 \times 10^{-12} \exp\left(-\frac{188}{T_g}\right) \quad \text{(R6, [235])}$$
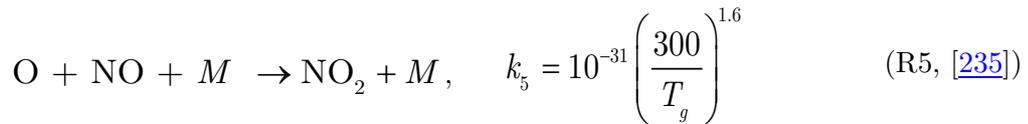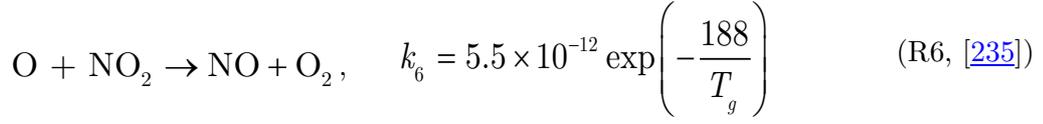
In addition, the ozone is also eliminated by successive oxidation of nitrogen oxides:

$$O_3 + NO \rightarrow O_2 + NO_2, \quad k_7 = 2.5 \times 10^{-13} \exp\left(-\frac{765}{T_g}\right) \quad \text{(R7, [235])}$$

$$O_3 + NO_2 \rightarrow O_2 + NO_3, \quad k_8 = 1.2 \times 10^{-13} \exp\left(-\frac{2450}{T_g}\right) \quad \text{(R8, [235])}$$
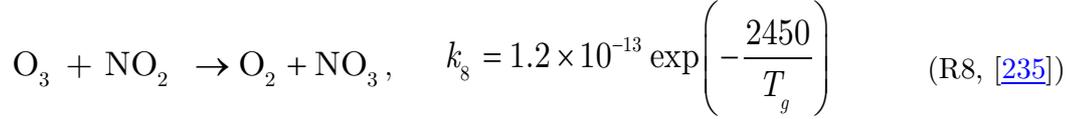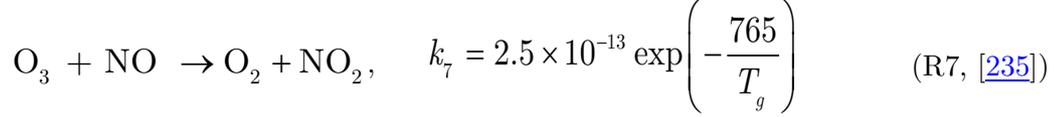
Kogelschatz and Eliasson [192], [227] studied the ozone production of a silent discharge operating at atmospheric pressure in oxygen and air. They showed that ozone concentration reaches a maximum at 0.1 eV/molec input energy. At higher input energy (0.5 eV/molec), ozone production efficiency decreases because of NOₓ formation. Their model did not include reaction R4 however it fitted correctly the experimental data. The reaction R4 was introduced later as an additional source of NO in kinetic models [232], [236].

- Thermal decomposition of ozone

The elevated gas temperature causes the drop of ozone production efficiency in air and oxygen discharge [192], [237] because of ozone thermal decomposition [238]–[241]:

$$O_3 + M \rightarrow O_2 + O + M, \quad k_9 = \gamma 6.6 \times 10^{-10} \exp\left(-\frac{11600}{T_g}\right) \quad \text{(R9, [235])}$$
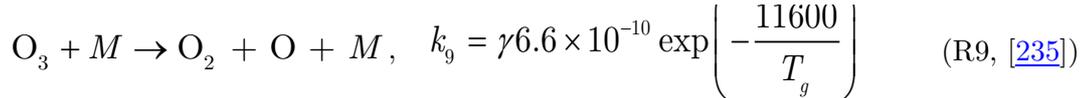
with γ=0.38 for M=O₂ and γ=1 for M=N₂. As a result, the production of ozone is suppressed, and the residual O atoms produce nitrogen oxides. This initiates the discharge poisoning effect, which is amplified at high gas temperature.

Recently Bansemer et al. [242] measured the transition temperature from an O₃ regime to NOₓ regime at the exit of a DBD working at sub-atmospheric pressures (200-600 mbar). Using a reduced kinetic model which did not include the reverse reaction of reaction R9, they could reproduce the main behaviors of their experimental data, i.e. the ozone extinction and the NO rise at the transition temperature. It can be inferred from their experimental results that the transition was not influenced by reaction R9. Let us define Γ that is the ratio of the characteristic time of reactions R7 and R9:

$$\Gamma = \frac{k_7[NO]}{k_9[\text{M}]} \tag{III.19}$$

For $\Gamma \gg 1$, thermal decomposition is negligible in the balance equation of ozone. The variation of Γ with temperature is calculated in air for different NO mole fractions in Figure III.23. The transition temperatures observed by Bansemer et al. were all below 400 K, and the maximum NO_X mole fraction was 70 ppm. At 70 ppm, thermal decomposition competes with discharge poisoning only if the gas temperature is greater than 640 K.

To conclude, the transition from the O_3-rich to the NO_X-rich modes is controlled by a complex relation between the NO_X concentration and the gas temperature. At low gas temperature, the decay of ozone is due to the temperature dependence of the reaction coefficients of NO production. At high gas temperature, thermal dissociation induces a sharp decrease of O_3 combined with an increase of NO production.
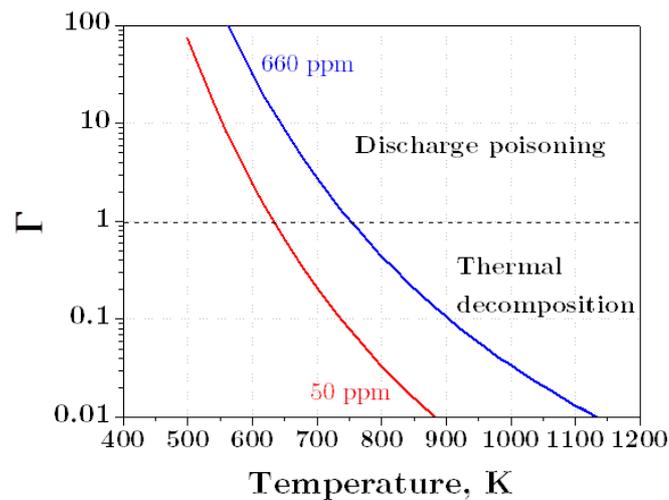
Figure III.23 : Ratio of characteristic times of discharge poisoning (reaction R7) to ozone thermal decomposition (reaction R9) calculated for two NO mole fractions (50 and 660 ppm).

6. Mole fraction and energy cost of RONS produced by NRP discharge

The energy cost is a useful parameter to optimize the RONS production. The energy cost of molecule X can be expressed as follows:

$$\text{energy cost} = \frac{EF}{\Phi[X]} \tag{III.20}$$

where E is the energy per pulse, F the pulse repetition rate, Φ the air flow rate, and [X] the concentration of species X. We now consider the efficiency of RONS production by NRP discharges, and we compare it with the efficiency of other atmospheric pressure air plasma sources reported in the literature.

- Ozone

Figure III.24 shows the mole fraction and energy cost of ozone determined from our measurements. A comparison is presented with efficient ozone sources including surface DBD, pulsed DBD, and corona discharges. The corona discharge is the most common system used for ozone production at industrial scale [227]. Minimum energy costs vary between 15 eV/molec for the pulsed DBD, and 50 eV/molec for the NRP discharge. These values are above those measured in oxygen-fed ozonizers (about 7 eV/molec [192]). This is because ozone synthesis in oxygen is not affected by nitrogen oxides and the discharge poisoning effect. Except for the pulsed DBD, a local minimum energy cost is observed at about 30-40 eV/molec. This minimum corresponds to a transition in energy conversion, associated to discharge poisoning [192]. In our case the sharp increase of the energy cost at high energy densities is an indication of the temperature-induced transition from the O_3-mode to NO_X mode.

Recently, energy costs as low as 5.1 eV/molec and 7.17 eV/molec were obtained in air nanosecond pulsed DC discharge and glow discharge, [243], [244] respectively. These values are closed to the theoretical limit of an ideal dry air-fed ozonizer determined by Deryugin et al. [245] and confirmed by the experimental work of Plank et al. [244]: 6.4 eV/molec at E/N=200 Td. The energy cost values for air NRP discharge are about an order of magnitude higher than this limit because the filamentary structure of the discharge causes local overheating.
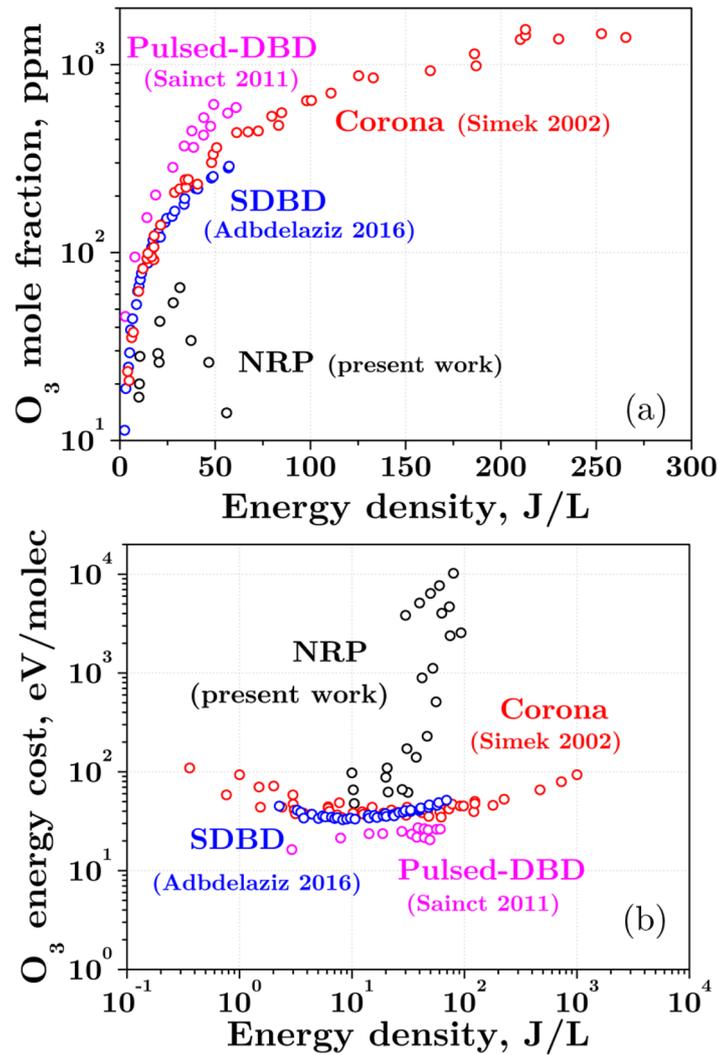
Figure III.24 : (a) O_3 mole fraction and (b) O_3 energy cost as a function of the input energy density. Red, blue and magenta circles are SDBD, corona, and pulsed DBD data from Refs. [246], [247] and [248], respectively. Conditions are the same as in Figure III.21.

- Nitric oxide

Figure III.25 shows the energy cost of the nitric oxide produced by the NRP. Comparison is done with microwave, pulsed spark, DC arc, and RF-APPJ plasma sources. For all considered plasma sources, the NO molar fraction increases with the input energy density. The energy cost of NO molecule is found to be strongly dependent on the energy density deposited in the discharge. Using the NRP discharge the lowest energy cost is obtained at 190 J/L and equals 65 eV/molec. For the RF-APPJ, the energy cost is found much higher. There are two reasons for this. First, the RF-APPJ operates in a gas mixture with low air-content (typically Ar-air with less than 1% air). So, the

productivity is limited by the low content of air molecules to convert. Second, the energy density in the discharge is much lower than with the other plasma sources referred here. However, the NO concentrations produced are of interest for medical applications of plasma, i.e. a few ppm. Thermal plasma sources (microwave, plasmatron) show excellent efficiency of NO production because of the Zel'dovich mechanisms of NO formation. However, thermal plasmas convert the input energy into multiple degrees of freedom that are not helpful for NO generation, and thus limiting the energy efficiency of NO production [234]. This possibly explains the drop of the efficiency of NO production by microwave plasma at near-atmospheric pressure. The most energy-efficient source to our knowledge is a plasmatron producing up to 3000 ppm of NO for an energy cost of 40 eV/molec.
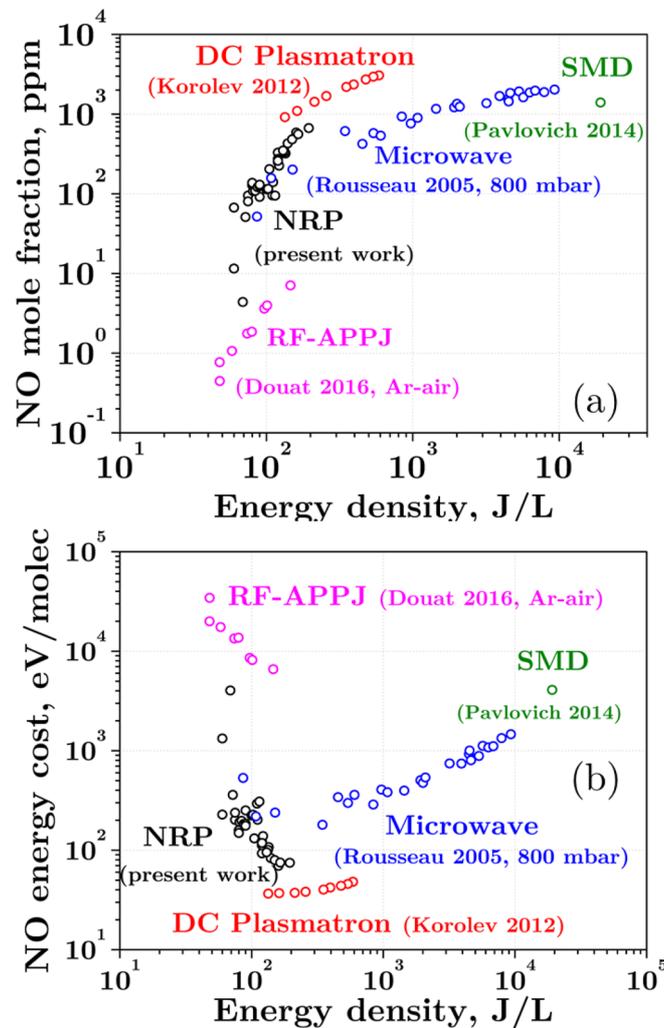
Figure III.25 ; (a) NO mole fraction and (b) NO energy cost as a function of the input energy density. Red, blue, green and magenta circles are plasmatron, microwave,

SMD and RF-APPJ data from Refs [112], [249]–[251], respectively. Conditions are the same as in Figure III.21.

Recently, a surface micro-discharge (SMD) device was shown to generate up to 1400 ppm of NO in a closed 90-cm^3 chamber, initially filled with air (300 K, 1 atm), after 20 min of plasma processing at 0.62 W.cm^{-2} [112]. According to the authors, the temperature of the gas only increased by a few degrees despite a total energy deposited of 12.7 kJ after 20 min. The corresponding NO energy cost is 25700 eV/molec, i.e. about three orders of magnitude higher than the values measured with the NRP and the plasmatron.

- Nitrogen dioxide

Figure III.26 shows that, similarly to NO, the NO_2 mole fraction increases with the input energy density for all plasma sources considered. However, above a certain energy threshold, dependent on the plasma source, the NO_2 concentration reaches a plateau, thus increasing the energy cost. With the NRP discharge, the minimum energy cost is 100 eV/molec for an energy density of about 80 J/L. This minimum energy cost also corresponds to the peak NO_2 mole fraction. With the SDBD, the NO_2 mole fraction reaches the plateau at about 30 J/L.

The observed plateau can be attributed either to the complete consumption of ozone by NO molecules, or to oxidation of NO_2 to higher oxidative states such as N_2O_5 and NO_3 [246]. On long timescales (tens of minutes), NO is oxidized by O_2 into NO_2.
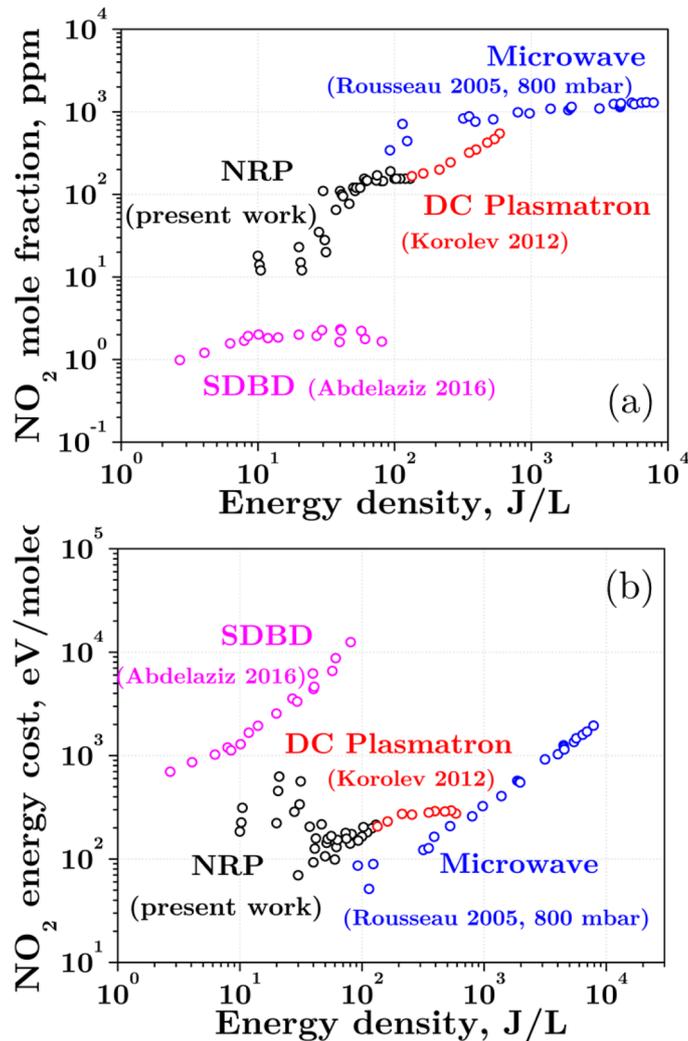
Figure III.26 : NO₂ mole fraction (a) and energy cost (b) as a function of the input energy density. Red, blue, and magenta circles are plasmatron, microwave, and SDBD data from Refs [246], [249], [250]. Conditions are the same as in Figure III.21.

- Summary

Of the various discharges presented in the previous sections, two of them (SDBD and NRP) have the ability to operate both in the O_3 and NO_x regimes, depending on the energy density input. Furthermore, the NRP discharge provides RONS densities approaching the highest values obtained by any of techniques (within a factor of 4), and energy costs approaching the lowest values of the other techniques (within a factor of 2-3). In addition, the NRP discharge keeps the effluents at low gas temperature, typically less than 65°C at 2 cm downstream of the discharge. This is in contrast with the thermal discharges that typically produce effluents at temperatures that can reach several thousand degrees Celsius, e.g. [116]. Thus NRP discharges provide a way to test

new decontamination strategies by alternating different RON species. The tuning between RONS is obtained by simply varying the pulse repetition frequency. This strategy is presented in the following section.

7. Application to decontamination

In the previous section, we saw that changing the gas flow rate and the pulse repetition frequency of the NRP discharge allows to tune the RONS produced from an ozone-rich regime to a NO_x-rich regime. In both regimes, high concentrations of NO_X and O_3 are produced at low energy cost. In this section, we investigate the effect of RONS-tuning during microbial treatments. Microbiological tests were perfomed to investigate the effect of successive exposures of microorganisms to the ozone-rich mode (F=15 kHz, U=8 kV, air flow rate=40 slpm) and the NO_x-rich mode (F=65 kHz, U=8 kV, air flow rate=10 slpm) corresponding to the maximal concentrations of O_3 and NO, respectively.

7.1. Microbiological test procedure

The microbiological tests were performed at the Bio-clin laboratory (Saint Aubin, France). *P. Aeruginosa* (ATCC 15442), *S. Aureus* (ATCC 6538) bacteria, *C. Albicans* (ATCC 10321) fungi and *B. Subtilis* (ATCC 6632) endospores were investigated. Suspensions of microorganisms were prepared at concentrations between 10^6 and 10^8 cfu/mL using tryptone-salt as a diluent. 50 µL of the suspension was dropped on two sterile square glass slides (1 cm^2 area). The slides were then dried at ambient temperature for 50 min. One of the slides was then treated by the plasma at a distance of 2 cm from the electrodes, whereas the other one was used as a control sample. The gas temperature at the surface where microorganisms are deposited was previously measured with a thermocouple. After 10 min of plasma treatment, the maximum temperature was below 65°C at 2 cm from the electrodes. Preliminary tests had shown that exposure to 40 slpm of dry air for 10 min causes less than 0.2 log reduction of bacteria as a result of mechanical removal of microorganisms.

Right after plasma treatment, the microorganisms were extracted by vortex agitation in 10 mL of DNP (diluent) with 1 gram of sterile glass beads for 10 min. The control of surviving microorganisms was based on norms NF 14561, NF 14562, NF 14563. The obtained suspensions were serially diluted and then plated out in tryptone soy agar (TSA) plates. The enumeration of microorganisms was performed by a direct plate

counting method. Direct counting was done after 24-48 h of incubation at 30-37°C depending on the microorganism.
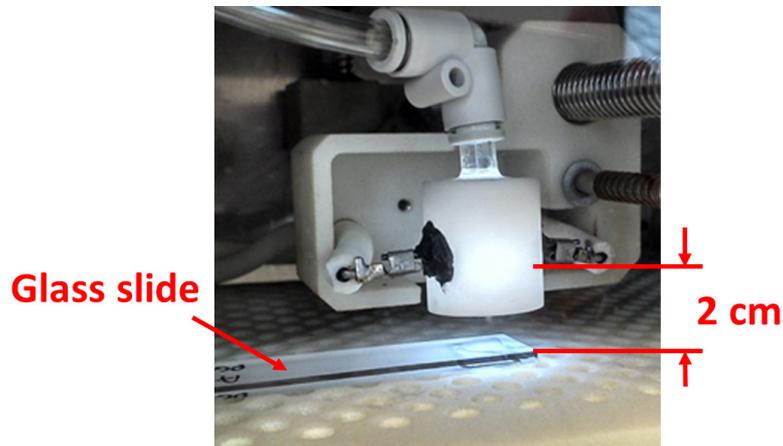
Figure III.27: Air plasma treatment of microorganisms dried on a glass slide. The slide is placed 2 cm downstream from the electrodes.

7.2. Effect of successive exposure to NO_X-rich and O_3-rich modes on microorganisms

Figure III.28 shows the inactivation results of microorganisms treated for 10 minutes: (a) in the NO_X-rich mode (blue bars), and (b) in five 2-min sequences alternating the NO_X and O_3-rich modes (red bars). The temperature of the gas at the surface of the glass holder was monitored using a thermocouple. After 10 minutes of exposure to the NO_x-rich mode, the maximum gas temperature reached 65°C. Alternating the NO_x-rich and O_3-rich modes, the maximum temperature was 55°C.

For all microorganisms studied, the combination of the NO_x-rich and O_3-rich regimes was more efficient than the NO_x-rich mode, even though the total exposure time was the same in both tests. For vegetative bacteria (P. *Aeruginosa* and S. *Aureus*), the results show a stronger reduction with the combined treatment, with an increase of the log-reduction factor from 5 to 6.1 for P. *Aeruginosa*. For C. *Albicans* fungi and B. *Subtilis* endospores, the log-reduction factor is even higher.

The results on B. *Subtilis* are particularily surprising because Ref. [102] showed that a 10-min exposure to dry gaseous ozone had minimal effects on B. *Subtilis* dried on a glass substrate. This leads us to believe that the effect of the O_3-rich mode may come from other species such as $O_2(^1\Delta)$ metastables [252], [253] or atomic oxygen.
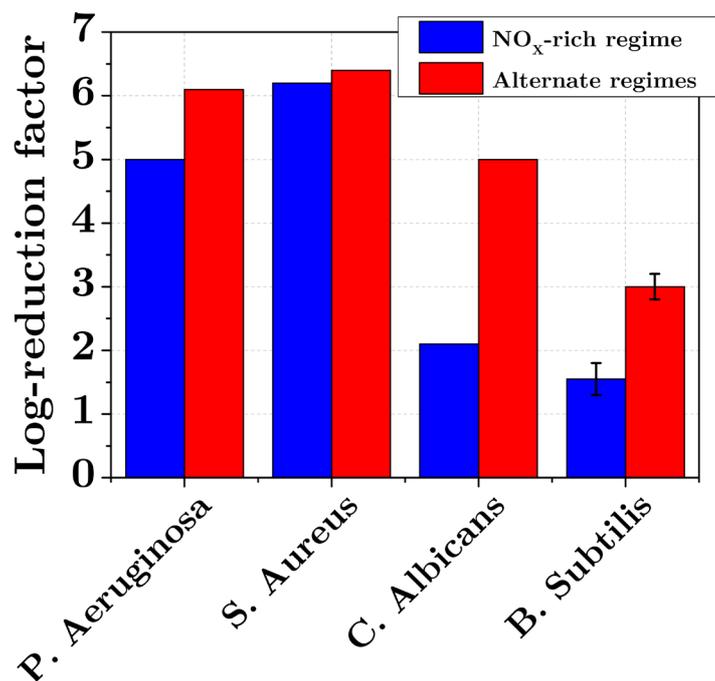
Figure III.28: Inactivation of Gram-positive (*P. Aeruginosa*), Gram-negative (*S. Aureus*), fungi (*C. Albicans*) and endospore (*B. Subtilis*) microbes dried on glass holders (area 1 cm^2) after 10 min exposure to NO_x-rich regime (blue columns) and alternating NO_x-rich with O_3-rich regimes 2 minutes each for a total exposure time of 10 min. Conditions: NO_x-rich mode (F=65 kHz, U=8 kV, air flow rate=10 slm), O_3-rich mode (F=15 kHz, U=8 kV, air flow rate=40 slm).

Another possible explanation is the synergetic effect between species produced in the O_3-rich and NO_x-rich regimes. Bermudez et al. [80] studied the single-strand break of DNA in alveolar macrophages of rats exposed to ozone and nitrogen dioxide. The rats were divided into three groups exposed for three days to (a) 1.2 ppm of NO_2, (b) 0.3 ppm of ozone, or (c) a combination of 0.3 ppm of ozone and 1.2 ppm of NO_2. No single-strand breaks of DNA were reported on the group of rats treated by NO_2 only because, according to the authors, the treatment dose was below the lethal dose. In the group of rats exposed to O_3 alone, DNA single-strand breaks were observed. However, the highest amount of single-strand breaks was reported in the group of rats exposed to the mixture of NO_2 and O_3. This experiment supports the existence of a synergetic mechanism between NO_2 and ozone, which may explain the increased efficiency of the NO_x-rich and O_3-rich modes combination. A first way to confirm this would be to study the variation of the DNA breaks in the case of alternative exposure to NO_x-rich and O_3-rich regimes. A second way would be to provide two sources of NO_2 and ozone to see if the combination of these sources induces a higher biocidal efficiency.

8. Conclusions

In this chapter, we characterized the production of RONS (NO, NO_2 and O_3) by a Nanosecond Repetitively Pulsed discharge operating in dry air at atmospheric pressure and ambient temperature. The concentrations of these species were measured 2 cm downstream of the discharge. The pulses were 10-ns in duration and 8 kV in amplitude. The energy density was varied from 1 to 220 J/L by adjusting the pulse repetition frequency from 1 to 60 kHz, and the air flow rate from 10 to 45 slpm. The density of NO was measured by mid-IR QCLAS, and the densities of O_3 and NO_2 by broadband UV-visible absorption.

These experiments showed a transition from an O_3-rich mode to a NO_x-rich mode at an energy density of about 40 J/L. This sharp transition is controlled by the gas temperature and the amount of nitric oxide generated by the NRP discharge. In the O_3-rich mode, up to 65 ppm of ozone is produced at an energy cost of 50 eV/molec. Increasing the energy density, up to 660 ppm of NO was produced at an energy cost of 65 eV/molec. For NO_2, the minimum energy cost was obtained at 95 J/L . At this energy density, the NRP discharge produced about 145 ppm of NO_2 at an energy cost of 60 eV/molec. The concentrations and energy costs of RONS produced by the NRP discharge are comparable to those obtained with reference sources of O_3 (e.g. corona) and NO_X (e.g. plasmatron). Thus, the NRP discharge allows to tune the RONS composition for decontamination applications.

We tested a decontamination approach based on the alternance of O_3-rich and NO_X-rich modes. With this combined regime, a 5-6 log-reduction of bacteria dried on a glass holder was obtained after 10 minutes of plasma treatment. For *C. Albicans* fungi and *B. Subtilis*, the combination of the regimes had an even stronger positive effect. The high efficiency of the process on *B. Subtilis* was surprising because dry gaseous ozone had been shown to have limited effects on *B. Subtilis* even after hours of exposure (Ref. [102]). The interesting effect observed here may be attributed to a synergetic effect of NO_2 and ozone on single-strand breaks of DNA, as reported in Ref. [80]. Thus, the results obtained with the combined mode regime may open the way to more effective strategies for plasma decontamination.

Chapter IV –Time-resolved QCLAS and PLIF measurements of NO density
and gas temperature after a nanosecond spark discharge

100

Chapter IV

Time-resolved QCLAS and PLIF measurements of NO density and gas temperature after a nanosecond spark discharge

The hydrodynamic motion of the gas following a nanosecond spark leads to a recirculation of the surrounding gas between the electrodes and to the expansion of the discharge products into a toroidal volume [254]. The gas recirculation causes dilution of the species and fast gas cooling [255], [256]. This feature may ensure the low temperature of RONS for surface decontamination. However, the gas cooling and expansion may significantly influence RONS production and loss mechanisms in the postdischarge by modifying the coupling between subsequent discharge pulses and recombination mechanisms of RONS. The aims of this chapter are: i/ to quantify the decrease of the gas temperature during gas recirculation and ii/ to investigate the influence of gas recirculation on NO production.

The chapter is divided as follows. First we study the conditions of occurrence of gas recirculation after a nanosecond spark by planar laser induced fluorescence (PLIF) of NO. Three reference cases corresponding to three different gas hydrodynamic motions are identified. In a second part, the effect of gas recirculation on gas temperature and NO formation is studied combining PLIF images with time-resolved quantum cascade laser absorption spectroscopy (QCLAS) of NO.

1. Hydrodynamic effects following a nanosecond pulse

The intense heat release during the discharge pulse produces a shock wave that propagates outward the interelectrode gap within a few microseconds [188], [254], [257]. A heated gas core (kernel) is formed at the center of the electrodes and expands because of the high temperature inside the channel [254], [258]. The volume of the expanding kernel is first cylindrical. The density inside the channel decreases because of expansion of gas and cooling by radiation and conduction. The pressure inside the channel drops

and recessive motion of the channel boundary is initiated from the edge of the electrodes. The kernel develops into a torus because of fresh gas recirculation between the electrodes. This effect is observed since 1950's, e.g. [254], by Schlieren [259], [260] (see Figure IV.1) , PIV [261], and PLIF [261] measurements, in a wide variety of gas [260], and electrode shapes [259]. These studies were mainly carried out in the frame of ignition of combustible mixtures [254], [259], [261]. The gas recirculation is also important in plasma chemistry on the microsecond time scale. The rapid gas cooling due to turbulent mixing [255], [256], [259], [262], and dilution of the discharge products that can modify the reaction pathways of species. In NRP discharges, the gas recirculation removes the discharge products from the electrodes gap thus potentially reducing the synergy between pulses [263]. This can impact the efficiency of RONS production by NRP. In this section, the existence of the gas recirculation is investigated in a repetitive mode by planar laser induced fluorescence (PLIF). Gas cooling and production of nitric oxide are also investigated by time-resolved QCLAS in three cases of gas recirculation determined by PLIF. To our knowledge, this work provides the first direct measurement of the gas cooling rate after a nanosecond spark.
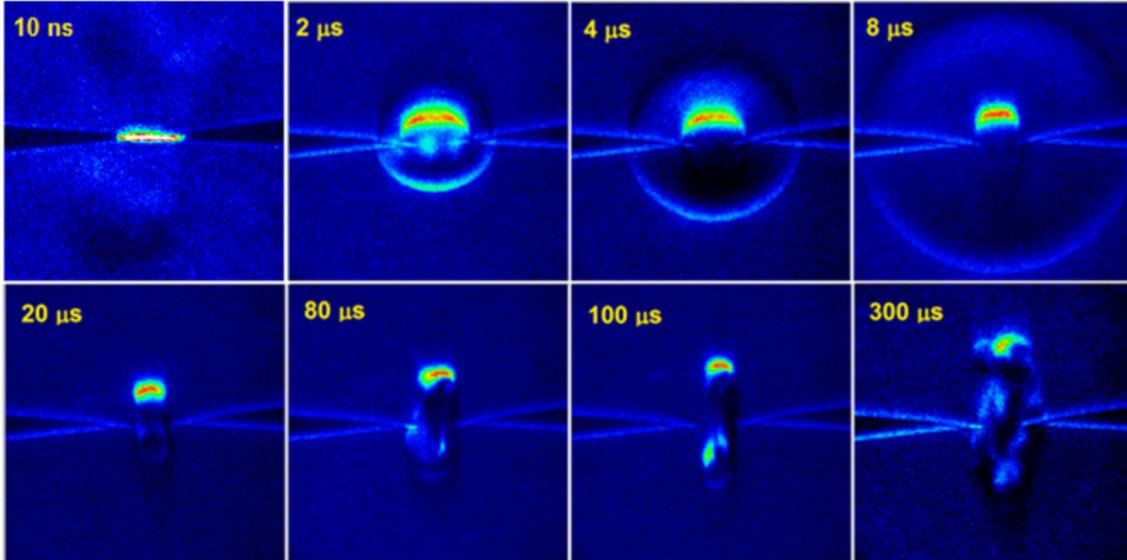
Figure IV.1: Schlieren images obtained for a single nanosecond spark in air at P=1 atm, U=36 kV, taken from [260]**.** Note that in pictures only the upper part of the toroidal shape is seen, as it depends on the Schlieren setup.

Chapter IV –Time-resolved QCLAS and PLIF measurements of NO density
and gas temperature after a nanosecond spark discharge

102

2. Experimental methods and setup

2.1. Plasma reactor and discharge generation

The discharge is produced between two electrodes separated by a gap of 2 mm for all the following results. In almost all experiments, the electrodes are tungsten paraboloid pins of 2 mm thickness. A pulser (FID, FPG 30-100MC4K) produces 10 ns duration pulses, with amplitude up to 42 kV and repetition rate up to 100 kHz. Energy measurements are carried out as described in Chapter III, section 2.2.

The electrodes are placed in open air right above the center of a cylinder of 5 cm diameter which delivers dry air at a flow rate adjusted by a Bronkhorst mass flow controller. In all the following results, the flow rate was adjusted to have an average air flow velocity of v=1.7 m/s, in order to avoid accumulation of NO on the optical path between the electrodes. The diffusion coefficient of NO equals D_{NO}=0.21 cm^2/s [264] at 300 K and atmospheric pressure, and the Peclet number equals Pe=uL/D_{NO}≈800, so the diffusive transport can be neglected. A drawing out was places above the electrodes system in order to evacuate the discharge products and prevent the accumulation of NO in the experimental room.

2.2. Time-resolved QCLAS

The QCLAS diagnostic is similar to that used for NO measurement in Chapter III. The laser operates in the intrapulse mode using 100 ns duration pulses. By modifying the temperature of the QCL we scanned different overlapping spectral ranges from 1899.8 cm^{-1} to 1900.8 cm^{-1} where up to three NO absorption lines can be observed: for T=300-1000 K, NO($X_{1/2}$, v"=0→$X_{1/2}$, v'=1) R(6.5), NO($X_{3/2}$, v"=0→$X_{3/2}$, v'=1) R(6.5), and in addition for T>1000 K, NO($X_{1/2}$, v'=1→$X_{1/2}$, v"=2) R(16.5). Two QCL temperatures are sufficient to scan the whole spectral range, but in order to avoid possible artefacts at the edge of the laser pulse due to the discharge electromagnetic noise, up to five QCL temperatures were used to perform the spectral scan. The spectral shift induced by a change of the QCL temperature was determined using the MCT detector and a calibration cell filled with pure NO. The shift of the peak absorption of NO at 1900.07 and 1900.51 cm^{-1} as a function of the temperature was recorded (see Appendix C). The spectral rate was about 0.8 cm^{-1}/K. Detailed characterization of the intrapulse mode of the QCL, and validation of the method using a NO reference cell was presented in Chapter III, section 3.1.4. The analysis of the error sources in time-resolved QCLAS is done in Appendix B. In Appendix C, the method is validated using 10 ns duration

QCL pulses. However, measurements at sub-microsecond timescale after the spark discharge were not possible because of destructive interferences between the QCL and the hot gas channel. This interference was observed using an IR camera in Appendix C.
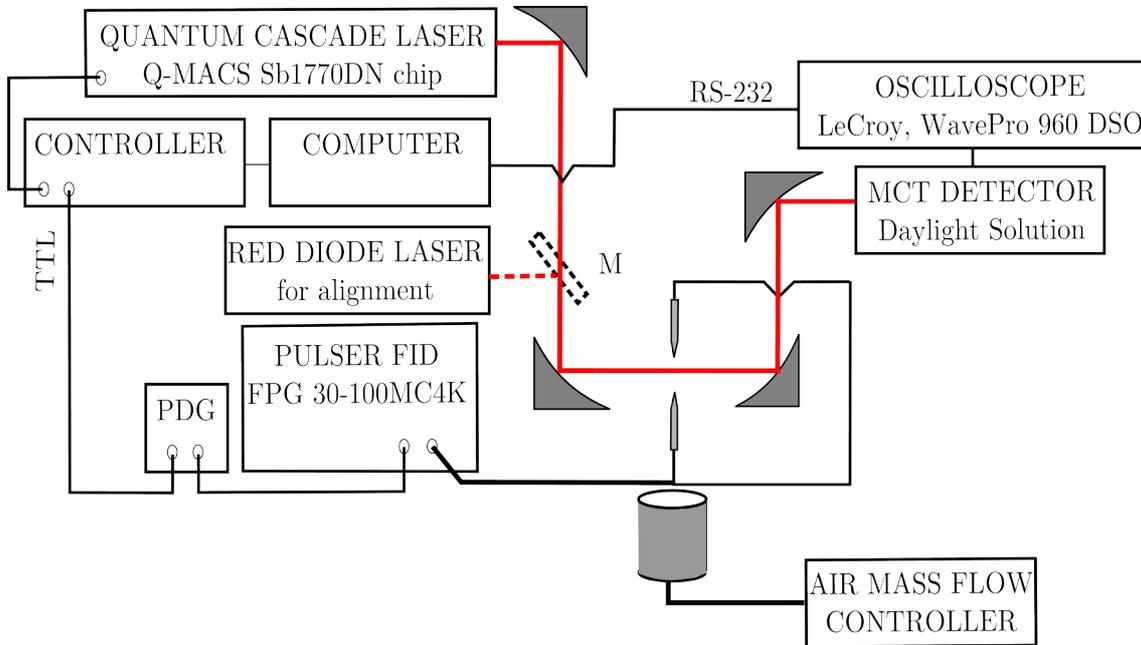
Figure IV.2: Experimental setup for NO-quantum cascade laser absorption spectroscopy time-resolved. M: mirror mounted on a flexible mount used for alignment with the visible diode laser; PDG: pulse & delay generator

Figure IV.2 shows the experimental setup used for the QCLAS measurement. The QCL is synchronized with the pulser using a pulse & delay generator (4 channels, BNC model 555). The QCL is collimated by placing the laser chip at the focal point of an off-axis parabolic (OAP) mirror (f=1 inch)). A second OAP (f=10 cm) focuses the beam between the electrodes. The laser spot size at the focus (beam waist) and the field-depth were determined by placing an infrared camera (IRC 806) at the focal point and by translating it along the optical axis (see Appendix B). We found a field depth of about 2 cm and a QCL beam waist of 320 μm in diameter. Two OAP mirrors then focus the QCL beam on an MCT detector similar to that used in the previous section. The optical scheme is adjusted to observe both IR emission of the discharge and laser pulse.

Alignment of the QCLAS laser beam is particularly difficult because there is no commercially available detection card sensitive enough in the mid-IR to directly measure its position. Therefore a red diode laser was used as a source for the alignment of the optical path. A flat mirror mounted on a flipping mount was placed on the optical path. The alignment was done as follows. The IR camera was placed right after the first OAP collimating the QCL beam. The camera was translated along the optical

Chapter IV –Time-resolved QCLAS and PLIF measurements of NO density
and gas temperature after a nanosecond spark discharge

104

path to ensure that the QCL beam was well collimated. Then three diaphragms were placed between the flipping mount of the mirror and the camera in order to locate the position of the QCL beam. The position of mirror M was then inserted on the optical path and adjusted so that the diode laser could pass at the center of the diaphragms. Finally, the rest of the optical setup could be aligned using the diode laser, without changing the position of the QCL. Following this procedure we considerably reduced the difficulty of the alignment.

The experiments were carried out as follows. First, the discharge was ignited for at least five minutes until reaching a steady state regime. Second, two thousands phase–locked QCL shots measured by the MCT detector were accumulated by the oscilloscope. The QCL temperature was tuned from 13.5°C to 17.5°C in steps of 1°C in order to ensure sufficient overlap between spectra. At each QCL temperature the measurement was repeated. The transmittance spectra were merged in order to build a single transmittance spectrum between 1899.8 cm^{-1} and 1900.8 cm^{-1}. The transmittance spectrum was fitted using the Q-MACS Soft HT software and the HITEMP database. A typical transmittance spectrum is shown in Figure IV.3.
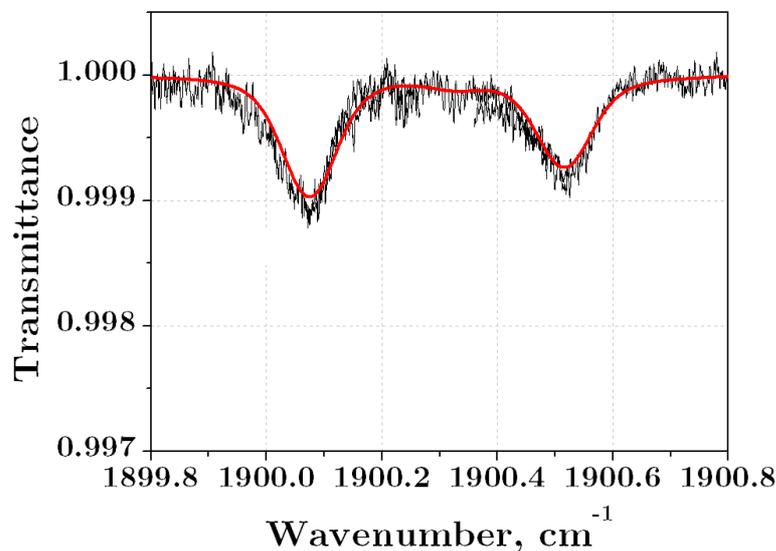
Figure IV.3 : Typical measured (black line) and calculated (red line) transmittance spectra. Experimental conditions: t=80 µs, QCL pulse duration: 100 ns, 2000 accumulations, TQCL=13.5°C, 15.5°C, 17.5°C. Calculation conditions: T=800 K, x(NO)=0.006, absorption length=0.22 cm, P=1 bar, apparatus function 0.04 cm-1.

Because of the hydrodynamic motion of the gas, the absorption length changes with time, so the QCLAS diagnostic was combined with planar laser-induced fluorescence

(PLIF) of NO in order to determine the NO absorption length. The setup for PLIF is presented in the next section.

2.3. Planar laser-induced fluorescence (PLIF)

Planar Laser-Induced Fluorescence (PLIF) is a standard technique used for the detection of molecules. A pump laser is used to form a laser sheet to excite the molecules contained in a 2D plane. The fluorescence is then collected with a CCD camera in a direction perpendicular to the laser beam direction. (see for instance Ref. [265]).

Several difficulties need to be circumvented in PLIF. First, the excited ro-vibrational transition must be well isolated in order to avoid excitation of other overlapping features, and the transition should have a high line strength.. Second, the measured fluorescence depends on the quenching rate of the excited state and the energy fluctuations in the laser sheet. The quenching rate is difficult to estimate in most cases because the quenching rate coefficients and the collider concentrations are not always well-known. However, these quantities are not required here because the PLIF images are only used to estimate the NO absorption length during the hydrodynamic motion of the gas, and not to quantify NO concentrations.

We excited $NO(X^2\Pi_{1/2}$, v"=0$\rightarrow A^2\Sigma^+$, v'=0$)(^QP_{21}+Q_1)$ band head at 226.287 nm [266], and the fluorescence of $NO(A^2\Sigma^+$, v'=0$\rightarrow X^2\Pi_{1/2}$, v"=1$)$ was collected in the 236-246 nm spectral range. We selected these excitation lines because they have minimal overlap with $O_2(B^3\Sigma_u^- - X^3\Sigma_g^-)$ Schuman-Runge absorption lines [267] which can cause significant interferences with NO fluorescence [268] at high temperature (above 1000 K) and pressure (several bars).

2.3.1. Optical setup

Figure IV.4 shows the experimental setup used for PLIF diagnostics. In order to produce the 226.287 nm radiation required to excite the $NO(X^2\Pi_{1/2}$, v"=0$\rightarrow A^2\Sigma^+$, v'=0$)(^QP_{21}+Q_1)$ transitions, the third harmonic of a pulsed Nd:YAG laser (Nd:6000 Continuum, 8 ns duration FWHM, 10-Hz frequency) was used to pump a mixture of Rhodamine 590 and Rhodamine B dyes. The output frequency was selected using a Moya oscillator working with 2400 gr/mm grating. The output of the dye laser was then doubled using a β-barium borate (BBO) crystal and mixed with the fundamental of the Nd:YAG laser at 1064 nm. The output energy of about 1.1 mJ/pulse was measured using an Ophir powermeter. The laser linewidth was about 0.1 cm^{-1}. A cylindrical lens and a spherical lens (10-cm focal lengths) were used to shape the beam to form a laser sheet focused between the electrodes. The sheet was approximately 5 mm in

Chapter IV –Time-resolved QCLAS and PLIF measurements of NO density and gas temperature after a nanosecond spark discharge

106

height and 0.25 mm in width. Images of the NO($A^2\Sigma^+$, v'=0→$X^2\Pi_{1/2}$, v''=2) fluorescence were acquired with an ICCD camera (PI-MAX II, Roper Scientific) equipped with a UV lens (Nikkor – UV 105 mm f/4.5). The fluorescence was filtered with a 236-246 nm bandpass filter in order to remove fluorescence from other species. A pulse & delay generator (BNC model 555) was used to synchronize the Q-switch and the flash lamp of the Nd:YAG laser with the ICCD camera and the pulser.
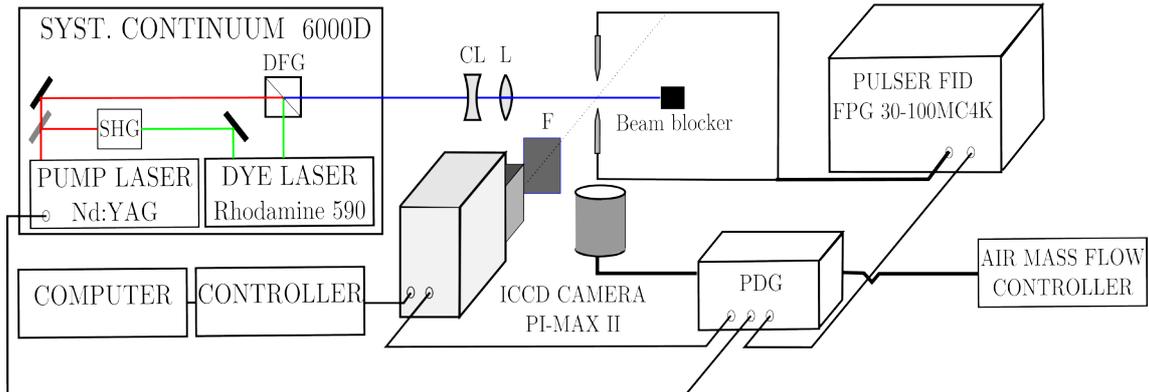
Figure IV.4 : Experimental setup for NO-planar laser induced fluorescence. CL: cylindrical lens; L: lens; F: bandpass filter; PDG: pulse & delay generator; DFG: difference frequency generation; SHG: second harmonic generation.

3. Characterization of the hydrodynamic expansion by PLIF

3.1. Recirculation cases

Figure IV.5 shows three series of PLIF images obtained for three different cases of gas motion. In the first case (left) the fluorescence of NO comes from a cylinder of constant volume of about 1.5 mm diameter. The fluorescence profile was unchanged during the whole period of the discharge pulse. Therefore this case is named here the "no-recirculation" regime. In the second case (center), the pulse repetition frequency is divided by a factor of two. The kernel is initially cylindrical and turns to a toroidal shape when gas recirculation starts at about 100 µs after the discharge. In the third case (right), the energy deposited is increased by almost a factor two. The gas recirculation occurs much earlier than in the second case (about 40 µs after the discharge). So the two latter cases are named here weak and strong recirculation regimes. Experimental conditions of the reported cases are described in Table IV.1.
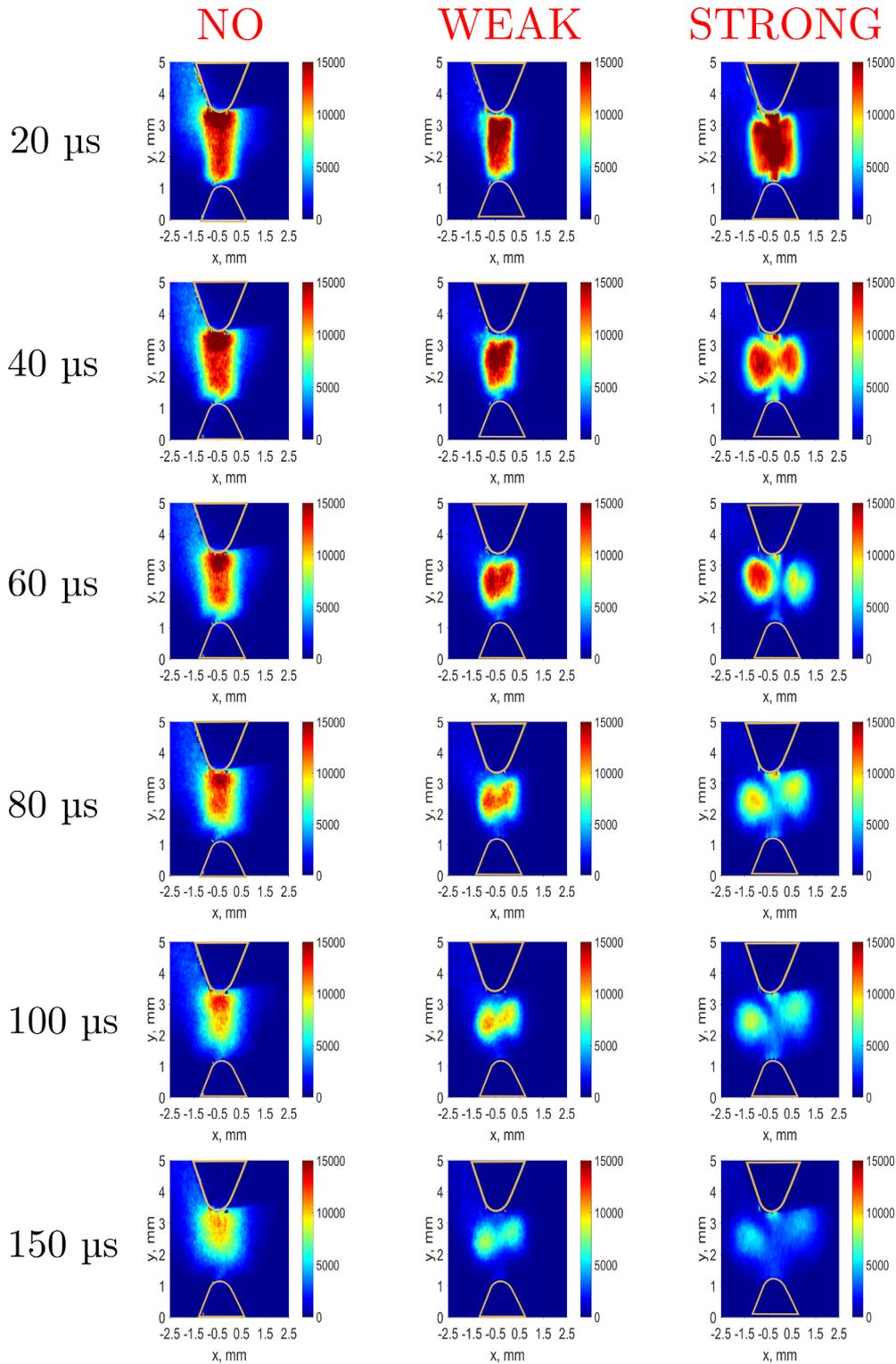
Figure IV.5: Three regimes of gas recirculation observed with NO-PLIF images at between 20 and 150 µs after the discharge pulse: no, weak and strong gas recirculation regimes. The contour of the electrodes is outlined in orange. Discharge settings are given in Table IV.1, gate exposure time: 100 ns, number of accumulations: 200.

Chapter IV –Time-resolved QCLAS and PLIF measurements of NO density
and gas temperature after a nanosecond spark discharge

108

Table IV.1 : Conditions of the three investigated regimes: air flow velocity: 1.7 m.s^{-1}, inter-electrode distance: 2 mm, $T_0 = 300K$, P = 1 atm. PRF: pulse repetition frequency

Recirculation regime	PRF (kHz)	Voltage (kV)	Energy (mJ/pulse)
Strong	1	9	2.04 ± 0.16
Weak	1	5	1.26 ± 0.09
No	2	5	1.04 ± 0.06

3.2. Kernel expansion velocity

The expansion of the hot gas kernel was characterized by measuring the propagation distance in the three regimes. Results are shown in Figure IV.6. As expected, for the no-recirculation case the dimension of the kernel stays nearly constant in time, about 1.35 mm. For the weak and strong recirculation cases, the kernel expands with a constant velocity V_1 up to time 60 µs and a lower velocity V_2 of about 4 m/s afterwards. V_1 is 11.7 and 24.5 m.s^{-1} in the weak and strong recirculation cases, respectively.
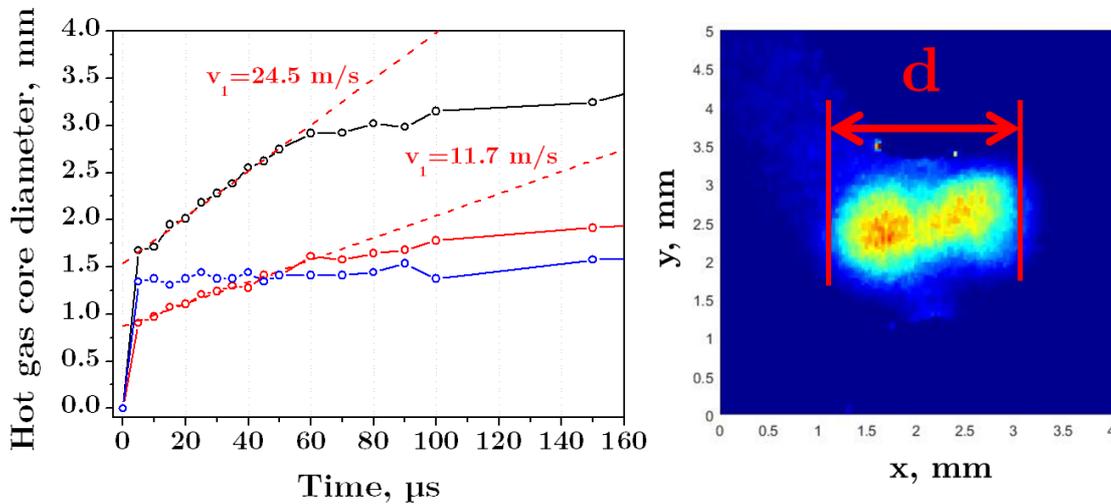
Figure IV.6 : Propagation distance of the hot gas core (left) measured using PLIF images (right) in the no (blue), weak (red) and strong (black) recirculation regimes

Figure IV.7 shows the expansion velocity of the hot gas kernel as a function of the energy-per-pulse. The two data points labeled "weak" and "strong" recirculation correspond to the measurements shown in Figure IV.6. The point labeled "Schlieren" was obtained using Schlieren measurements in earlier work by our group (Figure 4c in Ref. [260]). These previous measurements were obtained under similar conditions, except that the gap distance was 1 mm.

Based on the data shown in Figure IV.7, it appears that the velocity, and thus the propagation distance, increases linearly with the energy-per-pulse at a rate of 10.3 $m.s^{-1}.J^{-1}$.
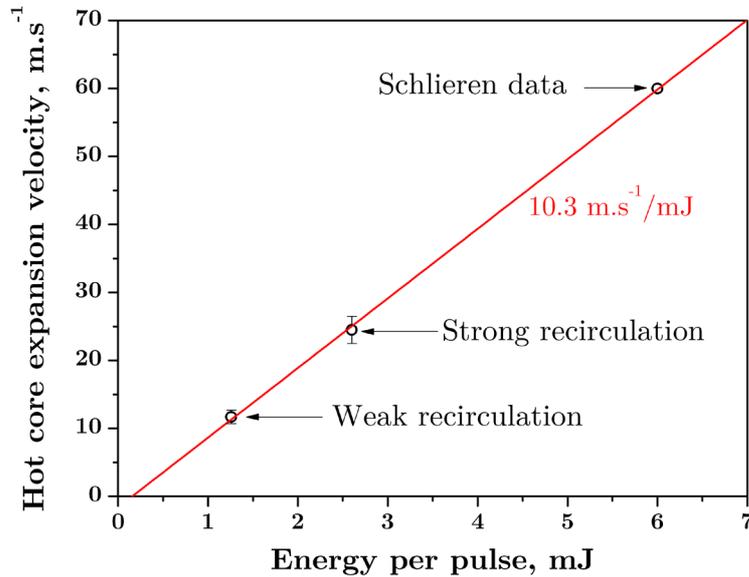
Figure IV.7 : Expansion velocity of the hot gas kernel as a function of the energy deposited in air by the nanosecond spark.

3.3. Conditions of occurrence of gas recirculation

In the weak-recirculation case, the period between pulses is twice longer and the energy 20% higher than in the no-recirculation case. In both cases, the residence time of the flow in the interelectrode gap was about 1.2 ms (air flow velocity: 1.7 m/s, gap: 2 mm). The period between pulses was 0.5 ms (F = 2 kHz) for the no-recirculation case, and 1 ms (F = 1kHz) for the weak-recirculation case. Thus, the discharge products were not totally refreshed between two consecutive pulses in the no-recirculation case. Therefore the transition between the weak and no-recirculation cases can be attributed either to the coupling between subsequent pulses or to a threshold energy required to produce gas recirculation.

The reason why coupling between pulses would inhibit the propagation of the kernel is unclear. The effect of the pulse repetition rate on the kernel expansion was earlier studied by Schlieren in our laboratory [188]. Figure IV.8 shows Schlieren images obtained for different frequencies at about 2 µs before the next pulse of a NRP discharge. At the lowest frequency F=1 kHz, the expanding torus characteristic of gas recirculation is observed. On the other hand, at 10 kHz kernel expansion is not observed, despite the

Chapter IV –Time-resolved QCLAS and PLIF measurements of NO density and gas temperature after a nanosecond spark discharge

110

higher energy per pulse. This is similar to the no-recirculation case. The results of Xu et al. [188] are thus globally consistent with our observations.

These results are also consistent with those reported by Leonov et al [269] who showed that the gas kernel produced after a spark does not expand if the channel is continuously heated, even with a small residual current. A detailed numerical analysis of the sort performed by Shneider [256] would be necessary to shed light on the mechanism of the transition to recirculation.

T_0	300 K	300 K
E	0.15 mJ	0.5 mJ
F	1 kHz	10 kHz
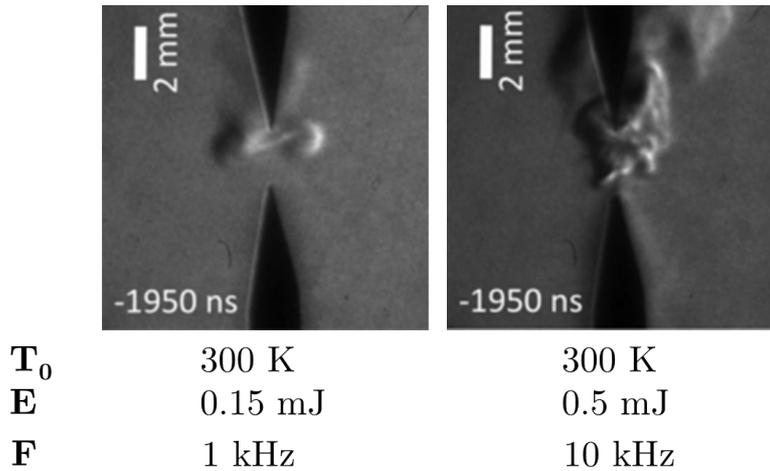
Figure IV.8 : Single-shot Schlieren images in NRP discharges in ambient air, measured about 2 µs before the next pulse, vertical flow of 0.5 m.s^{-1}, modified from [188]

To conclude, above a certain threshold energy or when the pulses are decoupled from one another, the gas kernel heated by the nanosecond spark expands under the form of a torus. The dynamics and scale of propagation of the torus are mainly determined by the deposited energy in the plasma (weak and strong recirculation cases). We found that in our conditions the kernel expands at a rate of 10.3 m.s^{-1}.mJ^{-1}.

4. Gas cooling and effects on NO formation

4.1. Effect of gas recirculation on the gas temperature

Time-resolved QCLAS measurements were performed in the three recirculation cases reported in the previous section. The measured transmittance spectra acquired at 30, 60 and 80 µs are shown in Figure IV.9. These spectra were fitted with the HITEMP database, with the absorption lengths determined from Figure IV.6. The emerging results are shown in Figure IV.11.
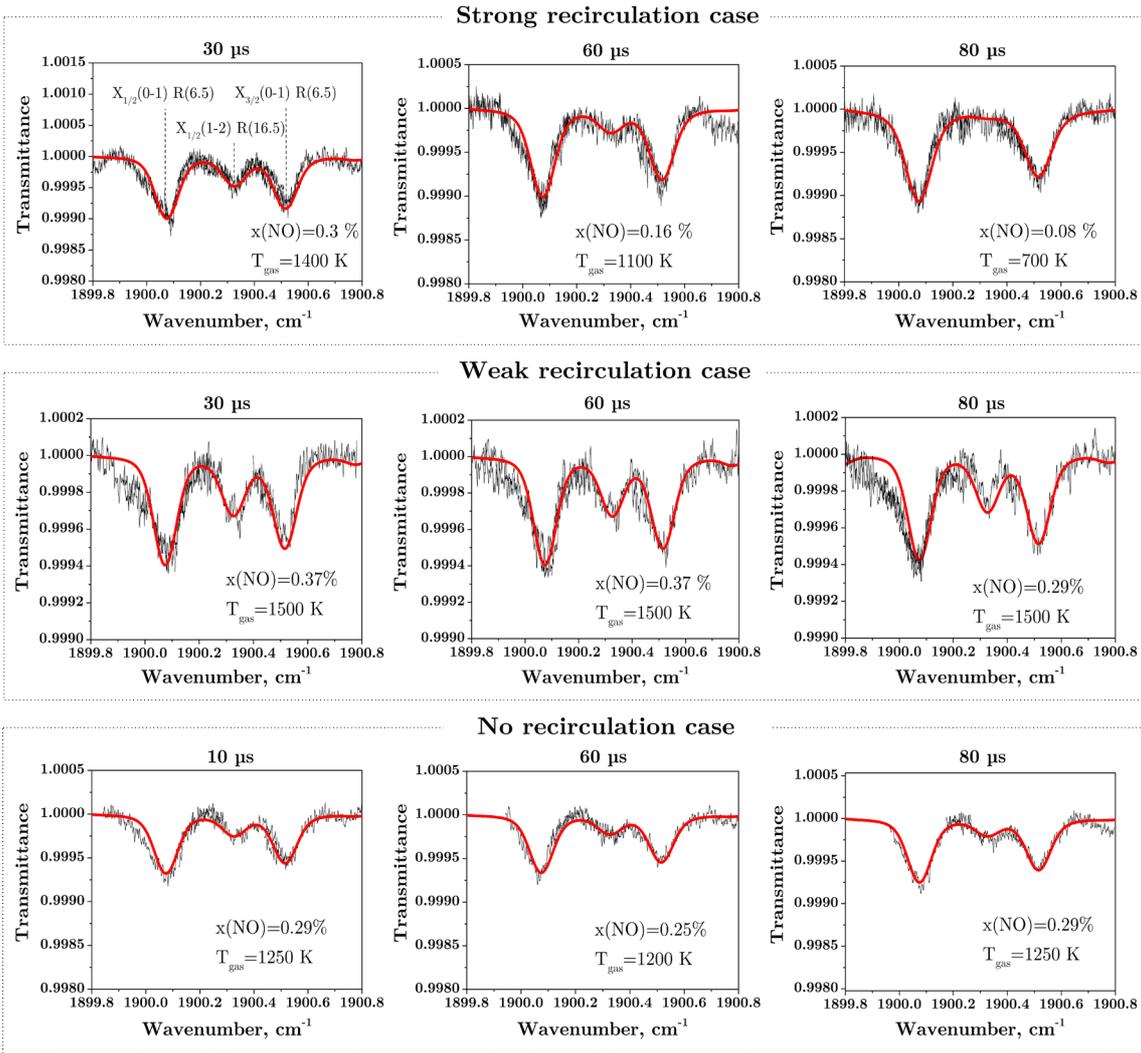
Figure IV.9 : Transmittance spectra measured in the three recirculation cases (black line) and modeled with the HITEMP database (red line) using gas temperature and NO mole fraction as fitting parameters.

Figure IV.10 shows that the gas temperature is nearly constant and equal to 1200 and 1500 K, respectively, in the no and weak recirculation regimes. In contrast, the temperature rapidly decreases from 1400 to 700 K between 30 and 80 µs in the strong recirculation case. This decay corresponds to a cooling rate of 14 K/µs. Over this time period (i.e. < 80 µs), recirculation has not yet begun in the weak recirculation case. So, the conditions are quite similar to the no-recirculation case. The difference in gas temperature between the no- and weak-recirculation cases can be attributed to the higher energy deposition in the weak recirculation case. Indeed the energy deposited and the gas temperature both increase by 20 % from the no-recirculation to the weak-recirculation cases. In the strong-recirculation case, the recirculation starts earlier, between 20 and 50 µs. So, the decrease of the gas temperature can be attributed to the mixing of the

surrounding fresh gas with the kernel as seen in the simulation results of Ref [259]. To our knowledge this is the first quantitative and direct measurement of gas cooling on the sub-millisecond timescale following a nanosecond spark in air.
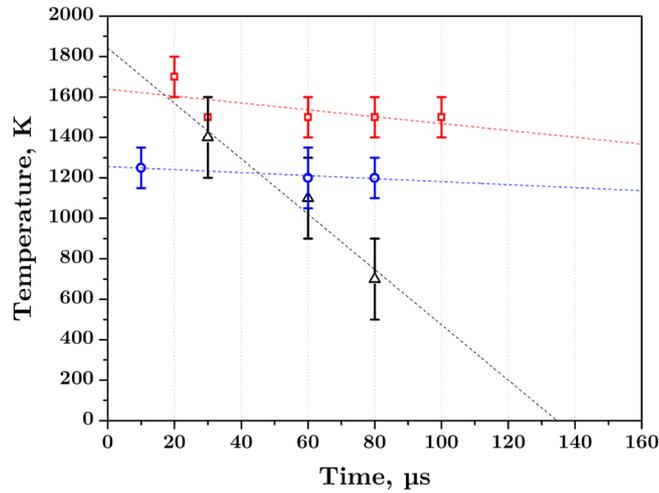
Figure IV.10: Gas temperature inside the kernel in the three recirculation cases investigated: no (blue), weak (red) and strong (black) recirculation cases.

4.2. Effect of gas recirculation on NO density

Figure IV.11 shows the density of nitric oxide measured by QCLAS. In the no-recirculation and weak-recirculation cases, the NO density is nearly constant at about 1.5×10^{16} cm^{-3}. In the strong recirculation case, the NO density decreases by a factor of two between 30 and 80 µs. The data shown in Figure IV.11 represent values averaged over the expanding kernel along the QCL optical path. Therefore, gas dilution affects the results.
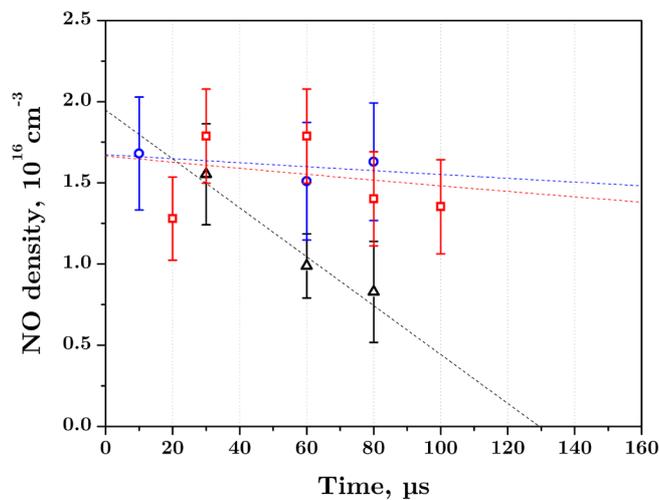
Figure IV.11: NO density (averaged along the QCL beam path) in the three recirculation cases: no recirculation (blue), weak (red) and strong (black) recirculation cases.

In order to compare the production of NO in the three recirculation cases, we calculate the number of NO molecules present inside the volume of the kernel. In the weak and no recirculation cases, the kernel is a cylinder of diameter L(t), i.e. the absorption length. The QCLAS measurement provides the average NO density inside the cylinder. The height of the cylinder is determined by the waist of the QCL ω=320 µm (measured in Appendix B), which corresponds to the spatial resolution of the measurement.

In the strong recirculation case, the kernel is toroidal (with minor radius r, and major radius R) at t>40 µs according to the fluorescence images (Figure IV.5). However, the relative NO density at the center of the profile the fluorescence is unknown because it is strongly influenced by the quenching, as shown in Appendix B. In the QCLAS measurements, the absorption length is the distance between the two extreme lobes of the torus, i.e. L=2×(R+r) (see Figure IV.6). Because of the axial symmetry of the torus, the QCLAS measurement thus provides the average NO density inside a cylinder of diameter L, and height ω.

In the three recirculation cases, the number of NO molecules N(NO) contained inside the fraction of the kernel of height ω=320 µm is the product of the cylindrical volume of diameter and the average NO density $\left\langle [NO](t) \right\rangle_{QCL}$ inside the volume, measured by QCLAS:

$$N(NO) = \left\langle [NO](t) \right\rangle_{QCL} \times \omega \pi \left(\frac{L(t)}{2} \right)^{2} \tag{III.21}$$

Figure IV.12 shows the number of NO molecules in this volume in the three recirculation cases. The number of NO molecules is nearly constant with time in the three cases. Therefore the observed variations in the transmittance spectra with time are only due to the decrease of the gas temperature and to gas dilution but not to a change of the number of NO molecules. This means that recirculation does not affect the recombination of NO. However it is possible that the sources of NO in the discharge phase are influenced by the reduced coupling between pulses expected in the strong recirculation case. Figure IV.13 shows that the number of NO molecules produced in each regime increases linearly with the energy per pulse. This is consistent with the results of Chapter III, Figure III.25 showing a linear increase of the NO mole fraction with the energy density. Therefore there is no evidence that the gas recirculation influences the production or the recombination of NO in our case. This may be because the pulses repetition rate is too low to observe significant coupling between pulses in the investigated cases (F<2 kHz).

Chapter IV –Time-resolved QCLAS and PLIF measurements of NO density and gas temperature after a nanosecond spark discharge

114
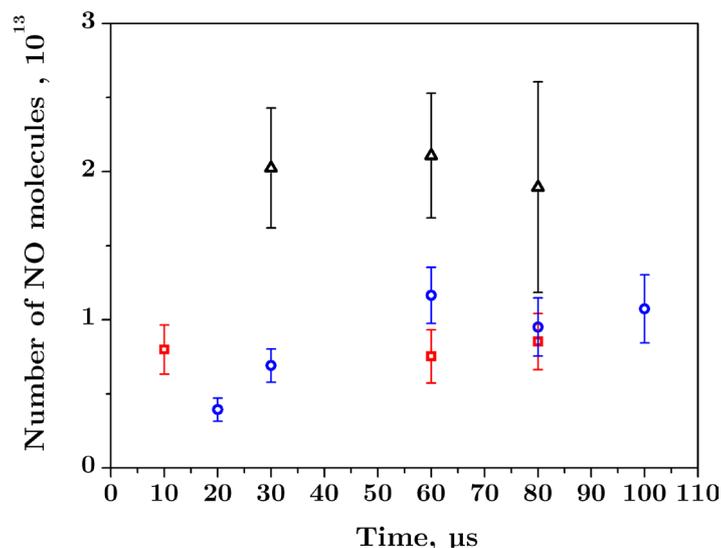
Figure IV.12 : Number of NO molecules contained in the kernel in the no, weak and strong recirculation regimes, calculated using equation (IV.1).
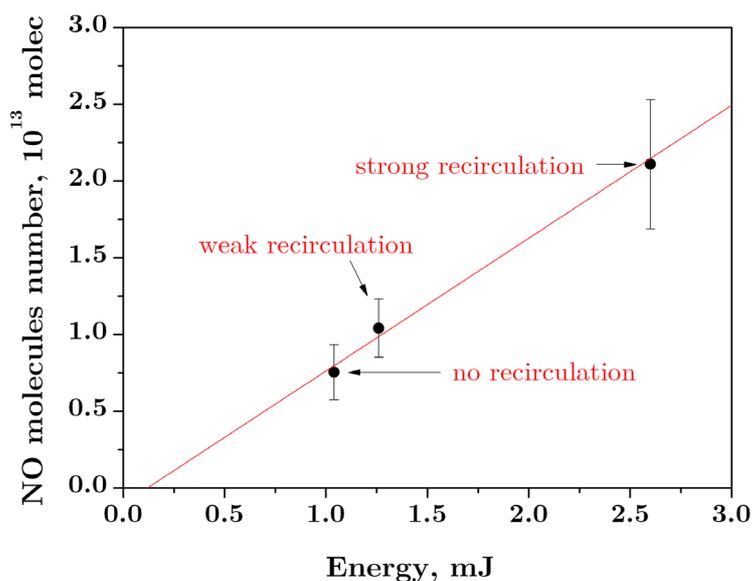
Figure IV.13 : Number of NO molecules at t=60µs calculated using equation (IV.1) as a function of the input energy.

5. Conclusions

The effect of gas recirculation on the formation of NO and gas cooling was investigated. Using NO PLIF, we identified three conditions with various degrees of recirculation. The analysis shows that the energy deposited has a significant impact on the dynamics of recirculation. The velocity of the kernel propagation increases linearly with the input

energy. The transition from the weak to no recirculation is probably dependent on a minimum energy threshold.

In the strongest recirculation regime, a gas cooling rate of 12 K/µs between 30 and 80 µs was measured by time-resolved QCLAS. In the other regimes, the gas temperature was nearly constant.

The effect of recirculation on the NO density was also studied by time-resolved QCLAS combined with PLIF images to determine the absorption length of NO. We analyzed the results by taking into account the dilution of the discharge products during the kernel expansion. The production of NO was not influenced by the gas recirculation in our conditions, but rather was controlled by the input energy.

The gas cooling induced by the recirculation thus ensures a low temperature of the RONS produced by the spark without affecting their production efficiency. This feature of the nanosecond spark discharge may be used to produce NO at low gas temperature for decontamination applications but also wound healing [199].

General conclusions

1. Contributions of the thesis

The aim of the thesis was to study the production and transport of RONS generated by pulsed discharges in nitrogen and air at atmospheric pressure.

In the first chapter of the thesis, an overview of the inactivation rate of commonly used bio-indicators showed that various plasma sources are as efficient as standard low-temperature decontamination methods, i.e. 6-log reduction within 10 -1000 s of endo-spores. However plasma decontamination at atmospheric pressure is limited by the low volume/surface accessible by the antimicrobial agents. Reactive oxygen and nitrogen species (RONS) produced by the plasma can be transported away from the discharge, thus possibly allowing treatment on larger areas. This approach motivated the investigations done in this thesis on the production of RONS by pulsed systems.

In the second chapter, the transport of antimicrobial $N(^4S)$ ground state nitrogen atoms was studied in the afterglow of a pure atmospheric pressure nitrogen discharge flowing inside a polyurethane tube, typically used in catheters. In this setup, $N(^4S)$ atoms are transported over long distances, thus allowing the decontamination of the inner surface of the tube. However, the mechanisms of $N(^4S)$ losses inside the tube are complex and not accurately known. In this thesis we have re-evaluated the rate coefficient of $N(^4S)$ three-body recombination using a new approach. The 3D distribution of $N(^4S)$ inside the tube was measured with a method based on absolute emission spectroscopy combined with an Abel inversion. Using a Fluent CFD model of turbulence and an emission-based method to measure the $[O]/[N]$ ratio, we found that the $N(^4S)$ atoms measured at the the center of the tube are mainly lost by three-body recombination in our case. Fitting the inverse decay of the $N(^4S)$ density, we found a rate coefficient $k=7.77\pm1.04 \times10^{-33}$ cm^6.s^{-1}. This value was validated by the successful modelling of published experimental data sets of recombining nitrogen experiments at atmospheric pressure. This result was used to determine the probability of surface recombination of $N(^4S)$ on the polyurethane surface: $\gamma_N=7.7\pm2\times10^{-5}$. An alternative method of $N(^4S)$ measurement based on relative emission spectroscopy was also presented and discussed, and recommendations for its use were presented. Finally, the model of $N(^4S)$ recombination was used to determine the exposure time required to decontaminate endoscopes of different lengths and diameters contaminated by *E. Coli.*

In the third chapter, we conducted a parametric study of the production of ozone and NO_X, i.e. NO, NO_2, in the afterglow of a nanosecond repetitively pulsed (NRP) discharge in atmospheric pressure air using absorption techniques: quantum cascade laser absorption spectroscopy (QCLAS) and UV broadband absorption spectroscopy. By varying the pulse repetition rate and air flow rate, we found that RONS production rapidly changes from a regime dominated by ozone to a regime dominated by NO_X. The mechanism of the transition between the two regimes was discussed and attributed to gas temperature effects and fast ozone oxidation of NO_X. The energy cost of RONS production by the NRP discharge is approaching the lowest values obtained with other plasma sources (within a factor of 2-3). Minimal energy costs of 50, 65 and 60 eV/molec were obtained for ozone, NO and NO_2, respectively. The ability of the NRP to adjust the RONS composition in the afterglow is interesting for decontamination because it may extend the antimicrobial spectrum of the afterglow and the material compatibility. In addition, we investigated the effect of successive exposure to the ozone-rich and NO_X-rich regimes on the inactivation of microorganisms. The sporicidal activity of the NRP on *Bacillus Subtilis* endospores was greatly enhanced (by 1.5 log) in this case, thus giving a possible new strategy for the treatment microorganisms. Additional work would be necessary to explain these observations. A possible mechanism is the enhanced single strand break of DNA promoted by the simultaneous exposure of microorganisms to NO_2 and O_3 as reported in Ref. [80].

In the fourth chapter, we studied the effect of gas expansion following a nanosecond spark discharge on the gas temperature and NO formation in air. On ~10 µs timescale after the discharge, the discharge products are advected out of the inter-electrode gap in a toroidal expanding volume, while the fresh surrounding gas recirculates between the electrodes. This effect was characterized using planar laser-induced fluorescence (PLIF) of NO. It was shown that the recirculation phenomenon is dependent on the energy density deposited in the discharge. The effect of the recirculation on the discharge products was studied in three cases of gas expansion (with or without gas recirculation) by time-resolved QCLAS of NO combined with PLIF images for the determination of the NO absorption length. It was shown that the gas recirculation causes fast cooling of the gas at a rate of 12 K/µs. The temperature decreases from 1400 to 600 K between 30 and 80 µs, in the case studied in this thesis. If recirculation is not observed, the temperature stays constant between 30 and 100 µs. The measured NO densities were corrected for gas dilution. It was found that the number of NO molecules produced is independent of the recirculation regime, but increases linearly with the energy deposited. The gas cooling induced by the recirculation thus ensures the low temperature of the RONS produced by the spark without affecting their production efficiency.

2. Recommendations for future work

The results obtained in this thesis open several paths for future work.

Bio-decontamination:

- Confirmation of the sporicidal activity of the alternating ozone-rich and NO_X-rich modes of the NRP discharge, and investigation of the mechanism. Possible reasons include enhanced DNA break induced by simultaneous exposure to ozone and nitrogen dioxide, significant concentration of $O_2(^1\Delta)$ and O atoms.
- Microbiological tests in a closed volume of air treated by a burst of NRP discharges. In this case, the concentration of RONS is increased because of the confinement of the discharge products while gas expansion accelerates the transport of the species in the volume.

N_2 afterglow:

- Extension of the study to N_2-xO_2 afterglows. In particular, the addition of O_2 in nitrogen discharges increases the probability of surface recombination of N atoms according to Ref. [134]. Acceleration of $N(^4S)$ recombination in an atmospheric pressure N_2 afterglow with added O_2 impurities was shown in Ref. [42] and attributed to increased surface recombination. However the authors did not investigate possible volumetric losses of $N(^4S)$ due to O and NO. This can be done using the method developed in this thesis by measuring the decay of $N(^4S)$ in the volume for different amount of O_2 impurities.

Gas recirculation and hydrodynamic expansion:

- Extension of the gas cooling rate measurements in the case of a burst of nanosecond pulses and wider range of input energies. The cooling rate may increase linearly with the input energy. If this is verified, the gas temperature in the afterglow of the nanosecond spark may be predicted from the input energy, thus facilitating the consideration of gas temperature in the modelling.

RONS kinetic

- Time-resolved ozone and temperature measurements near the transition between the ozone-rich and the NO_X-rich regime. With this information, it can be confirmed that the transition is caused by thermal dissociation or oxidation of ozone by NO_X.

Diagnostics:

- Comparison of the absolute OES method used in the thesis for ground state N density measurements with planar quenching-free TALIF using femtosecond laser [152].
- Validation of time-resolved QCLAS with 10-ns time resolution in glow or pre-heated discharges, where interferences due to refractive index gradients are reduced.

Appendices

Appendix A

Effect of spatial inhomogeneities on emission-based $N(^4S)$ measurement

In nitrogen late afterglow, the $N_2(B^3\Pi_g$, v=11) emission is related to the density of $N(^4S)$ by:

$$[N_2(B,v=11)] = \frac{k_1}{k_2}[N(^4S)]^2 \qquad (A.1)$$

An usual assumption is that $N(^4S)$ density profile is homogenous over the emission column length L. Measuring the emission intensity across a tube of radius R, the average emissivity can be obtained as:

$$\frac{1}{L}\int_0^L \varepsilon(x)dx \propto \frac{k_1}{k_2}\frac{1}{L}\int_0^L [N(^4S)]^2 dx \qquad (A.2)$$

So that:

$$\langle \varepsilon \rangle \propto \langle [N(^4S)]^2 \rangle \qquad (A.3)$$

Where $<>$ brackets stand for a spatial average quantity over the emission column length. The averaged $N(^4S)$ density is then determined assuming that:

$$\langle [N(^4S)] \rangle = \sqrt{\langle [N(^4S)]^2 \rangle} \qquad (A.4)$$

This is only valid a priori if the density profile is homogeneous. The aim of this annex is to determine the error propagated by this assumption in case of a parabolic profile. Let us define $n_N(r)$, the radial density profile of nitrogen atoms in an axisymmetric discharge. The profile can be fitted by a pth order polynomial law:

$$n_N(r) = \sum_{k=0}^{p} a_k r^k \qquad (A.5)$$

The average of the profile over the cross section of a tube of radius R is given by:

$$\langle n_N(r) \rangle = \frac{1}{R}\int_0^R \sum_{k=0}^{p} a_k r^k dr \qquad (A.6)$$

This gives the following expression:

$$\langle n_N(r) \rangle = \frac{1}{R} \sum_{k=0}^{p} \frac{a_k}{k+1} R^{k+1}$$

(A.7)

We want to compare this expression with the expression of $<n_N(r)^2>$. Note that:

$$\langle n_N(r)^2 \rangle = \frac{1}{R} \int_0^R \left(\sum_{k=0}^{p} a_k r^k \right)^2 dr$$

(A.8)

The squared of the polynomial can be decomposed:

$$\left(\sum_{k=0}^{p} a_k r^k \right)^2 = \sum_{k=0}^{p} (a_k r^k)^2 + 2 \sum_{k=0}^{p-1} \left(a_k r^k \sum_{j=k+1}^{p} a_j r^j \right)$$

(A.9)

We can get this new expression:

$$\langle n_N(r)^2 \rangle = \frac{1}{R} \int_0^R \sum_{k=0}^{p} (a_k r^k)^2 dr + \frac{2}{R} \int_0^R \sum_{k=0}^{p-1} \sum_{j=k+1}^{p} a_k a_j r^{j+k} dr$$

(A.10)

The final result is obtained after integration:

$$\langle n_N(r)^2 \rangle = \frac{1}{R} \sum_{k=0}^{p} \frac{a_k^2}{2k+1} R^{2k+1} + \frac{2}{R} \sum_{k=0}^{p-1} \sum_{j=k+1}^{p} \frac{a_k a_j}{j+k+1} r^{j+k+1}$$

(A.11)

We note that the square root of equation (A.11) differs from equation (A.6). Figure A.1 compares the estimation of $\langle n_N^2 \rangle^{1/2}$ and $\langle n_N \rangle$ for a radial parabolic profile, which is typically observed in laminar flow tube. In this case, $\langle n_N^2 \rangle^{1/2}$ is slightly higher than $\langle n_N \rangle$ by 11%.
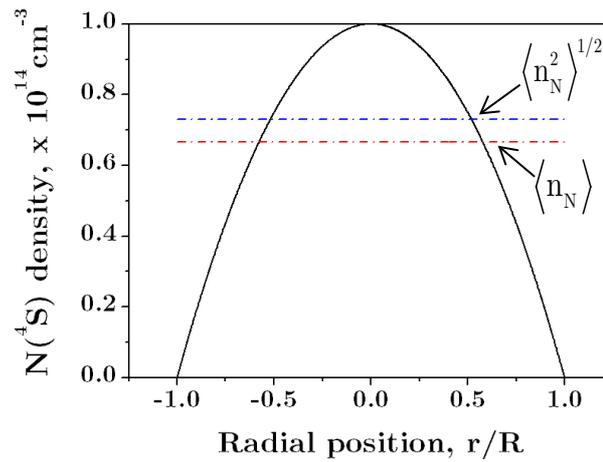
Figure A.1: Calculation results of $\langle n_N \rangle$ and $\langle n_N^2 \rangle^{1/2}$ using a parabolic radial profile

Thus, the equation (A.4) needs to be corrected if the profile is not uniform across the tube radius.

Appendix B

Analysis of error sources in time-resolved QCLAS

The present appendix analyses three error sources in time-resolved quantum cascade laser absorption spectroscopy (QCLAS). First, the estimation of the absorption length from PLIF pictures is discussed. Second, a procedure of determination of the errors on gas temperature and NO mole fraction due to the fitting of transmittance spectra is presented. Finally, since NO is transported radially, we ensured that the divergence of the QCL beam could not affect the measurement.

B.1. Fitting of transmittance spectra

- ### Absorption length

The absorption length is determined from the PLIF pictures of NO. Figure B.1 shows a typical PLIF image and the associated fluorescence profile
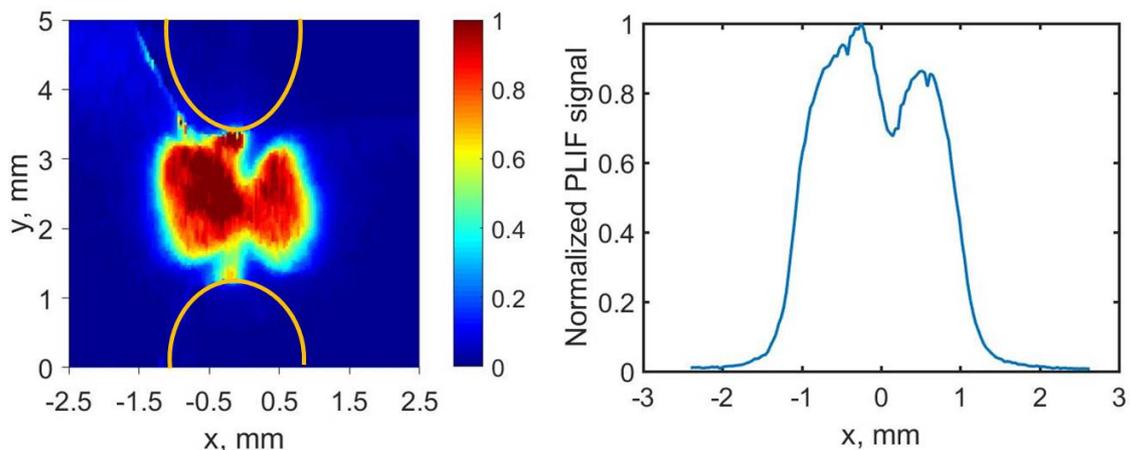
Figure B.1: Normalized PLIF image at 30 µs after the discharge in the strong recirculation case (left) and lateral fluorescence profile at y=2.5 mm and averaged on the waist of the QCL beam dy=320 µm (right).

In the linear regime the fluorescence profile is dependent on the gas temperature because of the quenching rate. Therefore the temperature profile may influence the estimation of the absorption length. In this paragraph, we calculate the quenching rate of NO($A^2\Sigma^+$,v=0) for various Gaussian temperature profiles and we correct the LIF profile

to determine the NO relative density for each temperature profile. Comparing the obtained density profiles, we will see if the temperature can significantly influence the determination of the NO absorption length.

At the time scale studied with PLIF images, the main colliding partners of excited $NO(A^2\Sigma^+)$ are oxygen and nitrogen molecules. In Ref. [270], it was shown that the quenching coefficients are the same for all rotational levels of $NO(A^2\Sigma^+, v=0)$ state at 300 K. The authors determined the quenching rate constant for $NO(A^2\Sigma^+,v=0)$ by O_2 and N_2. . Their value is in good agreement with the calculations of Drake et al. [271] and the measurements of Tamura et al. [272]. Tamura [272] gave the following expression for the quenching rate coefficients of $NO(A^2\Sigma^+,v=0)$ by N_2 and O_2 in the temperature range T=300-2500 K :

$$k_Q^{N_2} = 3.87 \times 10^{-13} \sigma_Q^{N_2}(T) \, T^{0.5} \tag{B.1}$$

$$k_Q^{O_2} = 3.7 \times 10^{-13} \sigma_Q^{O_2}(T) \, T^{0.5} \tag{B.2}$$

where $\sigma_Q^{O_2}(T)$ and $\sigma_Q^{N_2}(T)$ are the quenching cross-sections:

$$\sigma_Q^{N_2}(T) = 0.88 \exp\left(-\frac{1440}{T(K)}\right) + 3.1 \exp\left(-\frac{4800}{T(K)}\right) \tag{B.3}$$

$$\sigma_Q^{O_2}(T) = 21 \exp\left(\frac{27}{T(K)}\right) \tag{B.4}$$

In Figure B.2, twelve temperature profiles are considered and used to calculate the quenching frequency of $NO(A^2\Sigma^+,v=0)$ by air molecules. The quenching profile is used to correct the LIF signal and to infer the relative NO density profile for each temperature condition. It is shown that the temperature profile strongly influences the center of the NO relative density profile while the edges are almost not modified. Therefore the absorption length can be readily estimated from the LIF profile. The absorption length varies by less than 5 % in the considered profiles as seen in Table B.1.
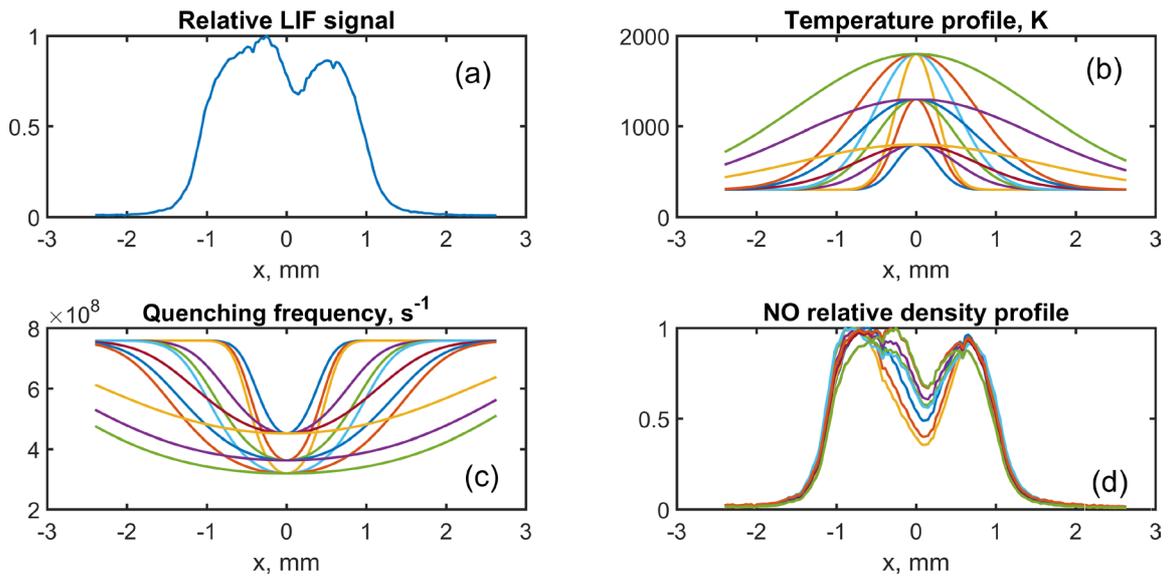
Figure B.2: (a) PLIF intensity profile, (b) Gaussian gas temperature profiles, (c) corresponding NO quenching frequency, and (d) NO relative density profiles corrected from the quenching for each temperature profile.

Table B.1: Absorption lengths determined from the Gaussian temperature profiles shown in Figure B.2. $T = T_{peak} \exp\left(-x^2/2\sigma^2\right) + 300$ K.

Profile number	T_{peak}(K)	σ (mm)	Absorption length, mm
1	500	0.25	2.48
2	500	0.5	2.48
3	500	0.75	2.48
4	500	1.5	2.55
5	1500	0.25	2.58
6	1500	0.5	2.61
7	1500	0.75	2.51
8	1500	1.5	2.55
9	2200	0.25	2.58
10	2200	0.5	2.44
11	2200	0.75	2.48
12	2200	1.5	2.48

- Gas temperature and NO mole fraction

In order to estimate the errors on temperature and NO mole fraction measurements, each transmittance spectrum was fitted at several temperatures around the conditions of best fit, using the NO mole fraction as a fitting parameter. Figure C.2 shows three calculated spectra at 1200, 1400 and 1600 K using NO mole fractions of 0.24%, 0.3% and 0.36% respectively.
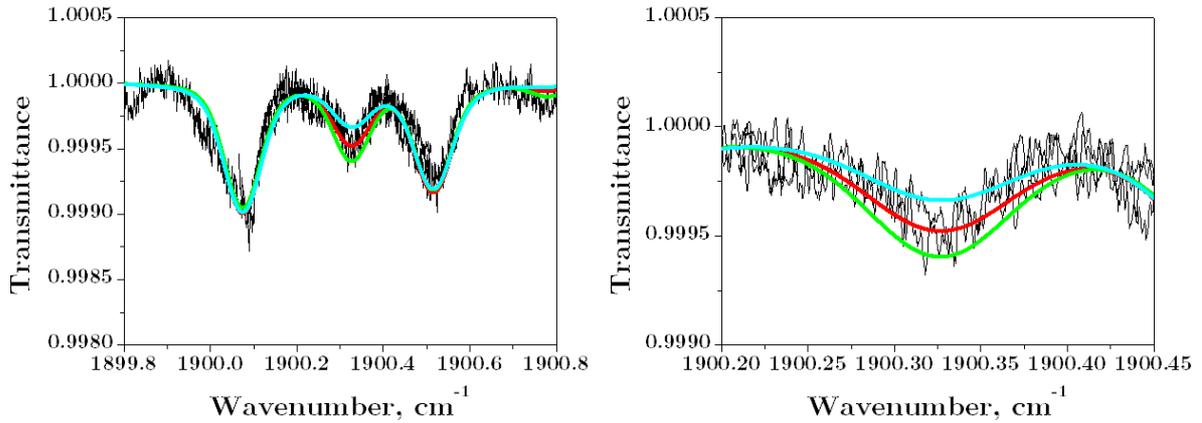
Figure B.3: Transmittance spectrum at 30 µs in the strong recirculation case. Conditions - cyan: T=1200 K, x(NO)=0.24%; red: T=1400 K, x(NO)=0.3%; green: T=1600 K, x(NO)=0.36% ; absorption length=2.28 mm

B.2. Beam divergence

The maximum propagation length of the thermal jets is about 3 mm in diameter in the strong recirculation case. So, we have to ensure that the beam diameter remains constant over the kernel extent. We placed the IR camera described in section at the location of the focus. We found a beam diameter of 320 µm, full-width half maximum (Figure B.3). After a displacement of 5 cm of the camera along the optical path, the laser beam diameter increased to about 420 µm.
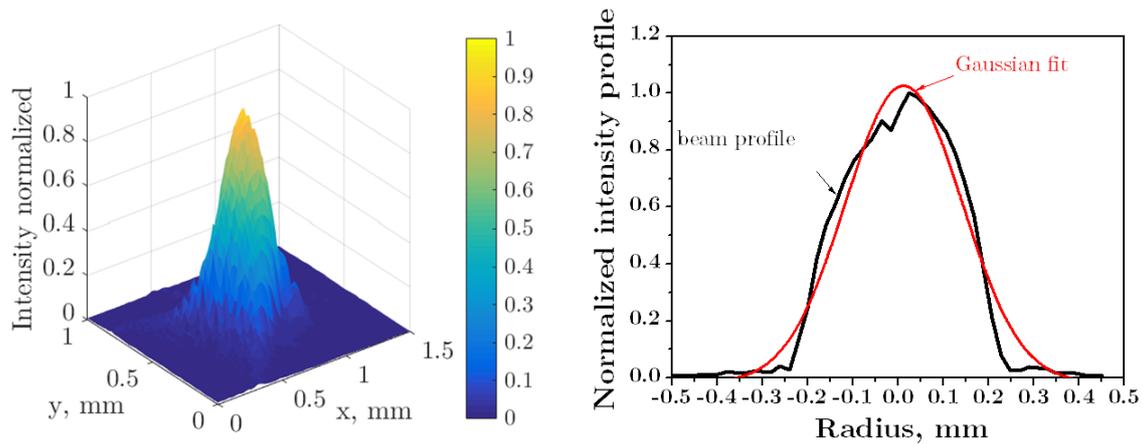
Figure B.4: Normalized distribution of the QCL intensity at the focus measured by the IR camera (left), and radial profile of the emission (black line) fitted by a Gaussian curve (red line, right).

The data were well fitted by the equation of propagation of Gaussian beam, as seen in Figure B.:

$$\omega(z) = \omega_0 \sqrt{1 + \left(\frac{\lambda}{\pi\omega_0} z\right)^2} \tag{B.5}$$

Where ω_o is the waist of the beam measured at the focus and λ is the wavelength of the QCL and equals 5.2 µm. We could thus estimate that on a scale of 1.5 mm the size of the beam varies by less than 0.1%. Therefore this effect has negligible impact on the QCLAS measurement of NO in the thermal jets.
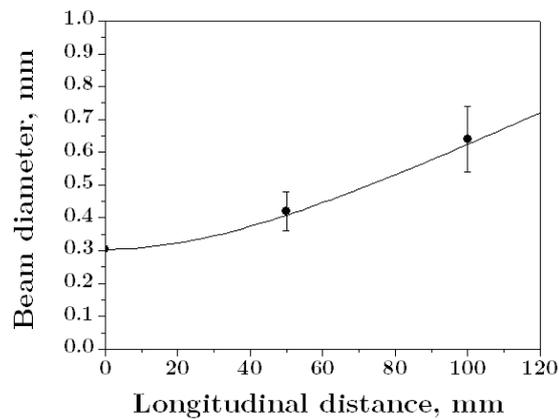
Figure B.5: Beam diameter of the QCL measured at different longitudinal (black symbols), and calculation using the equation of propagation of Gaussian beam with λ=5.2 µm and ω_o=320 µm (black line).

Appendix C

Demonstration of time-resolved QCLAS with 10 ns resolution and limitation for the use in the spark discharge

Here, we demonstrate the use of time-resolved QCLAS with 10 ns time-resolution using a MCT semiconductor detector and an IR camera. Validation of the technique is done using a reference NO cell. The technique is then tested in a spark discharge to measure the NO density on the sub-microsecond timescale. Unfortunately, interferences between the QCL beam and the spark made the measurement impossible as described in a second part.

C.1. Time-resolved QCLAS with 10 ns resolution

- Method principle

At atmospheric pressure an absorption line cannot be entirely scanned by a single laser pulse of 10 ns duration (spectral range of ~0.05 cm^{-1}). The approach used here consists in reproducing the absorption measurement at multiple QCL temperatures in order to widen the spectral range of the scan. Because the spectral range scanned by a laser pulse is much narrower than the absorption line, the measured absorption can be considered as a single point on the absorption spectrum. Therefore the spectral range scanned by a pulse has no importance, and it is thus acceptable to integrate the laser signal. Here, an IR camera (Table C.1) is used for the QCL detection, and results are compared with the MCT detector (one pixel) used in the rest of thesis. In order to validate the approach, absorption measurements are performed in a reference cell filled with 2.5 % NO mixed with He at 442 mbar.

Table C.1: Characteristics of the Infrared Camera

Model	IRC 806
Detector type	Indium Antimonide (InSb)
Spectral response	<1 µm to 5.3 µm
Resolution (pixels)	640 × 512
Pixel pitch	20 µm
Exposure time	>150 ns
Frame rate at max windows size	119 Hz

- ## Experimental setup

The QCL beam is direct to the reference cell using an off-axis parabolic mirror, as seen in Figure C.1. The transmitted beam is splitted and the two branches are sent to the IR camera and to the MCT detector. The NO pressure inside the reference cell is measured using a MKS Baratron pressure gauge. The line is evacuated using a Pfeiffer vacuum rotary vane pump to a pressure <0.1 mbar. Two micrometric valves permit to adjust the NO and helium pressure inside the cell. Air could not be used because of catalytic oxidation of NO by oxygen molecules in the presence of copper or inox tube. This effect rapidly removes NO molecules within a minute.
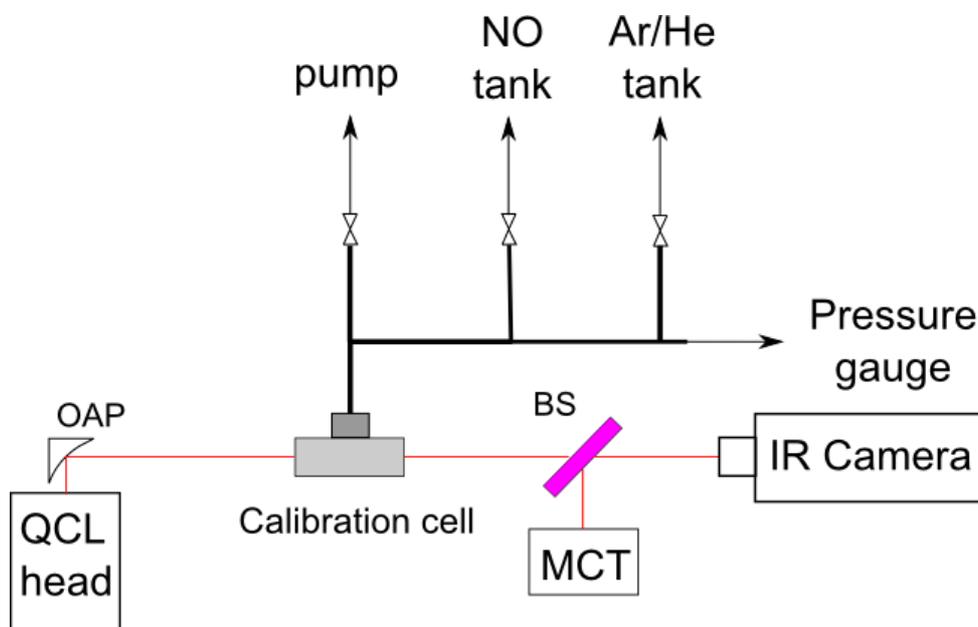
Figure C.1: Calibration setup – OAP: off-axis parabolic mirror, BS: beamsplitter, MCT: HgCdTe IR detector

- ## Wavenumber calibration

The wavenumber shift $\Delta \nu$ induced by a temperature shift ΔT of the QCL is determined using a reference cell filled containing NO at a low pressure (<1 mbar). The absorption spectra are recorded at different QCL temperature and the wavenumber shift is recorded, as seen in Figure C.2. Two absorption features were used in this study: NO ($X_{1/2}$, v'=0 $\rightarrow X_{1/2}$, v"=1) R(6.5) at 1900.076 cm^{-1} (T_{QCL}=18°C) and NO ($X_{3/2}$, v'=0 $\rightarrow X_{3/2}$, v"=1) R(6.5) at 1900.517 cm^{-1} (T_{QCL}=15.5°C). The QCL wavenumber is shifted proportionally to the QCL temperature shift, and in both spectral regions, the rate equals:

$$\frac{\Delta \nu}{\Delta T} = 0.14 \ \text{cm}^{-1}/°C \tag{C.1}$$
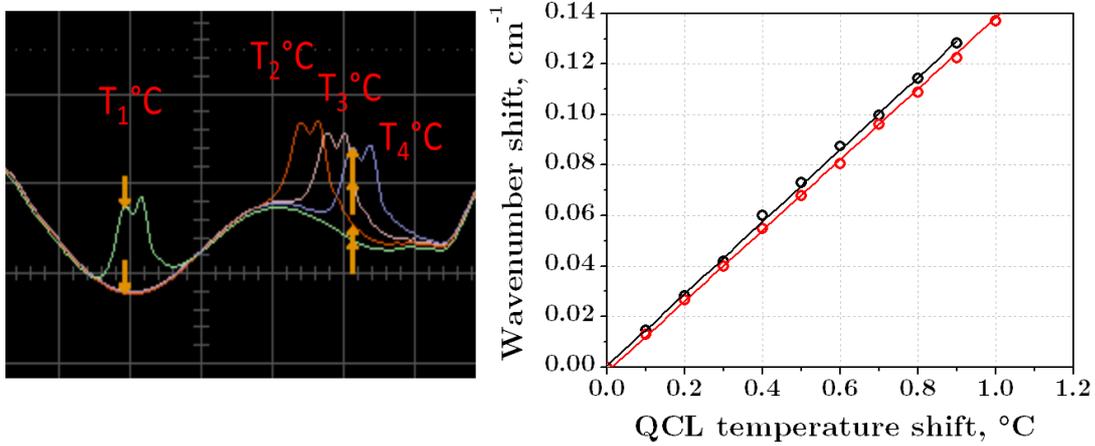
Figure C.2: Recorded NO absorption spectrum at different QCL temperature (left, oscilloscope screen shot). The shift of the absorption profile is measured, and plotted as a function of the QCL temperature (right). Two NO absorption features observed at 18°C and 15.5°C were used in this study. The measured rate equals 0.14 cm⁻¹/°C.

- Validation of the method

The absorbance spectra measured by the MCT and the IRC are shown in Figure C.3.a. The transmittance spectrum could not be fitted because the collisional broadening parameters of NO absorption lines by He are not known. We fitted the absorbance profile with a Lorentzian profile and integrated it to measure the NO density. Figure C.3.b shows a good agreement between the NO density determined from its partial pressure and determined using the MCT and IRC detectors. This confirms that at this QCL voltage and gas pressure, artefacts such as power saturation, rapid passage effects [211], [216] did not have any effects on the measurement. Finally, this procedure validates the QCLAS technique with 10 ns time-resolution at atmospheric pressure.
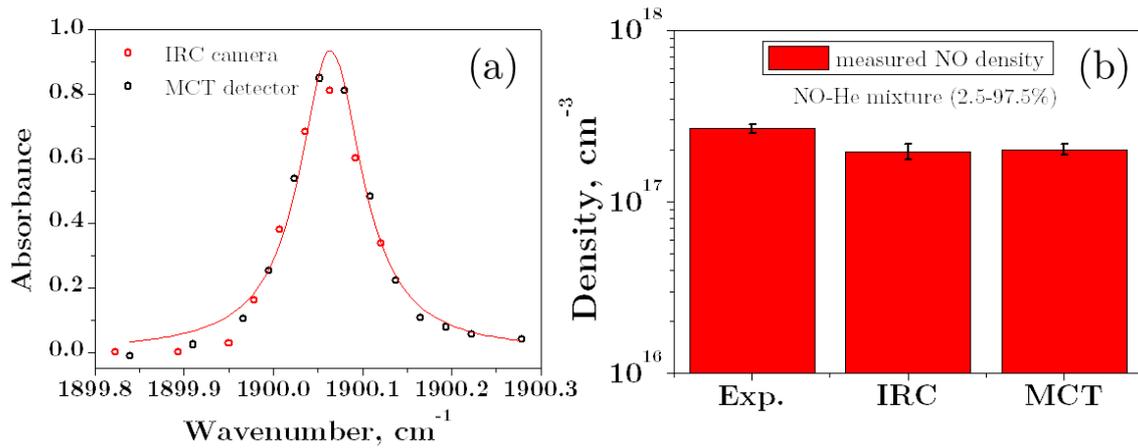
Figure C.3: Photograph Absorbance spectrum of the reference cell filled with 2.5 % NO in He atmosphere at 442 mbar measured using 10 ns QCL pulses at different QCL temperatures (a). The transmitted beam was measured by the IR camera (red circles) and the MCT detector (black circles). The NO density obtained after integration is in agreement with the NO density determined from the NO molar fraction and gas pressure in the reference cell (b).

C.2. Interferences between the QCL beam and the spark discharge

Time-resolved quantum cascade laser absorption spectroscopy was experienced using an IR camera to detect the QCL beam with 10 ns spatial resolution in a nanosecond spark discharge.

The experimental setup is shown in Figure C.4. The QCL is collimated by an off-axis parabolic (OAP) mirror, and focused between the electrodes using another OAP (f=10 cm). A bandpass filter around 5.2 µm and an IR polarizer are placed on the optical path in order to remove the emission from the discharge. A set of two CaF_2 IR lens (f=10 cm and f=1m) collect and focus the QCL beam on the IR camera. The distance between the discharge and the QCL and camera was voluntarily maximized in order to reduce the risks of mis-triggering of the equipment because of the electromagnetic noise generated by the pulser. A time delay generator triggers the QCL, the camera acquisition and the pulser. Figure C.5 shows an image of the shadow of the electrodes illuminated by the laser by placing the QCL out of the focus of the OAP.
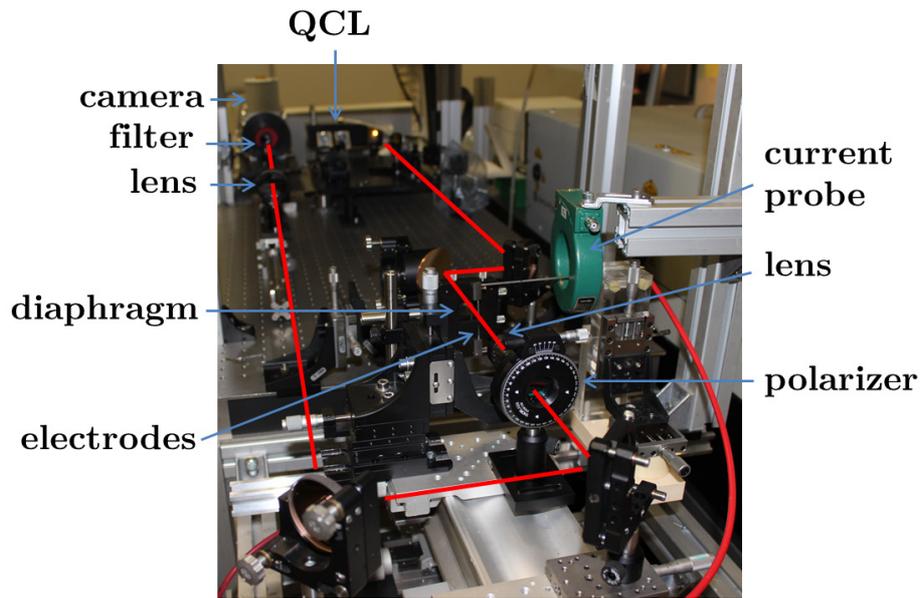
Figure C.4: Photograph of the experimental setup
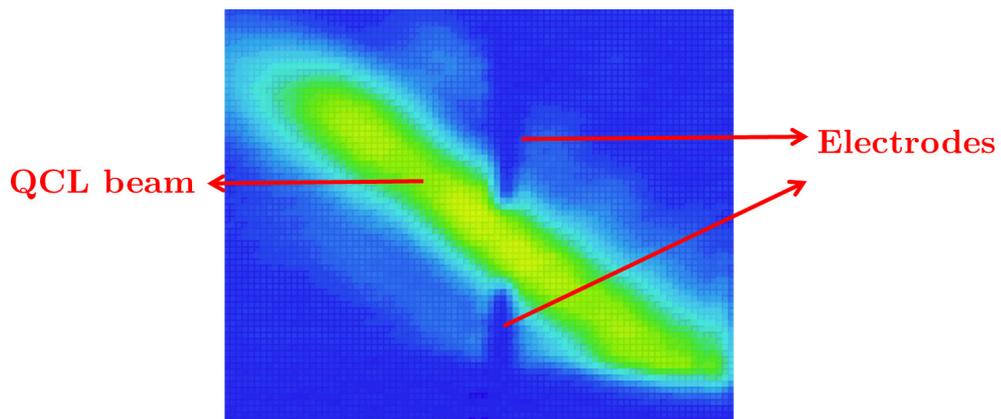
Figure C.5: Image of the QCL beam passing between the electrodes measured by the IR Camera. The laser beam was slightly expanded in order to observe the shadow of the electrodes

The absorption technique requires a longer acquisition time of about 45 minutes in order to scan a single absorption line shapes over the QCL temperatures. To facilitate the scan, we developed a C++ code using the functions of the Q-MACS library to control the laser. The scan was synchronized with the time delay generator in order to automate the acquisition of spectra in the discharge.

When the discharge is turned on, the intensity of the laser is attenuated by about 30 % in a filamentary region corresponding to the spark region as seen in Figure D.6. This attenuation is decreasing when increasing the delay between the laser and the discharge

pulses, but it is still observable up to 1 µs after the discharge pulse (about 1% of attenuation). The other lobes observed at the bottom of the image are not caused by the discharge but by multiple reflections on the window facing the QCL laser chip, as explained in Ref. [273]. This effect was not influenced by the QCL wavenumber, so the observation was not due to NO absorption.
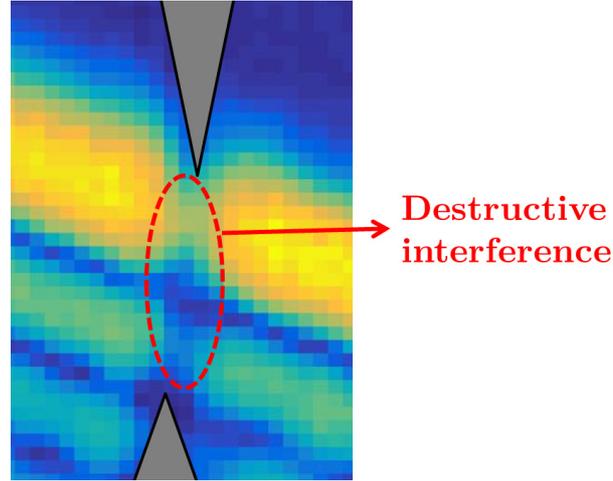
Figure C.6: Evidence of the destructive interference of the QCL induced by the spark in air.

A possible explanation to the observed interference comes from the strong variation of the refractive index within the plasma channel. In the spark, the refractive index at wavelength λ equals, [274], [275]:

$$n = 1 - \frac{e^2}{2c^2 m_e \varepsilon_0 4\pi^2} \lambda^2 n_e + \left(A + \frac{B}{\lambda^2} \right) \frac{n_g}{n_{g0}} \tag{C.2}$$

where n_g and n_e are the gas and electron densities, e is the charge of the electron, c is the speed of light in vacuum, m_e is the mass of an electron, ε_0 is the permittivity of vacuum, A and B are specific constants that depend on the gas species, and n_{g0} is the gas number density at standard temperature and pressure. Variation of the refractive index induce phase shifts between optical trains of the laser thus inducing interferences, especially taking into account the coherence properties of the QCL due to its narrow linewidth (0.006 cm⁻¹). As a consequence of the variation of the refractive index, we observed beam steering by blocking the non-deviated light with a blade placed in front of the electrodes. Beam steering induces a difference in the optical path that can also be a source of interferences when deviated and non-deviated beams recombine on the camera.

Consequently, the NO QCLAS could not be performed on sub-microsecond timescale because the variation of intensity induced by the interferences (more than 10 %) were much higher than the estimated NO absorption (less than 1%).

Appendix D

Data of endospores inactivation by plasma and standard low temperature sterilizers

Endospores are microorganisms commonly used as bio-indicator in various sterilization processes. There is no bio-indicator for plasma sterilizers because of the different mechanisms of sterilization among the plasma sources (UV, charged species, radicals,…). We have reviewed experimental data of inactivation of spores deposited on surfaces by atmospheric pressure and reduced pressure plasma operating in various conditions. The most significant parameters are given including the type of microorganism, the strain, the intial load (N_O) and concentration in cfu/cm^2, assuming homogenous deposition, the material of the surface treated, the pressure, the exposure time, the operating gas mixture and conditions of the plasma source.

Table D.1 : Literature review of the inactivation of spores by low temperature plasmas at reduced and atmospheric pressure on dried surfaces and comparison with conventional decontamination methods

Reduced Pressure Plasma

Author	Ref	Microorg.	Strain	N_O	N_O/cm^2	Surface	Source	Gas	Pressure	Time	Distance	RF
Halfman et al.	[60]	*B. Subtilis*	ATCC 51189	10^6	–	Glass	RF ICP, 1kW	Ar-H_2	10 Pa	40 s	direct	6
								Ar-O_2	10 Pa	60 s	direct	6
		A. Niger	ATCC 6275	10^6				Ar-H_2	10 Pa	60 s	direct	6
Moisan et al.	[114]	*B. Atrophaeus*	ATCC 9372	10^7	10^5	Polystyrene, 95 cm^2	MW, 400W, 50 L chamber	N_2-O_2	470 Pa	45 min	>82 cm	6
							MW, 120W, 5.5 L chamber	N_2-O_2 0.37 %	670 Pa	60 min		<6
		G. Stearother-mophilius	ATCC 7953	10^7								>6
		B. Pumilus	ATCC 27142	10^7								5
Nagatsu et al.		*G. Stearother-mophilius*	ATCC 12980	$2x10^6$	–	Stainless steel	MW, 300 W, 11 L chamber	Synthetic air	90 Pa	30 min	direct	7
Levif et al.		*B. Atrophaeus*	ATCC 9372			Polystyrene, 9 cm^2	MW, 5.5 L chamber	N_2-O_2		60 min	direct	4.5
Kawamura et al.	[122]	*G. Stearother-mophilius*	ATCC 7953	10^6	$7x10^4$	Paper, 14.3 cm^2	RF-plasma jet	N_2	31 kPa	10 min	direct	4.5
						Stainless steel				15 min	direct	4
Stapelman et al.	[59]	*B. Pumilus*	SAFR-032		–	Stainless steel screw	MW, 400W	H_2	5 Pa	4 min	direct	6
		B. Subtilis	DSM 402							2 min		6
Lerouge et al.	[65]	*B. Subtilis*	ATCC 9372	10^7	$2x10^6$	Glass	MW, 200W	O_2-CF_4	80 mTorr	5 min	direct	4

Atmospheric Pressure Plasma

Author	Ref	Microorg.	Strain	N_O	N_O/cm^2	Surface	Source	Gas	Flow velocity	Time	Distance	RF
Lim et al.	[276]	*B. Subtilis*	ATCC 9372	2.10^7	–	Glass	RF-APPJ, 130W,	Ar-O_2	8.6 cm/s	40 s	5 mm	7
											10 mm	3
											15 mm	<1
Brandenburg et al.	[277]	*B. Atrophaeus*	ATCC 9372	$2x10^6$	$7.8x10^5$	Polyethylene, 2.56 cm^2	RF-APPJ, 20W, 20 slm	Ar	8.6 m/s	420 s	22 mm	4.3
Herrmann et al.	[278]	*B. Globigii (Atrophaeus)*	–	10^7	$5x10^7$	Glass, 20 mm^2	RF-APPJ, 300W, 92 slm	He-O_2	30 m/s	30 s	5 mm	7
Tseng et al.	[279]	*B. Subtilis*	ATCC 6633	10^6	–	Polystyrene plate	RF-APPJ, Atom-flo™ 250 System, 100W, 20.4 slm	He-N_2	–	20 min	7 mm	6
		B. Stearother-mophilius	ATCC 7953									4.2
		C. Botulinum Type A	ATCC 3502									2.48
		C. Botulinum Type E	NCTC 11219									5.78
		C. sporogenes	ATCC 3584									3.8
		C. difficile	6871									6
		C. perfringens	ATCC 3624									6
Van Bokhorst–van de Veen et al.	[69]	*B. Cereus*	ATCC 14579	10^6	$5.9 x10^4$	GSWP filter, cellulose, 17 cm^2	AC-APPJ, CP121 plasma demonstrator, 50 Hz, 3 kV, 15 slm	N_2	80 m/s	20 min	12 cm	3.5
					–	Glass slide						0.8
Klämpfl et al.	[95]	*B. Subtilis*	ATCC 6633	10^6	$5x10^5$	Stainless steel, 2cm^2	SMD, 35 mW/cm^2	Air	Static,110cl	30 s	5 mm	0.5

Author	Ref	Microorg.	Strain	N_O	N_O/cm^2	Surface	Source	Gas	Flow velocity	Time	Distance	RF
Klämpfl et al.	[280]	*C. Albicans*	ATCC 90028	$2x10^6$	10^6	Agar plate,	SMD, 35 mW/cm^2	Air	Static, $V \simeq 110$cl	30 s	8mm	4
		G. Stearother-mophilius	ATCC 7953			stainless steel, 1.80 cm^2				3 min		3
		B. Atrophaeus	ATCC 9372									>5
		B. Subtilis	DSM 13019									4.5
		B. Pumilus	ATCC 27142									>5
Shimizu et al.	[117]	*B. Atrophaeus*	DSM 675	10^7	10^7	Aluminium, 95 mm^2	SMD, 0.4W/cm^2, chamber	Ambient air	Static, V=2.16 L	20 min	21 cm	>3
Boudam et al.	[41]	*B. Subtilis*	−	10^6	10^6	Polystyrene, 1cm^2	DBD, Townsend	N_2-N_2O	∼ 5 m/s	10 min	direct	>5
Muranyi et al.	[45]	*B. Atrophaeus*	DSM 2277	10^6	$6.2x10^4$	PET, 16 cm^2, spray	CDBD, 130 W	Air	−	1 s	direct	5.1
Muranyi et al.	[106]	*B. Subtilis*	DSM 4181	10^6	$6.2x10^4$	PET, 16 cm^2, spray	CDBD, 170 W	Air, 70% RH	−	1 s	direct	2.8
		A. Niger	DSM 1957									1.2
Venezia et al.	[281]	*B. Atrophaeus*	ATCC 9372	10^6	$1.1x10^6$	Stainless steel, 88 mm^2	DBD, PlasmaSol sterilizer, 30 W, 1slm, container	N_2-O_2[a]	−	2 min	indirect	>5
		G. Stearother-mophilius	ATCC 7953							10 min		>5
Heise et al.	[96]	*B. Subtilis*	DSM 2277	10^6	$2.6x10^4$	PET, sprayed on 38.5 cm^2	DBD, 7 W/cm^2	Ar	−	25 s	direct	5
								N_2				<5
								Air synthetic				1
							CDBD	O_2		10 s		6
		A. Niger	DSM 1957				DBD	Ar				6
								N_2				2
								Air synthetic				4
							CDBD	Ar				6

Author	Ref	Microorg.	Strain	N_O	N_O/cm^2	Surface	Source	Gas	Flow velocity	Time	Distance	RF
Schnabel et al.	[116]	*B. Subtilis*	−	10^6	~2.5 x10^4	Glass bottle, 250 mL (about 40 cm^2)	MW, 1.2 kW, 13 slm, 7s on	Air, 20% RH	−	5 min	25 cm	2
										30 min		7
Lai et al.	[282]	*B. Cereus*	ATCC 1178	10^6	1.2x10^6	Glass, 0.8 cm^2	MW, 700 W, 25 slm	Air	3.4 m/s	10 s	3 cm	5
										14 s	4 cm	5
										20 s	5 cm	5
Kuo et al.	[283]	*B. Cereus*	ATCC 1178	10^6	10^6	Paper, 1 cm^2	MW, 25 slm	Air	3.4 m/s	3 s	4 cm	1
Kovalova et al.	[284]	*B. Cereus*	−	−	−	Polypropylene foil, 12.5 cm^2	Negative corona	Ambient air	Static	10 min	direct	2.2
							Positive corona					1.5
Akitsu et al.	[285]	*B. Atrophaeus*	ATCC 9372	2x10^6	10^6	Cellulose, 1.8 cm^2	RF Glow, 670W	He-H$_2$O 3.2%	0.3 m/s	30 min	direct	>6
		B. Stearother-mophilius	ATCC 7953	1.3 x 10^6	7.2x10^5							>6
Pointu et al.	[42]	*G. Stearother-mophilius*	CIP 52.82	2x10^4	1.1 x10^4	Glass, 1.80 cm^2	NRP, 15 W	N$_2$ pulsed DC	13.2 m/s	50 min	10 cm	2.5
Ben Gadri et al.	[286]	*B. Subtilis* (vegetative)	−	1.5 x 10^4	−	Glass	DBD Glow	Air		60 s	Direct	>3
		D. Radiodurans	−	10^7						45 s		>2
		B. Stearother-mophilius	−	10^6		Nitrocellulose				5.5 min		>5
		B. Pumilus	−			Paper				2.4 min		>4
		B. Subtilis niger	−									>4
Patil et al.	[104]	*B. Atrophaeus*	ATCC 9372			Strip, polypropylene container	CCP, 40 W, 20 mm gap	Air, 3 % RH	−	60 s	direct	0.9
								Air, 70% RH			indirect	5.5

Author	Ref	Microorg.	Strain	N_O	N_O/cm^2	Surface	Source	Gas	Flow velocity	Time	Distance	RF
Mahfoudh et al.	[102]	*B. Atrophaeus*	ATCC 9372	10^6	1.6x10^5	Silicone, 6.25 cm^2	–	Dry ozone (RH<2%)		60 min	direct	4.7
						Polyurethane						2.04
						HD Polyethylene						0.19
						PTFE						0.17
						Polymethyyl						0.11
						Polypropylene						0.07
						Pyrex glass						0.27
		B. Pumilus										0.1
		G. Stearother-mophilius										0.9
		B. Atrophaeus				Polystyrene						0.69
		B. Pumilus										1.5
		G. Stearother-mophilius										2.8

Note: 1) *Bacillus Atrophaeus* and *Geobacillus Stearothermophilius* were formerly known as *B. Subtilis var. niger* or *B. Globigii*, [101] and *B.Stearothermophilius* [287] respectively. 2) *Bacillus Atrophaeus* and *B. Subtilis* are very similar.

[a] humidified, and 1% ethylene admixture; [b] EtO tests were always followed by 13-15h of aeration

Appendix E
Résumé étendu de la thèse

Les méthodes de stérilisation à basse température prennent une importance croissante pour la décontamination de matériaux thermosensibles utilisés dans les appareils exposés aux risques microbiologiques tels que les endoscopes dans les hôpitaux, les emballages dans l'industrie agroalimentaire, ou les équipements soumis aux agents microbiologiques de guerre dans les zones de conflits. Les méthodes de stérilisation standards non-thermiques souffrent de limitations liées à leur toxicité, leurs coûts élevés, leurs faibles compatibilités avec les matériaux, et/ou leurs longs cycles de stérilisation (quelques heures). Une approche alternative consiste à utiliser des plasmas hors équilibre à pression atmosphérique produits par décharges électriques. Les plasmas permettent des cycles de stérilisation plus courts car les surfaces traitées sont exposées à de nombreux agents biocides, notamment à du rayonnement, à des espèces réactives oxygénées et azotées (RONS), et à des espèces chargées. Cependant, à pression atmosphérique, le volume du plasma est généralement faible. Les traitements en post-décharge permettent d'augmenter la surface de traitement, tout en réduisant la dégradation du matériau par les espèces chargées. Dans la post-décharge, les principaux agents biocides sont les RONS. L'objectif de cette thèse est d'étudier la production et le transport des RONS générés par des décharges pulsées non-thermiques dans l'air et l'azote à pression atmosphérique.

E.1. Introduction à la décontamination de surface par plasma

Une large introduction à la microbiologie est donnée dans un premier temps dans le premier chapitre dans le but de cibler les principaux microorganismes d'intérêt pour l'étude de la décontamination par plasma. Nous focalisons d'abord notre étude sur la structure des bactéries et des champignons et sur leurs mécanismes de résistances contre les agents biocides. Les spores bactériennes sont largement reconnues comme étant les plus résistantes et sont pour cette raison utilisées comme bio-indicateur pour attester de l'efficacité d'une méthode de décontamination. Ensuite, nous présentons les méthodes permettant d'évaluer l'efficacité de décontamination d'un procédé. La décroissance exponentielle du nombre de bactéries avec la dose (rayonnement, concentration chimique, temps d'exposition) utilisée est observée avec les méthodes thermiques de décontamination et permet donc d'extrapoler la dose requise pour garantir la stérili-

té d'une surface qui correspond à la probabilité de trouver un organisme vivant sur un million d'articles traités par la méthode de décontamination et initialement contaminés par 106 microorganismes. Pour les méthodes basses températures telles que les plasmas froids étudiés dans cette thèse, la décroissance des microbes comporte plusieurs phases à différentes exponentielles ne permettant pas d'extrapoler la décroissance et donc de garantir la stérilité des surfaces. Pour cette raison nous parlerons de désinfection de haut niveau par plasma et non de stérilisation.

Dans un second temps, nous présentons le principe de génération des plasmas hors-équilibre au moyen de décharge électrique ainsi que les principaux agents biocides générés par un plasma : les espèces chargées (et le champ électrique associé) conduisant à la lyse cellulaire, le rayonnement UV fortement absorbé par l'ADN, ainsi que les espèces réactives à base d'oxygène et d'azote (RONS) ciblant divers composants fonctionnels (protéines, ADN) et structurels (membrane bi-lipidique) des microbes.

Nous effectuons une revue approfondie de littérature qui nous permet d'abord d'identifier les principaux facteurs environnementaux pouvant influencer les résultats d'inactivation de microbes traités par plasma. Cette étude permet de souligner les facteurs à considérer dans la définition de protocoles standardisés pour les tests microbiologiques de décontamination par plasma. Le rôle de la concentration surfacique initiale de microbes réside dans le fait que les espèces biocides ne peuvent pas rapidement diffuser à travers plusieurs couches de microbes. La porosité du matériau de la surface semble être un paramètre clé dans la résistance des microbes traités par une méthode chimique car les microbes peuvent diffuser à l'intérieur du matériau et ainsi réduire leur concentration surfacique. L'humidité relative est aussi un facteur augmentant le contenu en eau des spores qui initialement sont vidées de leur eau lors de la sporulation. La présence d'eau permet la production d'espèces actives (notamment OH) à l'intérieur de la spore contribuant à une augmentation de l'effet biocide.

Le second objectif de la revue est de référencer les résultats de microbiologies obtenus par plasma et par des méthodes standards basses températures contre des spores bactériennes. Ce travail permet de montrer que des inactivations de 6-log sont possibles en des temps de traitement comparables ou inférieurs à ceux nécessaires dans les traitements standards basses températures (EtO, H2O2,…). Cependant, en raison du faible volume des plasmas produits à pression atmosphérique et de la possible dégradation des espèces dues aux espèces chargées, il est souvent approprié de travailler dans la post-décharge pour réduire la dégradation et augmenter la surface de traitement. En produisant des concentrations suffisantes de RONS, des études ont montré que des réductions significatives de spores (>4 log) étaient possibles en quelques dizaines de minutes. Il est

clair que si le transport de ces RONS ainsi que leur production pouvaient être amélio-rées, des réductions similaires en des temps d'exposition plus courts pourraient être atteintes. L'objet des trois chapitres est d'étudier le transport et la production de RONS dans le cadre du projet Desdemona financé par la Direction Générale de l'Armement (DGA) qui vise deux applications : la décontamination d'endoscopes et le traitement d'objets contaminés par des agents microbiologiques de guerre.

Pour la décontamination d'endoscope la post-décharge d'une source pulsée microse-conde appliquée à un écoulement d'azote à pression atmosphérique est utilisée. Dans ce système la présence d'azote atomique à l'état fondamental est clairement associé à l'efficacité biocide dans la post-décharge et est également associée à l'émission caracté-ristique dîtes de Lewis-Rayleigh afterglow observable plusieurs mètres après la décharge dans un tube de petit diamètre (<1 cm). La longue distance de propagation des agents biocides est un aspect clé de l'efficacité de ce dispositif. Notre objectif est d'étudier le transport de $N(^4S)$ dans des tubes de polyuréthane couramment utilisés en milieux hos-pitaliers.

Pour la décontamination d'agents microbiologiques de guerre, une chambre de tests microbiologiques est dimensionnée pour le traitement d'objets contaminés. Les objets sont traités par les RONS produits par plasma d'air généré par une décharge Nanose-conde Répétitive Pulsée bipolaire (NRP). L'objectif est de quantifier la production de RONS par la décharge NRP et de réaliser des premiers tests microbiologiques sur sur-face. Le dernier chapitre a pour but d'étudier la possibilité de décroitre la distance entre le plasma produit par NRP et la surface. Pour cela, nous étudions la capacité des effets hydrodynamiques suivant une décharge nanoseconde à refroidir les espèces actives sans réduire la formation de NO.

E.2. Etude du transport de $N(^4S)$ dans un tube pour la décontamination d'endoscopes par une post-décharge d'azote

Dans le second chapitre, le transport de l'azote atomique dans l'état fondamental $N(^4S)$ à l'intérieur de longs tubes de polyuréthane est examinée à l'aide d'une technique basée sur la spectroscopie d'émission absolue du premier système positif de l'azote $N_2(B^3\Pi_g, v' \rightarrow A^3\Sigma_u^+, v'')$. La distribution vibrationnelle $N_2(^3\Pi_g, v')$ est mesurée à partir du fit du spectre calibré à l'aide du modèle spectroscopique hors-équilibre Specair. Le dé-séquilibre autour du $11^{\text{ème}}$ niveau vibrationnel de $N_2(^3\Pi_g)$ est typique de l'afterglow d'azote. Il est dû à la recombinaison de $N(^4S)$ produisant l'état pré-dissociatif

$N_2(a'^5\Sigma_g^+,v')$ dont la courbe potentiel coupe celle de $N_2(B^3\Pi_g,v')$ au $11^{\text{ème}}$ niveau vibrationnel, ce qui permet un transfert collisionnel intersystème (ICT) de l'excitation. En assumant un état stationnaire, l'équation bilan sur $N_2(^3\Pi_g,v'=11)$ permet d'obtenir une relation entre $[N(^4S)]^2$ et $[N_2(^3\Pi_g,v'=11)]$, mesuré par spectroscopie d'émission absolue. De plus, étant donné la symétrie cylindrique du tube dans lequel s'écoule l'afterglow, une inversion d'Abel réalisée sur les profils latéraux d'émission mesurés à différentes positions dans le tube permet de déterminer le profil spatial 3D de la densité de $N(^4S)$ à l'intérieur du tube sur plus de 60 cm.

La distribution obtenue est utilisée pour construire un modèle cinétique de la décroissance de $N(^4S)$ dans le tube. Trois réactions sont typiquement prises en compte dans les pertes de $N(^4S)$ dans l'afterglow : i/ la recombinaison avec les impuretés de O, NO ii/ la recombinaison à trois corps et iii/ la recombinaison en surface se produisant avec une probabilité γ_N. Toutefois les concentrations de O et NO sont mal connues dans notre système. De plus, la probabilité γ_N et la constante de réaction de ii/ est mal connue. L'objectif est de déterminer ces valeurs et de prédire sous quelles conditions la pureté du gaz est suffisamment haute pour négliger l'effet des impuretés de O et NO.

i/ Nous déterminons un critère permettant d'indiquer sous quelles conditions, les impuretés de O et NO sont négligeables. L'oxygène atomique est formé par la dissociation d'impuretés de dioxygène O_2 et de vapeur d'eau H_2O. L'oxygène formé se recombine rapidement avec l'azote atomique pour former les bandes de NO-beta et gamma. Le NO formé consomme alors rapidement un second atome d'azote via une réaction de titrage très connue. Ainsi on peut calculer le taux global de cette chaîne de deux réactions et le comparer avec le taux de recombinaison à trois corps pour identifier sous quelles conditions ce taux est négligeable. Une condition sur le ratio [O]/[N] peut alors être trouvée. Le ratio [O]/[N] peut être déterminé à partir de l'émission de NO-beta si la densité [N] est préalablement connue. Dans nos conditions nous avons pu montrer que le ratio satisfait le critère défini et donc que les impuretés de O et NO peuvent être négligées.

ii/ Pour déterminer le coefficient de réaction de la recombinaison à trois corps nous considérons la décroissance de $N(^4S)$ dans le volume au centre du tube. L'équation de transport de $N(^4S)$ nous permet d'identifier trois termes : diffusif, convectif et de perte (recombinaison à trois corps). L'utilisation du logiciel de CFD Fluent nous permet de confirmer que le terme diffusif est négligeable même dans nos conditions d'écoulement turbulent. Dans ce cas la solution de l'équation de transport prédit une décroissance inverse de $[N(^4S)]$ le long du tube, ce qui correspond à notre mesure. Le fit inverse de la

décroissance permet d'obtenir une valeur de la constante de recombinaison à trois corps : k=7.7×10^{-33} cm^6.s^{-1}

iii/ La recombinaison en surface a été considérée en prenant la valeur moyennée sur une section de tube de la densité de N(^{4}S). Dans ce cas l'expression décrivant la décroissance de N(^{4}S) prend en compte un terme de perte hétérogène incluant la probabilité de recombinaison en surface qui a été choisi comme paramètre de fit pour modéliser la décroissance mesurée de N(^{4}S) : γ_N =7.7×10^{-5}

Le modèle ainsi construit de la décroissance de N(^{4}S) dans le tube de polyuréthane peut servir de première pierre pour prédire la longueur de tube décontaminée par l'afterglow d'azote. Nous cherchons à donner une illustration de cette possibilité. Pour cela, nous nous servons des résultats de Limam et al. [170] qui montrent que *E. Coli* peut être réduit de 12 log en 145 min sur du quartz si une concentration [N(^{4}S)]=5×10^{13} cm^{-3} est obtenue. Ainsi, une réduction minimale de 12 log est attendue en 145 min dans la section du tube où la densité de [N(^{4}S)] est au moins égale à 5×10^{13} cm^{-3}. Ainsi, nous pouvons déterminer la longueur de tube décontaminée, et vérifier l'influence de divers paramètres tels que la probabilité de recombinaison en surface, le diamètre du tube, ainsi que la densité initiale de N(^{4}S) sur la longueur de tube décontaminée. Cette approche peut être utilisée pour évaluer la capacité de décontamination de la post-décharge d'azote pour une application donnée, et pour ajuster la stratégie de décontamination.

Enfin nous décrivons une méthode alternative basée sur la spectroscopie d'émission relative pour déterminer la concentration de N(^{4}S) à l'intérieur d'un tube. Celle-ci est basée sur l'enregistrement de l'émission du premier système positif de N$_2$ le long du tube. Si la décroissance de N(^{4}S) est uniquement due à la recombinaison à trois corps (ce qui peut être vérifié a posteriori à partir de l'émission de NO-beta, et en choisissant un tube en verre dont la probabilité de recombinaison en surface est connue pour être faible), et si le coefficient de recombinaison à trois corps est connu, il est possible de déterminer une constante de calibration du système optique qui peut être utilisée pour déterminer simplement la concentration de N(^{4}S) dans le tube.

E.3. Quantification et efficacité biocide des RONS produits par une décharge nanoseconde répétitive pulsée dans l'air

Dans le troisième chapitre, la production de NO, NO$_2$ et O$_3$ par une décharge NRP placée à l'intérieur d'une enceinte est mesurée par spectroscopie d'absorption par laser

à cascade quantique (QCLAS) moyen infrarouge (NO), et spectroscopie d'absorption UV large bande (O_3). La mesure QCLAS est réalisée dans une cellule multi-passage de type White permettant d'augmenter significativement la longueur d'absorption (2 m) et donc la sensibilité de la mesure. Un autre avantage de la mesure QCLAS est la grande sélectivité de l'absorption due à la finesse spectrale du laser à cascade quantique ($\Delta\nu$=0.006 cm^{-1}). Concernant la mesure UV, le principal avantage est la sensibilité de la mesure due aux fortes sections efficaces d'absorption de NO_2 et de O_3 dans la gamme 250-500 nm. Il faut toutefois considérer un possible recouvrement d'absorption de différentes espèces, en particulier les espèces hydrogénées et les états d'oxydation élevés de NO. Dans nos conditions l'air est sec, il n'y a donc pas d'interférences avec les espèces hydrogénées. Les spectres d'absorbance sont précisément fittés en considérant uniquement NO_2 et O_3 comme étant les principales espèces absorbantes.

Les résultats d'une étude paramétrique indiquent deux régimes de production des RONS par la décharge NRP : une à basse fréquence produisant des concentrations importantes d'ozone (O_3) et une à haute fréquence produisant des concentrations importantes d'oxydes d'azote (NO, NO_2). Cette transition entre les deux régimes implique d'abord une chute rapide de la concentration d'ozone puis à une montée progressive des concentrations des oxydes d'azote à mesure que la fréquence est augmentée. Cette transition est due à une combinaison de deux mécanismes : i/ la dissociation thermique de l'ozone dont l'importance est prédominante à T>500 K, ii/ à l'effet d' « empoisonnement » de la décharge correspondant à la formation et à l'oxydation par l'ozone des oxydes d'azote générés par le plasma. Cette transition se produit à une densité d'énergie d'environ 40 J/L. Pour comprendre quelle est la part des deux mécanismes dans la transition du régime O_3 au régime NO_x il est nécessaire de connaitre les mécanismes de formation de NO dans une décharge plasma. Or, ceux-ci sont encore très discutés de nos jours. C'est dans l'optique de mieux comprendre la contribution des états électroniques excités produits par le plasma à la formation de NO que nous avons développé une méthode de QCLAS de NO avec une résolution temporelle de 10 ns dont le principe est décrit et testé dans une cellule de référence puis dans la décharge spark dans l'appendice C.

La capacité de la décharge NRP à produire NO, NO_2 et O_3 en modifiant seulement deux paramètres (débit d'air et fréquence) est une caractéristique unique du système étudié. L'étude paramétrique a été complétée avec une étude du coût énergétique de production des RONS. Cette étude montre que la source NRP est capable de produire des concentrations de ces espèces à des coûts énergétiques comparables aux sources plasmas les plus efficaces comme le plasmatron pour les NO_x ou la décharge couronne pour O_3.

La capacité de ce système à produire différents type de RONS peut être utilisée pour étudier de nouvelles approches de décontamination. Ici, nous avons proposé une stratégie basée sur l'exposition des microbes à une alternance de régime à forte concentration de NO_x et de régime à forte concentration de O_3. Les résultats préliminaires indiquent que l'alternance des régimes permet d'atteindre des niveaux d'inactivation plus importants sur l'ensemble des microorganismes testés que dans le cas de l'exposition à des NO_x uniquement. Des travaux devront être réalisés pour confirmer l'efficacité du régime d'alternance et pour en comprendre les mécanismes.

E.4. Etude des effets de la recirculation du gaz dans une décharge NRP sur la température du gaz et la concentration de NO par QCLAS résolue temporellement et PLIF

Le quatrième chapitre vise à proposer une méthode d'optimisation de la décontamination de surface par la NRP. La stratégie envisagée est de réduire la distance entre la surface traitée et le plasma afin d'augmenter la concentration de RONS et donc l'efficacité biocide. Cependant, la décharge chauffant le gaz à plus de 1000 K, une importante dégradation de la surface est attendue si le matériau est thermosensible et s'il est placé trop près de la décharge. Aussi, nous étudions les effets hydrodynamiques suivants une décharge nanoseconde dans l'espoir qu'ils puissent servir à refroidir plus rapidement les espèces actives sans affecter l'efficacité de production des RONS par la NRP.

Les effets hydrodynamiques observés sont les suivants. D'abord une onde de choc est générée suite à la surpression provoquée par l'intense et brutal dégagement de chaleur durant la décharge nanoseconde. Il s'ensuit une expansion des espèces actives dans un volume cylindrique entre les deux électrodes en pointe entre lesquelles le plasma est généré. Si les gradients de température entre le kernel et le gaz alentour est suffisamment important, une recirculation du gaz frais alentour peut s'effectuer à partir du côté des électrodes vers le centre du gap inter-électrodes. A ce moment, les espèces actives se concentrent dans un tore en expansion radiale. Cet effet a d'abord été constaté dans une décharge mono-impulsionelle nanoseconde dans l'air ambiant statique par Schlieren et fluorescence planaire induite par laser (PLIF) de OH.

Afin de voir si la recirculation de gaz peut également être observée dans un régime impulsionnel répétitif, nous avons mis au point une mesure de NO par PLIF qui permet d'avoir une image de la distribution de NO dans une section du gap inter-électrodes.

Nous avons ensuite réalisé une étude paramétrique afin de voir dans quelles conditions la recirculation du gaz peut être observée. Les séquences d'images PLIF obtenues indiquent qu'à hautes fréquences (F>2 KHz dans nos conditions), la recirculation n'a pas lieu, certainement en raison des trop faibles gradients de température entre les espèces actives et le gaz environnant, due à un renouvellement du gaz frais trop peu important. A F=1 kHz, la recirculation est observée et commence 40 à 100 µs après la décharge selon l'énergie déposée dans le plasma. Une analyse des images PLIF permet de montrer que la vitesse d'expansion radiale du tore contenant les espèces actives augmente linéairement avec l'énergie déposée dans le plasma. Nous avons isolé trois cas de recirculation : un où la recirculation n'est pas observée, un ou la recirculation ne commence qu'à 100 µs après la décharge, et un où la recirculation commence dès 40 µs après la décharge. L'objectif est de déterminer l'évolution de la concentration de NO et de la température du gaz dans ces trois régimes de recirculation.

Pour cette étude, nous avons mis au point un diagnostic de spectroscopie d'absorption par laser à cascade quantique (QCLAS) résolu en temps (100 ns de résolution temporelle). La méthode de mesure a d'abord été validée sur une cellule de référence contenant un mélange NO/He connu à pression proche atmosphérique. Afin d'améliorer la sensibilité trois transitions de NO ont été scannées entre 1900 et 1900.7 cm^{-1}. Un fit de cette région spectral utilisant la base de données HITEMP permet de déterminer la température et la concentration de NO. La longueur d'absorption a été déterminée à partir des images de PIF. Des analyses d'erreurs sur la détermination de la longueur d'absorption par la PLIF, et sur la qualité des fits basés sur HITEMP sont données dans l'appendice B. Les mesures indiquent que la température du gaz décroit fortement en raison de la recirculation de gaz. Un taux maximum de refroidissement de 12K/µs est mesuré, ce qui correspond à une décroissance de la température du gaz de 1400 à 700 K en 60 µs, ce qui indique que la recirculation du gaz est capable de refroidir rapidement la température des espèces actives produites par la décharge NRP. Concernant la production de NO, les premières analyses indiquent que la densité de NO moyennées sur le volume des espèces actives décroit en raison de la recirculation. La baisse de la densité est en réalité due à une dilution de NO avec l'air ambiant en raison de la recirculation. Il est possible de corriger cet effet dans nos analyses en calculant le nombre de molécules présentes dans une section du volume des espèces actives. Cette précaution permet de montrer que la recirculation n'affecte pas le nombre de molécules de NO produites en sortie de la décharge NRP. Par conséquent, la mesure QCLAS permet de confirmer que la recirculation du gaz permet de refroidir significativement la température du gaz sans affecter le nombre de molécules de NO formées.

E.5. Conclusions

Le but de cette thèse était d'étudier la production et le transport des espèces réactives à base d'oxygène et d'azote (RONS) générés par des décharges impulsionnelles dans l'azote et l'air à pression atmosphérique pour la décontamination de tubes et autres surfaces.

Dans le premier chapitre, une revue de l'inactivation de bio-indicateurs communément utilisés montre que les différents plasmas froids évalués sont au moins aussi efficaces que les techniques de décontamination standards à basse température sur de nombreux types de surfaces. Cependant, la décontamination par plama à pression atmosphérique est limitée par le faible volume/surface accessible aux agents biocides générés. Les RONS produits par plasma peuvent être transportés en dehors de la zone plasma et donc traiter possiblement des surfaces plus importantes. Cette approche a motivé les études réalisées dans le cadre de cette thèse sur la production de RONS par des décharges pulsées.

Dans le second chapitre le transport de l'azote à l'état fondamental N(^{4}S) a été étudié dans un écoulement afterglow d'une décharge d'azote pure à pression atmosphérique. Dans ce système, l'azote atomique biocide est transporté sur de longues distances, ce qui permet de traiter la surface interne de longs tubes. Cependant les mécanismes de perte de N(^{4}S) à l'intérieur d'un tube sont complexes et imprécis. Dans cette thèse la distribution 3D de N(^{4}S) à l'intérieur du tube a été mesurée au moyen d'une technique de spectroscopie d'émission quantitative (calibration absolue) combinée à une inversion d'Abel. Ces données nous ont permis d'évaluer des constantes nécessaires pour construire un modèle cinétique de la décroissance de N(^{4}S) dans l'afterglow. En particulier nous avons donné un critère permettant de vérifier si les impuretés de O et NO influencent la décroissance de N(^{4}S) ainsi qu'une technique de mesure permettant de vérifier ce critère. A partir de l'étude de la décroissance volumique de N(^{4}S), nous avons pu déterminer une valeur pour le coefficient de recombinaison à trois corps de N(^{4}S) : k=7.7×10^{-33} cm^6.s^{-1}. Cette valeur est confirmée sur divers sets de données de N(^{4}S) dans l'afterglow. Nous avons déterminé également la probabilité de recombinaison sur la surface de polyuréthane γ_N =7.7×10^{-5} à partir de la décroissance de N(^{4}S) moyennée sur une section du tube. Une méthode alternative de mesure de N(^{4}S) basée sur de la spectroscopie d'émission relative a également été démontrée et discutée. Enfin, le modèle de recombinaison de N(^{4}S) a été utilisée pour déterminer la longueur de tube décontaminée par l'afterglow d'azote.

Dans le troisième chapitre, nous avons réalisé une étude paramétrique sur la production d'ozone, et d'oxydes d'azotes par une décharge NRP par spectroscopie d'absorption UV et spectroscopie d'absorption par laser à cascade quantique (QCLAS). Deux régimes de production de RONS ont été identifiés : mode O_3 à faible fréquence, et mode NO_x à haute fréquence. Les RONS produits par ce système sont produits à un coût énergétique faible comparé aux autres sources plasmas. Les mécanismes à l'origine de la transition entre les deux modes de production des RONS sont également discutés. Des tests microbiologiques révèlent l'efficacité biocide des RONS générés. En particulier l'exposition des microbes à une alternance de mode O_3 et NO_x montre une efficacité intéressante qui doit encore être confirmée.

Dans le quatrième chapitre, nous étudions la possibilité de réduire la distance entre le plasma et la surface traitée avec une NRP dans l'air. Nous focalisons notre étude sur les effets hydrodynamiques suivant une décharge nanoseconde afin de voir s'ils permettraient de réduire la température des espèces entrant en contact avec la surface traitée. Dans un premier temps des images PLIF montrent que les effets hydrodynamiques de recirculation du gas alentours entre les électrodes ne sont observés qu'à relativement basse fréquence et haute énergie. Des mesures QCLAS résolues en temps de NO et de la température du gaz montrent que le gaz est fortement refroidi par l'effet de recirculation (taux de refroidissement maximum de 12 K/µs) sans que le nombre de molécules de NO formées n'en soit affecté.

Lexicon on bio-decontamination

<u>Aerobic</u>**:** microorganism requiring oxygen for growth

<u>Biofilm</u>**:** structure of cells (possibly of different nature) aggregated on a surface. Compared to isolated microorganisms, i.e. planktonic state, biofilms are resistant because of their thickness and inter-cell communications.

<u>Biological indicator (BI)</u>**:** microorganism (usually bacterial spores) used as a reference to assess the efficiency of a sterilizer. It is the most resistant microorganism to a given sterilization technique, e.g. *B. Pumilus* for e-beam radiation, *B. Atrophaeus* for dry heat and ethylene oxide, *G. Stearothermophilius* for steam heat and hydrogen peroxide.

<u>Chitin</u>**:** fibrous substance made of polysaccharides, it is the main component of the cell wall of fungi

<u>Cleaning</u>: physical removal of body material, dust or foreign material from a surface.

<u>Denaturation</u>**:** change of the conformation of some key proteins involved in mechanisms necessary for cell survival

<u>Disinfectant</u>; chemical agent capable of killing microorganisms except bacterial spores

<u>Eukaryote</u>: unicellular organism containing a nucleus.

<u>Fungi</u>: one of the kingdoms of microorganisms

<u>Lipopolysaccharide (LPS)</u>: a compound of Gram negative bacteria cell wall.

<u>Mold</u>: type of multicellular fungi, e.g. A. Niger. Mold can be either in a sporulate or vegetative form.

<u>Mycobacteria</u>: type of Gram positive bacteria containing mycolic acid in their cell wall

<u>Peptidoglycan</u>: polymer composed of sugar and amino acids, forming a mesh-like barrier in the cell walls of bacteria

<u>Protein</u>: large molecules composed of amino acids

<u>Prokaryote</u>: unicellular organism that lacks a membrane-bound nucleus.

Pyrogens: toxic substances released by bacteria during cell lysis, e.g. lipopolysaccharides in Gram negative bacteria and lipoteichoic acid in Gram positive bacteria. Pyrogens can induce fever and septic shock in case of contact with blood.

Safety/Sterility assurance level (SAL): probability that at least one viable microorganism survived to a sterilization cycle.

Sterilization: complete removal or destruction of microorganisms, including bacterial spores.

Yeast: type of unicellular fungi, e.g. *Candida Albicans.*

Acronyms

<u>BSA</u>: bovine serum albumin

<u>CCP</u>: capacitively coupled plasma

<u>CDBD</u>: cascaded dielectric barrier discharge

<u>EtO</u>: Ethylene Oxide

<u>HCFC</u>: hydrochlorofluorocarbon

<u>ICP</u>: inductively coupled plasma

<u>LIF</u>: laser induced fluorescence

<u>LPS</u>: lipopolysaccharide

<u>MBMS</u>: molecular beam mass spectrometry

<u>MHC</u>: micro-hollow cathode

<u>MW</u>: microwave

<u>mM/nM</u>: milli/nano-mole per liter

<u>NRP</u>: nanosecond repetitively pulsed discharge

<u>PET</u>: polyethylene terephthalate

<u>PRF</u>: pulses repetition frequency

<u>PTFE</u>: Teflon (polytetrafluoroethylene–$(CF_2\text{-}CF_2)_n$-)

<u>ppm</u>: parts per million

<u>QCLAS</u>: tunable diode laser absorption spectroscopy

<u>RF</u>: log-reduction factor

<u>RF-APPJ</u>: radio frequency atmospheric pressure plasma jet

<u>RH</u>: relative humidity

<u>RONS</u>: reactive oxygen and nitrogen species

<u>SMD</u>: surface micro-discharge

<u>SAL</u>: safety/sterility assurance level

<u>slpm</u>: standard liters per minute

<u>TDLAS</u>: tunable diode laser absorption spectroscopy

References

[1] World Health Organization., "Decontamination and Reprocessing of Medical Devices for Health-care Facilities," pp. 1–120, 2016.

[2] M. E. Flanagan, C. A. Welsh, C. Kiess, S. Hoke, and B. N. Doebbeling, "A national collaborative for reducing health care-associated infections: Current initiatives, challenges, and opportunities," *Am. J. Infect. Control*, vol. 39, no. 8, pp. 685–689, 2011.

[3] M. Ruddy and C. C. Kibbler, "Endoscopic decontamination: An audit and practical review," *J. Hosp. Infect.*, vol. 50, no. 4, pp. 261–268, 2002.

[4] D. H. Spach, F. E. Silverstein, and W. E. Stamm, "Transmission of infection by flexible gastrointestinal endoscopy and bronchoscopy.," *Ann. Intern. Med.*, vol. 118, pp. 117–128, 1993.

[5] W. A. Rutala and D. J. Weber, "Reprocessing endoscopes: United States perspective," *J. Hosp. Infect.*, vol. 56, no. SUPPL. 2, 2004.

[6] N. S. Chu, D. Mcalister, and P. A. Antonoplos, "Natural bioburden levels detected on flexible gastrointestinal endoscopes after clinical use and manual cleaning," pp. 137–142, 1974.

[7] W. A. Rutala and D. J. Weber, "Guideline for disinfection and sterilization in healthcare facilities, 2008.," 2008.

[8] A. H. C. Uttley and R. A. Simpson, "Audit of bronchoscope disinfection : a survey of procedures in England and Wales and incidents of mycobacterial contamination," vol. 26, pp. 301–308, 1994.

[9] S. Park, J. Y. Jang, J. S. Koo, J. B. Park, Y. J. Lim, S. J. Hong, S. W. Kim, and H. J. Chun, "A review of current disinfectants for gastrointestinal endoscopic reprocessing," *Clin. Endosc.*, vol. 46, no. 4, pp. 337–341, 2013.

[10] J. W. Bradley, "Technology Moving Forward - Plasma for the Food Industry."

[11]   P. J. Fellows, *Food Processing Technology*, CRC Press. Woodhead Publishing Limited, 1988.

[12]   World Health Organization., "WHO estimates of the global burden of diseases," 2015.

[13]   M. Z. Jeddi, M. Yunesian, M. E. haghi Gorji, N. Noori, M. R. Pourmand, and G. R. J. Khaniki, "Microbial evaluation of fresh, minimally-processed vegetables and bagged sprouts from chain supermarkets," *J. Heal. Popul. Nutr.*, vol. 32, no. 3, pp. 391–399, 2014.

[14]   J. D. Rummel, "Planetary protection policy overview and application to future missions," *Adv. Sp. Res.*, vol. 9, no. 6, pp. 181–184, 1989.

[15]   "Cole   Parmer."   [Online].   Available: https://www.mathesongas.com/pdfs/products/Materials-Compatibility-Guide.pdf.

[16]   International atomic Energy Agency, "Guidelines for industrial radiation sterilization of disposable medical products," Vienna, 1990.

[17]   L. Hall-Stoodley, J. W. Costerton, and P. Stoodley, "Bacterial biofilms: from the Natural environment to infectious diseases," *Nat. Rev. Microbiol.*, vol. 2, no. 2, pp. 95–108, 2004.

[18]   K. Lewis, "Persister cells, dormancy and infectious disease," *Nat. Rev. Microbiol.*, vol. 5, no. 1, pp. 48–56, 2007.

[19]   Z. Kovalova, "Bio-decontamination of biofilms on surfaces by cold plasma," Université Paris Saclay, 2016.

[20]   E. Hernández-Jiménez, R. del Campo, V. Toledano, M. T. Vallejo-Cremades, A. Muñoz, C. Largo, F. Arnalich, F. García-Rio, C. Cubillos-Zapata, and E. López-Collazo, "Biofilm vs. planktonic bacterial mode of growth: Which do human macrophages prefer?," *Biochem. Biophys. Res. Commun.*, vol. 441, no. 4, pp. 947–952, 2013.

[21]   G. J. Tortora, B. R. Funke, and C. L. Case, *Microbiology: an introduction.* 2010.

[22]   M. Salton and K. KS., "Structure," in *Medical microbiology*, 4th editio., S. Baron, Ed. 1996, p. chapter 2.

[23]   J. Hanuš, T. Steinhartová, O. Kylián, and H. Biederman, "Plasma post-treatment of Cu/a-C:H nanocomposite thin films," in *International Symposium on Plasma Chemisty, 22*, 2015.

[24]   E. Sysolyatina, A. Mukhachev, M. Yurova, M. Grushin, V. Karalnik, A. Petryakov, N. Trushkin, S. Ermolaeva, and Y. Akishev, "Role of the charged particles in bacteria inactivation by plasma of a positive and negative corona in ambient air," *Plasma Process. Polym.*, vol. 11, no. 4, pp. 315–334, 2014.

[25]   A. Mahfoudh, "Étude des mécanismes d 'inactivation des microorganismes suite à un traitement à l'ozone," 2009.

[26]   M. J. Leggett, G. Mcdonnell, S. P. Denyer, P. Setlow, and J. Y. Maillard, "Bacterial spore structures and their protective role in biocide resistance," *J. Appl. Microbiol.*, vol. 113, no. 3, pp. 485–498, 2012.

[27]   P. Setlow, "Spores of Bacillus subtilis: Their resistance to and killing by radiation, heat and chemicals," *J. Appl. Microbiol.*, vol. 101, no. 3, pp. 514–525, 2006.

[28]   M. Faller, M. Niederweis, and G. E. Schulz, "The Structure of a Mycobacterial Outer-Membrane Channel," *Science (80-.).*, vol. 1189, p. 1189, 2004.

[29]   Z. Bohrerova and K. G. Linden, "Assessment of DNA damage and repair in Mycobacterium terrae after exposure to UV irradiation," *J. Appl. Microbiol.*, vol. 101, no. 5, pp. 995–1001, 2006.

[30]   J. Peccia and M. Hernandez, "UV-induced inactivation rates for airborne Mycobacterium bovis BCG.," *J. Occup. Environ. Hyg.*, vol. 1, no. 7, pp. 430–5, 2004.

[31]   G. Avramidis, B. St??we, R. Wascher, M. Bellmann, S. Wieneke, A. von

Tiedemann, and W. Vi??l, "Fungicidal effects of an atmospheric pressure gas discharge and degradation mechanisms," *Surf. Coatings Technol.*, vol. 205, no. SUPPL. 1, pp. S405–S408, 2010.

[32] S. S. Magill, J. R. Edwards, W. Bamberg, Z. G. Beldavs, G. Dumyati, M. A. Kainer, R. Lynfield, M. Maloney, L. McAllister-Hollod, J. Nadle, S. M. Ray, D. L. Thompson, L. E. Wilson, and S. K. Fridkin, "Multistate Point-Prevalence Survey of Health Care–Associated Infections," *N. Engl. J. Med.*, vol. 370, no. 13, pp. 1198–1208, 2014.

[33] J. P. Latgé, "The cell wall: A carbohydrate armour for the fungal cell," *Mol. Microbiol.*, vol. 66, no. 2, pp. 279–290, 2007.

[34] S. S. Gonçalves, A. C. R. Souza, A. Chowdhary, J. F. Meis, and A. L. Colombo, "Epidemiology and molecular mechanisms of antifungal resistance in Candida and Aspergillus," *Mycoses*, vol. 59, no. 4, pp. 198–219, 2016.

[35] Z. A. Kanafani and J. R. Perfect, "Resistance to Antifungal Agents: Mechanisms and Clinical Impact," *Clin. Infect. Dis.*, vol. 46, no. 1, pp. 120–128, 2008.

[36] G. Mc Donnell and A. D. Russell, "Antiseptics and disinfectants: Activity, action, and resistance," *Clin. Microbiol. Rev.*, vol. 12, no. 1, pp. 147–179, 1999.

[37] H. Shintani, "Current Mistaken Interpretation of Microbiological Data on Gas Plasma Sterilization," *Pharm. Regul. Aff.*, vol. 4, no. 2, p. 1000138, 2015.

[38] T. Von Woedtke, A. Kramer, and K. Weltmann, "Plasma Sterilization : What are the Conditions to Meet this Claim ?," pp. 534–539.

[39] J. Ehlbeck, U. Schnabel, M. Polak, J. Winter, T. von Woedtke, R. Brandenburg, T. von dem Hagen, and K.-D. Weltmann, "Low temperature atmospheric pressure plasma sources for microbial decontamination," *J. Phys. D. Appl. Phys.*, vol. 44, no. 1, p. 13002, Jan. 2011.

[40] M. Moisan, J. Barbeau, S. Moreau, J. Pelletier, M. Tabrizian, and L. Yahia, "Low-temperature sterlization using gas plasmas: a review of the experiment and an analysis of the inactivation mechanisms," *Int. J. Pharm.*, vol. 226, pp.

1–21, 2001.

[41] M. K. Boudam, M. Moisan, B. Saoudi, C. Popovici, N. Gherardi, and F. Massines, "Bacterial spore inactivation by atmospheric-pressure plasmas in the presence or absence of UV photons as obtained with the same gas mixture," *J. Phys. D. Appl. Phys.*, vol. 39, no. 16, pp. 3494–3507, Aug. 2006.

[42] A.-M. Pointu, A. Ricard, E. Odic, and M. Ganciu, "Nitrogen Atmospheric Pressure Post Discharges for Surface Biological Decontamination inside Small Diameter Tubes," *Plasma Process. Polym.*, vol. 5, no. 6, pp. 559–568, Aug. 2008.

[43] K. Becker, A. Koutsospyros, S. Yin, and C. Christodoulatos, "Environmental and biological applications of microplasmas," vol. 513, 2005.

[44] T. Von Woedtke and W. Ju, "Sterilization of enzyme glucose sensors : problems and concepts," vol. 17, pp. 373–382, 2002.

[45] P. Muranyi, J. Wunderlich, and M. Heise, "Sterilization efficiency of a cascaded dielectric barrier discharge.," *J. Appl. Microbiol.*, vol. 103, no. 5, pp. 1535–44, Nov. 2007.

[46] M. Raguse, M. Fiebrandt, K. Stapelmann, K. Madela, M. Laue, J.-W. Lackmann, J. E. Thwaite, P. Setlow, P. Awakowicz, and R. Moeller, "Improvement of biological indicators by using standardized Bacillus subtilis spore monolayers for the evaluation of study of enhanced spore decontamination technologies," *Appl. Environ. Microbiol.*, vol. 82, no. January, pp. 2031–2038, 2016.

[47] Y. P. Raizer, *Gas discharge physics*, Springer. Berlin, 1991.

[48] C. Tendero, C. Tixier, P. Tristant, J. Desmaison, and P. Leprince, "Atmospheric pressure plasmas: A review," *Spectrochim. Acta Part B At. Spectrosc.*, vol. 61, no. 1, pp. 2–30, Jan. 2006.

[49] P. Bruggeman and R. Brandenburg, "Atmospheric pressure discharge filaments and microplasmas: physics, chemistry and diagnostics," *J. Phys. D. Appl. Phys.*, vol. 46, no. 46, p. 464001, Nov. 2013.

[50] G. J. M. Hagelaar and L. C. Pitchford, "Solving the Boltzmann equation to obtain electron transport coefficients and rate coefficients for fluid models," *Plasma Sources Sci. Technol.*, vol. 14, no. 4, pp. 722–733, 2005.

[51] "Phelps database." [Online]. Available: www.lxcat.net.

[52] "Morgan database." [Online]. Available: www.lxcat.net.

[53] A. Bogaerts, E. Neyts, R. Gijbels, and J. Van der Mullen, "Gas discharge plasmas and their applications," *Spectrochim. Acta - Part B At. Spectrosc.*, vol. 57, no. 4, pp. 609–658, 2002.

[54] L. Ling, J. Jiafeng, L. Jiangang, S. Minchong, H. Xin, S. Hanliang, and D. Yuanhua, "Effects of cold plasma treatment on seed germination and seedling growth of soybean," *Sci. Rep.*, vol. 4, no. 1, p. 5859, 2014.

[55] A. B. Shekhter, V. a Serezhenkov, T. G. Rudenko, A. V Pekshev, and A. F. Vanin, "Beneficial effect of gaseous nitric oxide on the healing of skin wounds," *Nitric Oxide*, vol. 12, no. 4, pp. 210–9, Jun. 2005.

[56] S. J. Kim and T. H. Chung, "Cold atmospheric plasma jet-generated RONS and their selective effects on normal and carcinoma cells," *Sci. Rep.*, vol. 6, no. 1, p. 20332, 2016.

[57] M. G. Kong, G. Kroesen, G. Morfill, T. Nosenko, T. Shimizu, J. Van Dijk, and J. L. Zimmermann, "Plasma medicine: An introductory review," *New J. Phys.*, vol. 11, 2009.

[58] F. Rossi, R. De Mitri, S. Bobin, and R. Eloy, "Plasma Sterilisation : Mechanisms Overview and Influence of Discharge Parameters," in *Plasma Processes and Polymers*, Wiley-VCH., C. O. and M. R. W. R. d'Agostino, P. Favia, Ed. 2005.

[59] K. Stapelmann, M. Fiebrandt, M. Raguse, P. Awakowicz, G. Reitz, and R. Moeller, "Utilization of Low-Pressure Plasma to Inactivate Bacterial Spores on Stainless Steel Screws," *Astrobiology*, vol. 13, no. 7, pp. 597–606, 2013.

[60] H. Halfmann, N. Bibinov, J. Wunderlich, and P. Awakowicz, "A double inductively coupled plasma for sterilization of medical devices," *J. Phys. D. Appl. Phys.*, vol. 40, no. 14, pp. 4145–4154, 2007.

[61] F. Rossi, O. Kylián, and M. Hasiwa, "Decontamination of surfaces by low pressure plasma discharges," *Plasma Process. Polym.*, vol. 3, no. 6–7, pp. 431–442, 2006.

[62] T. P. Coohill and J. L. Sagripanti, "Overview of the inactivation by 254 nm ultraviolet radiation of bacteria with particular relevance to biodefense," *Photochem. Photobiol.*, vol. 84, no. 5, pp. 1084–1090, 2008.

[63] G. Chevrefils, É. Caron, H. Wright, G. Sakamoto, P. Payment, B. Barbeau, and B. Cairns, "UV Dose Required to Achieve Incremental Log Inactivation of Bacteria , Protozoa and Viruses," *IUVA News*, vol. 8, no. 1, pp. 38–45, 2006.

[64] D. Irving, D. A. Lamprou, M. Maclean, S. J. MacGregor, J. G. Anderson, and M. H. Grant, "A comparison study of the degradative effects and safety implications of UVC and 405 nm germicidal light sources for endoscope storage," *Polym. Degrad. Stab.*, vol. 133, pp. 249–254, 2016.

[65] S. Lerouge, A. C. Fozza, M. R. Wertheimer, R. Marchand, and L. Yahia, "Sterilization by low-pressure plasma: the role of vacuum-ultraviolet radiation," *Plasmas Polym.*, vol. 5, no. 1, pp. 31–46, 2000.

[66] M. Laroussi and F. Leipold, "Evaluation of the roles of reactive species, heat, and UV radiation in the inactivation of bacterial cells by air plasmas at atmospheric pressure," *Int. J. Mass Spectro.*, vol. 233, pp. 81–86, 2004.

[67] M. Laroussi and F. Leipold, "Evaluation of the roles of reactive species, heat, and UV radiation in the inactivation of bacterial cells by air plasmas at atmospheric pressure," *Int. J. Mass Spectrom.*, vol. 233, no. 1–3, pp. 81–86, Apr. 2004.

[68] M. Mols, H. Mastwijk, M. Nierop Groot, and T. Abee, "Physiological and transcriptional response of Bacillus cereus treated with low-temperature nitrogen gas plasma.," *J. Appl. Microbiol.*, vol. 115, no. 3, pp. 689–702, Sep. 2013.

[69] H. van Bokhorst-van de Veen, H. Xie, E. Esveld, T. Abee, H. Mastwijk, and M. Nierop Groot, "Inactivation of chemical and heat-resistant spores of Bacillus and Geobacillus by nitrogen cold atmospheric plasma evokes distinct changes in morphology and integrity of spores," *Food Microbiol.*, vol. 45, pp. 26–33, 2015.

[70] T. von Woedtke, S. Reuter, K. Masur, and K.-D. Weltmann, "Plasmas for medicine," *Phys. Rep.*, vol. 530, no. 4, pp. 291–320, Sep. 2013.

[71] T. Lai, B. Li, G. Qin, and S. Tian, "Oxidative damage involves in the inhibitory effect of nitric oxide on spore germination of penicillium expansum," *Curr. Microbiol.*, vol. 62, no. 1, pp. 229–234, 2011.

[72] D. B. Graves, "The emerging role of reactive oxygen and nitrogen species in redox biology and some implications for plasma applications to medicine and biology," *J. Phys. D. Appl. Phys.*, vol. 45, no. 26, p. 263001, Jul. 2012.

[73] O. Lunov, V. Zablotskii, O. Churpita, A. Jäger, L. Polivka, E. Sykova, A. Dejneka, and S. Kubinova, "The interplay between biological and physical scenarios of bacterial death induced by non-thermal plasma," *Biomaterials*, vol. 82, pp. 71–83, 2016.

[74] S.-H. Hong, E. J. Szili, A. Toby, A. Jenkins, and R. D. Short, "Ionized gas (plasma) delivery of reactive oxygen species (ROS) into artificial cells," *J. Phys. D Appl. Phys.*, vol. 47, p. 362001, 2014.

[75] E. J. Szili, S. Hong, and R. D. Short, "On the effect of serum on the transport of reactive oxygen species across phospholipid membranes," *Biointerphases*, vol. 10, p. 29511, 2015.

[76] E. J. Szili, J. W. Bradley, and R. D. Short, "A 'tissue model' to study the plasma delivery of reactive oxygen species," *J. Phys. D. Appl. Phys.*, vol. 47, no. 15, p. 152002, Apr. 2014.

[77] H. Yasuda, M. Hashimoto, M. Rahman, K. Takashima, and A. Mizuno, "States of Biological Components in Bacteria and Bacteriophages during Inactivation by Atmospheric Dielectric Barrier Discharges," pp. 615–621, 2008.

[78] M. Repetto, J. Semprine, and A. Boveris, "Lipid peroxidation: Chemical

mechanism, biological implications and analytical determination," *Lipid Peroxidation*, pp. 3–30, 2012.

[79] L. Han, S. Patil, D. Boehm, V. Milosavljević, P. J. Cullen, and P. Bourke, "Mechanisms of inactivation by high-voltage atmospheric cold plasma differ for Escherichia coli and Staphylococcus aureus," *Appl. Environ. Microbiol.*, vol. 82, no. 2, pp. 450–458, 2016.

[80] E. Bermúdez, S.-F. Ferng, C. E. Castro, and M. G. Mustafa, "DNA Strand Breaks Caused by Exposure to Ozone and Nitrogen Dioxide," *Environ. Res. Sect. A*, vol. 81, pp. 72–80, 1999.

[81] C. Chen, S. W. Smye, M. P. Robinson, and J. A. Evans, "Membrane electroporation theories: A review," *Med. Biol. Eng. Comput.*, vol. 44, no. 1–2, pp. 5–14, 2006.

[82] Y. Yonemoto, T. Yamashita, M. Muraji, W. Tatebe, H. Ooshima, J. Kato, A. Kimura, and K. Murata, "Resistance of yeast and bacterial spores to high voltage electric pulses," *J. Ferment. Bioeng.*, vol. 75, no. 2, pp. 99–102, 1993.

[83] F. Pillet, C. Formosa-Dague, H. Baaziz, E. Dague, and M.-P. Rols, "Cell wall as a target for bacteria inactivation by pulsed electric fields," *Sci. Rep.*, vol. 6, no. February, p. 19778, 2016.

[84] V. Heinz, S. T. Phillips, M. Zenker, and D. Knorr, "Inactivation of Bacillus subtilis by high intensity pulsed electric fields under close to isothermal conditions," *Food Biotechnol.*, vol. 13, no. 2, pp. 155–168, 1999.

[85] T. Grahl and H. Märkl, "Killing of micro-organisms by pulsed electric fields. Applied Microbiology and Biotechnology," *Appl. Microbiol. Biotechnol.*, vol. 45, pp. 148–157, 1996.

[86] K. Reineke, F. Schottroff, N. Meneses, and D. Knorr, "Sterilization of liquid foods by pulsed electric fields-an innovative ultra-high temperature process," *Front. Microbiol.*, vol. 6, pp. 1–11, 2015.

[87] S. Toepfl, A. Mathys, V. Heinz, and D. Knorr, "Review: Potential of High Hydrostatic Pressure and Pulsed Electric Fields for Energy Efficient and

Environmentally Friendly Food Processing," *Food Rev. Int.*, vol. 22, no. 4, pp. 405–423, 2006.

[88] R. P. Joshi, Q. H. Q. Hu, and K. H. Schoenbach, "Modeling studies of cell response to ultrashort, high-intensity electric fields-implications for intracellular manipulation," *IEEE Trans. Plasma Sci.*, vol. 32, no. 4, pp. 1677–1686, 2004.

[89] P. Levif, J. Séguin, M. Moisan, and J. Barbeau, "Depyrogenation by the Flowing Afterglow of a Reduced-Pressure N_2 -O_2 Discharge (Gaseous Plasma Treatment)," *Plasma Process. Polym.*, vol. 11, no. 6, pp. 559–570, Jun. 2014.

[90] M. Laroussi, "Low temperature plasma-based sterilization: Overview and state-of-the-art," *Plasma Process. Polym.*, vol. 2, no. 5, pp. 391–400, 2005.

[91] M. Laroussi, D. A. Mendis, and M. Rosenberg, "Plasma interaction with microbes," *New J. Phys.*, vol. 5, 2003.

[92] T. C. Montie, K. Kelly-Wintenberg, and J. Reece Roth, "An overview of research using the one atmosphere uniform glow discharge plasma (OAUGDP) for sterilization of surfaces and materials," *IEEE Trans. Plasma Sci.*, vol. 28, no. 1, pp. 41–50, 2000.

[93] D. Dobrynin, G. Friedman, A. Fridman, and A. Starikovskiy, "Inactivation of bacteria using dc corona discharge: Role of ions and humidity," *New J. Phys.*, vol. 13, 2011.

[94] M. J. Alfa, P. DeGagne, N. Olson, and T. Puchalski, "Comparison of ion plasma, vaporized hydrogen peroxide, and 100% ethylene oxide sterilizers to the 12/88 ethylene oxide gas sterilizer," *Infect. Control Hosp. Epidemiol.*, vol. 17, no. 2, pp. 92–100, 1996.

[95] T. G. Klämpfl, T. Shimizu, S. Koch, M. Balden, S. Gemein, Y.-F. Li, A. Mitra, J. L. Zimmermann, J. Gebel, G. E. Morfill, and H.-U. Schmidt, "Decontamination of Nosocomial Bacteria Including Clostridium difficile Spores on Dry Inanimate Surface by Cold Atmospheric Plasma," *Plasma Process. Polym.*, vol. 11, no. 10, pp. 974–984, Oct. 2014.

[96] M. Heise, W. Neff, O. Franken, P. Muranyi, and J. Wunderlich, "Sterilization

of polymer foils with dielectric barrier discharges at atmospheric pressure," *Plasmas Polym.*, vol. 9, no. 1, pp. 23–33, 2004.

[97] H. Shintani, N. Shimizu, Y. Imanishi, T. Sekiya, K. Tamazawa, A. Taniguchi, and N. Kido, "Inactivation of microorganisms and endotoxins by low temperature nitrogen gas plama exposure," *Biocontrol Sci.*, vol. 12, no. 4, pp. 131–143, 2007.

[98] A. Fernández, N. Shearer, D. R. Wilson, and A. Thompson, "Effect of microbial loading on the efficiency of cold atmospheric gas plasma inactivation of Salmonella enterica serovar Typhimurium," *Int. J. Food Microbiol.*, vol. 152, no. 3, pp. 175–180, 2012.

[99] Y. F. Li, T. Shimizu, J. L. Zimmermann, and G. E. Morfill, "Cold atmospheric plasma for surface disinfection," *Plasma Process. Polym.*, vol. 9, no. 6, pp. 585–589, 2012.

[100] H. Lu, S. Patil, K. M. Keener, P. J. Cullen, and P. Bourke, "Bacterial inactivation by high-voltage atmospheric cold plasma: Influence of process parameters and effects on cell leakage and DNA," *J. Appl. Microbiol.*, vol. 116, no. 4, pp. 784–794, 2014.

[101] D. Fritze and R. Pukall, "Reclassification of bioindicator strains Bacillus subtilis DSM 675 and Bacillus subtilis DSM 2277 as Bacillus atrophaeus," *Int. J. Syst. Evol. Microbiol.*, vol. 51, no. 1, pp. 35–37, 2001.

[102] A. Mahfoudh, M. Moisan, J. Séguin, J. Barbeau, Y. Kabouzi, and D. Kéroack, "Inactivation of Vegetative and Sporulated Bacteria by Dry Gaseous Ozone," *Ozone Sci. Eng.*, vol. 32, no. 3, pp. 180–198, 2010.

[103] G. L. Gilbert, V. M. Gambill, D. R. Spiner, R. K. Hoffman, and C. R. Phillips, "Effect of Moisture on Ethylene Oxide Sterilization.," *Appl. Microbiol.*, vol. 12, no. 6, pp. 496–503, 1964.

[104] S. Patil, T. Moiseev, N. N. Misra, P. J. Cullen, J. P. Mosnier, K. M. Keener, and P. Bourke, "Influence of high voltage atmospheric cold plasma process parameters and role of relative humidity on inactivation of Bacillus atrophaeus spores inside a sealed package," *J. Hosp. Infect.*, vol. 88, no. 3, pp. 162–169,

2014.

[105] M. Hähnel, T. Von Woedtke, and K. D. Weltmann, "Influence of the air humidity on the reduction of Bacillus spores in a defined environment at atmospheric pressure using a dielectric barrier surface discharge," *Plasma Process. Polym.*, vol. 7, no. 3–4, pp. 244–249, 2010.

[106] P. Muranyi, J. Wunderlich, and M. Heise, "Influence of relative gas humidity on the inactivation efficiency of a low temperature gas plasma," *J. Appl. Microbiol.*, vol. 104, no. 6, pp. 1659–1666, 2008.

[107] V. Sigwarth and A. Stark, "Effect of carrier materials on the resistance of spores of Bacillus stearothermophilus to gaseous hydrogen peroxide," *PDA J. Pharm. Sci. Technol.*, vol. 57, no. 1, pp. 3–11, 2003.

[108] J. V. Rogers, C. L. K. Sabourin, Y. W. Choi, W. R. Richter, D. C. Rudnicki, K. B. Riggs, M. L. Taylor, and J. Chang, "Decontamination assessment of Bacillus anthracis, Bacillus subtilis, and Geobacillus stearothermophilus spores on indoor surfaces using a hydrogen peroxide gas generator," *J. Appl. Microbiol.*, vol. 99, no. 4, pp. 739–748, 2005.

[109] J. V. Rogers, Y. W. Choi, W. R. Richter, D. C. Rudnicki, D. W. Joseph, C. L. K. Sabourin, M. L. Taylor, and J. C. S. Chang, "Formaldehyde gas inactivation of Bacillus anthracis, Bacillus subtilis, and Geobacillus stearothermophilus spores on indoor surface materials," *J. Appl. Microbiol.*, vol. 103, no. 4, pp. 1104–1112, 2007.

[110] "Good Fellow." [Online]. Available: http://www.goodfellow.com/.

[111] P. Levif, J. Séguin, M. Moisan, and J. Barbeau, "Influence of substrate materials on inactivation of B. atrophaeus endospores in a reduced-pressure argon plasma," *Plasma Process. Polym.*, vol. 8, no. 7, pp. 617–630, 2011.

[112] M. J. Pavlovich, D. S. Clark, and D. B. Graves, "Quantification of air plasma chemistry for surface disinfection," *Plasma Sources Sci. Technol.*, vol. 23, no. 6, p. 65036, Dec. 2014.

[113] T. Shimizu, J. L. Zimmermann, and G. E. Morfill, "Inactivation effect using

surface microdischarge plasma," pp. 9–10, 2015.

[114] M. Moisan, K. Boudam, D. Carignan, D. Kéroack, P. Levif, J. Barbeau, J. Séguin, K. Kutasi, B. Elmoualij, O. Thellin, and W. Zorzi, "Sterilization/disinfection of medical devices using plasma: the flowing afterglow of the reduced-pressure N_2-O_2 discharge as the inactivating medium," *Eur. Phys. J. Appl. Phys.*, vol. 63, no. 1, p. 10001, Jul. 2013.

[115] M. Moisan, P. Levif, J. Seguin, and J. Barbeau, "Sterilization/disinfection using reduced-pressure plasmas: some differences between direct exposure of bacterial spores to a discharge and their exposure to a flowing afterglow," *J. Phys. D Appl. Phys.*, vol. 47, p. 285404, 2014.

[116] U. Schnabel, M. Andrasch, K.-D. Weltmann, and J. Ehlbeck, "Inactivation of Vegetative Microorganisms and Bacillus atrophaeus Endospores by Reactive Nitrogen Species (RNS)," *Plasma Process. Polym.*, vol. 11, no. 2, pp. 110–116, Feb. 2014.

[117] S. Shimizu, S. Barczyk, P. Rettbergb, T. Shimizu, T. Klaempfl, J. L. Zimmermann, T. Hoeschenc, C. Linsmeierd, P. Weber, G. E. Morfill, and H. M. Thomas, "Cold Atmospheric Plasma – a New Technology for Spacecraft Component Decontamination," *Planet. Space Sci.*, vol. 90, pp. 60–71, 2014.

[118] A. Vesel and M. Mozetič, "Modification of PET surface by nitrogen plasma treatment," *J. Phys. Conf. Ser.*, vol. 100, p. 12027, 2008.

[119] E.-T. Es-Sebbar, C. Sarra-Bournet, N. Naudé, F. Massines, and N. Gherardi, "Absolute nitrogen atom density measurements by two-photon laser-induced fluorescence spectroscopy in atmospheric pressure dielectric barrier discharges of pure nitrogen," *J. Appl. Phys.*, vol. 106, no. 7, p. 73302, 2009.

[120] N. A. Popov, "Dissociation of nitrogen in a pulse-periodic dielectric barrier discharge at atmospheric pressure," *Plasma Phys. Reports*, vol. 39, no. 5, pp. 420–424, 2013.

[121] D. Tsyganov and S. Pancheshnyi, "Simulation of N-atom production in dielectric-barrier discharge in nitrogen at atmospheric pressure," *Plasma Sources Sci. Technol.*, vol. 21, no. 6, p. 65010, Dec. 2012.

[122] K. Kawamura, A. Sakuma, Y. Nakamura, T. Oguri, N. Sato, and N. Kido, "Evaluation of bactericidal effects of low-temperature nitrogen gas plasma towards application to short-time sterilization.," *Microbiol. Immunol.*, vol. 56, no. 7, pp. 431–40, Jul. 2012.

[123] F. J. J. Peeters, R. Yang, and M. C. M. van de Sanden, "The relation between the production efficiency of nitrogen atoms and the electrical characteristics of a dielectric barrier discharge," *Plasma Sources Sci. Technol.*, vol. 24, no. 4, p. 45006, 2015.

[124] S. E. Babayan, G. Ding, and R. F. Hicks, "Determination of the Nitrogen Atom Density in the Afterglow of a Nitrogen and Helium , Nonequilibrium , Atmospheric Pressure Plasma," *Plasma Chem. Plasma Process.*, vol. 21, no. 4, p. 505, 2001.

[125] G. Oinuma, Y. Inanaga, Y. Tanimura, M. Kuzumoto, Y. Tabata, and K. Watanabe, "A comparative study of the surface recombination of nitrogen atoms on various materials at atmospheric pressure," *J. Phys. D. Appl. Phys.*, vol. 43, no. 25, p. 255202, 2010.

[126] J.-P. Sarrette, B. Rouffet, and A. Ricard, "Determination of Nitrogen Atoms Loss Probabilities on Copper, Aluminium, Alumina, Brass and Nylon Surfaces," *Plasma Process. Polym.*, vol. 3, no. 2, pp. 120–126, Feb. 2006.

[127] S. F. Adams and T. a Miller, "Surface and volume loss of atomic nitrogen in a parallel plate rf discharge reactor," *Plasma Sources Sci. Technol.*, vol. 9, no. 3, pp. 248–255, Aug. 2000.

[128] T. Yamashita, "Rate of recombination of nitrogen atoms," *J. Chem. Phys.*, vol. 70, no. 9, p. 4248, 1979.

[129] K. M. Evenson, "Atomic-Nitrogen Recombination," *J. Chem. Phys.*, vol. 45, no. 7, p. 2450, 1966.

[130] J. T. Herron, J. L. Franklin, P. Bradt, and V. H. Dibeler, "Kinetics of Nitrogen Atom Recombination," *J. Chem. Phys.*, vol. 30, no. 4, p. 879, 1959.

[131] P. Harteck, R. R. Reeves, and G. Mannella, "Rate of Recombination of

Nitrogen Atoms," *J. Chem. Phys.*, vol. 29, no. 3, p. 608, 1958.

[132] M. A. A. Clyne and D. H. Stedman, "Rate of recombination of nitrogen atoms," *J. Phys. Chem.*, vol. 71, no. 9, p. 3071, 1967.

[133] B. Rouffet, F. Gaboriau, and J. P. Sarrette, "Pressure dependence of the nitrogen atom recombination probability in late afterglows," *J. Phys. D. Appl. Phys.*, vol. 43, no. 18, p. 185203, May 2010.

[134] B. Gordiets, C. M. Ferreira, J. Nahorny, D. Pagnon, M. Touzeau, and M. Vialle, "Surface kinetics of N and O atoms in discharges," *J. Phys. D. Appl. Phys.*, vol. 29, no. 4, pp. 1021–1031, Apr. 1996.

[135] A. Ricard, S. Oh, and V. Guerra, "Line-ratio determination of atomic oxygen and $N_2(A)$ metastable absolute densities in an RF nitrogen late afterglow," *Plasma Sources Sci. Technol.*, vol. 22, no. 3, p. 35009, Jun. 2013.

[136] B. A. Thrush, "The recombination of nitrogen atoms and the nitrogen afterglow," *Proc. R. Soc. Lond. A. Math. Phys. Sci.*, vol. 296, no. 1445, pp. 201–221, 1967.

[137] T. C. Marshall, "Studies of Atomic Recombination of Nitrogen , Hydrogen , and Oxygen by Paramagnetic Resonance," *Phys. Fluids*, vol. 5, no. 7, p. 743, 1962.

[138] W. Brennen and E. C. Shane, "The nitrogen afterglow and the rate of recombination of nitrogen atoms in the presence of nitrogen, argon and helium," *J. Phys. Chem.*, vol. 75, no. 10, p. 1552, 1971.

[139] S. Miyazaki and S. Takahashi, "Reactions of Nitrogen Atom with Methane and with Ethylene," *Bull. Chem. Soc. Japan*, vol. 41, no. 6, pp. 1456–1458, 1967.

[140] C. B. Kretschmer and H. L. Petersen, "Kinetics of Three Body Atom Recombination," *J. Chem. Phys.*, vol. 39, p. 1772, 1963.

[141] I. A. Kossyi, A. Y. Kostinsky, A. A. Matveyev, and V. P. Silakov, "Kinetic scheme of the on-equilibrium discharge in nitrogen-oxygen mixtures," *Plasma Sources Sci. Technol.*, vol. 1, pp. 207–220, 1992.

[142] H. Partridge, S. R. Langhoff, C. W. Bauschlicher, and D. W. Schwenke, "Theoretical study of the A' $^5\Sigma^+_g$ and C' $^5\Pi_u$ states of N$_2$: Implications for the N$_2$ afterglow," *J. Chem. Phys.*, vol. 88, no. 5, p. 3174, 1988.

[143] K. Niemi, D. O'Connell, N. de Oliveira, D. Joyeux, L. Nahon, J. P. Booth, and T. Gans, "Absolute atomic oxygen and nitrogen densities in radio-frequency driven atmospheric pressure cold plasmas: Synchrotron vacuum ultra-violet high-resolution Fourier-transform absorption measurements," *Appl. Phys. Lett.*, vol. 103, no. 3, p. 34102, 2013.

[144] D. Douai, J. Berndt, and J. Winter, "Quantitative analysis of the atomic nitrogen concentration in a remote plasma by means of mass spectrometry," *Plasma Sources Sci. Technol.*, vol. 11, no. 1, pp. 60–68, 2002.

[145] M. Mrazkova, P. Vasina, V. Kudrle, A. Talsky, C. D. Pintassilgo, V. Guerra, M. Mrázková, P. Vašina, and A. Tálský, "On the oxygen addition into nitrogen post-discharges," *J. Phys. D Appl. Phys.*, vol. 42, no. 7, p. 75202, Apr. 2009.

[146] P. Vasina, V. Kudrle, A. Tálský, P. Boto, M. Mrázková, and M. Mesko, "Simultaneous measurement of N and O densities in plasma afterglow by means of NO titration," *Plasma Sources Sci. Technol.*, vol. 13, no. 4, pp. 668–674, Nov. 2004.

[147] V. Kudrle, P. Vašina, A. Tálský, M. Mrázková, O. Štec, and J. Janča, "Plasma diagnostics using electron paramagnetic resonance," *J. Phys. D. Appl. Phys.*, vol. 43, p. 124020, 2010.

[148] J. Henriques, S. Villeger, J. Levaton, J. Nagai, S. Santana, J. Amorim, and A. Ricard, "Densities of N and O-atoms in N$_2$–O$_2$ flowing glow discharges by actinometry," *Surf. Coatings Technol.*, vol. 200, no. 1–4, pp. 814–817, Oct. 2005.

[149] J. C. Thomaz, J. Amorim, and C. F. Souza, "Validity of actinometry to measure N and H atom concentration in N$_2$–H$_2$ direct current glow discharges," *J. Phys. D Appl. Phys.*, vol. 32, pp. 3208–3214, 1999.

[150] Andrei V Klochko, Arthur Salmon, Joseph Lemainque, Nikolay A. Popov, Jean-Paul Booth, Zhongmin Xiong, Mark J. Kushner, and Svetlana M.

Starikovskaia, "Experimental and numerical study of fast gas heating and O atom production in a capillary nanosecond discharge," in *52nd AIAA*.

[151] K. Niemi, V. S. der Gathen, and H. F. Döbele, "Absolute calibration of atomic density measurements by laser-induced fluorescence spectroscopy with two-photon excitation," *J. Phys. D. Appl. Phys.*, vol. 34, no. 15, pp. 2330–2335, 2001.

[152] J. B. Schmidt, S. Roy, W. D. Kulatilaka, I. Shkurenkov, I. V Adamovich, W. R. Lempert, and J. R. Gord, "Femtosecond, two-photon-absorption, laser-induced-fluorescence (fs-TALIF) imaging of atomic hydrogen and oxygen in non-equilibrium plasmas," *J. Phys. D. Appl. Phys.*, vol. 50, no. 1, p. 15204, 2017.

[153] G. D. Stancu, "Laser based spectroscopic diagnostics from UV to Mid-IR applied to the study of atmospheric pressure discharges," in *VKI lecture series*, Rhode-Saint-Genèse (Belgium), 2014.

[154] S. E. Babayan, G. Ding, and R. F. Hicks, "Determination of the nitrogen atom density in the afterglow of a nitrogen and helium, nonequilibrium, atmospheric pressure plasma," *Plasma Chem. Plasma Process.*, vol. 21, no. 4, pp. 505–521, 2001.

[155] J. Berkowitz, W. A. Chupka, and G. B. Kistiakowsky, "Mass Spectrometric Study of the Kinetics of Nitrogen Afterglow," *J. Chem. Phys.*, vol. 25, no. 3, p. 457, 1956.

[156] L. G. Piper, "State-to-state $N_2(A^3\Sigma^+_u)$ energy-pooling reactions. I. The formation of $N_2(C\ ^3\Pi_u)$ and the Herman infrared system," *J. Chem. Phys.*, vol. 88, no. 1, p. 231, 1988.

[157] C. Laux and C. H. Kruger, "Arrays of radiatie transition probabilities for the N_2 first and second positive, NO beta and gamma, N_2^+ first negative, and O_2 Schumann-Runge band systems," *J. Quant. Spectrosc. Radiat. Transf.*, vol. 48, no. 1, pp. 9–24, 1992.

[158] A. Ricard, J. Tétreault, and J. Hubert, "Nitrogen atom recombination in high pressure Ar-N_2 flowing post-discharges," *J. Phys. B At. Mol. Opt. Phys.*, vol.

24, pp. 1115–1123, 1991.

[159] L. G. Piper, "State-to-state $N_2(A^3\Sigma_u^+)$ energy pooling reactions. II. The formation and quenching of $N_2(B^3\Pi_g$, v'=1–12)," *J. Chem. Phys.*, vol. 88, no. 11, p. 6911, 1988.

[160] R. A. Young, G. Black, and T. G. Slanger, "Vacuum-Ultraviolet Photolysis of N_2O. II. Deactivation of $N_2(A^3\Sigma_u^+)$," *J. Chem. Phys.*, vol. 50, no. 1, p. 303, 1969.

[161] C. O. Laux, T. G. Spence, C. H. Kruger, and R. N. Zare, "Optical diagnostics of atmospheric pressure air plasmas," *Plasma Sources Sci. Technol.*, vol. 12, no. 2, pp. 125–138, May 2003.

[162] "Plasmabiotics." [Online]. Available: http://www.plasmabiotics.com/docs/brochure_generateurs_Plasmabiotics_200 62014.pdf. [Accessed: 02-Dec-2017].

[163] C. O. Laux, "Optical diagnostics and radiative emission of air plasma," Stanford university, 1993.

[164] Specair, "www.spectralfit.com." .

[165] "Ansys Fluent 12.0 User's Guide," 2009. [Online]. Available: http://www.afs.enea.it/project/neptunius/docs/fluent/html/th/node128.htm. [Accessed: 02-Dec-2017].

[166] G. N. Hays, "Surface catalytic efficiency of a sputtered molybdenum layer on quartz and Pyrex for the recombination of nitrogen atoms," *J. Chem. Phys.*, vol. 60, no. 5, p. 2027, 1974.

[167] R. W. F. Gross and N. Cohen, "Temperature dependence of chemiluminescent reactions. II. Nitric oxide Afterglow," *J. Chem. Phys.*, vol. 48, no. 1968, pp. 2582–2588, 1968.

[168] C. D. Pintassilgo, J. Loureiro, and V. Guerra, "Modelling of a N_2–O_2 flowing afterglow for plasma sterilization," *J. Phys. D. Appl. Phys.*, vol. 38, no. 3, pp.

417–430, Feb. 2005.

[169] P. Fromy, A.-M. Pointu, M. Ganciu, and J. Orphal, "Transportation of nitrogen atoms in an atmospheric pressure post-discharge of pure nitrogen," *J. Phys. D. Appl. Phys.*, vol. 39, no. 1, pp. 108–112, Jan. 2006.

[170] S. Limam, E. Odic, M. J. Kirkpatrick, and A. M. Pointu, "Bacterial decontamination of the inner wall of narrow tubes by a nitrogen afterglow at atmospheric pressure and its relation to local atomic nitrogen concentration," *Plasma Process. Polym.*, vol. 10, no. 8, pp. 679–685, 2013.

[171] O. Mrad, J. Saunier, C. Aymes Chodur, V. Rosilio, F. Agnely, P. Aubert, J. Vigneron, a. Etcheberry, and N. Yagoubi, "A comparison of plasma and electron beam-sterilization of PU catheters," *Radiat. Phys. Chem.*, vol. 79, no. 1, pp. 93–103, Jan. 2010.

[172] A. Vesel, "Heterogeneous surface recombination of neutral nitrogen atoms," *Mater. Technol.*, vol. 46, no. 1, pp. 7–12, 2012.

[173] D. L. Rusterholtz, D. A. Lacoste, G. D. Stancu, D. Z. Pai, and C. O. Laux, "Ultrafast heating and oxygen dissociation in atmospheric pressure air by nanosecond repetitively pulsed discharges," *J. Phys. D. Appl. Phys.*, vol. 46, no. 46, p. 464010, 2013.

[174] G. D. Stancu, F. Kaddouri, D. A. Lacoste, and C. O. Laux, "Atmospheric pressure plasma diagnostics by OES, CRDS and TALIF," *J. Phys. D. Appl. Phys.*, vol. 43, no. 12, p. 124002, 2010.

[175] C. Kruger, C. Laux, L. Yu, D. Packan, and L. Pierrot, "Non-Equilibrium Discharges in Air and Nitrogen Plasmas at Atmospheric Pressure," *Pure Appl. Chem.*, vol. 74, no. 3, pp. 337–347, 2002.

[176] D. M. Packan, "Repetitive nanosecond glow discharge in atmospheric pressure air," Stanford University, 2003.

[177] D. Packan, L. Yu, C. O. Laux, and C. H. Kruger, "Repetitively-Pulsed DC Glow Discharge in Atmospheric Pressure Air: Modeling and Experiments with a 12 kV, 10 ns, 100 kHz Pulse Generator," in *Proceedings of the 28th IEEE*

International Conference on Plasma Science, 2001, p. 259.

[178] G. D. Stancu, F. Kaddouri, D. A. Lacoste, and C.O. Laux, "Investigations of the rapid plasma chemistry induced by nanosecond discharges in atmospheric pressure air using advanced optical diagnostics," in *AIAA, 40th Plasmadynamics and Lasers Conference*, 2009.

[179] D. Z. Pai, D. A. Lacoste, and C. O. Laux, "Transitions between corona, glow, and spark regimes of nanosecond repetitively pulsed discharges in air at atmospheric pressure," *J. Appl. Phys.*, vol. 107, no. 9, pp. 1–15, 2010.

[180] A. Starikovskiy and N. Aleksandrov, "Plasma-assisted ignition and combustion," *Prog. Energy Combust. Sci.*, vol. 39, no. 1, pp. 61–110, 2013.

[181] X. Duten, D. Packan, L. Yu, C. O. Laux, and C. H. Kruger, "DC and pulsed glow discharges in atmospheric pressure air and nitrogen," *IEEE Trans. Plasma Sci.*, vol. 30, no. 1 I, pp. 178–179, 2002.

[182] D. Z. Pai, D. A. Lacoste, and C. O. Laux, "Nanosecond repetitively pulsed discharges in air at atmospheric pressure—the spark regime," *Plasma Sources Sci. Technol.*, vol. 19, no. 6, p. 65015, Dec. 2010.

[183] D. Rusterholtz, "Nanosecond Repetitively Pulsed Discharges in Atmospheric Pressure Air," vol. 33, no. 1, 2012.

[184] D. Z. Pai, "Etude des plasmas générés par des impulsions électriques répétitives dans l'air préchauffé à pression atmosphérique," vol. 4, p. 185, 2008.

[185] A. Lo, A. Cessou, P. Boubert, and P. Vervisch, "Space and time analysis of the nanosecond scale discharges in atmospheric pressure air: I. Gas temperature and vibrational distribution function of N_2 and O_2," *J. Phys. D. Appl. Phys.*, vol. 47, no. 11, p. 115201, Mar. 2014.

[186] N. A. Popov, "Investigation of the mechanism for rapid heating of nitrogen and air in gas discharges," *Plasma Phys. Reports*, vol. 27, no. 10, pp. 886–896, 2001.

[187] N. A. Popov, "Kinetic processes initiated by a nanosecond high-current discharge in hot air," *Plasma Phys. Reports*, vol. 37, no. 9, pp. 807–815, 2011.

[188] D. A. Xu, D. A. Lacoste, D. L. Rusterholtz, P. Q. Elias, G. D. Stancu, and C. O. Laux, "Experimental study of the hydrodynamic expansion following a nanosecond repetitively pulsed discharge in air," *Appl. Phys. Lett.*, vol. 99, no. 12, pp. 21–24, 2011.

[189] D. Z. Pai, G. D. Stancu, D. A. Lacoste, and C. O. Laux, "Nanosecond repetitively pulsed discharges in air at atmospheric pressure—the glow regime," *Plasma Sources Sci. Technol.*, vol. 18, no. 4, p. 45030, Nov. 2009.

[190] N. A. Popov, "Fast Gas Heating Initiated by Pulsed Nanosecond Discharge in Atmospheric Pressure Air," in *AIAA Aerospace Sciences Meeting and Exhibit*, 2013, no. January, pp. 1–20.

[191] M. Salvermoser, D. E. Murnick, and U. Kogelschatz, "Influence of Water Vapor on Photochemical Ozone Generation with Efficient 172 nm Xenon Excimer Lamps," *Ozone Sci. Eng.*, vol. 30, no. 3, pp. 228–237, 2008.

[192] B. Eliasson and U. Kogelschatz, "Modeling and applications of silent discharge plasmas," *IEEE Trans. Plasma Sci.*, vol. 19, no. 2, pp. 309–323, 1991.

[193] R. Ono and T. Oda, "Ozone production process in pulsed positive dielectric barrier discharge," *J. Phys. D. Appl. Phys.*, vol. 40, no. 1, pp. 176–182, 2007.

[194] J.-G. Kim, A. E. Yousef, and M. A. Khadre, "Ozone and Its Current and Future Application in the Food Industry," *Adv. Food Nutr. Res.*, vol. 45, pp. 0–12, 2003.

[195] US Environmental Protection Agency, "Nitrogen Oxides (NO_x), Why and How They Are Controlled," 1999.

[196] C. T. Bowman, "Control of combustion-generated nitrogen oxide emissions : technology driven by regulation," in *Twenty-Fourth Symposium (International) on Combustion*, 1992, pp. 859–878.

[197] C. T. Bowman, "Kinetics of pollutant formation and Destruction in

Combustion," *Prog. Energy Combust. Sci.*, vol. 1, p. 33, 1975.

[198] R. F. Furchgott, "Endothelium-derived relaxing factor: discovery, early studies, and identification as nitric oxide," *Biosci. Rep.*, vol. 19, no. 4, pp. 235–251, 1999.

[199] A. W. Carpenter and M. H. Schoenfisch, "Nitric oxide release: Part II. Therapeutic applications," *Chem. Soc. Rev.*, vol. 41, no. 10, pp. 3711–3742, 2012.

[200] J. Liebmann, J. Scherer, N. Bibinov, P. Rajasekaran, R. Kovacs, R. Gesche, P. Awakowicz, and V. Kolb-Bachofen, "Biological effects of nitric oxide generated by an atmospheric pressure gas-plasma on human skin cells.," *Nitric Oxide*, vol. 24, no. 1, pp. 8–16, Jan. 2011.

[201] B. Yu, S. Muenster, A. Blaesi, D. B. Bloch, and W. M. Zapol, "Producing nitric oxide by pulsed electrical discharge in air for inhalation therapy," *Am. J. Respir. Crit. Care Med.*, vol. 191, no. 294, 2015.

[202] F. C. Fang, "Mechanisms of nitric oxide-related antimicrobial activity," *J. Clin. Invest.*, vol. 99, no. 12, pp. 2818–2825, 1997.

[203] W. K. Subczynski, M. Lomnicka, and J. S. Hyde, "Permeability of Nitric Oxide through Lipid Bilayer Membranes," *Free Radic. Res.*, vol. 24, no. 5, pp. 343–349, 1996.

[204] S. Burney, J. L. Caulfield, J. C. Niles, J. S. Wishnok, and S. R. Tannenbaum, "The chemistry of DNA damage from nitric oxide and peroxynitrite," *Mutat. Res. - Fundam. Mol. Mech. Mutagen.*, vol. 424, no. 1–2, pp. 37–49, 1999.

[205] Noxilizer Inc., "Overview of the Nitrogen Dioxide Sterilization Process," 2012. [Online]. Available: http://www.noxilizer.com/pdf/news/WhitePaper-Mechanism_Overview_6_14_12.pdf. [Accessed: 01-Sep-2017].

[206] J. Kulla, R. Reich, and S. B. Jr, "Sterilizing combination products using oxides of nitrogen," *Med. Device Diagnostic Ind.*, 2009.

[207] M. Shomali, D. Opie, T. Avasthi, and A. Trilling, "Nitrogen dioxide sterilization in low-resource environments: A feasibility study," *PLoS One*, vol. 10, no. 6, pp. 1–11, 2015.

[208] S. Gorsdorf, K. E. Appel, C. Engeholm, and G. Obe, "Nitrogen dioxide induces DNA single-strand breaks in cultured Chinese hamster cells," *Carcinogenesis*, vol. 11, no. 1, pp. 37–41, 1990.

[209] T. Hirohisa, K. Atsuko, Y. Daisuke, and G. Fujio, "Chromosomal aberrations and sister-chromatid exchanges induced by gaseous nitrogen dioxide in cultured chinese hamster cells," *Mutat. Res. Toxicol.*, vol. 89, no. 4, pp. 303–309, 1981.

[210] Mathesongas, "Materials compatibility kit." [Online]. Available: https://www.mathesongas.com/pdfs/products/Materials-Compatibility-Guide.pdf.

[211] M. S. Simeni, "Quantum cascade laser absorption studies of nitric oxide production by nanosecond pulsed discharges in air and in combustible mixtures," CentraleSupélec, 2015.

[212] M. Simeni Simeni, C. O. Laux, and G. D. Stancu, "High-spatial resolution measurements of NO density and temperature by Mid-IR QCLAS in open-air confined plasmas," *J. Phys. D. Appl. Phys.*, vol. 50, p. 274004, 2017.

[213] S. Welzel, "New enhanced sensitivity infrared laser spectroscopy techniques applied to reactive plasmas and trace gas detection," Universität Greifswald, 2009.

[214] G. D. Stancu, A. V. Pipa, G. Lombardi, P. B. Davies, A. Gicquel, B. P. Lavrov, and J. Röpcke, "On the reaction kinetics of chemically active molecular microwave plasmas," *Contrib. to Plasma Phys.*, vol. 45, no. 5–6, pp. 358–368, 2005.

[215] X. Chao, J. B. Jeffries, and R. K. Hanson, "In situ absorption sensor for NO in combustion gases with a 5.2 um quantum-cascade laser," *Proc. Combust. Inst.*, vol. 33, no. 1, pp. 725–733, 2011.

[216] J. Röpcke, P. B. Davies, N. Lang, a Rousseau, and S. Welzel, "Applications of

quantum cascade lasers in plasma diagnostics: a review," *J. Phys. D. Appl. Phys.*, vol. 45, no. 42, p. 423001, Oct. 2012.

[217] S. Welzel, F. Hempel, M. Hübner, N. Lang, P. B. Davies, and J. Röpcke, "Quantum cascade laser absorption spectroscopy as a plasma diagnostic tool: an overview.," *Sensors*, vol. 10, no. 7, pp. 6861–6900, Jan. 2010.

[218] G. D. Stancu, N. Lang, J. Röpcke, M. Reinicke, a Steinbach, and S. Wege, "In Situ Monitoring of Silicon Plasma Etching Using a Quantum Cascade Laser Arrangement," *Chem. Vap. Depos.*, vol. 13, no. 6–7, pp. 351–360, 2007.

[219] L. S. Rothman, C. P. Rinsland, a. Goldman, S. T. Massie, D. P. Edwards, J.-M. Flaud, a. Perrin, C. Camy-Peyret, V. Dana, J.-Y. Mandin, J. Schroeder, a. Mccann, R. R. Gamache, R. B. Wattson, K. Yoshino, K. V. Chance, K. W. Jucks, L. R. Brown, V. Nemtchinov, and P. Varanasi, "the Hitran Molecular Spectroscopic Database and Hawks (Hitran Atmospheric Workstation): 1996 Edition," *J. Quant. Spectrosc. Radiat. Transf.*, vol. 60, no. 5, pp. 665–710, Nov. 1998.

[220] N. Jacquinet-Husson, N. A. Scott, A. Chédin, L. Crépeau, R. Armante, V. Capelle, J. Orphal, A. Coustenis, C. Boonne, N. Poulet-Crovisier, A. Barbe, M. Birk, L. R. Brown, C. Camy-Peyret, C. Claveau, K. Chance, N. Christidis, C. Clerbaux, P. F. Coheur, V. Dana, L. Daumont, M. R. De Backer-Barilly, G. J. Di Lonardo, M. Flaud, A. Goldman, A. Hamdouni, M. Hess, M. D. Hurley, D. Jacquemart, I. Kleiner, P. Köpke, J. Y. Mandin, S. Massie, S. Mikhailenko, V. Nemtchinov, A. Nikitin, D. Newnham, A. Perrin, V. I. Perevalov, S. Pinnock, L. Régalia-Jarlot, C. P. Rinsland, A. Rublev, F. Schreier, L. Schult, K. M. Smith, S. A. Tashkun, J. L. Teffo, R. A. Toth, V. G. Tyuterev, J. Vander Auwera, P. Varanasi, and G. Wagner, "The GEISA spectroscopic database : Current and future archive for Earth and planetary atmosphere studies," *J. Quant. Spectrosc. Radiat. Transf.*, vol. 109, pp. 1043–1059, 2008.

[221] A. Rogalski, "Infrared detectors: An overview," *Infrared Phys. Technol.*, vol. 43, no. 3–5, pp. 187–210, 2002.

[222] S. Reuter, J. S. Sousa, G. D. Stancu, and J.-P. Hubertus van Helden, "Review on VUV to MIR absorption spectroscopy of atmospheric pressure plasma jets," *Plasma Sources Sci. Technol.*, vol. 24, no. 5, p. 54001, 2015.

[223]   J. Orphal, "A critical review of the absorption cross-sections of O_3 and NO_2 in the ultraviolet and visible," *J. Photochem. Photobiol. A Chem.*, vol. 157, no. 2–3, pp. 185–209, May 2003.

[224]   B. Kirmse, A. Delon, and R. Jost, "NO_2 absorption cross section and its temperature dependence," *J. Geophys. Res.*, vol. 102, pp. 16089–16098, 1997.

[225]   V. Gorshelev, A. Serdyuchenko, M. Weber, W. Chehade, and J. P. Burrows, "High spectral resolution ozone absorption cross-sections - Part 1: Measurements, data analysis and comparison with previous measurements around 293 K," *Atmos. Meas. Tech.*, vol. 7, no. 2, pp. 609–624, 2014.

[226]   K. Bogumil, J. Orphal, and J. Burrows, "Temperature dependent absorption cross sections of O_3, NO_2, and other atmospheric trace gases measured with the SCIAMACHY spectrometer," *Proc. ERS-Envisat- Symp.*, no. 2, 2000.

[227]   U. Kogelschatz and B. Eliasson, "Ozone generation from oxygen and air: discharge physics and reaction mechanisms," *Ozone Sci. Eng.*, vol. 10, pp. 367–378, 1987.

[228]   H. Hippler, R. Rahn, and J. Troe, "Temperature and pressure dependence of ozone formation rates in the range 1–1000 bar and 90–370 K," *J. Chem. Phys.*, vol. 93, no. 9, p. 6560, 1990.

[229]   D. L. Baulch, M. J. Pilling, C. J. Cobos, R. A. Cox, P. Frank, G. Hayman, T. Just, J. A. Kerr, T. Murrells, J. Troe, R. W. Walker, and J. Warnatz, "Evaluated Kinetic Data for Combustion Modeling. Supplement I," *J. Phys. Chem. Ref. Data*, vol. 23, no. 6, pp. 847–848, 1994.

[230]   C. D. Pintassilgo, O. Guaitella, and A. Rousseau, "Heavy species kinetics in low-pressure dc pulsed discharges in air," *Plasma Sources Sci. Technol.*, vol. 18, no. 2, p. 25005, 2009.

[231]   V. Guerra and J. Loureiro, "Non-equilibrium coupled kinetics in stationary N_2-O_2 discharges," *J. Phys. D. Appl. Phys.*, vol. 28, p. 1903, 1995.

[232]   I. Shkurenkov, D. Burnette, W. R. Lempert, and I. V Adamovich, "Kinetics of excited states and radicals in a nanosecond pulse discharge and afterglow in

nitrogen and air," *Plasma Sources Sci. Technol.*, vol. 23, no. 6, p. 65003, Dec. 2014.

[233] D. Burnette, A. Montello, I. V Adamovich, and W. R. Lempert, "Nitric oxide kinetics in the afterglow of a diffuse plasma filament," *Plasma Sources Sci. Technol.*, vol. 23, no. 4, p. 45007, Aug. 2014.

[234] A. Fridman, *Plasma chemistry.* 2008.

[235] M. Capitelli, C. M. Ferreira, B. F. Gordiets, and A. I. Osipov, *Plasma Kinetics in Atmospheric Gases*, Springer. 2000.

[236] T. Shimizu, Y. Sakiyama, D. B. Graves, J. L. Zimmermann, and G. E. Morfill, "The dynamics of ozone generation and mode transition in air surface micro-discharge plasma at atmospheric pressure," *New J. Phys.*, vol. 14, 2012.

[237] R. Peyrous, P. Pignolet, and B. Held, "Kinetic simulation of gaseous species created by an electrical discharge in dry or humid oxygen," *J. Phys. D. Appl. Phys.*, vol. 22, pp. 1658–1667, 2000.

[238] S. W. Benson and A. E. Axworthy Jr, "Mechanism of the Gas Phase, Thermal Decomposition of Ozone," *J. Chem. Phys.*, vol. 26, no. 6, pp. 1718–1726, 1957.

[239] W. Jones and N. Davidson, "The Thermal Decomposition of Ozone in a Shock Tube," *J. Am. Chem. Soc.*, vol. 84, no. 15, pp. 2868–2878, 1962.

[240] J. V Michael, "Thermal Decomposition of Ozone," *J. Chem. Phys.*, vol. 54, p. 4455, 1971.

[241] M. L. Thoma and F. J. Hindelang, "Experiments on Shock-Heated Ozone Dissociation Oxygen/Air Using UV Laser Spectroscopy," vol. 1, no. 1962, pp. 9–10, 1995.

[242] R. Bansemer, A. Schmidt-Bleker, U. van Rienen, and K.-D. Weltmann, "Investigation and control of the O_3 to NO-transition in a novel sub-atmospheric pressure dielectric barrier discharge," *Plasma Sources Sci. Technol.*, 2017.

[243] Z. Buntat, I. R. Smith, and N. A. M. Razali, "Ozone generation using atmospheric pressure glow discharge in air," *J. Phys. D. Appl. Phys.*, vol. 42, no. 23, p. 235202, 2009.

[244] T. Plank, A. Jalakas, M. Aints, P. Paris, F. Valk, M. Viidebaum, and I. Jõgi, "Ozone generation efficiency as a function of electric field strength in air," *J. Phys. D. Appl. Phys.*, vol. 47, no. 33, p. 335205, 2014.

[245] A. Deryugin, A. Napartovich, C. Gorse, F. Paniccia, and M. Capitelli, "Ozone production and de-NO_x modeling in dry air electrical discharges," *Plasma Chem. Plasma Process.*, vol. 17, no. 1, pp. 79–91, 1997.

[246] A. A. Abdelaziz, T. Ishijima, T. Seto, N. Osawa, H. Wedaa, and Y. Otani, "Characterization of surface dielectric barrier discharge influenced by intermediate frequency for ozone production," *Plasma Sources Sci. Technol.*, vol. 25, no. 3, p. 35012, 2016.

[247] M. Simek and M. Clupek, "Efficiency of ozone production by pulsed positive corona discharge in synthetic air," *J. Phys. D. Appl. Phys.*, vol. 35, no. 11, pp. 1171–1175, 2002.

[248] F. P. Sainct, N. Mericam-Bourdet, D. a Lacoste, M. J. Kirkpatrick, E. Odic, and C. O. Laux, "Efficiency of ozone generation by atmospheric pressure air DBD using different pulsed voltage sources," *30th ICPIG, Belfast*, pp. 28–30, 2011.

[249] Y. D. Korolev, O. B. Frants, N. V. Landl, and A. I. Suslov, "Low-Current Plasmatron as a Source of Nitrogen Oxide Molecules," *IEEE Trans. Plasma Sci.*, vol. 40, no. 11, pp. 2837–2842, 2012.

[250] A. Rousseau, A. Dantier, L. Gatilova, Y. Ionikh, J. Röpcke, and Y. Tolmachev, "On NO_x production and volatile organic compound removal in a pulsed microwave discharge in air," *Plasma Sources Sci. Technol.*, vol. 14, no. 1, pp. 70–75, 2005.

[251] C. Douat, S. Hübner, R. Engeln, and J. Benedikt, "Production of nitric/nitrous oxide by an atmospheric pressure plasma jet," *Plasma Sources Sci. Technol.*, vol. 25, no. 2, p. 25027, 2016.

[252] J. S. Sousa, G. Bauville, B. Lacour, V. Puech, M. Touzeau, and J. L. Ravanat, "DNA oxidation by singlet delta oxygen produced by atmospheric pressure microdischarges," *Appl. Phys. Lett.*, vol. 97, no. 14, pp. 9–12, 2010.

[253] J. S. Sousa, K. Niemi, L. J. Cox, Q. T. Algwari, T. Gans, J. S. Sousa, K. Niemi, L. J. Cox, Q. T. Algwari, T. Gans, and D. O. Connell, "Cold atmospheric pressure plasma jets as sources of singlet delta oxygen for biomedical applications," vol. 123302, 2011.

[254] H. L. Olsen, R. B. Edmonson, and E. L. Gayhart, "Microchronometric schlieren study of gaseous expansion from an electric spark," *J. Appl. Phys.*, vol. 23, no. 10, pp. 1157–1162, 1952.

[255] J. R. Greig, R. E. Pechacek, and M. Raleigh, "Channel cooling by turbulent convective mixing," *Phys. Fluids*, vol. 28, no. 8, p. 2357, 1985.

[256] M. N. Shneider, "Turbulent decay of after-spark channels," *Phys. Plasmas*, vol. 13, no. 7, 2006.

[257] D. A. Xu, M. N. Shneider, D. a Lacoste, and C. O. Laux, "Thermal and hydrodynamic effects of nanosecond discharges in atmospheric pressure air," *J. Phys. D. Appl. Phys.*, vol. 47, no. 23, p. 235202, 2014.

[258] M. Castela, B. Fiorina, a Coussement, O. Gicquel, C. O. Laux, and N. Darabiha, "Direct Numerical Simulations of Plasma-Assisted Ignition in Quiescent and Turbulent Flow Conditions," pp. 2–4.

[259] S. P. M. Bane, J. L. Ziegler, and J. E. Shepherd, "Investigation of the effect of electrode geometry on spark ignition," *Combust. Flame*, vol. 162, no. 2, pp. 462–469, 2015.

[260] S. Stepanyan, J. Hayashi, A. Salmon, G. D. Stancu, and C. O. Laux, "Large-volume excitation of air , argon , nitrogen and combustible mixtures by thermal jets produced by nanosecond spark discharges," *Plasma Sources Sci. Technol.*, vol. 26, pp. 1–7, 2017.

[261] A. Seydou, A. Claverie, J. Sotton, and M. Bellenoue, "Experimental investigation of the effects of nanosecond repetitive pulsed (NRP) discharges

on ignition of methane-air mixtures," 2017.

[262] S. V. Leonov, Y. I. Isaenkov, and M. N. Shneider, "Suppression of the turbulent decay of an afterspark channel with residual current," *Phys. Plasmas*, vol. 14, no. 12, pp. 1–5, 2007.

[263] M. L. G. B. Castela, "Direct Numerical Simulations of plasma-assisted ignition in quiescent and turbulent flow conditions," 2016.

[264] W. J. Massman, "A review of the molecular diffusivities of H_2O, CO_2, CH_4, CO, O_3, SO_2, NH_3, N_2O, NO, and NO_2 in air, O_2 and N_2 near STP," *Atmos. Environ.*, vol. 32, no. 6, pp. 1111–1127, 1998.

[265] J. Apeloig, Barviau, and F. G. Coria, "PLIF Measurements of Nitric Oxide and Hydroxyl Radicals Distributions in Swirled Stratified Premixed Flames PLIF Measurements of Nitric Oxide and Hydroxyl Radicals Distributions in Swirled," no. July, 2016.

[266] S. De Benedictis, P. F. Ambrico, and G. Dilecce, "LIF investigations of O and NO products in air like RF plasma jet," *J. Phys. Conf. Ser.*, vol. 227, p. 12019, 2010.

[267] B. E. Battles and R. K. Hanson, "Laser-induced fluorescence measurements of NO and OH mole fraction in fuel-lean, high-pressure (1–10 atm) methane flames: Fluorescence modeling and experimental validation," *J. Quant. Spectrosc. Radiat. Transf.*, vol. 54, no. 3, pp. 521–537, 1995.

[268] W. G. Bessler, C. Schulz, T. Lee, J. B. Jeffries, and R. K. Hanson, "Strategies for laser-induced fluorescence detection of nitric oxide in high-pressure flames. I. A-X(0,0) excitation," *Appl. Opt.*, vol. 41, no. 18, pp. 3547–3557, 2002.

[269] S. V. Leonov, Y. I. Isaenkov, and M. N. Shneider, "Suppression of the turbulent decay of an afterspark channel with residual current," *Phys. Plasmas*, vol. 14, no. 12, pp. 10–15, 2007.

[270] I. S. Mc Dermid and J. B. Laudenslager, "Radiative lifetimes and electronic quenching rate constants for single-photon-excited rotational levels of NO ($A^2\Sigma^+$, $v' = 0$)," *J. Quant. Spectrosc. Radiat. Transf.*, vol. 27, no. 5, pp. 483–

492, 1982.

[271] M. C. Drake and J. W. Ratcliffe, "High temperature quenching cross sections for nitric oxide laser-induced fluorescence measurements," *J. Chem. Phys.*, vol. 98, no. 5, p. 3850, 1993.

[272] M. Tamura, P. A. Berg, J. E. Harrington, J. Luque, J. B. Jeffries, G. P. Smith, and D. R. Crosley, "Collisional quenching of CH(A), OH(A), and NO(A) in low pressure hydrocarbon flames," *Combust. Flame*, vol. 114, no. 3–4, pp. 502–514, 1998.

[273] B. Röben, M. Wienold, L. Schrottke, and H. T. Grahn, "Multiple lobes in the far-field distribution of terahertz quantum-cascade lasers due to self-interference," *AIP Adv.*, vol. 6, no. 6, pp. 1–7, 2016.

[274] F. Leipold, R. H. Stark, A. El-Habachi, and K. H. Schoenbach, "Electron density measurements in an atmospheric pressure air plasma by means of infrared heterodyne interferometry," *J. Phys. D. Appl. Phys.*, vol. 33, pp. 2268–2273, 2000.

[275] K. Urabe, T. Akiyama, and K. Terashima, "Application of phase-modulated dispersion interferometry to electron-density diagnostics of high-pressure plasma," *J. Phys. D. Appl. Phys.*, vol. 47, no. 26, p. 262001, Jul. 2014.

[276] J. P. Lim, H. S. Uhm, and S. Z. Li, "Influence of oxygen in atmospheric-pressure argon plasma jet on sterilization of Bacillus atrophaeous spores," *Phys. Plasmas*, vol. 14, no. 9, 2007.

[277] R. Brandenburg, J. Ehlbeck, M. Stieber, T. V. Woedtke, J. Zeymer, O. Schlüter, and K. D. Weltmann, "Antimicrobial treatment of heat sensitive materials by means of atmospheric pressure RF-driven plasma jet," *Contrib. to Plasma Phys.*, vol. 47, no. 1–2, pp. 72–79, 2007.

[278] H. W. Herrmann, I. Henins, J. Park, and G. S. Selwyn, "Decontamination of chemical and biological warfare (CBW) agents using an atmospheric pressure plasma jet (APPJ)," *Phys. Plasmas*, vol. 6, no. 5, pp. 2284–2289, 1999.

[279] S. Tseng, N. Abramzon, J. O. Jackson, and W.-J. Lin, "Gas discharge plasmas

are effective in inactivating Bacillus and Clostridium spores.," *Appl. Microbiol. Biotechnol.*, vol. 93, no. 6, pp. 2563–70, Mar. 2012.

[280] T. G. Klämpfl, G. Isbary, T. Shimizu, Y. F. Li, J. L. Zimmermann, W. Stolz, J. Schlegel, G. E. Morfill, and H. U. Schmidt, "Cold atmospheric air plasma sterilization against spores and other microorganisms of clinical interest," *Appl. Environ. Microbiol.*, vol. 78, no. 15, pp. 5077–5082, 2012.

[281] R. A. Venezia, M. Orrico, E. Houston, S.-M. Yin, and Y. Y. Naumova, "Lethal Activity of Nonthermal Plasma Sterilization Against Microorganisms," *Infect. Control Hosp. Epidemiol.*, vol. 29, no. 5, pp. 430–436, 2008.

[282] W. Lai, H. Lai, S. P. Kuo, O. Tarasenko, and K. Levon, "Decontamination of biological warfare agents by a microwave plasma torch," *Phys. Plasmas*, vol. 12, no. 2, p. 23501, 2005.

[283] S. P. Kuo, O. Tarasenko, S. Popovic, and K. Levon, "Killing of bacterial spores contained in a paper envelope by a microwave plasma torch," *IEEE Trans. Plasma Sci.*, vol. 34, no. 4 II, pp. 1275–1280, 2006.

[284] Z. Kovalova, K. Tarabová, K. Hensel, and Z. Machala, "Decontamination of Streptococci biofilms and Bacillus cereus spores on plastic surfaces with DC and pulsed corona discharges," *Eur. Phys. J. Appl. Phys.*, vol. 61, no. 2, p. 24306, 2013.

[285] T. Akitsu, H. Ohkawa, M. Tsuji, H. Kimura, and M. Kogoma, "Plasma sterilization using glow discharge at atmospheric pressure," *Surf. Coatings Technol.*, vol. 193, no. 1–3 SPEC. ISS., pp. 29–34, 2005.

[286] R. Ben Gadri, J. R. Roth, T. C. Montie, K. Kelly-Wintenberg, P. P.-Y. Tsai, D. J. Helfritch, P. Feldman, D. M. Sherman, F. Karakaya, and Z. Chen, "Sterilization and plasma processing of room temperature surfaces with a one atmosphere uniform glow discharge plasma (OAUGDP)," *Surf. Coatings Technol.*, vol. 131, no. 1–3, pp. 528–541, 2000.

[287] T. N. Nazina, T. P. Tourova, A. B. Poltaraus, E. V. Novikova, A. A. Grigoryan, A. E. Ivanova, A. M. Lysenko, V. V. Petrunyaka, G. A. Osipov, S. S. Belyaev, and M. V. Ivanov, "Taxonomic study of aerobic thermophilic

bacilli: Descriptions of Geobacillus subterraneus gen. nov., sp. nov. and Geobacillus uzenensis sp. nov. from petroleum reservoirs and transfer of Bacillus stearothermophilus [...] to G. Stearothermophilius [...]," *Int. J. Syst. Evol. Microbiol.*, vol. 51, no. 2, pp. 433–446, 2001.

Titre : Diagnostics et cinétiques des espèces réactives oxygénées et azotées dans des décharges hors-équilibre à pression atmosphérique pour la bio-décontamination

Mots clés : NRP, decontamination, RONS, QCLAS, spectroscopie d'émission absolue, PLIF

Résumé : Les méthodes de stérilisation à basse température prennent une importance croissante pour la décontamination de matériaux thermosensibles utilisés dans les appareils exposés aux risques microbiologiques tels que les endoscopes dans les hôpitaux, les emballages dans l'industrie agroalimentaire, ou les équipements soumis aux agents microbiologiques de guerre dans les zones de conflits. Les méthodes de stérilisation standards non-thermiques souffrent de limitations liées à leur toxicité, leurs coûts élevés, leurs faibles compatibilités avec les matériaux, et/ou leurs longs cycles de stérilisation (quelques heures). Une approche alternative consiste à utiliser des plasmas hors équilibre à pression atmosphérique produits par décharges électriques. Les plasmas permettent des cycles de stérilisation plus courts car les surfaces traitées sont exposées à de nombreux agents biocides, notamment à du rayonnement, à des espèces réactives oxygénées et azotées (RONS), et à des espèces chargées. Cependant, à pression atmosphérique, le volume du plasma est généralement faible. Les traitements en post-décharge permettent d'augmenter la surface de traitement, tout en réduisant la dégradation du matériau par les espèces chargées. Dans la post-décharge, les principaux agents biocides sont les RONS. L'objectif de cette thèse est d'étudier la production et le transport des RONS générés par des décharges pulsées non-thermiques dans l'air et l'azote à pression atmosphérique au moyen de diagnositcs de spectroscopie d'absorption UV et mid-IR (QCLAS), de fluorescence induite par laser (PLIF) et d'émission absolue.

Title : Diagnostics and kinetics of reactive oxygen and nitrogen species in atmospheric pressure non-equilibrium discharges for bio-decontamination

Keywords : NRP, decontamination, RONS, QCLAS, absolute emission spectroscopy, PLIF

Abstract : Low-temperature sterilization methods are of increasing importance for the decontamination of heat-sensitive materials in devices exposed to biohazards, such as endoscopes in hospitals, containers in the food industry, or contaminated equipment in areas exposed to war acts. Standard non-thermal sterilization methods suffer from limitations related to their toxicity, high cost, low material compatibility, and/or long sterilization cycles (several hours). An alternative approach consists in using atmospheric pressure nonequilibrium plasmas produced by electric discharges. Plasmas provide shorter sterilization cycles because they combine various biocidal agents including radiation, reactive oxygen and nitrogen species (RONS), and charged species. However, at atmospheric pressure the plasma volume is usually small. Post-discharge treatment allows to increase the treated surface area, and in addition to reduce surface degradation by charged species. In post-discharge treatment, the main biocidal agents are the RONS. The objective of this thesis is to study the production and transport of RONS generated by non-thermal pulsed discharges in nitrogen and air at atmospheric pressure by means of UV and mid-IR (QCLAS) absorption spectroscopy, planar laser induced fluorescence (PLIF), and absolute emission spectroscopy.